Freie Universität Berlin

Dissertation

Magnetic Impurities on a Superconductor: from Single Atoms to Coupled Chains

von

Michael Kleinert
(unter dem offiziellen Pseudonym Michael Ruby)

im
Fachbereich Physik
der
Freien Universität Berlin
eingereichte Dissertation

17.1.2017

Erstgutachterin: Prof. Dr. Katharina FRANKE

Zweitgutachterin: Prof. Dr. Stephanie REICH

Tag der Disputation: 22. Juni 2017

"The only source of knowledge is experience."

Albert Einstein (1879-1955)

Abstract

Magnetic Impurities on a Superconductor: from Single Atoms to Coupled Chains

by Michael KLEINERT

Motivated by one of the most intriguing devices in modern technology, the quantum computer, we investigate the interplay between magnetism and conventional superconductivity on the nano-scale. The inherent contradiction at the interface — magnetic versus superconducting order — promises topological edge states at the boundaries of the system. Moreover, these states may provide a stable system immune to quantum decoherence which is a prerequisite on the long term to bring quantum computation from the lab to a broad range of applications.

We study here the coupling of magnetic impurities on a conventional superconductor by means of low-temperature scanning tunneling microscopy (STM) and scanning tunneling spectroscopy (STS). This work comprises experiments that start with the bare superconducting substrate, and end at one-dimensional magnetic chains of nano-meter length scale adsorbed on the substrate's surface. Although lead (Pb) is among the best characterized type I superconductors available, we observed a subtle detail in the spectral intensity of superconducting lead (Pb) single crystals which, so far, has not been ambiguously explained: it is the double-peak nature of the superconducting gap. For the first time, it is proven experimentally by our experiment that Pb is a two-band superconductor.

Our journey continues to single non-magnetic adsorbates, which influence the transport properties from a probe electrode to the substrate. Introducing additionally a local magnetic moment induces bound states in the substrate at subgap energies. The experimental signature is a manifold of resonances in STS. In collaboration with theorists, we elaborated the transport mechanisms through these states. Finally, we could explain the formation of a *manifold* of subgap states by a *single* atomic transition metal impurity. Unlike previously anticipated, we found that it originates from the atomic orbitals of each impurity. Moreover, if two of such impurities lie close to each other, they form a dimer. Strong experimental evidence was found that bonding and anti-bonding states are formed by hybridization of subgap states with different symmetries. The strength of the hybridization depends on the relative orientation and distance with respect to each other.

In the end, we focus on larger systems, namely on nano-meter scale one-dimensional transition metal chains. The coupling within the chain is of a ferromagnetic order. Nevertheless, proximity to the substrate induces superconductivity within the chain, and sets the system into a topological regime. At this limit, so-called Majorana zero modes (MZMs) had been predicted to be localized at the ends of the chains. Those are prime candidates for fault-tolerant information storage in quantum computers. We elucidate the subtle differences in the spectroscopic details of two different systems, namely in iron (Fe) and cobalt (Co) chains. Only the first provided evidence for MZMs. In collaboration with theorists, we suggest a possible explanation for this behavior.

All these investigations ask for further experiments on similar systems. As an outlook, we provide preliminary results of manganese (Mn) chains with substantially different structures.

Kurzfassung

Magnetic Impurities on a Superconductor: from Single Atoms to Coupled Chains

von Michael KLEINERT

Motiviert durch die Vision des Quantencomputers untersuchten wir die Wechselwirkung zwischen Magnetismus und Supraleitung auf der Nanoebene. Es wird angenommen, dass der Widerspruch zwischen supraleitender und magnetischer Ordnung zu topologischen Zuständen an der Grenzschicht zwischen beiden Ordnungen führt. Diese vielversprechenden Zustände könnten die Dekohärenz von Quanten-Zuständen vermeiden, unter welcher aktuelle Experimente zu Quantencomputern leiden.

Die Kopplung von magnetischen Atomen, die auf der Oberfläche eines konventionellen Supraleiters adsorbiert sind, wurden mit Hilfe von Rastertunnelmikroskopie und -spektroskopie untersucht. Unsere Experimente begannen mit Messungen an der sauberen Substratoberfläche und endeten bei eindimensionalen Ketten magnetischer Atome mit Nanometerlänge. Obwohl Blei zu den am besten charakterisierten Typ I Supraleitern zählt, konnte die in Experimenten beobachtete Doppel-Peak Struktur der supraleitenden Bandlücke bis zu unserer Untersuchung nicht eindeutig erklärt werden. Wir zeigten experimentell, dass diese Struktur auf die Zwei-Band-Supraleitung in Blei zurückgeführt werden kann.

Nach Aufbringen nicht-magnetischer Atome auf einen Bleikristall untersuchten wir deren Einfluss auf die Transport-Eigenschaften zwischen der Spitze und der Oberfläche der Probe. Bei Durchführung des Experiments mit Atomen der Übergangsmetalle, welche ein zusätzliches magnetisches Moment besitzen, konnten wir zusätzliche lokalisierte und gebundene Zustände bei Energien innerhalb der supraleitenden Bandlücke finden. Durch die Kombination von Theorie und Experiment konnten wir den Transport durch diese Zustände erklären. Schließlich widmeten wir uns der Frage, wie ein einzelnes Atom eine Vielzahl solcher Zustände erzeugen kann. Anders als bisher angenommen sehen wir, dass im Falle von Einzelatomen deren jeweilige Atomorbitale für diese Zustände verantwortlich sind.

Der nächste Schritt unserer Untersuchung befasste sich mit der Kopplung von Atomen in Dimeren. Wir fanden bindende und antibindende Gesamtzustände vor, welche durch die Hybridisierung der lokalen Einzelzustände erzeugt wurden und von der Symmetrie und dem Abstand der Atome im jeweiligen Dimer abhingen.

Abschließend untersuchten wir eindimensionale magnetische Übergangsmetallketten von mehreren Nanometern Länge. Die Ketten waren ferromagnetisch, wurden jedoch durch die Nähe zum Bleisubstrat supraleitend. Dies erzeugte an den Enden der Ketten lokalisierte topologische Zustände, die sogenannten Majorana-Zustände. Diese spielen möglicherweise eine wichtige Rolle für die Entwicklung von fehlerresistenten Quanten-Speichern. In unseren Forschungen fanden wir Unterschiede zwischen Eisen- und Kobalt-Ketten. Nur in Eisen-Ketten zeigten sich Majorana-Zustände. In Zusammenarbeit mit Theoretikern konnten wir zeigen, dass sich dies möglicherweise durch eine Änderung des Fermi-Niveaus erklären lässt.

All diese Resultate weisen darauf hin, dass weitere Experimente an ähnlichen System erforderlich sind. Als Ausblick präsentierten wir einige unserer vorläufigen Resultate von Messungen an Mangan-Ketten, welche eine völlig unterschiedliche Struktur zu den Eisen- und Kobalt-Ketten aufweisen.

Contents

Chapter 1

Magnetism and superconductivity: a path towards quantum computers

The ignition point of nano-physics dates back to the late 1950s, when physicists started to have a vision of nanoscopic devices, built from scratch, atom by atom. One of the most cited contributions was R.P. Feynman's talk at CALTECH in 1959, entitled "There's Plenty of Room at the Bottom". A major breakthrough in this field was the invention of the scanning tunneling microscope in 1981 which allowed the imaging of surfaces and adsorbates in atomic scale precision.

The difference between nanoscopic devices and their larger classical counterparts is the non-deterministic quantum behavior of the former. At nanoscopic length scales, effects such as the uncertainty principle set in. This settles an unbreakable barrier to the ongoing miniaturization of classical devices and circuits of today's information technology.

1.1 Classical versus quantum computation

Classical computer chips require deterministic results. They store information, and perform calculations in units of bits, which are represented by currents controlled via transistors. Either the circuit is open (representing a binary 0), or closed (representing a binary 1). An operational unit manipulating such states is called a *gate*.

In a quantum device, the information is stored by the wave function of a physical system, a so-called *qubit*. In such a device, only probabilities (a^2 and b^2) are fixed to find the qubits in a specific state ($a\left|1\right\rangle + b\left|0\right\rangle$). Certainly, in larger physical systems more than two levels are imaginable. The quantum gates performing operations on the qubits are designed to induce constructive and destructive interference of the wave function, such that they reduce or increase selectively the amplitudes a^2 and b^2. This is done by manipulation of the phase factor. The final result is then obtained *after* all operations of the quantum gates by simply 'measuring' the final state of the system.

In the 1980s several proposals had the long term vision to use the non-deterministic behavior of a quantum state to actively process information [1, 2]. An important milestone in this emerging field was the publication of an efficient algorithm that factorizes large integers into their prime number components by P.W. Shor in 1994 [3]. It scales only polynomially with the length of the number N, compared to its classical counterpart which scales exponentially in N. Most of today's public-private key encryption methods used in the end-to-end communication of modern computer networks rely on this fact (e.g. the RSA algorithm [4]). It is an unsolvable task for classical systems to factorize large numbers N.

Another charming capability of quantum computation is the so-called quantum annealing, which solves optimization algorithms in far less time [5–8]. It targets technical topics, for example in database searches, path finding algorithms, and financial markets. It is also useful in reasearch, for example in physical simulations of large systems. A prominent use case for the latter are protein folding dynamics in bio-physics. There, it is of immense computational cost to obtain an optimized spatial structure of a large molecule on a classical computer, as the problem is defined in a high-dimensional parameter space. Classical optimization algorithms, such as the Levenberg-Marquardt [9] or Nelder-Mead [10] algorithm, start with an initial set of parameters, and 'walk' step-by-step through the multi-dimensional potential landscape until they are trapped in a local, or at best, in the global minimum. Independent of the algorithm, this optimization method is prone to steep local minima, and therefore it requires a careful choice of the initial conditions. Generally speaking, one has to know in advance a roughly optimized set of parameters, or use some tricks to avoid the trapping at local minima. E.g., by simulated annealing one randomly increases some parameters to jump out of a local minimum. In a quantum computer the parameters are encoded in a quantum mechanical state. Thus, the system tends to transit by itself to the global potential minimum, namely its ground state. This is even possible without any external influence by quantum tunneling through the potential barriers.

1.2 Open challenges in quantum computation

A major challenge in the development of quantum computers is to reduce the sources of external perturbations. This increases the decoherence time of the wave function at which the information encoded in the quantum state is lost. On the other hand, within that time, the system must allow a control by an external circuit. The initial state prior to the calculation has to be set, the logical operations have to be performed successively, and finally the state of the system has to be measured to obtain the outcome.

In the mid 1990s, the first lab experiments started with a few qubits at the NATIONAL INSTITUTE OF STANDARDS AND TECHNOLOGY in Colorado by using a trapped atom [11]. Afterwards, it was demonstrated that devices made up by such 'natural' systems can efficiently solve simple algorithms. The trapped ions were cooled to their ground-state where all degrees of freedom freeze out [11, 12]. Later, one focussed on the more isolated spins of nuclei, using the well-established technique of nuclear magnetic resonance (NMR) at larger ensembles [13, 14]. Experiments with solid state devices stood in contrast to these approaches. Here, the quantum information is encoded in excitations, e.g., in the spin of a quantum dot [15]. A breakthrough was the first commercially available quantum computation chip, published in 2008 by the company D-WAVE SYSTEMS. It was based on circular Josephson junctions, and encoded information in magnetic flux quanta [16]. However, the challenge to reduce quantum decoherence effects remains. The experiments rely on a proper cooling to milli-Kelvin temperatures, and devices for real world scenarios require error correction algorithms.

A new idea targeting this issue is topological quantum computation (TQC), which seeks to store the information in a way that it is protected to any kind of external perturbation. It is based on topological phases of many-body systems — a topic, which also gained the Nobel prize in 2016 to D.J. Thouless, F.D.M. Haldane, and J.M. Kosterlitz. In a topological system, the information can be stored in a non-local way. Physically, a qubit in such a system comprises two spatially separated states that do not appear individually in any Hamiltonian. Weak local perturbations, such as the noise of a gate electrode can only act on a pair of states. Therefore, the system is immune to any local interaction which unlikely acts on both states simultaneously if they are separated in space, and allow the realization of fault-tolerant topological quantum computation.

An approach to find a system that enters such a topological state, is to combine two types of order, magnetism and conventional superconductivity. Each order by itself is well understood. Until now, people also described theoretically the fundamental mechanisms of the interaction of a local magnetic moment with a superconductor. However, experimentally many questions were unsolved. Moreover, the advances in experimental techniques provide a higher energy resolution which may reveal subtle, formerly hidden spectroscopic features. As it turns out, even in the simplest type of system such features are found, namely at single magnetic atoms adsorbed on a conventional superconductor. This requires a reinterpretation of earlier experimental observations, before proceeding to larger nano-structures, which may be suitable candidates for topological systems.

1.3 Outline

The topics discussed in this thesis are sketched in fig. 1.1. From left to right we start from scratch with a clean substrate, and end at a larger, nanoscopic system. We first characterize the clean superconducting substrates employed in the follow-up experiments, and clarify spectroscopic details, such as the — so far — unambiguously explained double-gap structure of the superconducting gap. We continue with the investigation of the influence of non-magnetic adsorbates on the transport to the superconducting substrate. We proceed with changing the impurity to a transition metal element, giving it a magnetic moment. A pure potential scatterer has no effect on the delocalized many-body ground state of the superconductor. However, a magnetic impurity breaks time-reversal symmetry, which introduces local bound states within the superconducting

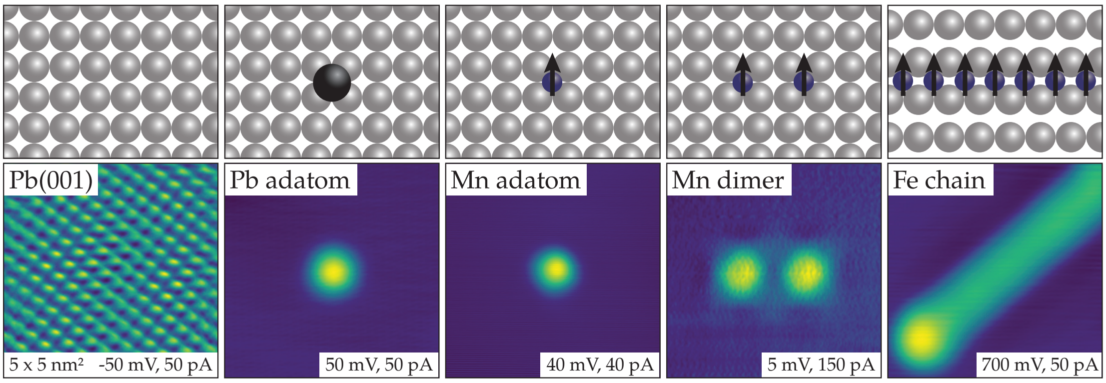

FIGURE 1.1: Topics discussed in this thesis (from left to right). The system is sketched in the top row, and the analogous experimental observation is given in the bottom row. First, spectroscopic details on the bare substrate are discussed. Second, the influence of non-magnetic local impurities on the transport process is investigated. Third, local bound states induced by magnetic adatoms are analyzed. The transport through these states, the nature of these states, and their lateral decay within the substrate are treated. Fourth, evidences for the coupling between two adatoms are given. Finally, the properties of magnetic transition metal chains are mapped, and the dependence of the acquired data on the element of the chain is tested.

gap by exchange scattering with the many-body system. We also investigate in detail the transport mechanisms through these states, their nature, and their lateral decay within the substrate. With this knowledge, we continue with two atoms at close distance, where the local bound states start to overlap, and finally couple. Last but not least, we investigate the properties of linear nanoscopic transition metal chains, where we observe signatures of states localized at the end of iron (Fe) chains. These states are predicted to be a key ingredient in TQC. Finally, we test the universality of their appearance with different transition elements as alternative building blocks of the chains. The majority of the results presented in this thesis were published in peer-reviewed research articles. They are reprinted in appendix B.

In each chapter we first introduce the theoretical background and finally present the main message of the article, which puts the individual publications into a larger framework. Unpublished results are discussed in more detail. Chapter 2 starts with experiments on the clean superconductor. In chapter 3 we continue with experiments on single atomic adsorbates. Finally, in chapter 4, we discuss the one-dimensional transition metal chains. A summary and an outlook to the upcoming challenges in this field of research are given in chapter 5. The experimental methods employed in this work are described in appendix A, where also the evaluation software written by the author of this thesis is briefly introduced.

Chapter 2

Lead (Pb): a (not so) simple conventional superconductor

In the last decades, experiments on superconductors gained a large interest, as they possess some unique properties. They have a small energy gap in the band structure around the Fermi energy, and show a characteristic behavior under the influence of an external magnetic field. We briefly introduce the basics of superconductivity in section 2.1, and discuss the mechanism of Bardeen-Cooper-Schrieffer (BCS) or 'conventional' superconductivity in section 2.2. Then, we have a detailed look at the superconductivity of lead (Pb) single crystals in section 2.3. It is of a BCS-type nature, but details in spectroscopy reveal a two-band character. The sample preparation is described in appendix A.4.

2.1 Introduction to superconductivity

Superconductivity describes the spontaneous drop of resistance, which appears in many solids if they are cooled below a critical temperature. For pure elements within the periodic table, those with the highest transition temperatures are niobium (Nb) (9.5 K), technetium (Tc) (7.8 K), and lead (Pb) (7.2 K). Low temperatures, required to observe the drop of resistance, hindered the discovery of superconductivity. Only after the technologically challenging liquefaction of helium (He) by H.K. Onnes in 1908 the basis for superconductivity was laid. In addition, he was the first in 1911, who observed the loss of resistance in mercury (Hg) when cooled below 4.2 K. Both discoveries awarded him the Nobel Prize in 1913.

The first phenomenological description of superconductivity was based on the observation of the Meissner-Ochsenfeld effect, which is the perfect diamagnetic behavior of superconductors below a critical external magnetic field (susceptibility $\chi = -1$). Two brothers, E. and F. London, suggested that the total expel of a magnetic field requires an electron density at the surface that flows in a circular current to compensate the external field. Within a thin layer the external field decays exponentially with $e^{-x/\lambda}$. The penetration depth λ is usually in the order of several tenth of nanometers.

An important theoretical step forward in the understanding of superconductivity was the Ginzburg-Landau theory [17]. It treats superconductivity in terms of a second order phase transition, in accordance with the general Landau theory of phase transitions [18]. The free energy $F(\mathbf{r}, T)$ of the system in the Landau expansion is given by

$$F(\mathbf{r}, T) = F_0(\mathbf{r}, T) + \alpha|\psi|^2 + \frac{\beta}{2}|\psi|^4 + \alpha\xi^2|\nabla\psi|^2 \,. \tag{2.1}$$

The parameters α and β are phenomenological. The so-called order field ψ is obtained by a mean-field approach. It describes the superconducting electrons. Later on, we will define it as the superconducting wave function. The last term originates from the interaction between the electrons in the system. It implies the existence of a coherence length ξ, and it defines the length scale over which the order field varies. For Pb at zero temperature, the length scale is $\xi_0 = 96$ nm [19]. It gets as large as $\xi_0 = 1600$ nm for aluminum (Al) [20]. The ratio between the two length scales λ and ξ is the Ginzburg-Landau-parameter $\kappa = \lambda/\xi$. It is used to classify superconductors into two types: In a type I superconductor the coherence length is much larger than the penetration depth ($0 < \kappa < 1/\sqrt{2}$). Thus superconductivity is maintained up to a critical field. For a type II superconductor the penetration depth is much larger than the coherence length ($\kappa > 1/\sqrt{2}$), which allows the field to penetrate the material even at low fields in certain domains by the formation of vortices [21]. The actual size of the parameters λ and ξ, however, can only be determined in a microscopic description of superconductivity.

The most important milestone was reached in 1957 with the so-called BCS theory. It was observed that not only different elements show different transition temperatures, but also different isotopes of the same element. This so-called 'isotope effect' was already reported in 1950 for the species ^{202}Hg and ^{198}Hg [22]. The effect requires that superconductivity depends on the weight of the nuclei, and hence that lattice vibrations of the solid (phonons) play a crucial role.

2.2 BCS theory of superconductivity

The BCS theory of superconductivity, published in 1957 [23, 24], earned J. Bardeen, L.N. Cooper, and J.R. Schrieffer the Noble Prize in physics in 1972. The quantum mechanical Hamiltonian of the system considers all interactions between the electrons and the lattice:

$$H = H_{\text{el.}-\text{el.}} + H_{\text{ph.}-\text{ph.}} + H_{\text{el.}-\text{ph.}} \,. \tag{2.2}$$

The components on the right side in eq. (2.2) are given by the electron-electron, the phonon-phonon, and the electron-phonon interaction, respectively:

$$H_{\text{el.}-\text{el.}} = \sum_{\mathbf{k},\sigma} \varepsilon_{\mathbf{k}}\, a^{\dagger}_{\mathbf{k},\sigma}\, a_{\mathbf{k},\sigma} + \sum_{\mathbf{k}',\mathbf{k},\mathbf{q},\sigma,\sigma'} V_{\text{Coulomb}}(\mathbf{k},\mathbf{k}',\mathbf{q})\, a^{\dagger}_{(\mathbf{k}+\mathbf{q}),\sigma}\, a^{\dagger}_{(\mathbf{k}'-\mathbf{q}),\sigma'}\, a_{\mathbf{k},\sigma}\, a_{\mathbf{k}',\sigma'} \tag{2.3}$$

$$H_{\text{ph.}-\text{ph.}} = \sum_{\mathbf{k}} \omega_{\mathbf{k}}\, C^{\dagger}_{\mathbf{k}}\, C_{\mathbf{k}} \tag{2.4}$$

$$H_{\text{el.}-\text{ph.}} = \sum_{\mathbf{k}',\mathbf{k}} M_{\mathbf{k}',\mathbf{k}} C_{(\mathbf{k}'-\mathbf{k})}\, a^{\dagger}_{\mathbf{k}',\sigma}\, a_{\mathbf{k},\sigma} + \sum_{\mathbf{k}',\mathbf{k}} M^{*}_{\mathbf{k}',\mathbf{k}} C^{\dagger}_{(\mathbf{k}'-\mathbf{k})}\, a^{\dagger}_{\mathbf{k},\sigma}\, a_{\mathbf{k}',\sigma} \,. \tag{2.5}$$

Here, $a^{\dagger}_{\mathbf{k},\sigma}$, $a_{\mathbf{k},\sigma}$ and $C^{\dagger}_{\mathbf{k}}$, $C_{\mathbf{k}}$ are the electron and phonon creation and annihilation operators, respectively. The initial electron momenta $\mathbf{k}$ and $\mathbf{k}'$ are changed by the momentum $\mathbf{q}$ that is transferred between the electrons with spin σ. The energy of the electrons is introduced by $\varepsilon_{\mathbf{k}}$, and the energy of the phonons by $\omega_{\mathbf{k}}$. The size of the Coulomb repulsion between the electrons is expressed by V_{Coulomb}, and the scattering amplitude between electrons and phonons by $M_{\mathbf{k}',\mathbf{k}}$.

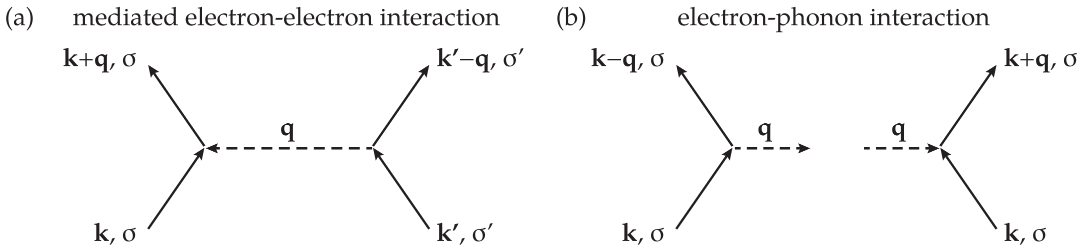

FIGURE 2.1: Interactions described by the Hamiltonians in eq. (2.5). (a) Electron-electron interaction mediated by a photon or a phonon q, which changes the electron momenta $\mathbf{k}$ and $\mathbf{k}'$, and leaves the electron spin σ unchanged. (b) Electron-phonon interaction leading to an emission or an absorption of a phonon. Diagrams adapted from [20].

The interactions described by the Hamiltonians are sketched as Feynman diagrams in fig. 2.1(a) and (b). The electron-electron interaction is mediated by the emission and re-absorption of a photon or a phonon. The electron-phonon interaction leads to a phonon-creation or -annihilation by the scattering of an electron, which is possible because the number of phonons is not conserved.

The Coulomb interaction is commonly known to induce a long-range repulsion between two electrons. Notwithstanding this common knowledge, L.N. Cooper discovered that, under certain conditions, the weak attractive electron-phonon interaction excels the Coulomb repulsion. In an intuitive picture, he considered that the time scales of both interactions are inherently different. The Coulomb repulsion is an instantaneous process, as it is mediated by a photon. In direct comparison, the coupling of electrons via phonons is slow, as the decay of lattice vibrations is slow. Thus, the electron travels a long distance after an interaction, before the phonon decays. Within that time a second electron can interact with the not-yet-decayed phonon, without being repelled by the first electron. This leads to a weak attractive interaction over a range in the order of the coherence length ξ.

However, the maximum energy transferred through phonons is limited by the Debye frequency ω_D, which is two to three orders of magnitude smaller than typical electronic energies defined by the Fermi energy E_F. Hence, the attractive interaction mediated by phonons is weak, whereas the repulsive electronic interaction is strong. Therefore an overall attractive interaction is achieved only for the smallest possible value of the Coulomb repulsion. A Fourier transformation of the Coulomb potential for two electrons to reciprocal space gives:

$$\begin{aligned} V_\mathrm{Coulomb}(r) &= \frac{e^2}{r} \\ V_\mathrm{Coulomb}(\mathbf{q}) &= \frac{4\pi e^2}{\mathbf{q}^2} \\ V_\mathrm{Coulomb}(\mathbf{q}) &= \frac{4\pi e^2}{\mathbf{q}^2 + (1/r_0)^2}\,. \end{aligned} \tag{2.6}$$

Here $\mathbf{q}$ is the difference between the momenta of both electrons. The last equation includes a shielding of the electrons in the range of r_0, which avoids the unphysical divergence at $\mathbf{q} = 0$. Hence, the electrons must have opposite momenta $\mathbf{k} = -\mathbf{k}'$ to decrease the repulsive potential as much as possible. Furthermore, the exchange energy is the weakest for electrons with opposite spin. All these conditions allow to summarize

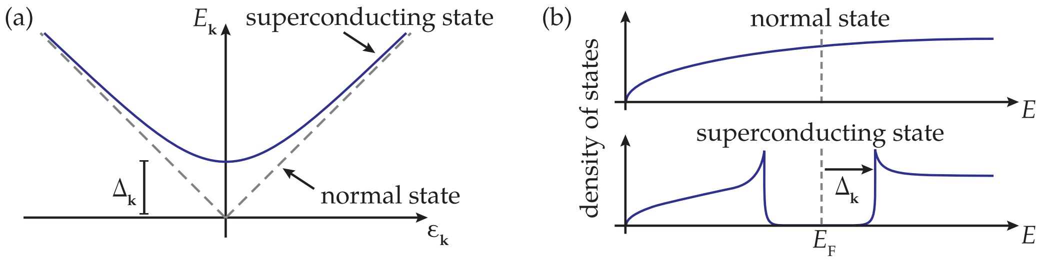

FIGURE 2.2: (a) Dispersion relation of the single-particle excitation energy $E_{\mathbf{k}}$ in comparison to the normal state energy $\varepsilon_{\mathbf{k}}$. (b) Single-particle density of states of a 3D metal in the normal state ($\sqrt{E}$ behavior), and in the superconducting state with a gap of $2\Delta_{\mathbf{k}}$ around the Fermi level E_{F}.

the interactions in a mean-field approach, with an effective attractive potential $V_{\mathbf{k}',\mathbf{k}}$ for particles with opposite spin and momenta, and for energies in the range of $\hbar\omega_{\mathrm{D}}$ around the Fermi level. This simplifies eq. (2.5) to:

$$H = \sum_{\mathbf{k},\sigma} \varepsilon_{\mathbf{k}} a^{\dagger}_{\mathbf{k},\sigma} a_{\mathbf{k},\sigma} + \sum_{\mathbf{k}',\mathbf{k},\sigma} V_{\mathbf{k}',\mathbf{k}}\, a^{\dagger}_{\mathbf{k},\sigma}\, a^{\dagger}_{-\mathbf{k},-\sigma}\, a_{-\mathbf{k}',-\sigma}\, a_{\mathbf{k}',\sigma}\,. \tag{2.7}$$

An important operation within the BCS theory was the adaptation of a Bogoljubov transformation to a system of fermions[1]. The system gets unstable against the formation of a new ground state of paired states in **k**-space, the so-called *Cooper-pairs* [26]. A gap-operator Δ is introduced, which is determined by the expectation value of a pair occupied or unoccupied [20]:

$$\Delta^{(\dagger)}_{\mathbf{k}} \equiv - \sum_{\mathbf{k}',\mathbf{k}} V_{\mathbf{k}',\mathbf{k}} \left\langle a^{(\dagger)}_{\mathbf{k},\sigma}\, a^{(\dagger)}_{-\mathbf{k},-\sigma} \right\rangle . \tag{2.8}$$

All other particles are transformed to spinless non-interacting quasi-particles $\eta^{(\dagger)}_{\mathbf{k}}$ and $\gamma^{(\dagger)}_{\mathbf{k}}$, which are linear combinations of the single electron operators $a^{(\dagger)}_{\mathbf{k}}$:

$$\begin{aligned} a_{\mathbf{k},\uparrow} &= u^{*}_{\mathbf{k}}\eta_{\mathbf{k}} + v_{\mathbf{k}}\gamma^{\dagger}_{\mathbf{k}} \\ a^{\dagger}_{-\mathbf{k},\downarrow} &= -v^{*}_{\mathbf{k}}\eta_{\mathbf{k}} + u_{\mathbf{k}}\gamma^{\dagger}_{\mathbf{k}}\,. \end{aligned} \tag{2.9}$$

The amplitudes $u_{\mathbf{k}}$ and $v_{\mathbf{k}}$ fulfill the relation $|u_{\mathbf{k}}|^2 + |v_{\mathbf{k}}|^2 = 1$ and give the probability to find a Cooper pair occupied or empty, respectively. Finally, the Hamiltonian becomes

$$H = \sum_{\mathbf{k},\sigma} \left(\varepsilon_{\mathbf{k}} + \Delta_{\mathbf{k}} \left\langle a^{\dagger}_{\mathbf{k},\sigma} a^{\dagger}_{-\mathbf{k},-\sigma} \right\rangle \right) + \sum_{\mathbf{k}} \sqrt{(\varepsilon_{\mathbf{k}} - \mu)^2 + \Delta^2_{\mathbf{k}}} \left(\eta^{\dagger}_{\mathbf{k}}\eta_{\mathbf{k}} + \gamma^{\dagger}_{\mathbf{k}}\gamma_{\mathbf{k}} \right) \ . \tag{2.10}$$

All single particle excitations have to break a Cooper-pair, which requires a minimum energy of $\Delta_{\mathbf{k}}$:

$$E_{\mathbf{k}} = \sqrt{(\varepsilon_{\mathbf{k}} - \mu)^2 + \Delta^2_{\mathbf{k}}}\,. \tag{2.11}$$

Here, μ is the chemical potential and $\varepsilon_{\mathbf{k}}$ the energy of a free electron in its normal conducting state. A comparison between the normal state and the superconducting state dispersion around zero energy is sketched in fig. 2.2(a). The particle-hole symmetry

---

[1] The initial Bogoljubov transformation was developed for bosons [25].

of the Hamiltonian in eq. (2.10) is an important property of superconductors. The condensate degree of freedom of the Cooper-pairs allows a hole to be transformed to a particle by the annihilation of a pair, and vice versa. This is of special interest if impurities are introduced to the system that break this symmetry. Such a scenario is discussed in section 3.2.

2.2.1 Superconducting density of states

In our experiment, we measure the conductance from the tip to the sample under variation of a bias voltage applied to the sample. The method of scanning tunneling spectroscopy (STS) is described in appendix A.2. The quantity we are interested in is usually the DOS of the sample. If we know the dispersion relation for single-particle excitations, we can derive the density of states easily by the integral over the momentum space:

$$N = V \int \frac{\mathrm{d}^3 p}{(2\pi)^3} = V \frac{4\pi}{(2\pi)^3} \int \mathrm{d}p \, p^2 = V \frac{4\pi}{(2\pi)^3} \int \mathrm{d}E \frac{1}{\mathrm{d}E/\mathrm{d}p} \, p^2 \,. \tag{2.12}$$

The dispersion relation for a conventional superconductor is given in eq. (2.11). We can transform this to

$$\frac{\mathrm{d}E}{\mathrm{d}p} = \frac{\partial E}{\partial \varepsilon} \frac{\mathrm{d}\varepsilon}{\mathrm{d}p} = \frac{\varepsilon - \mu}{\sqrt{(\varepsilon - \mu)^2 + \Delta^2}} \frac{p}{m_\mathrm{e}} = \frac{\sqrt{E^2 - \Delta^2}}{E} \frac{p}{m_\mathrm{e}} \,. \tag{2.13}$$

If we insert eq. (2.13) into eq. (2.12), and if we approximate that only a small range of energies around the Fermi level contributes to the current ($p = \sqrt{2mE_\mathrm{F}} = \text{const.}$), we obtain for the DOS:

$$\rho(E, \Delta) = \frac{\mathrm{d}N}{\mathrm{d}E} \frac{1}{V} = \sqrt{\frac{E_\mathrm{F} m_\mathrm{e}^3}{2\pi^4}} \, \Re\left(\frac{E}{\sqrt{E^2 - \Delta^2}} \right) \propto \Re\left(\frac{E}{\sqrt{E^2 - \Delta^2}} \right) . \tag{2.14}$$

It shows a gap of width 2Δ around the Fermi energy, which is sketched in fig. 2.2(b). At the gap edges, the DOS diverges into narrow quasiparticle resonances (QPRs) at $\pm\Delta$.

2.3 Scanning tunneling spectroscopy (STS) on Pb

Tunneling experiments are perfectly suited to probe superconductors and their properties, as they directly measure the electronic structure in the vicinity of the Fermi level with a high energy resolution. The prime candidate experiment to determine the band structure of a material — angle-resolved photo-emission spectroscopy (ARPES) — lacks the required energy resolution for superconducting gaps, which are usually in the order of a few meV. Thermal broadening sets the limit for the achieved resolution, and it would require cooling to millikelvin temperatures. However, tunneling experiments can overcome this limit by using a superconducting tip.

2.3.1 Spectroscopy with superconducting tips

The energy resolution of metal tips is limited by thermal occupation of the DOS. Following Fermi-Dirac statistics, each electrode has an electron distribution at the Fermi level with a full width at half maximum (FWHM) of $3.5\,k_\mathrm{B}T$. At a temperature of ≈ 1.1 K this leads to a Gaussian-like broadening of ≈ 331 μeV. If we cover the tip with a thick

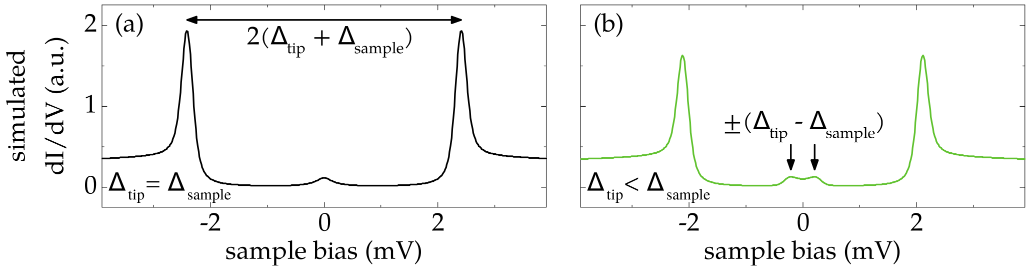

FIGURE 2.3: Simulated dI/dV spectra at elevated temperatures. In (a) the tip gap is equal to the sample gap ($\Delta_{tip} = \Delta_{sample} = 1.2$ mV), whereas in (b) is is smaller ($\Delta_{tip} = 1.0$ mV). Only in (b) the zero bias resonance is split. Spectra with a line shape as shown in (a) indicate good quality of the superconducting tip.

layer of Pb, the apex gets superconducting. This is done by deep indentations into the clean Pb surface while applying a high voltage. The DOS of the tip follows BCS theory. Together with an elaborated grounding and radio frequency filtering setup this yields an effective energy resolution of ≈ 50 μeV. However, it comes at the cost of a convolution of the densities of states of tip and substrate. Mainly, this induces an energy shift of all spectroscopic features in the sample by $\pm\Delta_{tip}$.

The tip quality after indentation is controlled by dI/dV spectra on the pristine substrate. For a good tip, this results in spectral line shapes resembling the textbook example of a superconductor-superconductor junction. If the tip and sample gaps are almost equal ($\Delta_{tip} \simeq \Delta_{sample}$) the measured gap of zero conductance amounts to $2(\Delta_{tip} + \Delta_{sample})$ [27]. At elevated temperatures (4.5 K), an additional zero bias resonance is found because of tunneling of thermally excited quasiparticles across the gap (see fig. 2.3).

SpectraFox, a software for data deconvolution and evaluation

Most of our experimental data is measured with superconducting tips. Hence, a deconvolution is required to extract the desired quantity, the sample DOS from the measured spectral intensity. We implemented such a procedure in the software 'SpectraFox', which was written in the framework of this thesis. In this software, we use an inverse approach. We convolve the DOS of a superconducting tip with a theoretical model of the superconducting DOS of the sample, and fit the result to the experimental data. This evaluation technique successfully contributed to several publications [28–33].

Furthermore, we extended the software to provide an elaborate system for displaying, evaluating and managing the experimental data of scanning tunneling microscopes of various manufacturers. An article describing all features of the software is published by M. Ruby. "SpectraFox: A free open-source data management and analysis tool for scanning probe microscopy and spectroscopy". In: *SoftwareX* 5 (2016), pp. 31–36. ISSN: 2352-7110. It is reprinted in appendix B.1. After publication of the article, the software was made publicly available under an open source license. It is thus open to other scientists. At the time of publication, the source code comprised $\approx$ 43 000 lines of code.

SpectraFox contributed a major part to the data evaluation presented in this thesis. It was furthermore used in Refs. [28–33, 35].

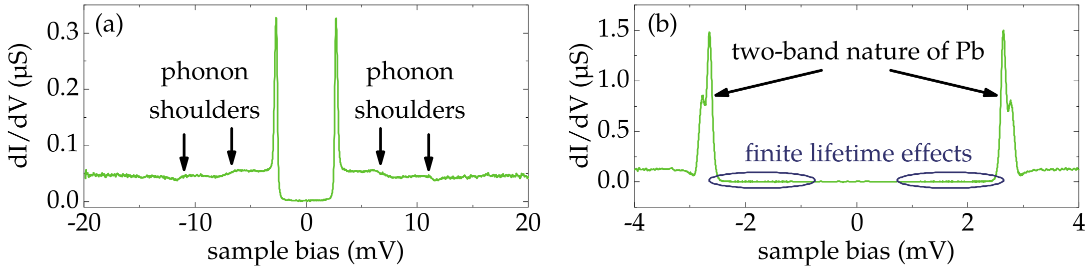

FIGURE 2.4: Experimental dI/dV-spectra on bare Pb(100), measured with a superconducting tip. Setpoints: (a) 20 mV, 900 pA, (b) 4 mV, 400 pA. Deviations from the ideal BCS-DOS are pinpointed. In (b), effects from finite lifetime of the quasi-particles are not observed, but the regions are marked where a finite signal is expected.

2.3.2 Experiment vs. theory: spectral features of lead (Pb)

Soon after the development of the BCS formalism, tunneling experiments on planar tunnel junctions were carried out on a variety of single crystal substrates. It turned out that even elemental superconductors such as Pb, vanadium (V), or tantalum (Ta) showed deviations from the expected BCS description of the DOS, which is given in eq. (2.14). In the particular example of Pb, effects from a finite quasi-particle lifetime, from strong electron-phonon coupling, and from the two-band nature of the substrate are observed. The deviations are highlighted in fig. 2.4.

Finite lifetime effects on the DOS

A common correction applied to eq. (2.14) when comparing it to experimental data is an additional broadening term, modeled by an imaginary damping factor $i\Gamma$ — often referred to as 'Dynes parameter' [36]. It transforms all energies E to $(E + i\Gamma)$, and accounts for a finite lifetime of the Cooper-pairs under a finite current, or for crystals with high impurity concentrations. In an intuitive picture, a current adds a common drift moment $\mathbf{K}$ to the Cooper-pairs, which slightly lifts the time-reversal symmetry for quasi-particles with opposite momenta $\mathbf{k} + \mathbf{K}$ and $-\mathbf{k} + \mathbf{K}$. This smears out the DOS, as it reduces the gap in this direction, and leads to a finite spectral intensity at subgap energies in the range $2\Delta > \varepsilon > \Delta$ [see fig. 2.4(b)]. However, none of these features were observed in most of our measurements.

Superconductors with strong electron-phonon coupling

Lead (Pb) has the special property of possessing a strong electron-phonon coupling. It implies that approximations made within the BCS framework become inaccurate. In particular, considering only electrons within the range of the finite energy cut-off with the highest phonon energy — the Debye frequency — the approximations do not hold anymore. Instead, electrons in a larger energy range have to be considered, especially, where the phonon DOS shows van Hove singularities. This leads to an energy dependent gap operator $[\Delta \rightarrow \Delta(E)]$ [37]. In dI/dV-spectra measured with a superconducting tip on Pb, so-called 'phonon shoulders' emerge at $\simeq \pm 11.1$ meV and $\simeq \pm 6.6$ meV [see fig. 2.4(a)]. They result from the phonon branches at 4.0 meV and 8.3 meV [38], respectively, as the sum of tip and sample gap gives an additional offset of $\simeq 2\Delta \approx 2.7$ meV to the energies of the van Hove singularities.

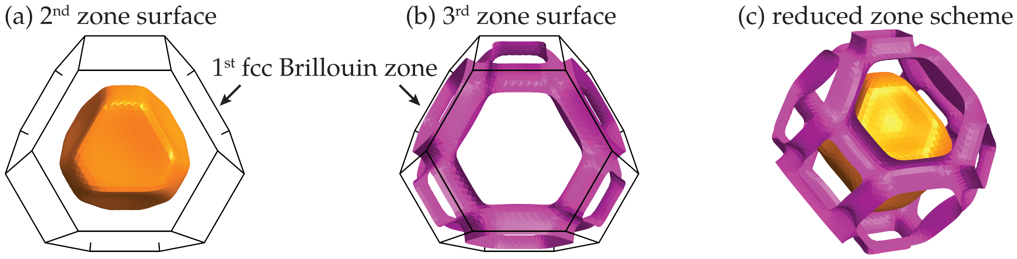

FIGURE 2.5: Fermi surface of Pb plotted in the reduced zone scheme in the first *fcc* Brillouin zone. The Fermi surface consists of a second zone surface (a) and a third zone surface (b), which are well separated from each other (c). The plotted Fermi surface data is from Ref. [43].

The two-band nature of Pb

Early measurements in planar Pb tunneling junctions with a high energy resolution revealed a spectrum with two QPRs, and thus two distinct gap parameters Δ [39–42] [see also fig. 2.4(b)]. The first interpretation of these experiments targeted the crystal anisotropy, which is reflected in both, the electronic and the phonon band structure. Especially the latter plays a crucial role in BCS theory.

Details of the Fermi surface of Pb were known quite early by experiments with the de Haas–van Alphen effect [44]. It consists of two well-separated sheets (see the plot of the reduced zone scheme in fig. 2.5). The inner Fermi surface is of spherical shape, whereas the outer surface has a tubular structure. The anisotropy in the electronic bands is accompanied by a strong anisotropy in the phonon bands [45]. Additionally, Pb has a strong electron-phonon coupling. The explanation of the observation of multiple QPRs was hence a $\mathbf{k}$-dependent order parameter within the crystal. Depending on the transport along a specific crystal orientation, a single superconducting gap is observed that varies in energy [46]. The observation of *multiple* gaps in a single measurement in planar tunneling experiments was explained by simultaneous tunneling into different crystal directions.

Decades after this explanation, composite superconductors, such as MgB_2 [47–51] and CaC_6 [52–55], were discovered. They gained a lot of interest because of their unexpected high transition temperatures (39 K and 11.5 K, respectively). Their band structure is highly anisotropic, and they show only two distinct gaps. Still, the latter could not be explained by the first. Instead, an old concept turned out to be of importance, which is multi-band superconductivity [56]. The overlapping bands of the two compounds possess different electron-phonon coupling strengths. This not only leads to two distinct gaps for each band, but it crucially contributes to the high transition temperatures [57].

The simple explanation for the nature of superconductivity in composite materials raised the need to reinvestigate the elemental superconductors with respect to a possible multi-band character. For Pb, density functional theory (DFT) calculations were performed by A. Floris *et al.* [58]. They concluded that the superconductivity in Pb is also of a two band-nature, which leads also in this case to the quite high critical temperature of 7.2 K. The two bands inherently distinguish themselves in their properties because of a hybridization of the original *p*-bands with *s*- and *d*-bands [59]. The compact second zone Fermi surface [fig. 2.5(a)] has a more delocalized *s*-*p* character, the tubular third zone Fermi surface has a more localized *p*-*d* character. They argued that the different orbital nature leads to different electron-phonon coupling strengths, and thus causes different pairing energies Δ for each band.

Experimentally, it is difficult to distinguish between the two-band model and the earlier explanation of an anisotropic variation of the order parameter by an anisotropic electron and phonon band structure. The experiments on planar tunnel junctions have always revealed two QPRs in the gap structure [39–42]. However, the disadvantage of planar junction is that they average over a large area, which includes step edges, vacancies, impurities, etc. The tunneling current is the sum of all tunneling paths, and thus the tunneling electrons may propagate into many different lattice directions in these experiments. This forbids an ambiguous decision between the two explanations.

We use the high lateral resolution of today's scanning tunneling microscopy (STM) experiments to avoid this shortcoming. Atomically flat surfaces are guaranteed, and scanning tunneling spectroscopy (STS) is used to explore the variations in the superconducting gap. The lateral precision allows to probe well-defined defects. We can also tune the tunneling contributions parallel to the surface by controlling the tip-substrate distance. The results of our experiments are presented in the article by M. Ruby *et al.* "Experimental Demonstration of a Two-Band Superconducting State for Lead Using Scanning Tunneling Spectroscopy". In: *Phys. Rev. Lett.* 114 (15 Apr. 2015), p. 157001, reprinted in appendix B.2.

We observe direct evidence for the two-band nature of superconductivity in Pb, as predicted by A. Floris *et al.* [58]. Measurements with high energy resolution reveal an energy separation of the two superconducting gaps of 150 μeV. The shape of the two gaps is still BCS-like. It can be modeled by a simple linear combination of two DOS, each given by eq. (2.14). Measurements on different surface orientations of the Pb single crystals prove two distinct gaps for the two different bands. Depending on the crystal orientation, the intensities of the QPR peaks vary, which we explain by k-selective tunneling into the two Fermi surfaces. In STS experiments the tunneling occurs mainly with k-vectors perpendicular to the surface. Because of the open pores in the third zone Fermi surface [see fig. 2.5(b)], the tunneling into this band is reduced significantly for crystal orientations with a pore perpendicular to the surface. The same is confirmed by approach experiments, where the tip-sample distance is varied.

Furthermore, our experiments answer the question which QPR, or rather which pairing energy, is associated to which particular Fermi surface. Our data confirms the prediction of A. Floris *et al.* [58] that the compact second zone surface [see fig. 2.5(a)] has a smaller gap than the tubular third zone surface [see fig. 2.5(b)]. In an intuitive picture the more localized p-d-like band couples stronger to phonons, as it is in average closer to the ion cores. Thus, it has a larger pairing energy. To prove this, we investigated scattering patterns around subsurface neon (Ne) impurities at the energies of the two QPRs. As a direct consequence of the anisotropy of the Fermi surfaces in k-space, an anisotropic electron propagator exists in the crystal [60–63]. This leads to characteristic signatures of the shape of the respective Fermi surfaces in the spatial scattering patterns, which allow us to assign the patterns at a specific energy to the originating Fermi surface.

Last but not least, we show that the distinct orbital character of the Fermi sheets is also reflected in spectra at local non-magnetic adatoms. The results will be discussed in more detail in section 3.1, which deals with single atomic impurities in superconductors.

Chapter 3

Atomic impurities on a BCS superconductor

Superconductivity relies on the formation of a tiny gap Δ which separates single-particle excitations from the Fermi level by bonding the electrons in Cooper pairs. This leads to zero electrical resistance, as any scattering event has to overcome the energy to break a pair[1]. An important property of superconductors is the inherent particle-hole symmetry, discussed in section 2.2. It raises the following questions: How do superconductors react on defects that break this symmetry? Moreover, the Cooper pairs in conventional superconductors form a spin singlet. Hence, magnetism and BCS superconductivity contradict each other. So, what is the effect of magnetic atoms adsorbed on a superconductor?

In general, one has to distinguish between high and low impurity concentrations, independent of their type of impurities. In this chapter, we focus on the low coverage regime, and investigate how single atoms affect the superconductivity in the vicinity of the adsorption site on the surface of a Pb single crystal. To do so, we first probed the influence of non-magnetic Pb adatoms on the substrate, where they act as *potential* scatterers (section 3.1). These have no effect on superconductivity by themselves, but change the local electronic structure of the substrate.

We continued our measurements with magnetic adatoms, namely we evaporated various transition metal atoms [scandium (Sc), V, Mn, Fe, Co, and nickel (Ni)], and the rare-earth element gadolinium (Gd). The preparation of the samples is described in appendix A.4.1. The magnetic moment of such an adatom interacts with superconductivity, and induces local bound states at energies within the superconducting gap. The measurements yield that only Mn and Fe adatoms show signatures of significant interaction.

A theory describing the scattering process was published in the 1960s. It is introduced in section 3.2. We solve the question how transport evolves through such an induced local bound state in experiment. As it is a subgap bound state, it is isolated by the superconducting gap and requires relaxation mechanisms. Later, by looking at the vicinity of the impurity, we discuss how a single impurity can lead to multiple subgap resonances. In fact, we discovered a spatial extension of the bound states within the substrate. Its origin is discussed in section 3.4. The observed lateral extension suggested a possible coupling between impurities, when bringing two impurities at close distance to each other. This is investigated at the example of two Mn adatoms in section 3.5.

---

[1] The interaction with the lattice vibrations is anyhow considered in BCS theory.

3.1 Non-magnetic impurities

In a conventional BCS superconductor the Cooper pairs form a singlet ground-state. Non-magnetic impurities are pure potential scatterers. They break particle-hole symmetry by a local Coulomb repulsion. Time-reversal symmetry, however, is untouched if the superconductor has an isotropic conventional pairing potential. Only for unconventional superconductors with an anisotropic pairing potential the broken particle-hole symmetry also diminishes the pairing mechanism.

The impurity density plays an important role for the effects on superconductivity. The Cooper pair wave function varies in the order of the coherence length ξ. If the average distance between the impurities is larger than ξ, only a weak perturbation acts on its pairs, but superconductivity is not affected at all. If the impurity density is larger, the superconductor has to be treated in the 'dirty' limit [64]. The lifetime of Cooper pairs is effectively decreased by the subsequent scattering events. This increases the Dynes parameter (introduced in section 2.2.1), which overall broadens the DOS, and leads to an averaging of the signal for transport into all lattice directions.

Examples for non-magnetic impurities are crystal defects, such as step edges and dislocations, or non-magnetic adsorbates, such as atoms and molecules. In our experiment, we investigated the influence of step edges, large sub-surface impurities, and single non-magnetic Pb adatoms on single crystal Pb. Parts of this observation were published by M. Ruby *et al.* "Experimental Demonstration of a Two-Band Superconducting State for Lead Using Scanning Tunneling Spectroscopy". In: *Phys. Rev. Lett.* 114 (15 Apr. 2015), p. 157001. The result was discussed already in parts in section 2.3.2, and is reprinted in appendix B.2.

Since Pb is a two-band superconductor it has two distinct superconducting gaps, originating from different bands. Independent of the exact type of local impurity, we observe that the intensity of the QPR peak with larger energy increases at the impurity site, in contrast to the QPR peaks with lower energy. We explain this phenomenon by the different localization of the bands, of which the two QPRs originate from. The electronic bands of the substrate are usually described by delocalized Bloch waves. A local impurity can only perturb the delocalized states in the vicinity of the impurity site. Hence, the QPR associated with the more localized *p*-*d*-like band is more influenced by a local impurity than the more delocalized *s*-*p*-derived states. This increases the probability of tunneling into these bands at the impurity site.

3.2 Yu-Shiba-Rusinov bound states at magnetic impurities

Magnetic impurities differ from non-magnetic ones by additionally breaking time-reversal symmetry. Their local magnetic potential acts on the spin-component of the Cooper pair wave function. Hence, they locally perturb the Cooper pairs independent of the pairing potential symmetry. This leads to the formation of localized bound states below the superconducting gap at the impurity site. The microscopic nature of these states was described in the 1960s by L. Yu, H. Shiba, and A.I. Rusinov [65–67]. They are often referred to as Yu-Shiba-Rusinov (YSR) or Shiba states[2].

---

[2] They should not be confused with Andreev bound states (also called multiple Andreev reflections), which also arise within the superconducting gap. These are a pure transport phenomenon which appears in mesoscopic superconductor-normal-superconductor junctions.

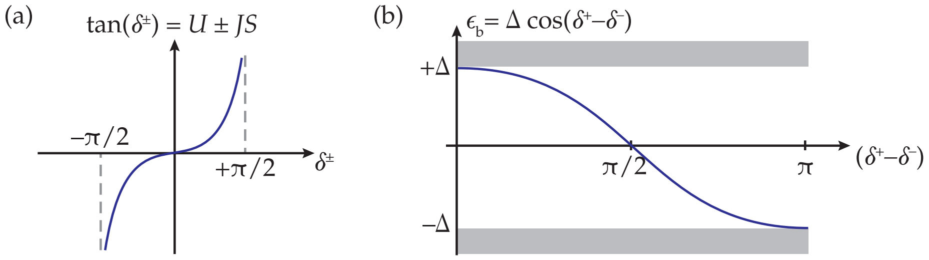

FIGURE 3.1: (a) Scattering phase $\delta^{\pm}$ as introduced by Rusinov [67], and defined by eq. (3.3), depending on the potential scattering strength U and the exchange scattering JS. The positive and negative components represent the hole-like and electron-like resonances, respectively. (b) Bound state energy ϵ_b versus the phase difference. According to eq. (3.4), ϵ_b shifts continuously through the gap between $\pm\Delta$.

The scattering between an incident quasi-particle with a magnetic impurity is described by the exchange interaction Hamiltonian:

$$H_\mathrm{exch.} = -\frac{J}{2N}\sum_{\mathbf{k},\mathbf{k}'} a^\dagger_\mathbf{k}\,\boldsymbol{\sigma}\,a_{\mathbf{k}'}\,\mathbf{S} \quad . \tag{3.1}$$

Here, J is the interaction strength, $\mathbf{S}$ is the impurity spin, $a^{(\dagger)}_\mathbf{k}$ is the incident (scattered) single-particle operator, and $\boldsymbol{\sigma}$ is the Pauli matrix that describes the incident electron spin. To simplify calculations, the impurity is often considered in the classical limit. The spin is assumed to be large ($S \to \infty$), but the total interaction should still be finite ($J \to 0$, $w = JS =$ finite). Within this approximation the impurity is immune to internal transitions. It only scatters the incoming particle. For nanoscopic impurities this scenario is not necessarily correct, however it is well suited to understand the scattering processes.

The exchange scattering of incident bulk spins with the impurity spin reduces locally the pairing energy of the Cooper pairs, and induces the YSR states. Because of the inherent particle-hole symmetry of the superconductor, each bound state is indicated by two resonances in the DOS, an electron-like and a hole-like peak. They lie symmetric in energy with respect to the Fermi-level at $\pm\epsilon_\mathrm{b}$, and within the superconducting gap ($\epsilon_\mathrm{b} < \Delta$). It is important to keep in mind that *both* resonances belong to the *same* bound state. The energy ϵ_b follows:

$$\epsilon_\mathrm{b} = \Delta\,\frac{1-[JS\pi\rho/2]^2}{1+[JS\pi\rho/2]^2}\,, \tag{3.2}$$

where $w = JS$ is the exchange interaction strength, and ρ is the normal state DOS at the Fermi level. The first experimental observation of these states was reported in tunneling experiments on single Mn and Gd atoms adsorbed on a Nb substrate [68].

Rusinov further modified eq. (3.2) by introducing a scattering phase $\delta^{\pm}$ for the hole-like and electron-like resonance, respectively. The phase is given by the exchange scattering $w = JS$, and the potential scattering from Coulomb interaction U:

$$\tan\delta^{\pm} = U \pm JS = U \pm w\,. \tag{3.3}$$

The relation is plotted in fig. 3.1(a). Potential scattering simply produces an offset, whereas exchange scattering leads to different values of $\delta^{\pm}$. The bound state energy is finally given by the difference between both phase components:

$$\epsilon_\mathrm{b} = \Delta \cos\left(\delta^{+} - \delta^{-}\right) . \tag{3.4}$$

The evolution of eq. (3.4) is plotted in fig. 3.1(b). A pure potential scatterer has a bound state energy of $\epsilon_\mathrm{b} = \Delta$. Thus its resonances are located at the superconductor's QPRs. When exchange scattering increases ($w = JS > 0$), the bound state shifts to lower energies. An important property of the two YSR resonances is their spin-polarized nature. For the case of a ferromagnetic coupling, the spin of the bound state is aligned parallel to the classical impurity spin; for the case of an anti-ferromagnetic coupling, it is aligned anti-parallel. The mirror-symmetric hole-component caused by the particle-hole symmetry of the superconductor has the opposite spin of the electron-component. This means that, lets say, an electron with spin-up would be equal to a hole with spin-down in a superconductor.

An interesting phenomenon occurs at a phase difference of $(\delta^{+} - \delta^{-}) = \pi/2$. At this point, the exchange interaction reaches a critical value $w = w_\mathrm{c}$, and the system gets unstable against a quantum phase transition, where the bound state crosses the Fermi level. As sketched in fig. 3.2(a) and (c), this changes the occupation of the bound state from unoccupied to occupied. Accordingly, the ground state of the superconductor changes from a $S = 0$ to a $S = 1/2$ spin state, with an electron in the bound state.

3.2.1 Tunneling into YSR states: the excitation picture

Employing tunneling experiments on magnetic impurities implies the successive injection or extraction of an electron into or out of the YSR bound states. Each process excites the system, which lifts it in energy. Therefore, compared to the simple bound state picture mentioned above, we can also sketch the 'excitation' picture [69–71]. It is shown in fig. 3.2(b) and (d). Tunneling into the weakly coupled YSR state increases the spin of the host from an $S = 0$ ground state to an $S = 1/2$ excited state. In the strong coupling regime, the ground state is already $S = 1/2$. Emptying the state by a tunneling event puts it into the $S = 0$ excited state.

The excitation picture is useful to understand an experiment by N. Hatter *et al.* [30], where molecules with a multitude of different adsorption sites are used to follow the phase transition between the weakly coupled and the strongly coupled regime. It is described in section 3.4.

3.3 Transport through YSR bound states

The excitation picture, introduced in section 3.2.1, describes a tunneling event to a YSR state in terms of population or depopulation of the state with a single electron. When probing YSR states in experiment by STS, a steady current through the state is established, which means a consecutive number of tunneling events occurs. However, the YSR state is isolated from the quasi-particle continuum by the superconducting gap. Therefore, the elemental question arises, which relaxation mechanisms are involved in bringing the system back to the ground state after each single excitation, in order to allow the subsequent excitation to occur. Moreover, the maximum current pushed through the state depends crucially on the involved processes. To interpret the measured signal, we need to investigate the details of the relaxation mechanisms. The results are published by

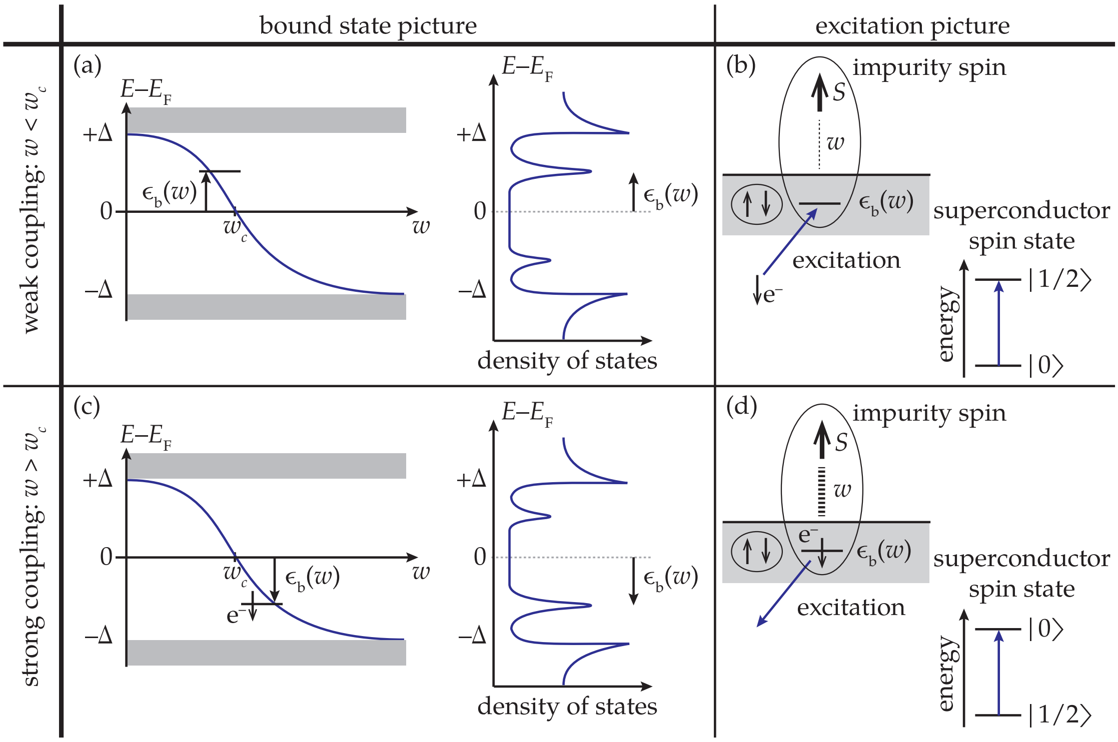

FIGURE 3.2: YSR bound states in weak coupling ($w < w_c$) and strong coupling ($w > w_c$). Within the bound state picture (a,c) the YSR state at ϵ_b crosses the Fermi level at a critical exchange coupling $J_c S = w_c$. At this point the system undergoes a quantum phase transition, which changes the occupation of the bound state. Here, the anti-ferromagnetic case is sketched, in which the bound state spin and the impurity spin are anti-aligned. The asymmetry of the resonances in the density of states is given by a local Coulomb interaction. The excitation picture (b,d) shows the change of the system under the lowest possible excitation. It is measured by electron tunneling in our case, and changes the spin state of the system. The classical impurity spin $S \to \infty$ is not affected at all. At the quantum phase transition, the bulk changes its ground state from an $S = 0$ to $S = 1/2$ spin configuration.

M. Ruby *et al.* “Tunneling Processes into Localized Subgap States in Superconductors”. In: *Phys. Rev. Lett.* 115 (8 July 2015), p. 087001. They are also reprinted in appendix B.3.

In our work we employed STS on single Mn adatoms on a Pb(111) single crystal. The data were measured with a superconducting tip. As described in section 2.3.1 we obtain high energy resolutions in the order of 50–70 μeV. Preceding work by S.-H. Ji *et al.* on this system showed two YSR resonances at the center of the impurity [72]. In our experiment we discovered that single atoms adsorb in two different sites on the surface substrate. Both species show significantly different spectral properties. Five pairs of YSR resonances were observed for atoms at the initial adsorption site, which all atoms reside in after evaporation. Because the adatoms appear with a lower topographical height, we name them $\mathrm{Mn}^{\mathrm{down}}_{\mathrm{Pb(111)}}$. We could prove that it is the same species as reported in Ref. [72]. An approach with the tip of our STM to a $\mathrm{Mn}^{\mathrm{down}}_{\mathrm{Pb(111)}}$ atom lifts it to the second adsorption site. It appears with a larger topographical height, and we name it $\mathrm{Mn}^{\mathrm{up}}_{\mathrm{Pb(111)}}$. It shows only three pairs of YSR resonances. The difference between the two adsorption sites and the origin of the multiple resonances will be discussed later, in section 3.4.

In this section we want to focus on the lowest energy YSR resonances appearing at $\epsilon_b \simeq \pm 0.22$ meV on the $\mathrm{Mn}^{\mathrm{up}}_{\mathrm{Pb(111)}}$ species. The resonance is pointed out in fig. 3.3(a). We

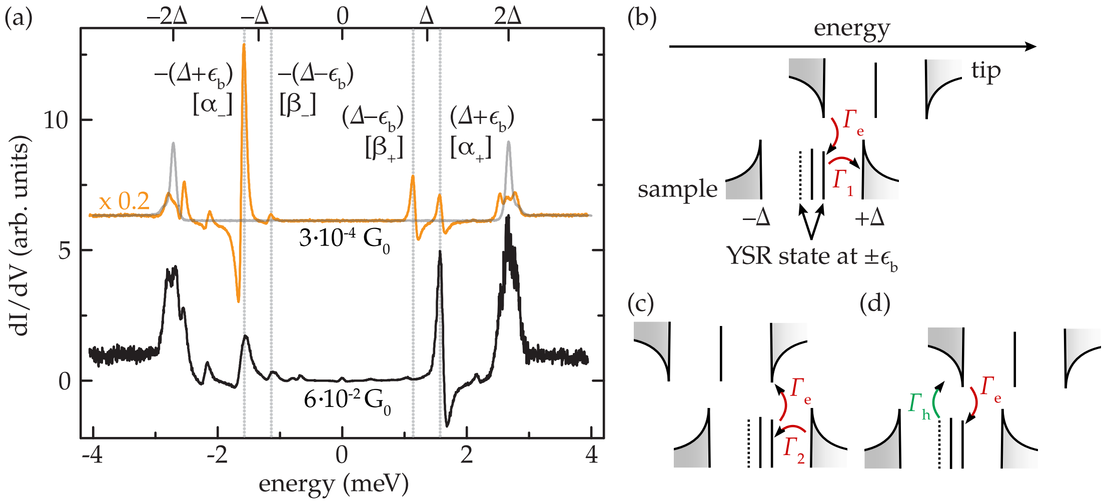

FIGURE 3.3: (a) $\mathrm{d}I/\mathrm{d}V$ spectra on a $\mathrm{Mn}^{\mathrm{up}}_{\mathrm{Pb}(111)}$ adatom at two different tip-sample distances. Spectra are normalized to the "normal-state" conductance measured at 4 meV, which is given in units of the quantum of conductance $G_0 = 2e^2/h$. The lowest energy YSR resonances and their thermal counterparts are marked by $\pm\alpha$ and $\pm\beta$, respectively. For clarity, an offset is applied to the spectra, and they are scaled when indicated for better visibility. For comparision, a spectrum acquired on the clean Pb(111) substrate overlays the top curve. The spectral intensity (recorded with a lock-in modulation amplitude of 15 μV$_{\mathrm{rms}}$ at a frequency of 912 Hz) changes between the two normal-state conductance values. (b–d) A current through a YSR bound state at ϵ_{b} requires relaxation processes after each excitation process. A tunnel event occurs with rate $\Gamma_{e,h}$, for electrons and holes, respectively. The rates for thermal relaxation to the continuum are given by $\Gamma_{1,2}$. Single electron tunneling from tip to sample and sample to tip is sketched in (b,c). An Andreev process incorporating two tunneling events is sketched in (d).

name it $\pm\alpha$. Additionally, each YSR state is accompanied by a thermal peak ($\pm\beta$) when tunneling thermally excited particles at the measurement temperature of 1.2 K. The spectra are recorded in two different conductance regimes, at high and low tip-sample distance, respectively. The values for the normal state conductance are indicated in the figure. Obviously, the spectral intensities of the resonances change between the two regimes. Moreover, the asymmetry between $\pm\alpha$ and $\pm\beta$ inverts. In collaboration with theorists we show that the inversion is inherently connected to two different relaxation processes of the excited YSR state after a tunneling event. These compete and contribute two separate components to the totally measured current.

The first is a single-particle relaxation process, which is thermally driven by absorption of phonons or photons from the bulk. It contributes a current I^{s}:

$$I^{\mathrm{s}} = e\int \frac{d\omega}{2\pi\hbar}\left\{\frac{\Gamma_1[\Gamma_e n_{\mathrm{F}}(\omega_-) - \Gamma_h n_{\mathrm{F}}(\omega_+)]}{(\omega-\epsilon_0)^2+(\Gamma/2)^2} - \frac{\Gamma_2[\Gamma_e(1-n_{\mathrm{F}}(\omega_-)) - \Gamma_h(1-n_{\mathrm{F}}(\omega_+))]}{(\omega-\epsilon_0)^2+(\Gamma/2)^2}\right\}. \tag{3.5}$$

The second mechanism is an Andreev relaxation process, which uses the condensate degree of freedom of the Cooper pairs to create and annihilate pairs from the bulk. Here, a second particle tunnels across the barrier. Overall, this contributes a current I^{a}:

$$I^{\mathrm{a}} = 2e \int \frac{d\omega}{2\pi\hbar} \frac{\Gamma_h \Gamma_e [n_{\mathrm{F}}(\omega_-) - n_{\mathrm{F}}(\omega_+)]}{(\omega - \epsilon_0)^2 + (\Gamma/2)^2} \,. \tag{3.6}$$

In eq. (3.5) and (3.6), the Fermi functions $n_{\mathrm{F}}(\omega)$ are evaluated at $\pm\alpha$, with $\omega_\pm = \omega \pm eV$. The broadening $\Gamma = \Gamma_e + \Gamma_h + \Gamma_1 + \Gamma_2$ is defined by the rates $\Gamma_{e,h}$ that transfer a particle or hole from the tip to the sample, respectively, and by the rates $\Gamma_{1,2}$ that thermally occupy or empty a state from or to the quasi-particle continuum. They are sketched in fig. 3.3(b–d).

The different nature of both processes leads to an opposite weight at weak and strong tunneling currents. The single-particle current [eq. (3.5)] only requires a single transition through the tunnel barrier between tip and sample (terms $\Gamma_{1,2}\Gamma_{e,h} \propto t^2$, with the tunnel matrix element t). However, elevated temperatures are needed for the relaxation processes $\Gamma_{1,2}$. The Andreev current [eq. (3.6)] crosses the tunnel barrier twice (terms $\Gamma_e\Gamma_h \propto t^4$), but it is independent of the temperature. Hence, in the low conductance regime we yield a spectrum which is dominated by the single-particle current because of the weakness of the Andreev current. The opposite is the case in the high conductance regime. Here, the Andreev contribution by far outruns the thermally limited single-particle current. We prove this additionally by measurements at elevated temperatures (4.5 K), where the transition point between the two regimes shifts. In the case of Mn adatoms on Pb(111), the thermal relaxation times at 1.2 K amount to $\hbar/\Gamma_1 \simeq 0.2$ ns and $\hbar/\Gamma_2 \simeq 0.6$ ns.

A main message of our work targets the data interpretation of the STS spectra in these different regimes. The $\mathrm{d}I/\mathrm{d}V$ signal in the low conductance regime is directly proportional to the sample DOS — besides the convolution of tip and sample DOS because of a superconducting tip. In the high conductance regime we can access the thermal relaxation rates of the system, but instead loose the direct access to the sample DOS.

Moreover, our experiments show that one can tune the system continuously between the two regimes. This bridges nanoscopic and mesoscopic physics. In nanoscopic physics, the currents are usually low. They are seen in the single-particle picture and are interpreted in terms of single-particle DOS. In mesoscopic physics, the currents are usually large. They are interpreted in the Andreev transport picture. Last but not least, we want to point out that our analysis is applicable to all bound states in superconductors, as long as they are isolated by a superconducting gap. Thus the results may be useful in a variety of fields dealing with transport in superconductors.

3.4 Multiple YSR bound states from a single impurity

In section 3.3 we discussed the transport through a single YSR state. In the following, we restrict our experimental data to the low conductance regime, where the $\mathrm{d}I/\mathrm{d}V$ signal is directly proportional to the DOS. Yet, we have not discussed how a single impurity can induce multiple pairs of YSR resonances, as it was first observed in the experiment of Ref. [72], as well as later by us in Ref. [29]. This phenomenon is barely explained in the YSR theory.

As it turns out, the bound state and the excitation picture, introduced in section 3.2, are helpful to describe an impurity with multiple magnetic moments. The two different extremal cases of the interaction of such an impurity with the substrate are sketched

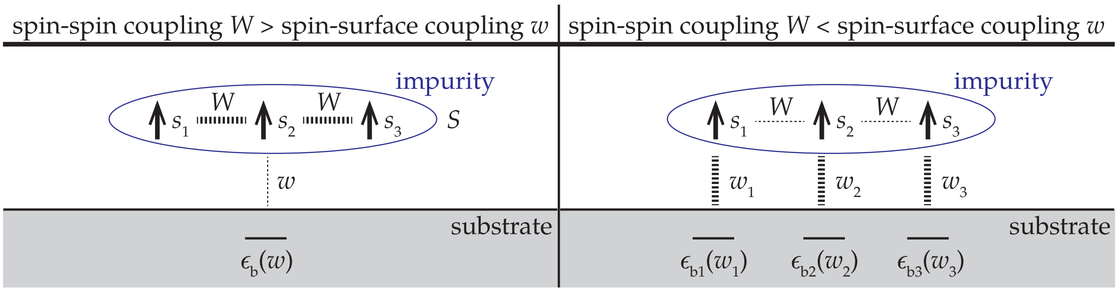

FIGURE 3.4: A magnetic impurity with multiple spins s_i induces a different number of YSR states in the superconducting substrate, depending on the coupling strength W between the spins within the impurity, and the coupling strength w_i of each spin to the substrate. (left) For $W > w$, the impurity with multiple spins can be approximated by an impurity with a single magnetic moment, which is the sum of the individual spin moments ($S = \sum s_i$). The large moment S induces a single YSR state with energy $\epsilon_b(w)$ in the substrate, but it may be split by a magnetic anisotropy. (right) For $W < w$, each impurity spin s_i couples individually to the substrate with different coupling strength w_i. This induces a single YSR state per spin at energy $\epsilon_{\mathrm{b}i}(w_i)$.

in fig. 3.4. In the first scenario, the coupling W between the spins of the impurity is larger than the coupling w of each spin to the substrate. The impurity with multiple spins may be approximated by an impurity with a single spin moment, which is the sum of the individual spin moments. Such an impurity induces only a single YSR state in the superconductor. However, in experiment, we may still observe more than a single pair of YSR resonances from tunneling into the bound state, because of excitations from different spin projections. An example for such a case is briefly discussed in section 3.4.1. In the second scenario, the coupling between the spins of the impurity is smaller than the coupling of each spin to the substrate. This requires that each spin is treated as individual scattering potential, which interacts independently with the substrate. Hence, there are as many YSR states as there are spins. Each state is observed as a single pair of resonances in spectroscopy, and follows the simple description given in eq. (3.4). An example for this case is discussed in section 3.4.2.

3.4.1 Multiple resonances of a YSR state split by magnetic anisotropy

Within the framework of this thesis, the first scenario plays only a minor role. Nevertheless, it is briefly discussed below as a short excursion. The presented results were obtained mainly by N. Hatter within the framework of his PhD thesis and are published in Ref. [30]. There, a molecular layer was evaporated on the superconducting substrate, in which each individual molecule is adsorbed at a slightly different site in a nanoscopic scale. The local variation of the environment changes the coupling strength JS to the substrate, and it shifts the observed YSR bound state through the quantum phase transition. Hence, a broad range from weakly coupled to strongly coupled molecules exists. In this particular molecular system, it changes the total ground state because of different screening from $S = 1/2$ to $S = 1$.

The experiment showed three pairs of YSR resonances in $\mathrm{d}I/\mathrm{d}V$ spectra on the molecules. While the resonances shifted in energy through the gap for the different coupling strengths of the molecules [remember eq. (3.4)], their separation in energy with respect to each other stayed constant. Moreover, only their relative intensities changed during the transition from the weak to the strong coupling regime.

This makes unlikely an interpretation in terms of multiple individual YSR states from the different spins within a single molecule. Instead, it suggests that the molecule is in a total spin state of $S = 1$, which acts as single scattering potential for the superconductor. We explain the observation of multiple resonances in experiment by a local crystal field splitting of the ground state or of the excited state with respect to the spin quantum number, and in dependence of the coupling strength, respectively. This splitting becomes visible, if the crystal field energy is in the same order as the transition energies of the YSR system (recall the excitation picture introduced in section 3.2.1). It is obvious that an additional splitting of, let's say, the excited state leads to a manifold of resonances corresponding to transitions from the ground state, although *all* excitations still belong to the *same* YSR scattering potential. Thus, their separation in energy will not change, unless the crystal field splitting is modified. The variation in intensity of the resonances is explained by the thermal occupation of the ground state. The levels are occupied with Maxwell-Boltzmann distribution if they are split, and thus lead to different transition probabilities for the transitions from these levels.

3.4.2 Multiple individual YSR states from a single magnetic impurity

The focus of this thesis, however, is laid on the second scenario, where the exchange coupling between the spins of an impurity is weaker than the coupling of the spins to the substrate. This leads to a single pair of YSR resonances for each individual spin.

In section 3.3 we already reported on the first experiment on single Mn adatoms on Pb(111) by S.-H. Ji *et al.* [72], where they observed two pairs of YSR resonances. Their explanation followed the initial theoretical prediction of A.I. Rusinov [67]. Higher order scattering channels with angular momenta ($l = 1, 2, \ldots$) would induce subsequent peaks next to the main YSR resonances which originate from isotropic scattering ($l = 0$). Thereby, the resonances shift closer to the gap edge ($\pm\Delta$) because the coupling strength decreases with increasing scattering order [73]. In addition, with increasing scattering order, the spectral intensity should decrease, as the processes get more unlikely.

At first sight, their explanation matches their experimental data. They observed two resonances up to the order of $l = 1$, which decrease in intensity with higher order. However, in our experiments on the same system (see section 3.3), we saw that the number of YSR resonances in this system is much larger than anticipated. We observed five pairs of resonances for the initial species that was found after evaporation ($\mathrm{Mn}^{\mathrm{down}}_{\mathrm{Pb(111)}}$), and three pairs for the species that was obtained after manipulation of the adatoms with the tip ($\mathrm{Mn}^{\mathrm{up}}_{\mathrm{Pb(111)}}$). Additionally, the intensities of the resonances do not decrease towards the gap edge. Hence, the explanation by the higher order channels is insufficient, and the appearance of multiple resonances requires an alternative interpretation which does not solely depend on the energetic alignment of the YSR resonances. This is why we again performed measurements on this system. However, this time, we focused on the *lateral* extension of the states. Our results showed that we can establish a link between the individual YSR states and the shape of the scattering potential that each state originates from, the latter being the orbital structure of the magnetic impurity. The results were published by M. Ruby *et al.* "Orbital Picture of Yu-Shiba-Rusinov Multiplets". In: *Phys. Rev. Lett.* 117 (18 Oct. 2016), p. 186801. The article is reprinted in appendix B.4.

In our experiment, we employed again single Mn adatoms on Pb, and used STS to measure the on-site conductance in the vicinity of the adatoms. The main advantage of this setup is that the adatoms are supposedly in the Mn^{++} configuration with five *d*-electrons and a fully emptied *s*-shell because of hybridization with the substrate. The electronic configuration of the Mn d-shell according to Hund's rules is ${}^6S_{5/2}$. Hence, it is spherically symmetric. As emphasized by J.R. Schrieffer [74], only $l = 2$ electrons can scatter at such an impurity. The ion cannot change the angular momentum of the itinerant conduction electrons in an isotropic environment and in the absence of spin-orbit coupling. Moreover, this implication was mainly ignored by literature (one exception being Ref. [75]).

In collaboration with theorists we showed that, indeed, the YSR states inherit the symmetry from the scattering potential. In this particular case, when scattering at atomic d-orbitals, the observed lateral scattering patterns in the vicinity of an adatom reflect these symmetries[3].

In our experiment we observed multiple pairs of YSR resonances at single adatoms. The scattering patterns at the different resonance energies distinguish significantly in shape. With the above explanation, this requires that each YSR state originates from scattering at different d-orbitals of the adatom. Moreover, the orbitals need to be separated in energy, namely without lifted degeneracies the scattering potential would be degenerate and fully spherically symmetric.

The most simple explanation is a crystal field splitting of the orbitals induced by the adsorption on the substrate. This yields degenerate and non-degenerate alignments of the orbitals to a scattering potential at a specific energy. Moreover, it implies that each of the scattering potentials is coupled stronger or weaker to the substrate. Hence, each potential creates a YSR state with different energy.

In our article, we studied different surface orientations of the substrate. In addition to the Pb(111) surface, known from above, we used a Pb(001) crystal. Here, the surface symmetry matches with that of the d-orbitals of the Mn adatoms, both being $C_{4\mathrm{v}}$. This reduces the effects of the lattice symmetry on the scattering patterns. We denote the Mn impurities on this substrate in the following by $\mathrm{Mn}^{\mathrm{down}}_{\mathrm{Pb(001)}}$. They show three pairs of YSR resonances. The adsorption at a high symmetry hollow site on Pb(001) leads to a square-pyramidal crystal field. In the ideal case, this splits the five d-orbitals into three levels, of which one of them is three-fold degenerate [77]. It matches with the number of YSR resonances obtained from experiment. Indeed, the lateral pattern of the states is a reminiscent d-orbital symmetry. However, it is an order of magnitude larger than the size of the d-orbitals themselves, and it is visible $\simeq 1.6$ nm away from the impurity center.

On the Pb(111) substrate we observed two adsorption sites of the Mn adatoms ($\mathrm{Mn}^{\mathrm{down}}_{\mathrm{Pb(111)}}$ and $\mathrm{Mn}^{\mathrm{up}}_{\mathrm{Pb(111)}}$). Both showed a different number of YSR states. Moreover, they also differ in their topographical shape. $\mathrm{Mn}^{\mathrm{down}}_{\mathrm{Pb(111)}}$ has a slightly oval shape, and $\mathrm{Mn}^{\mathrm{up}}_{\mathrm{Pb(111)}}$ is spherical symmetric. However, the adsorption geometry is a crucial ingredient for the crystal field splitting which determines the number of induced YSR states. The oval shape of $\mathrm{Mn}^{\mathrm{down}}_{\mathrm{Pb(111)}}$ indicates a low-symmetry adsorption site. So do the five pairs of YSR resonances, which require all d-orbital degeneracies to be lifted. The symmetric shape of $\mathrm{Mn}^{\mathrm{up}}_{\mathrm{Pb(111)}}$ indicates a high-symmetry adsorption site. The substrate Pb atoms of the (111) surface impose a trigonal-pyramidal crystal field. It splits the orbitals into a single degenerate and two double degenerate levels [77], which matches with the observed number of resonances for $\mathrm{Mn}^{\mathrm{up}}_{\mathrm{Pb(111)}}$. The lateral scattering patterns of the YSR states show only a slow decay along the high symmetry directions of the crystal.

---

[3] A similar conclusion was made in a parallel work by D.-J. Choi *et al.* [76], where they investigated chrome (Cr) adatoms on a Pb thin film with STS, and performed DFT calculations for the adsorption geometry and the observed scattering patterns.

The oscillations in the spectral intensity are visible up to 5 nm away from the impurity center.

Theoretically, the largest intensity of a YSR bound state is localized at the center of the impurity. Yet, its wave function has a finite decay with lateral distance r from the center. It differs between substrates with two and three dimensions, and is given by [67, 68, 71, 78]:

$$\psi^{\pm}_{3\mathrm{D}}(r) \;\propto\; \frac{\sin\left(k_\mathrm{F}\, r + \delta^{\pm}\right)}{k_\mathrm{F}\, r} \;\exp\left[-\left|\sin\left(\delta^{+} - \delta^{-}\right)\right| \frac{r}{\xi}\right], \tag{3.7}$$

$$\psi^{\pm}_{2\mathrm{D}}(r) \;\propto\; \frac{\sin\left(k_\mathrm{F}\, r - \pi/4 + \delta^{\pm}\right)}{\sqrt{k_\mathrm{F}\, r}} \;\exp\left[-\left|\sin\left(\delta^{+} - \delta^{-}\right)\right| \frac{r}{\xi}\right]. \tag{3.8}$$

Here, k_F is the Fermi wave vector, ξ is the coherence length, and $\delta^{\pm}$ is the scattering phase of the electron and hole component of the YSR state. The wave function amplitude decreases with r^{-1} in 3D substrates, and with $(\sqrt{r})^{-1}$ in two-dimensional (2D) materials[4]. Observation of the lateral decay in experiment is additionally influenced by the crystal. The symmetry of the host lattice is imprinted to the shape of the scattering pattern because of scattering at the anisotropic Fermi surface. This is discussed theoretically in Ref. [69], and is the same effect that we observed in experiments on non-magnetic neon impurities embed in Pb [28]. Interestingly, this effect is strong enough that it leads to a similar decay constant for the 3D substrate of our experiment and the recently reported one for a 2D superconductor [78].

When comparing our observations with the predicted behavior in eq. (3.7), we find a match of the oscillation period of the spectral intensity with the Fermi wavelength λ_F of the p-d-like Fermi surface of the Pb crystal. An intuitive explanation can be given in analogy to the scattering at non-magnetic impurities in section 3.1. Electrons from the more localized p-d-like band scatter stronger at a *local* magnetic impurity than those from the more delocalized s-p-like band of Pb.

The oscillations also yield the phase difference between the electron and the hole component of the YSR wave function $(\delta^{+} - \delta^{-})$. However, we obtain only a few data points, which are plotted in fig. 3.5 together with the theoretical prediction [eq. (3.4)]. The rough match between experiment and theory is acceptable, when considering the simplicity of the theoretical model.

3.5 Coupling of two magnetic impurities

One of the main observations in section 3.4.2 is the large lateral extension of the YSR states, which appear even on 3D bulk substrates. The slow decay raises the question of what happens when two impurities lie at close distance to each other, where their YSR states overlap. Answering this question helps to understand larger nano structures of magnetic impurities, and the nature of the coupling within such structures. Moreover, we can estimate the rough limits of the coupling between the two adatoms. Initially, the interaction starts as a small perturbation to the single atomic YSR states. Finally, it ends in the formation of a dimer with hybridized YSR states. In larger systems, it would even evolve to the formation of bands. However, the nature of the coupling, whether

---

[4] In close vicinity to the impurity, the exponential decay is negligible compared to the r^{-1} or $(\sqrt{r})^{-1}$ term, respectively. In particular, the coherence length is usually in the order of several 10 to 100 nm (see section 2.1).

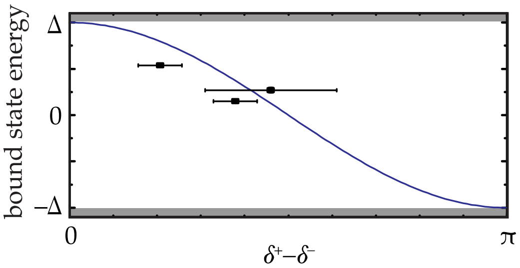

FIGURE 3.5: Energy of the YSR bound state versus the phase difference between the electron and the hole component ($\delta^+ - \delta^-$) of the bound states in $\mathrm{Mn}^{\mathrm{up}}_{\mathrm{Pb}(111)}$ adatoms. The difference was determined by the intensity oscillations of the laterally decaying YSR states. The solid line gives the expected behavior according to eq. (3.4).

it is ferromagnetic or anti-ferromagnetic, is yet unknown. To answer this question, we investigate pairs of atoms adsorbed at various distances and angles with respect to each other. The content presented in this section is not yet published, and hence elaborated in more detail.

Our experiment relies on arbitrarily adsorbed adatom pairs[5], which was tuned by different surface coverages of Mn adatoms up to 410 adatoms per $100 \times 100\ \mathrm{nm}^2$. Still, we stay below the regime where artifacts from high coverage appear, i.e., where YSR bands form across the whole surface. The spectra of single adatoms with a next-neighbor distance < 4 nm do not deviate from those recorded in the low coverage regime [32].

In Ref. [32] (section 3.4.2) we reported that $\mathrm{Mn}^{\mathrm{down}}_{\mathrm{Pb}(001)}$ adatoms show three pairs of YSR resonances. We named them $\pm\alpha$, $\pm\beta$, and $\pm\gamma$, and assigned them to scattering of incident Cooper-pairs at the atomic d-orbitals $d_{\mathrm{x}^2-\mathrm{y}^2}$, d_{z^2}, and $d_{\mathrm{xy,xz,yz}}$, respectively. In collaboration with theorists we showed that the spatial shape of the YSR states is inherited from the corresponding d-orbital. Hence, the spatial extension of β was the weakest, with the strongest intensity at the center of the impurity. The states α and γ were more extended within the surface plane, and weak at the center of the impurity. Both were hardly probed by STM because of a weak extension perpendicular to the surface. Moreover, we show evidence in this section that γ is actually a degenerate state. In addition to the orbital symmetry, each YSR state gets the symmetry of the host lattice imprinted on the shape of the scattering pattern because of scattering at the anisotropic Fermi surface.

In fig. 3.6 two $\mathrm{Mn}^{\mathrm{down}}_{\mathrm{Pb}(001)}$ are adsorbed along the [100] high symmetry crystal direction at a distance of $\simeq 1.5$ nm. All YSR wave functions overlap at this distance and angle. The $\mathrm{d}I/\mathrm{d}V$ spectrum recorded on top of one of the adatoms is shown in fig. 3.6(a) and (b) as red curve. In comparison with a single adatom (the blue dashed curve), each resonance $\pm\alpha$, $\pm\beta$, and $\pm\gamma$ is split into a pair of peaks, and furthermore shifted in energy. We denote the resonance which is lower in energy by the sub-index b and the one which lies higher in energy with sub-index a.

We recorded $\mathrm{d}I/\mathrm{d}V$-maps of the spectral intensity in the vicinity of the adatoms at the energies of the split resonances [see fig. 3.6(d–o)]. Interestingly, the ones denoted by sub-index b show an increased intensity between the adatoms [fig. 3.6(e,g,i,k,m,o)], whereas the opposite is observed in the maps of the resonances with a sub-index a.

---

[5] Lateral manipulation of adatoms with the STM tip would be the most elegant way to vary the angle and distance. However, it requires a weak coupling between the impurity and the substrate, which is not the case for Pb crystals.

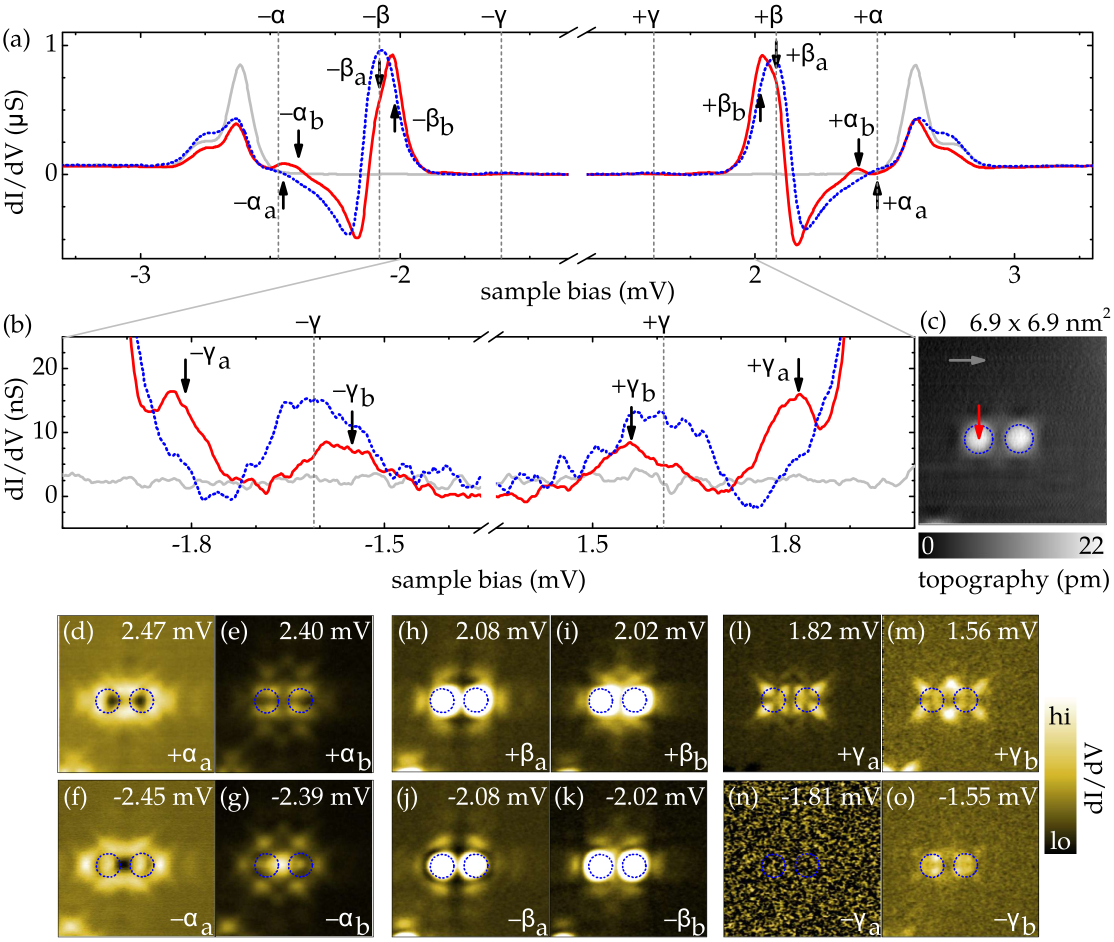

FIGURE 3.6: Two Mn adatoms at a distance of 1.54 ± 0.08 nm along the [100] direction. (a,b) $\mathrm{d}I/\mathrm{d}V$-spectra on top of the left adatom (solid red curve), and on the bare substrate (gray curve). The recorded locations are marked by arrows in the topography in (c). For comparison, the spectrum on a single adatom without a neighbor is shown as a blue dashed curve. The energies of the non-split resonances $\pm\alpha$, $\pm\beta$, and $\pm\gamma$ are indicated by vertical gray dashed lines. The subgap states are split into bonding and anti-bonding resonances $\alpha_{\mathrm{b,a}}$, $\beta_{\mathrm{b,a}}$, and $\gamma_{\mathrm{b,a}}$, respectively, and shifted in energy. Setpoint: 200 pA, 4 mV. Lockin modulation: 15 μV. (c) Topography of the adatoms. The positions of the adatoms are framed by blue dotted circles. Setpoint: 150 pA, 5 mV. (d–o) $\mathrm{d}I/\mathrm{d}V$-maps at the subgap resonance energies. The blue dotted circles mark the adatom positions, as depicted in (c). The bonding states ($\pm\alpha_{\mathrm{b}}$, $\pm\beta_{\mathrm{b}}$, $\pm\gamma_{\mathrm{b}}$) have a high spectral intensity between the adatoms. The anti-bonding states ($\pm\alpha_{\mathrm{a}}$, $\pm\beta_{\mathrm{a}}$, $\pm\gamma_{\mathrm{a}}$) show a reduced intensity and nodal-planes between the adatoms. The scale in (h–k) is cut to emphasize the laterally extended intensity around the high intensity at the impurity center.

There, a reduced spectral intensity and nodal-planes are observed between the adatoms [fig. 3.6(d,f,h,j,l)]. Still, the overall spatial symmetry of the resonances preserves the case of the single adatoms (see Ref. [32]), which strengthens the idea that the states keep their character, but split, and do not form new mixed states.

A closer look at fig. 3.6(a) and (b) reveals a different size of the splitting for α, β and γ. In this particular example, resonances $\alpha_{\mathrm{a,b}}$ are split with roughly $\simeq 140$ μV, resonances $\beta_{\mathrm{a,b}}$ with roughly 60 μV, and resonances $\gamma_{\mathrm{a,b}}$ with roughly 160 μV. Most probably this variation is caused by the different lateral shape and symmetry of the

YSR states. It implies a different overlap of the particular YSR states, depending on the relative orientation of the adatoms with respect to each other. Hence, we investigated the dependence of the splitting on the lateral arrangement of the adatoms by comparing many Mn pairs. We sorted the data in two categories: the data shown in fig. 3.7(a) and (b) are recorded at Mn pairs oriented along the [100] and [110] directions, but at different distances. The data shown in fig. 3.7(c–e) are recorded at Mn pairs with the same interatomic distance, but oriented along different directions.

In the $\mathrm{d}I/\mathrm{d}V$ spectra in fig. 3.7(a) the splitting of the states increases with decreasing distance between the adatoms. Thereby, all peaks are strongly split at close distance, but only γ maintains a large splitting at larger distances and at both orientations. This becomes obvious in fig. 3.7(b), where we plot the splitting of all resonances with respect to the distance. For an orientation along the [100] direction, α and β start to split simultaneously below distances of ≈ 1.75 nm. However, pairs along the [110] direction show a splitting below ≈ 1.25 nm. In both cases γ is split also at distances larger than 2 nm.

The $\mathrm{d}I/\mathrm{d}V$ spectra in fig. 3.7(c–e) emphasize the angular dependence of the splitting. This is a consequence of the different lateral shape of the YSR states, which they inherit from the atomic d-orbitals. In fig. 3.7(c), all states are strongly split, similar to the first dimer in fig. 3.7(a). With an increasing angle, the splitting reduces, first for α [fig. 3.7(d)], but later also for β [fig. 3.7(e)]. At this particular distance, γ is always split. Interestingly, in fig. 3.7(e), three resonances are visible for γ, proving the degenerate nature of the underlying YSR states (see section 3.4.2). The three-fold degeneracy of the $d_{\mathrm{xy,xz,yz}}$-orbitals is lifted, which leads to a splitting of one of the YSR bound states, but leaves the others untouched.

The observed splitting of the YSR states may help to answer the question whether the coupling between the impurity spins is ferromagnetic or anti-ferromagnetic. Recently, Refs. [79, 80] dealt with a very similar question, namely with the competing interaction processes between two impurities with classical spins at different arrangements. By the way, the question is quite old. Already the early work by A.I. Rusinov [67] discussed in detail how YSR bound states hybridize when overlapping.

Mainly two processes play a role, a direct exchange interaction between the impurity spins, and an indirect exchange interaction via the spins of the conduction electrons, the so-called Ruderman-Kittel-Kasuya-Yosida (RKKY) interaction [81–83]. The latter oscillates between ferromagnetic and anti-ferromagnetic coupling with the distance, and mainly dominates the coupling of bound states in metals at intermediate length scales. However, the distances where we observe a coupling in our experiment are quite short, and they are directly connected to the lateral extension of the YSR states which we observed in Ref. [32] (section 3.4.2). It is correlated with the order of the Fermi wave length of the crystal, rather than with superconducting length scales of the order of the coherence length ($\lambda_{\mathrm{F}} \ll \xi$).

In general, a ferromagnetic coupling splits the states into a 'bonding', and an 'anti-bonding' component. The first lies lower and the latter lies higher in energy. In addition, a Zeeman interaction between the impurities may give an overall shift in energy compared to the unperturbed states. In the anti-ferromagnetic case, the states will not split, as the spin-component is anti-symmetric. Still, the states are sensitive to the effective Zeeman interaction of the impurity field, which might shift the state. Hence, the strong splitting of all states, independent of the angle at close distance between the adatoms, suggests a ferromagnetic coupling. Furthermore, the $\mathrm{d}I/\mathrm{d}V$ maps reveal the characteristic spatial distribution of bonding and anti-bonding states. The resonances denoted by sub-index b and a in fig. 3.6 and fig. 3.7 have a bonding and an anti-bonding character, respectively. The size of the splitting is proportional to the coupling strength between the spins. Thus, the coupling of state γ is the strongest, whereas it is weaker for the states α and β. However, as the distance increases, the splitting successively vanishes. Either this indicates that the coupling gets too small, or that it changes to an anti-ferromagnetic nature, where only a shift of the states in energy is expected. To solve this question experimentally, one would need YSR states that decay even slower, which would allow to observe a much larger coupling range.

We also employed measurements with a spin-polarized tip to probe the magnetic moments of both adatoms in a direct way (the method is described later, in section 4.2.1). Yet, we did not observe any spin polarization of the adatoms. This is most probably caused by a missing or too small magnetic anisotropy that stabilizes the magnetic moments with respect to an easy axis of magnetization. Considering the involved energy scales, magnetic anisotropy energies of single atoms on metallic substrates are expected to be very small compared to the energy of the tunneling electron. This is mainly due to the interactions with the substrate. For a heavy element (holmium), and a special environment with several intrinsic symmetries (time reversal symmetry, the internal symmetries of the total angular momentum, and the point symmetry of the local environment of the magnetic atom), an anisotropy in the order of 8 meV is reported on a Pt(111) substrate [84]. For Mn with a much lower magnetic moment we expect the anisotropy energy to be considerably smaller. Hence, we have to compare this value to two quantities of our experiment: the bias voltage in the millivolt range required to probe the YSR states, and the temperature, providing energies in the order of ≈ 330 µeV at 1.1 K. We conclude that the magnetic moments of the adatoms most probably fluctuate in time — even when coupled together. If it is faster than the rate of the tunneling current, it averages out the spin sensitive signal to zero. For typical currents in the order of 100 pA this limit lies in the order of nanoseconds.

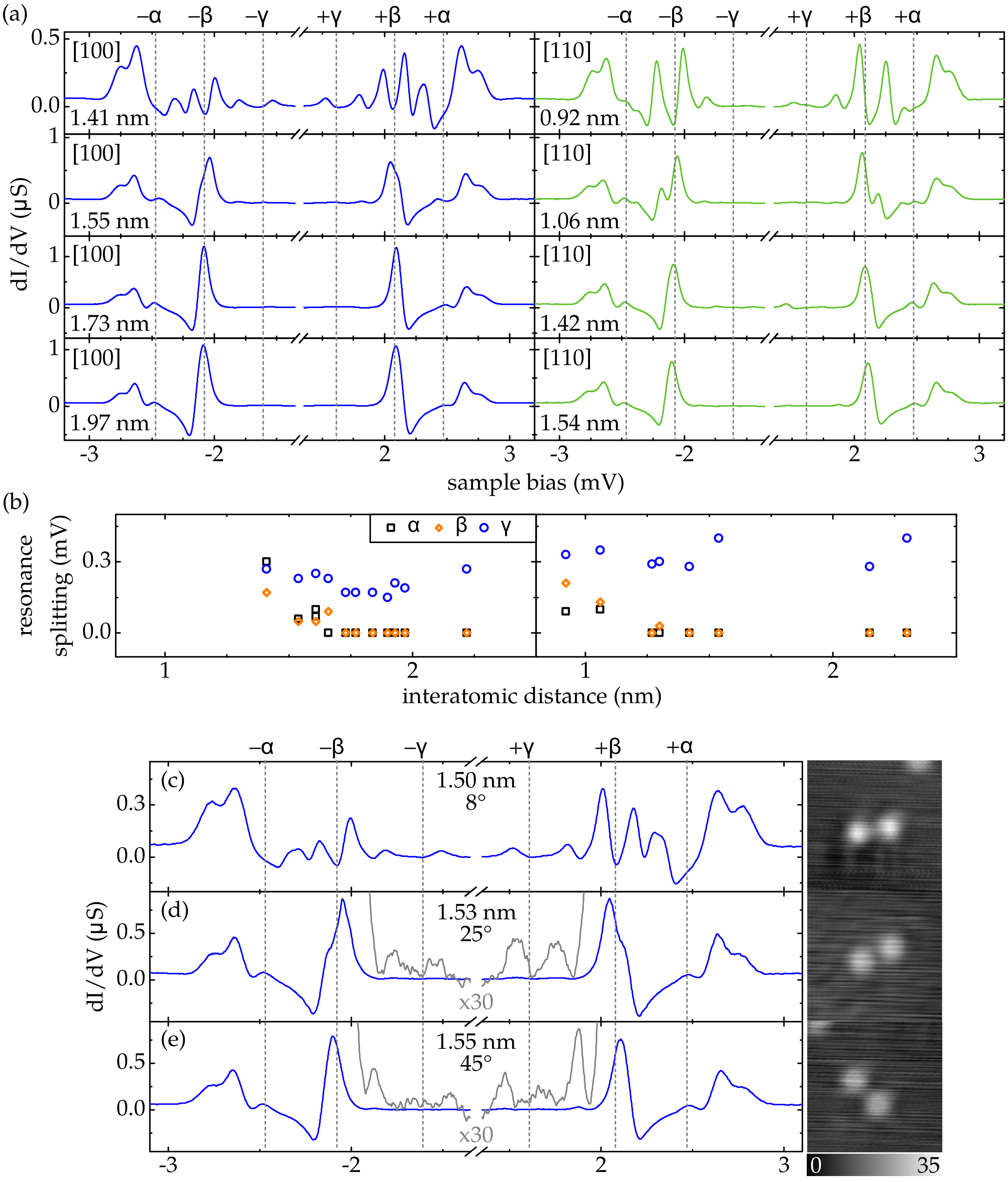

FIGURE 3.7: (a) dI/dV spectra of several Mn pairs ordered by their distance, and with the connection axis oriented along the surface lattice vectors [100] (blue solid lines) and [110] (orange solid lines). The energies of the non-split resonances $\pm\alpha$, $\pm\beta$, and $\pm\gamma$ of a single adatom without neighbor are indicated by gray dashed lines. The spectra are recorded at the center of one of the pair's adatoms, but the spectra at the respective other adatom are qualitatively the same. Setpoint: 200 pA, 4 mV. Lockin modulation: 15 µV. Accuracy of distance and angle: ±0.08 nm, ±4°. (b) Energy splitting of the peaks α, β and γ into bonding and anti-bonding resonances, depending on the interatomic distance for the angle defined above. (c–e) dI/dV spectra of several Mn pairs at the same distance of ≃ 1.5 nm, but at different angles of the connection axis with respect to the surface lattice vectors [100] and [110]. In (d) and (e), the spectrum multiplied by 30 is shown as gray overlay to emphasize the splitting of resonance γ. Setpoint: 200 pA, 4 mV. Lockin modulation: 15 µV

Chapter 4

Chains of coupled magnetic adatoms

In the preceding chapters we investigated the interaction of single magnetic impurities with a superconducting substrate. It appears as a single or as multiple YSR bound states induced in the substrate at energies within the superconducting gap. We observed a coupling of two impurities at close distance when the impurities were oriented in a way that their bound states overlap. In this chapter of the thesis, we finally focus on the vision of topological quantum computation (TQC), which promises fault-tolerant qubit operations [85]. This requires the qubits to be protected from external perturbations, which is achieved by a non-local way of information storage. In the following, we investigate a promising platform for such type of qubits, namely one-dimensional (1D) chains of magnetic adatoms on a conventional *s*-wave superconductor with strong spin-orbit coupling.

The elemental excitations we are looking for are so-called Majorana zero modes (MZMs), predicted to appear at the ends of magnetic 1D chains on superconductors [86]. A pair of these states may act as a single qubit, fulfilling the necessary conditions for TQC. Localized at the chain ends they are separated in space and, hence, immune to local perturbations. A brief introduction to the theory governing these excitations is given in section 4.1. Later, we report the results of experiments on Fe, Co, and Mn chains on Pb(110). Literature predicts a quite universal appearance of MZMs, which is independent of the individual element investigated. In collaboration with theorists we test this prediction for its validity in section 4.2.

An interesting property of MZMs is their non-abelian exchange statistics. They are neither fermions, nor bosons, but anyons [85]. For a pair of these states, the ground state is degenerate. After exchange of two particles the system is still in the ground state, but in a different absolute state ($|c_1, c_2\rangle = e^{i\Phi}|c_2, c_1\rangle$), indicated by the phase Φ. For bosons it would be 0, and for fermions if would be π. For anyons, however, it is arbitrary. Moreover, this makes a pair of MZMs a prime candidate for a qubit in TQC. It allows to store information in such a pair via the phase. The information may be accessed by so-called braiding operations, which are the controlled exchange operations triggered by low excitations.

4.1 Topological superconductivity and Majorana Zero Modes

The terminology of Majorana zero modes (MZMs) arises from the field of particle physics. There, one of the salient predictions — not yet experimentally confirmed — was made in 1937 by E. Majorana [87]. He forecast a particle which is its own anti-particle, a so-called 'Majorana fermion'. The most promising candidates in experiment are neutrinos, but to prove their existence a rare double-beta decay needs to be observed. There, the two neutrinos may annihilate, if they are Majorana particles [88].

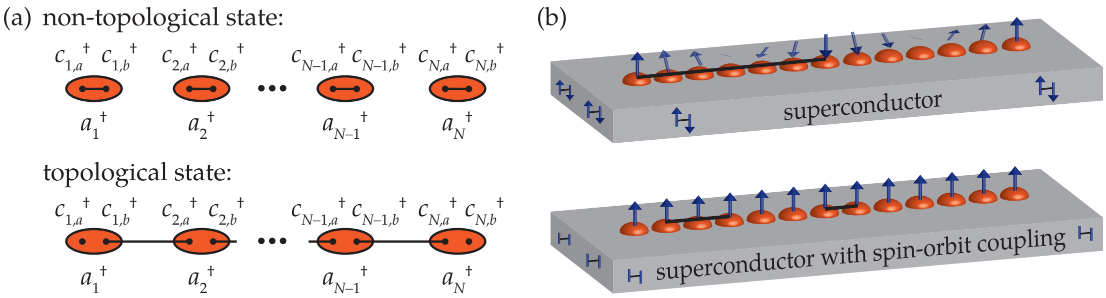

FIGURE 4.1: (a) Toy model of a 1D Kitaev chain with N electronic sites. Each site with creation operator $a_j^{\dagger}$ can be expressed by two Majorana operators $c_{j,a}^{\dagger}$ and $c_{j,b}^{\dagger}$. A superconducting gap and hopping of the c_j operators between different sites puts the chain into a topological state. Pairing of the operators in this state occurs between different sites, and it leaves two unpaired operators at the chain ends ($c_{1,a}^{\dagger}$ and $c_{N,b}^{\dagger}$). (b) Two proposals for the realization of a Kitaev chain that host MZMs at the chain ends. A magnetic chain with helical order on an s-wave superconductor (top), and a ferromagnetic chain on an s-wave superconductor with strong spin-orbit coupling (bottom). The latter weakens the singlet nature of the spins in the Cooper pairs. In both cases a fraction of the Cooper pairs may enter the chain giving rise to proximity superconductivity within the chain (indicated by black lines symbolizing the pairing between the individual sites).

Most often in condensed matter physics, the particles of interest are electrons. The analogue to an anti-particle is a ‘hole’. Hence, the profound question arises, if an emergent quasiparticle corresponding to a ‘Majorana fermion’ may exist in solid state systems as a collective many-body state. In this sense, superconducting materials are prime candidates to host such particles, as they provide an inherent particle-hole symmetry. It connects excitation of electrons and holes via the Cooper pair condensate. We have seen in chapter 3 that all states appear as a pair of resonances at positive and negative energy. A ‘Majorana excitation’ would thus require to be bound at zero energy. An interesting property of such an excitation becomes obvious when we think of an artificial defect that induces a *single* bound state of such a type. The state is fixed to zero energy to fulfill the Majorana condition for the creation and annihilation operators ($c^{\dagger} = c$), which gives it the name Majorana zero mode (MZM). Any interaction with this state would shift its energy away from zero. However, in a superconductor, a single state with *finite* energy requires always a second state, to fulfill the particle-hole symmetry. Hence, as long as no second MZM is close to the first, it is ‘topologically protected’ against any perturbation that would lift its energy away from zero.

4.1.1 Theoretical toy model: the Kitaev chain

The basic ingredients for a system to allow MZMs are rather general. First, it requires a laterally extended system to be able to separate states in space. Second, the electronic bands of the system must possess a finite energy gap at the Fermi level. This prevents the recombination of two spatially separated MZMs. Finally, the bands must have in total an odd number of Fermi points within the first half of the Brillouin zone. At each of these points a single MZM is induced. Hence, only for an odd number of states all but a single MZM recombine in pairs.

The most simple proposal to realize such a system was set up by A.Y. Kitaev [86]. His idea has the charming nature to be exactly solvable. He suggested a linear magnetic chain of single atomic sites on a conventional superconducting substrate. The magnetism of the chain implies that only bands of the same spin-flavor are located at the Fermi level. Moreover, this makes the spin superfluous, giving the band the property of being spin-less. To make the chain superconducting, even though it has magnetic order, Kitaev proposed to place it in proximity to a bulk superconductor, which transfers the pairing amplitude to the chain.

Furthermore, Kitaev assumed that each atomic site j of the chain has only a single electronic level. It is described by a pair of electron creation and annihilation operators ($a_j^{(\dagger)}$). Formally, he introduced the MZMs by splitting each site into two new operators, defined by

$$c_{j,a} = a_j + a_j^\dagger \,, \quad c_{j,b} = \frac{a_j - a_j^\dagger}{i} \,, \tag{4.1}$$

$$c_m = c_m^\dagger \,, \quad \{c_l, c_m\} = c_l c_m + c_m c_l = 2\delta_{lm} \,. \tag{4.2}$$

The model is sketched in fig. 4.1(a). Each operator can be seen as contributing 'half' a fermion.

The system enters a topological regime, when including the superconductivity of the chain, and when allowing a finite hopping amplitude w of the operators c_j between different chain sites. In this case, the operators pair between different sites (j and $j+1$), which is described by the simple Hamiltonian:

$$H = i\, w \sum_{j=1}^{N} c_{j,b}\, c_{j+1,a} \,. \tag{4.3}$$

In fact, this Hamiltonian ignores an unpaired operator at each chain end. Hence, as long as no second MZM is interacting with the first, it is immune to local perturbations introduced by the Hamiltonian. The system is 'topologically protected', unless the superconducting gap is closed.

Two proposals to realize a Kitaev chain in experiment are sketched in fig. 4.1(b). The first is a chain with a helical spin structure on an s-wave superconductor. The helicity of the spins allows the singlet Cooper pairs to enter the chain. The second system is a ferromagnetic chain on an s-wave superconductor with strong spin-orbit coupling. The latter softens the singlet nature of the Cooper pairs, which otherwise would not be able to enter the ferromagnetic band. In both scenarios a tiny part of the pairing amplitude is transferred to the band structure of the chain. This small induced gap is sufficient to protect the localized MZMs at the chain ends from the continuum of states.

4.1.2 Experimental realizations of a Kitaev chain

A first approach to realize a Kitaev chain experimentally was suggested by L. Fu and C.L. Kane [89]. They proposed a hybrid system, where the superconductivity of the host is combined with helical edge states of a topological insulator at the interface. The first salient success in building a mesoscopic system that hosts MZMs in experiment was achieved in 2012 [90]. They employed a semiconducting nanowire adsorbed on an s-wave superconductor under a magnetic field. It followed preceding theoretical suggestions [91–93], and was verified by other experimental work later [94–98]. Still, these types of experiments lack to show the spatial localization at the chain end, as they use mesoscopic methods [99].

A complete different proposal suggested a bottom-up fabrication of Kitaev chains using nanoscopic methods [100]. By means of STM one would be able to directly probe the MZMs at the chain ends. In 2014, S. Nadj-Perge *et al.* realized such a system in a ground breaking experiment [101]. They evaporated Fe chains on Pb(110), where chains grew up to 20 nm in length by self-assembly. These chains emerged from larger Fe clusters along the [110] direction of the substrate. However, chains without a cluster at one of the ends were not observed. The chains are ferromagnetic, and hence resemble a system similar to the one sketched in fig. 4.1(b, bottom). By DFT simulations, they gave evidence that the chains were arranged in a zig-zag stacking of three Fe atoms perpendicular to the surface. The neighboring Pb surface atoms stabilize the chain to a single atomic width. Although this system is far away from Kitaev's toy model, STS measurements indicated signatures of a single zero energy resonance localized at the free chain end (the one not attached to the Fe cluster). They attributed this to an isolated MZM.

4.1.3 Iron chains on Pb(110)

Reference [101] laid the ignition point for a manifold of further theoretical works discussing the particular investigated system [102–105]. However, several questions were still open from the experimental side, which asked for further investigations. The majority of spectra shown in Ref. [101] were measured with a metallic tip. At a temperature of $\simeq 1.4$ K this limited the energy resolution by Fermi-Dirac statistics to $\simeq 180$ µeV. As reported in chapter 3, a single adatom creates a variety of bound states, which additionally split when coupled with those of other adatoms. Therefore, a full chain of adatoms induce extended subgap bands, because of hybridization of all neighboring YSR states. Hence, measurements with a low resolution are not capable to distinguish between true zero energy states, and trivial resonances from YSR bands at low, but finite energy. A minority of spectra in Ref. [101] was measured with a superconducting tip. However, the data was only shown in half, just at positive bias voltages. Remember that measurements with a superconducting tip shift all spectra by the tip gap $\pm\Delta_{\text{tip}}$ because of the convolution of tip and sample DOS. Hence, a zero energy state appears as a pair of resonances at $\pm\Delta_{\text{tip}}$. Showing only the positive half of the spectrum forbids an analysis of the asymmetry of the two zero energy resonances. If they originate from a MZM, they have to be symmetric in intensity, as they indicate transport into the same state. Moreover, this is always the case, independent of whether being in the strong, or in the weak tunneling regime. Furthermore, such zero energy state facilitates perfect Andreev reflections, which leads to a quantized conductance with size $G = (4 - \pi)\, 2e^2/h$ [106].

To answer the open questions we employed the same experimental setup. We carried out high resolution measurements with a superconducting tip at $\simeq 1.1$ K on Fe chains on Pb(110). The results were published by M. Ruby *et al.* "End States and Subgap Structure in Proximity-Coupled Chains of Magnetic Adatoms". In: *Phys. Rev. Lett.* 115 (19 Nov. 2015), p. 197204. The article is reprinted in appendix B.5.

Our measurements reveal Fe chains up to $\simeq 10$ nm in length. They were obtained by slightly different preparation conditions than suggested in Ref. [101]. We performed STS on various chain ends. Only some of them exhibit clear zero-energy signatures, often accompanied by two resonances at higher energies. An important result is that all investigated chains showed a substantially different intensity between the positive and negative bias resonance (at $\pm\Delta_{\text{tip}}$). This indicates that they originate, at least not solely, from MZMs, but have some contribution from trivial YSR resonances.

Another outcome was that the resonance at lowest finite energy is observed at $\simeq 80\ \mu\text{eV}$. In terms of a topological system, this would indicate the edge of the induced topological gap, or at least give an upper limit for this quantity. It turns out to be much smaller than anticipated in Ref. [101], where they estimated values of $200 - 300\ \mu\text{eV}$ from their experiment.

In addition to $\mathrm{d}I/\mathrm{d}V$ spectra at the ends of the chains, we had a closer look at the full chain bodies. We found a localization of the zero-energy resonance at the chain end, whereas the low-energy excitations below $\simeq 100\ \mu\text{eV}$ appeared also along the chain, but with slightly varying energies and intensities. Interestingly, the other subgap resonances of the YSR bands oscillate in intensity along the chain. It appears correlated to some slight variations in the topography of the chain. Spectra at energies of the d-bands revealed a similar oscillation of these bands along the chain.

In close collaboration with theorists we were able to explain all these findings. Indeed, the oscillations of the YSR resonances and of the d-bands in energy are connected. They are given by local variations in the potential landscape. In contrast, the fluctuations of the low-energy resonance below $\simeq 100\ \mu\text{eV}$ (indicating the topological gap) are solely influenced by finite size effects, and they are insensitive to details of the impurity. Last but not least, the exponential localization of the zero-energy resonance at the chain end matches with a possible MZM. Its localization length is much shorter than the superconducting coherence length because of renormalization of the Fermi velocity within the chain [103].

Our experiment contributed important additional details to the system of Fe chains on Pb(110). We emphasized the advantages of measurements with a superconducting tip over a metal tip. It not only increases the energy resolution, but delivers information about the nature of the states by the asymmetry of their spectral intensities at positive and negative energies. However, a conclusive confirmation of MZMs is not possible with the energy resolutions of our setup. An unambiguous result requires considerably lower temperatures in future measurements.

Recently, the group of Ref. [101] implemented a follow-up experiment. Their new measurements were carried out in a dilution refrigerator setup at $20\ \text{mK}$ [107]. Using a metal tip, they confirmed a high intensity zero-energy resonance at the chain end, which was apparently separated from other states. Furthermore, in their experiments, the resonance did not deviate from zero energy within their resolution limit of $80\ \mu\text{eV}$. Following the suggestion of our work [31], they used superconducting tips. However, their resolution was even lower than what they achieved with their metal tips. Nevertheless, they reported symmetric zero-energy resonances for some tip-chain combinations, but also cases with asymmetric intensities. This confirms our observations. All in all it is clear that more effort is required to figure out the reason for these variations.

4.2 Other transition metal chains on Pb(110)

Literature predicts that linear suspended transition metal chains on Pb(110) are quite generic in hosting MZMs, as long as the chains exceed a certain length [102]. To test this hypothesis, we performed measurements at Co and Mn chains, which we report in the following sections. As chains of these elements were not investigated before, we first had to check thoroughly that all necessary conditions for a topological state were fulfilled, namely a ferromagnetic band structure, and topological superconductivity. The first was probed by spin-polarized scanning tunneling microscopy (SPSTM), a technique in which

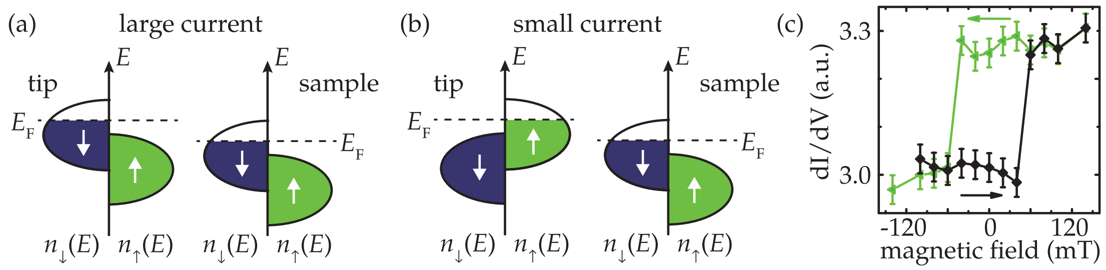

FIGURE 4.2: Spin-polarized tips have a majority and a minority spin density $n_{\uparrow/\downarrow}(E)$ at the Fermi level. The spin-sensitive current is large if the majority of spins in tip and sample are aligned (a), or else it is low (b). Both cases are measured in SPSTM to obtain the magnetization of the sample. Sketch adapted from Ref. [108]. The hysteresis loop of the tip used in section 4.2.2 is shown in (c). It has a remanence at zero field, and a coercivity of ≈ 50 mT.

a spin-sensitive current is measured. The latter was probed by high energy resolution measurements with superconducting tips, similar to the experiments described in the chapters above.

4.2.1 Spin polarized scanning tunneling microscopy (SPSTM)

The technique of spin-polarized scanning tunneling microscopy (SPSTM) uses a magnetized tip apex to probe the sample with a spin-polarized tunneling current [108, 109]. If tip and sample magnetization are aligned, the current is increased, in the opposite case, it is decreased versus measurements with an unpolarized tip. This is sketched in fig. 4.2(a) and (b), where each electrode possesses a density of states $n_{\uparrow/\downarrow}(E)$ for each spin-direction ($\uparrow$ / $\downarrow$).

To achieve a magnetization of the tip in experiment, we cover it with a thick layer of Co by electron beam evaporation at room temperature. The spin-sensitivity is checked prior to the measurements on two-monolayer high cobalt islands on copper (Cu)(111). The islands possess an out-of-plane magnetization and represent a standard reference system for SPSTM [110]. Our experimental setup allows an out-of-plane magnetic field up to ± 3 T, which we use to flip the out-of-plane component of the tip's magnetization. Hence, we are sensitive to any sizeable polarization of the sample in this direction. Spin-polarized measurements on superconductors at subgap energies require a remanence of the tip at zero field. Applying a magnetic field to align the tip during the measurement would quench the superconductivity. The hysteresis loop of the tip used in the following section is shown in fig. 4.2(c). It has a coercivity of ≈ 50 mT.

4.2.2 Co chains on Pb(110)

Deposition of Co onto Pb(110) yields clusters and 1D chains with lengths up to $\simeq 10$ nm. In topography, Co chains look like Fe chains. The chains emerge along the [110] direction of the crystal, and in most cases start at larger Co clusters. An overview image is shown in fig. 4.3(a).

We probed the magnetic properties of the Co chains by spin-polarized scanning tunneling microscopy (SPSTM), and observe a resonance at -0.17 V [see fig. 4.3(b)]. It exhibits different intensities for oppositely polarized tips (labeled by tip-$\uparrow$ and tip-$\downarrow$, respectively). We ascribe it to the van Hove singularity of a spin-polarized Co *d*-band.

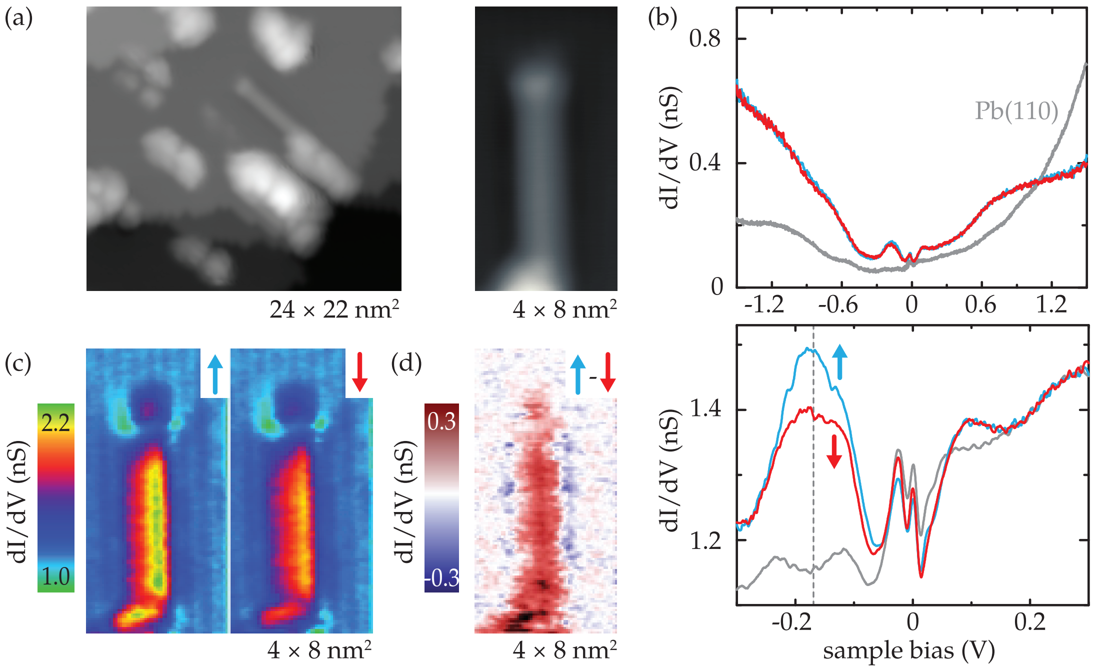

FIGURE 4.3: Co chain on Pb(110). (a) After deposition on Pb(110), Co forms clusters and 1D chains. The right panel shows a zoom-in of the chain of ≈ 5.5 nm length. Setpoint: 500 mV, 50 pA. (b) Spin-polarized $\mathrm{d}I/\mathrm{d}V$ spectra of the chain shown in (a) (*blue*, *red*) and of pristine Pb(110) (*gray*). The blue (*red*) curves are acquired in a $+(-)0.3$ T field along the surface normal, which ensures opposite tip magnetization (in the following denoted by ↑ and ↓). Setpoint: 1.5 V, 400 pA. The inset shows spectra in a narrower energy window. Setpoint: 300 mV, 400 pA. (c) shows $\mathrm{d}I/\mathrm{d}V$ maps at $V = -170$ mV in fields of ± 0.3 T, respectively, revealing spin-dependent $\mathrm{d}I/\mathrm{d}V$ intensities all along the chain. Feedback: 300 mV, 400 pA. (d) Difference map between both $\mathrm{d}I/\mathrm{d}V$ maps in (c).

The magnetic order along the entire chain is revealed by $\mathrm{d}I/\mathrm{d}V$ maps at the energy of this resonance. The maps in fig. 4.3(c) uncover that the intensity along the chain is stronger for tip-↑ than for tip-↓. This becomes clearer in the difference of both maps, shown in fig. 4.3(d). There, a positive contrast (*red*) is observed all along the chain, which suggests a ferromagnetic ground state, in full similarity to the Fe chains on Pb(110) reported in Ref. [101].

We performed a similar type of measurement at subgap energies. However, we relied in this case on a remanence in the tip at zero field[1]. The $\mathrm{d}I/\mathrm{d}V$ spectrum in fig. 4.4(a) on pristine Pb(110) shows a BCS-like gap. It is broadened by the Fermi-Dirac distribution of the normal state tip at 1.1 K. On the chain, there are broad resonances by YSR bands within the gap. They vary in intensity along the chain. When measured with opposite tip magnetization, the spectra are qualitatively similar everywhere, but they vary in their signal strength. The overall intensity at negative energies is stronger for $\text{tip}_{\uparrow}$ than for $\text{tip}_{\downarrow}$. Accordingly, at positive energies, it is the opposite. Again, to obtain the spin-texture of the entire chain, we recorded $\mathrm{d}I/\mathrm{d}V$ maps at both orientations of the tip magnetization. They are shown in fig. 4.4(c) and (d), respectively. The difference map in fig. 4.4(e) exhibits an overall positive polarization along the chain at -850 µV, but a negative polarization at $+850$ µV (not shown here). This sizable spin polarization is remarkable.

---

[1] The measurements at higher energies were carried out under an applied field. This quenches the superconductivity.

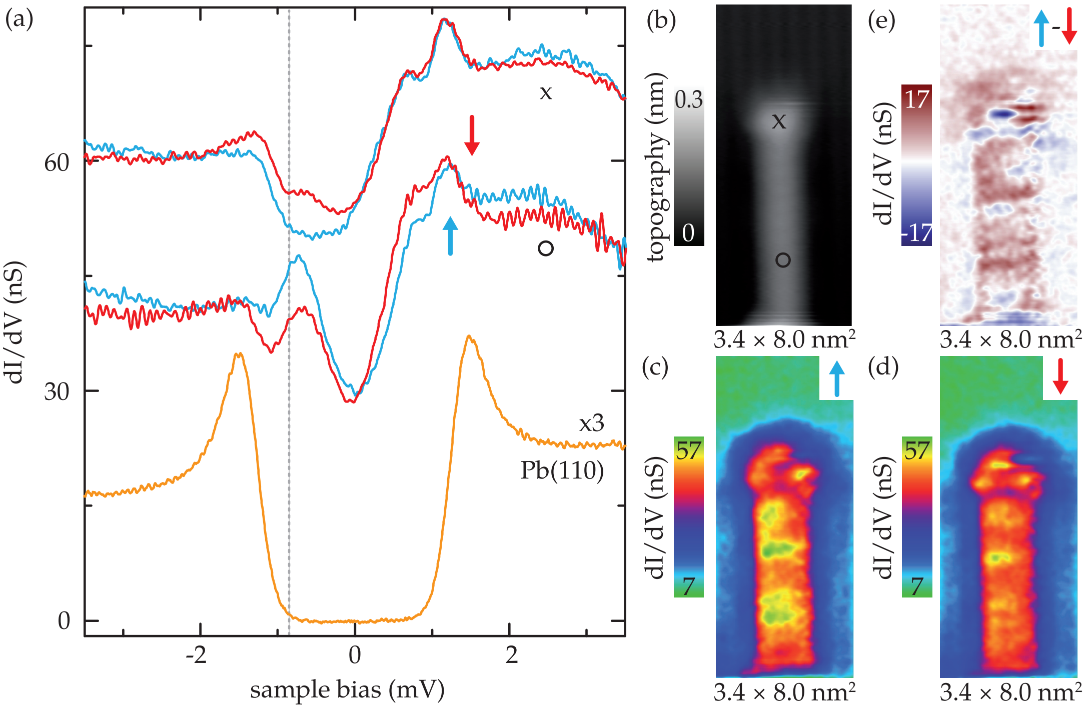

FIGURE 4.4: Co chain on Pb(110). (a) $\mathrm{d}I/\mathrm{d}V$ spectra taken at the two positions on the Co chain depicted in the topography in (b). For clarity, the spectrum on the bare surface is divided by three. The data is recorded at 0 T with a spin-polarized tip. It has an out-of-plane remanence perpendicular to the sample surface. Setpoint: 4 mV, 200 pA. The dashed line at −850 µV marks where the $\mathrm{d}I/\mathrm{d}V$ maps in (c,d) are recorded with parallel and anti-parallel tip-magnetization, respectively. The feedback was opened at 4 meV, 200 pA where no spin-polarization is observed. (e) Difference between (c) and (d) characterizing the spin-polarization of the chain.

It provides direct evidence for the magnetic nature of YSR states. The hybridization of states of neighboring adatoms along the chain results in entire spin-polarized YSR-bands. In section 4.1.3 we showed that confinement effects and variations in the local potential along the chain cause intensity variations of the YSR-bands. Still, the spin-polarization is uniform (at −850 µV). We detect only at the chain end a region of opposite polarization.

The robust ferromagnetic nature of the Co *d*- and YSR-bands was thus proven. Next, we investigated the subgap structure in more detail, and searched for possible MZM at the chain ends. Thus, we employed measurements with a superconducting tip to enhance the energy resolution.

The $\mathrm{d}I/\mathrm{d}V$-spectra along the chain in fig. 4.5(a) and (b) show a rich subgap structure, similar to the case of Fe chains. Three regions of resonances were observed, which are labeled α, β and γ in fig. 4.5(b). In the case of Fe chains, only a single pronounced resonance was resolved. Within these regions, the van Hove singularities of the YSR-bands of the Co chains vary in intensity and in energy because of a local variation of potential, and because of confinement effects [31]. At zero energy, i.e., at a bias voltage $\simeq \pm\Delta_{\mathrm{tip}}$, we observed resonances (or shoulders) which could at first sight be reminiscent of MZMs, albeit, the signal was present all along the chain with no sign of localization at the chain end.

A possible explanation for the missing localization of the zero-energy resonances at the chain end is a too short chain length, which allows hybridization of the MZM.

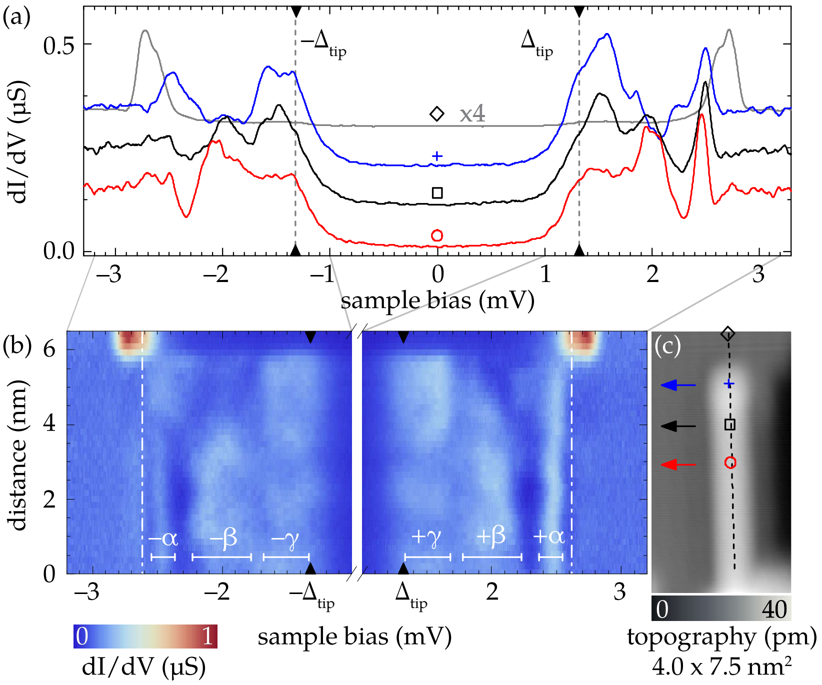

FIGURE 4.5: (a) dI/dV-spectra acquired with a superconducting tip at the positions which are indicated by symbols in the topography in (c). Chain length $\simeq 6.3$ nm. For clarity, the spectra are offset by 0.1 µS. The spectrum on the bare surface (*gray*) is divided by four. The tip gap is marked by dashed lines ($\pm\Delta_{\mathrm{tip}} = \pm 1.32$ meV). (b) False-color plot of 40 dI/dV spectra measured along the dashed black line in (c). Spectral intensity appears mainly in the six energy intervals ($\pm\alpha$, $\pm\beta$, $\pm\gamma$), with $\alpha \simeq (2.5 \pm 0.1)$ mV, $\beta \simeq (2.0 \pm 0.2)$ mV, and $\gamma \simeq (1.5 \pm 0.2)$ mV. As a guide, the dashed-dotted lines indicate the gap edge at $eV = \pm(\Delta_{\mathrm{tip}} + \Delta_{\mathrm{sample}})$. Setpoint: 4 mV, 500 pA.

In view of the expected localization length of the order of atomic distances [103], we assumed that the length is sufficiently long. Further measurements are required to testify this. The observed zero-energy resonance along the entire chain can be understood as a consequence of the subgap band structure. In the case of Fe chains, the induced superconducting gap amounts to at most 80 µV [31]. It is possible that the induced gap is even smaller in Co chains. With an experimental energy resolution of $\simeq 60$ µV, the coherence peaks associated with the gap edges would then not be resolved. Instead, they appear as a sizable feature at zero energy. Clearly, the coherence peaks are a bulk feature of the chain and the corresponding peaks in dI/dV should persist along the entire chain.

Anyhow, we want to discuss a possible explanation for the missing indications of MZMs in this particular system. All necessary ingredients for topological superconductivity and MZMs appear to be fulfilled. The chain is ferromagnetic, with spin-polarized bands at the Fermi level, and it is coupled to an *s*-wave superconductor with strong spin-orbit coupling.

Tight-binding calculations with the elemental bulk parameters [111] yield a rough idea of the band structure of linear suspended chains[2]. It is plotted for a free Co chain

---

[2] Ref. [112] points out that results, obtained by using the bulk tight-binding parameters, are not suited to reproduce exact details, such as the placement of the Fermi level. Hence, we rely on counting the number of valence electrons to place the Fermi level.

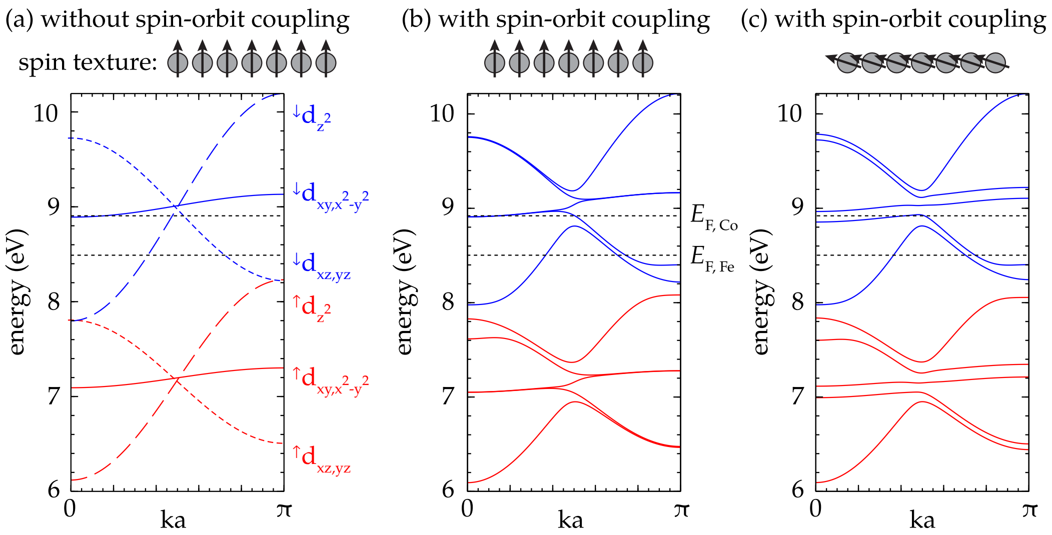

(a) without spin-orbit coupling (b) with spin-orbit coupling (c) with spin-orbit coupling

FIGURE 4.6: Tight-binding band structure in half of the Brillouin zone of a Co chain with a lattice constant of $a = 2.486$ Å. Within this simple model, the band structure for elements above a half filled d-shell is similar. An estimation for the Fermi levels in the atomic limit is sketched in (a–c) by dashed lines for the elements Fe, and Co. In (a), the calculations were done without spin-orbit coupling, and with the orientation of the magnetic moments perpendicular to the chain direction. The d-orbital character of the bands is indicated beneath. The majority and minority bands are split by exchange interaction. In (b) and (c), the calculations consider spin-orbit coupling with a coupling constant $\lambda_{\mathrm{so}} = 0.2$ eV, which intermixes the different d-characters. In (c), the spin texture of the chain is additionally altered by a canting of the magnetic moments with an angle of $2\pi/5$ with respect to the chain normal. Calculations were done by Y. Peng.

in fig. 4.6(a). In total, the atomic d-orbitals hybridize into three bands for each spin flavor, of which two are doubly degenerate. Two broad bands with a width of ≈ 2 eV originate from the d_{z^2} and $d_{\mathrm{xz,yz}}$ orbitals, and a more narrow band with a width of ≈ 0.3 eV originates from the d_{xy,x^2-y^2} orbitals. The ferromagnetic order leads to a strong exchange splitting of minority and majority spin bands, separating them in energy. The s-bands are higher in energy and thus have no significant overlap with the d-bands. The band structure is similar to the one obtained for Fe chains in Refs. [101, 102]. Without neglecting spin-orbit coupling, the bands intermix in their character and cannot be assigned to originate from specific d-orbitals anymore. Most significant, though, is the splitting of the bands, and the opening of gaps between them [fig. 4.6(b) and (c)].

A crucial difference to the Fe chains is the placement of the Fermi level. It is an important property for the formation of MZMs, as it determines the number of Fermi points of the band structure. In section 4.1.1 we emphasized that an odd number of points is required to establish a topological regime, as one MZM is induced at each point. Only with an odd number of MZMs, a single MZM remains after hybridization.

Two different plausible scenarios have to be distinguished for this system. The first is the atomic limit, in which the number of valence electrons is deduced from a single adatom on the Pb substrate. Within this picture, electrons are transferred into the bulk, and the atom gets a positive charge. Presumably, the s-shell is emptied, leading to an oxidation state of 2+ to 3+, which is the most common oxidation state of transition metals. Accordingly, the Fermi levels for the elements Fe and Co are sketched in fig. 4.6(b) and (c) by dashed lines.

The second scenario is the bulk limit. It considers *all* valence electrons. Thereby, the electrons in the *s*-bands redistribute partly to the *d*-bands [113] because of an energetic overlap between the bands. This is, however, sensitive to the bandwidth of the involved states. A change in coordination number from 3D to 1D reduces this width. As mentioned above, our calculations yield no significant overlap between the *d*- and *s*-bands for linear suspended chains.

In the following, we focus on the first scenario, which we consider the most likely. As shown in fig. 4.6(b), we find two broad minority bands crossing the Fermi energy E_F. One is twofold degenerate. In addition, a narrow, doubly degenerate band lies close to the Fermi level. This band might give rise to the resonance at -0.17 mV, which we observed in fig. 4.3(b). As long as the on-site magnetization is exactly perpendicular to the chain direction, the system has an *odd* number of Fermi points within half the Brillouin zone. However, a tilt of the magnetization parallel to the chain lifts all remaining degeneracies of the bands. This may yield an *even* number of Fermi points within half the Brillouin zone, as sketched in fig. 4.6(c) for a canting of $2\pi/5$ with respect to the chain normal. Hence, even if most prerequisites for the formation of MZMs are fulfilled, the hybridization between the Fermi points prevents establishing a topological phase. In the case of the Fe chain the adatoms have one less *d* electron, resulting in a correspondingly lower E_F. For comparison, this case is shown in fig. 4.6(b) and (c). There, three Fermi points are present. This is consistent with the formation of a topological state hosting MZMs, and it matches with the results reported in section 4.1.3.

4.2.3 Mn chains on Pb(110)

Let us now return to chains of the element at which our investigations for single impurities began, to Mn chains. We report here some preliminary results for measurements on this system, because they appear to provide interesting properties for future experiments.

The preparation conditions of Fe and Co chains did not suffice to form Mn chains. Only clusters were obtained. Already for Co chains, the maximum growth temperature was lower ($\simeq$ 263 K) than for Fe chains ($\simeq$ 290 K). We discovered that linear Mn structures are obtained when decreasing the temperature to $\simeq$ 170 K. To our surprise, the topography of these chains is substantially different [see fig. 4.7(a)]. The chains appear submerged below the surface. Topographies with atomic resolution suggests that the Mn chains are covered by the first surface layer. The Pb adatoms also rearrange over the chain, where two atomic rows of the surface along the [110] direction merge to a single row [see the blue lines in fig. 4.7(a)].

In search for MZMs, people came up recently with the idea to cover linear semiconducting nano-wires by an additional monolayer of the substrate, to enhance the coupling to the bulk [114]. A similar setup was suggested for the transition metal chains on Pb(110), e.g., by evaporation of an additional monolayer [107]. Hence, chains that grow by themselves below or within the first surface layer might be of high interest.

Our experiment started again by testing the spin-texture of the Mn chains. We employed measurements with oppositely polarized magnetic Co tips at zero-field, but with a non-zero remanence. The chains showed no resonances in the energy range of ±750 meV. However, at subgap energies, two broad YSR resonances at $\simeq \pm 600$ µV were observed in the entire chain region, which show a spin contrast [see fig. 4.7(b)]. Towards the chain ends, the resonances were shifted to lower energies. No zero-energy resonance was observed within the thermally limited resolution of $\simeq$ 330 µeV. To obtain the full spin-texture of the chain, we recorded $\mathrm{d}I/\mathrm{d}V$-maps at the energy of the

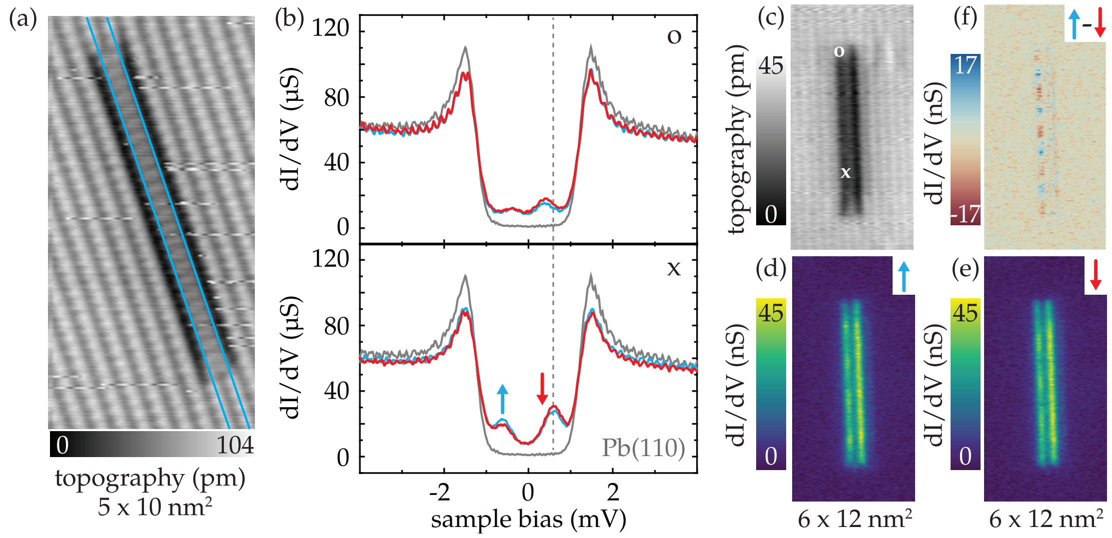

FIGURE 4.7: (a) Atomic resolution of a Mn chain on Pb(110). The chain appears as depression, suggesting that it is embedded below the surface. The surface Pb adatoms rearrange over the chain, where two atomic rows (marked by blue lines) merge to a single row. Setpoint: 70 pA, 500 mV. (b) dI/dV-spectra on the locations depicted by 'x' and 'o' in the topography in (c). Opposite tip magnetization is indicated by ↑ and ↓, respectively. (d,e) dI/dV maps at 600 μeV [marked by the dashed line in (b)]. The difference map (f) shows a spin contrast along the chain, which switches between positive and negative with a period of $\simeq 1.9$ nm. Setpoint: 200 pA, 4 mV. Lockin: 50 $\mu\mathrm{V}_{\mathrm{rms}}$.

YSR resonances with opposite tip magnetization [fig. 4.7(d) and (e)]. Interestingly, the two depleted rows, symmetric to the central axis of the chain, had the largest spectral intensity. Both rows were laterally separated by a region with almost no spectral intensity. This suggests that these Mn chains are actually more complex than assumed. They may consist out of two separated parallel rows of Mn, instead of a single row of adatoms.

The difference map in fig. 4.7(f) shows a strong periodic change between positive and negative spin contrast at the left row, which oscillates with a period of $\simeq 1.9$ nm. This is much larger than the atomic scale, and therefore opens the possibility of a helical spin arrangement. Such a case would not be distinguishable from an anti-ferromagnetic arrangement in our experiment. The right row shows almost no contrast, which may be a measurement artifact, occurring because of a weaker wave function overlap of tip and sample within this region.

The observations differ significantly from the ferromagnetic Fe and Co chains investigated so far. Moreover, further experiments are required to find out more details of the spin-texture of the Mn chains. To obtain these results requires a vector field, which allows to precisely control the orientation of the tip magnetization. Independent of this specific system, we suggest to investigate whether other transition elements form a similar type of buried structure. Chains of this kind could have a stronger coupling to the substrate, and thus an enhanced topological superconductivity.

Finally, the implications of a helical or an anti-ferromagnetic spin arrangement on the topological phase shall be discussed briefly. A helical arrangement of the spins within the chain may be a direct consequence of the low-dimensionality of the system. In particular, the spin-orbit coupling of the electrons in combination with the symmetry of the chain leads to an anisotropic super-exchange interaction between next-nearest neighbor atoms: the Dzyaloshinskii–Moriya interaction [115, 116]. It favors a successive canting of each spin with respect to the nearest neighbors. Compared to a ferromagnetic arrangement, such an arrangement allows a long-range hopping in the order of the helical period. We pointed out in section 4.1.1 that, in this case, superconductivity in the chain may be induced even without strong spin-orbit coupling of the substrate. Hence, topological superconductivity by proximity may establish on any *s*-wave superconductor for a helical spin arrangement, and thus may mediate a topological phase. This was discussed in many recent theoretical publications [117–124]. An important prerequisite for the system to host MZMs is a strong Rashba spin-orbit coupling along the wire, which leads to a spin-momentum locking. Additionally, a weak external magnetic field is required to open a tiny gap in the band structure for the bands with different spin directions, which closes at the chain ends, and which gives rise to the MZMs. Interestingly, the chain may be pushed as well into a topological regime by a local variation of the chemical potential, e.g., by gate electrodes underneath it [117]. This is a convenient property for TQC, as it allows to artificially manipulate the individual MZMs along the wire. However, in the particular system of Mn chains, the spin-orbit coupling may be too weak to facilitate a topological phase. This suggests to repeat the experiment with rare-earth elements, where this quantity is enhanced, and to search for chains of these elements with a similar arrangement.

In the second possible scenario, the oscillation between negative and positive spin-contrast along the Mn chain in fig. 4.7(f) may indicate an anti-ferromagnetic spin-texture. Such a coupling can also be mediated by an RKKY interaction through the electron gas. However, it forbids the formation of a Kitaev chain as described in section 4.1.1. In an anti-ferromagnetic chain, the individual YSR states are localized only at the atomic sites and not extended to electronic bands along the chain. Nevertheless, a proposal suggests a topological phase also in this scenario [125]. It requires a setup where a super-current is imposed to the superconductor parallel to the chain. This leads to a gradient in the phase of the superconducting order parameter along the chain, which changes the hopping amplitude between the individual sites, and imposes a time-reversal symmetry breaking. To push the system into a topological phase, an additional weak in-plane Zeeman field has to be applied, which lifts the spin degeneracy, and leads to an engineered spin-momentum locking. Then, MZMs may arise from the YSR states of the system at the edge of the chain. Interestingly, the MZMs are spin-polarized, which should be detectable with SPSTM. Moreover, the spins of the MZMs at opposite chain ends may be aligned anti-parallel for an odd number of adatoms in the chain.

Chapter 5

Summary

The research of this thesis deals with the coupling of magnetic impurities on a conventional s-wave superconductor by means of low-temperature scanning tunneling microscopy (STM) and scanning tunneling spectroscopy (STS). We started with clean surfaces of single crystal lead (Pb). This substrate is among the best characterized type I superconductors available. It provides a straight forward experimental preparation technique. We were able to resolve the double-peak nature of the superconducting gap in high-resolution measurements of the electronic structure around the Fermi level. This had been observed before, but to date two theoretical explanations regarding this feature were contradicting each other. It can be described by an anisotropic electron-phonon coupling term or by two distinct electronic bands at the Fermi level. The latter was supported by recent density functional theory calculations. Our first experiment showed clear fingerprints for the two-band nature of superconductivity. Furthermore, we could map the energetically well-separated Fermi-surfaces in real space by scattering at subsurface impurities. The different shapes of the Fermi surfaces lead to focusing along specific directions, and allowed to assign them to the two superconducting gaps.

Our journey continued to single non-magnetic atoms adsorbed on the substrate. It turned out that they locally influence the band-structure of the substrate, which favors tunneling into one of the bands. Together with the focusing properties of the curved Fermi surface, this specific behavior might be used in future tunneling devices for momentum-selective filtering. Moreover, it is important for the interpretation of experiments with all kinds of local adsorbates, such as molecules or larger structures.

We proceeded to single magnetic adatoms. These induce local bound states in superconductors at energies below the superconducting gap by breaking time-reversal symmetry with their local magnetic moment. In STS-spectra we observed a manifold of the subgap resonances. Our first investigation targeted different transport regimes through these states. If the local bound state is occupied by a single quasiparticle, it needs to relax, before a second quasiparticle can pass through the junction. In experiment, this yields a change of the spectral intensity of the subgap resonances at positive and negative energies with respect to the tunneling strength. By combining experiment with theory we could show that we probe the subgap states with both, single-electron and Andreev tunneling. In the weak-tunneling regime, the current is dominated by single-electron tunneling and it is linear in the normal-state conductance. The $\mathrm{d}I/\mathrm{d}V$-signal is proportional to the bound state wave function, according to what is usually assumed in STM-experiments. In the strong tunneling regime, the dependence on the normal-state conductance becomes sub-linear, and one can directly access the quasiparticle relaxation rates.

The second experiment on single magnetic adatoms focused on the number of subgap resonances, and their origin. Earlier experiments and theory assumed that multiple subgap states result from scattering channels with higher order angular momentum. Combining our experimental results with theory we could show that, instead, the dominant scattering channel is $l = 2$. To prove this, we investigated how the number of states of a single transition metal adatom evolves on different high symmetry surfaces of the substrate. It turned out that the adsorption site imposes a distinct crystal field splitting on the d-orbitals. The subgap resonances that appear because of scattering at these orbitals, inherit the symmetry. With spatially resolved conductance maps, we could identify the corresponding d-orbitals for each subgap resonance. It worked best on the Pb(001) surface, where the influence of the substrate on the symmetry of the state is diminished. On the Pb(111) surface, the strong influence of the anisotropic Fermi surface prevents an ambiguous assignment, but long range oscillatory patterns were observed, according to the theory of these subgap bound states. The oscillation period matched with the Fermi wavelength of one of the two Fermi surfaces of Pb. It proved a dominant scattering from the more localized bands.

The slow decay, and the directional nature of the subgap states make them promising candidates to design coupled adatom nano-structures. Hence, in our third experiment, we had a closer look at dimers of transition metal atoms. We observed a coupling of the adatoms, which manifested in a splitting of the subgap states. We investigated this coupling in dependence of distance and angle with respect to the substrate lattice underneath. In particular we could show that the bound states form bonding and antibonding states, if the bound state wave functions overlap. On the high symmetry Pb(001) surface, spatial conductance maps revealed nodal planes between two adatoms for the higher lying anti-bonding states, and a larger intensity between the adatoms for the lower lying bonding states. This is in full analogy to the standard textbook examples for the formation of a molecular orbital.

The last section of this thesis comprises investigations on one-dimensional transition metal chains, which are prime candidates for elemental building blocks in fault-tolerant quantum computers. The system can enter a topological state, in which it hosts a so-called Majorana zero mode (MZM) at the chain ends. As long as the states are separated by a superconducting gap, they are protected against any kind of local perturbation.

Recent experimental success in realizing a simple system of iron (Fe) chains on Pb(110) [101] motivated us to independently reproduce this experiment, and solve remaining open questions. Our investigations used superconducting tips, where MZMs are expected to appear as a pair of resonances at $\pm\Delta_{\mathrm{tip}}$, the superconducting gap of the tip, with symmetric spectral intensities. However, in all our chains we observed an asymmetric intensity. We associated this with a nearby low-energy subgap resonance at 80 µeV, which we interpreted as the coherence peak of the induced topological gap. An unambiguous proof of MZMs at the chain ends still requires further experiments at much lower temperatures. Moreover, our experiment investigated the subgap structure along the chain, which showed oscillatory variations in energy and in spectral intensity. With the help of theory, we could show that the variation of the first is induced by confinement effects, and of the second by a variation of the local potential in the vicinity of the chain.

Motivated by the prediction from theory that transition metal chains are a generic system hosting MZMs nearly independent of the element [102], we deposited cobalt (Co) and Mn on Pb(110) to check the formation of chains and their spectral properties. Chains of Co turned out to be structurally similar to Fe chains regarding their topographical appearance, and they also show ferromagnetic order. Furthermore, we found strong evidence that the subgap structure is spin-polarized. However, although all prerequisites for the formation of MZMs were fulfilled, we observed only delocalized resonances at, or close to, zero energy along the chains. We take this as an indication that no MZMs form in this system. In collaboration with theory model calculations were performed which explained the absence of a topologically non-trivial phase by an even number of Fermi level crossings of the *d*-bands. This originated from the larger electron occupation compared to Fe chains, which shifts the Fermi level in energy. The extended resonances close to zero energy along the entire chain might be ascribed to the induced topological gap, which is probably smaller than the experimental energy resolution and thus leads to the prominent features. Future experiments have to repeat the measurements, to see if this explanation holds as well for longer chains.

As an outlook, preliminary results of measurements on Mn chains are reported. Their topologic and spectroscopic structure is inherently different from what we observed before. They appear embedded in or below the first surface layer. We found evidence for either an anti-ferromagnetic or a helical spin-texture. Both are not distinguishable in our setup. They require further measurements.

5.1 The journey continues …

One dimensional transition metal chains on conventional superconductors are an intriguing platform for qubits that may be suited for topological quantum computation (TQC). The chase for topologically non-trivial particles with non-abelian counting statistics is well underway. However, many challenges are open — mainly from the experimental side. To get a rough idea of the future pathway in this field of research, we finally sketch here a possible setup which brings the 1D chains to an application.

The operations in a topological quantum computer are represented by braiding operations. In section 4.1.1 we discussed that the ground state of a system with MZMs is degenerate. An exchange of two MZMs acts in this degenerate space, and leads to the transition between the different ground states. This is possible by the so-called non-abelian statistics of anyons. An information encoded by the degenerate states is protected against local perturbations, but needs to be accessed to perform calculations. As Ref. [126] points out, linear 1D chains are not suited for braiding operations in general. As soon as two MZMs meet, they hybridize, and their statistics are mixed up. However, in a one-dimensional device they unavoidably meet. Hence, one requires at least a three terminal device, in which each site is separated from the others. The simplest setup are two wires perpendicular to each other, the 'T'-junction-geometry. To braid the particles one pushes the MZMs along the wires to the chain ends. We showed for Co chains that a variation in the Fermi level may inherently change the number of Fermi points of the system. An easy way to push the MZMs along the wires is to apply a local gate voltage, which intentionally puts the system locally into a non-topological regime.

However, it is still a long journey to develop such devices, either by a bottom-up approach of manipulating single adatoms, or by a top-down approach coming from nano-lithography.

Appendix A

Experimental details

The experimental techniques employed for our measurements comprise a combination of scanning tunneling microscopy (STM) and scanning tunneling spectroscopy (STS). The first is capable to resolve surface structures with atomic scale precision, and to address measurements to single adsorbates. It is often used to manipulate adsorbates on the sample by controlled contact or voltage pulses. As a spectroscopy tool it reveals the local electric structure around the Fermi level, the local spin-polarization, and the local transport properties of the sample. In this appendix we first give an introduction to the operating principle of STM, and a more elaborate picture of its capabilities for STS. Finally, we provide details of our setup, and of the preparation of our experiment.

A.1 Scanning tunneling microscopy (STM)

The idea of STM is based on the fundamental principle of tunneling in quantum mechanics. A quantum particle may cross a high narrow potential barrier, which would be impossible for its classical counterpart. Moreover, this process is extremely dependent on distance. Hence, one may use it to bring a nanoscopic probe close to the surface of a sample in order to analyze its topography. A first proof-of-principle of this concept was shown in 1972 [127], when scientists observed a distance dependent tunneling current at structures of a microscopic grating. They achieved lateral resolutions up to 400 nm. The first prototype, which is capable of resolving atomic resolution, was presented in 1981 by G. Binnig *et al.* at IBM Zürich [128, 129].

The salient invention of STM opened a manifold of new techniques in the early days of nano-physics. Five years after the first prototype was built, G. Binnig and H. Rohrer were awarded the Nobel price. Comparing it to older, but established experimental techniques, STM has the major advantage of working in real space. Furthermore, it neither requires a periodic ordering, nor it averages over large areas. Instead, it allows to observe local physical phenomena on the nanoscale. Today, STM has become a key technology in nano-science as a tool for electron spectroscopy. This comprises, e.g., inelastic tunneling spectroscopy [130–132], STM induced light emission [133–135], or spin-polarized scanning tunneling microscopy (SPSTM) [108, 136].

A.1.1 Theory of scanning tunneling microscopy

A standard textbook exercise is the calculation of the quantum tunneling probability of a plane electron wave through a barrier. Although this picture is extremely simplified, it provides one of the important relations relevant for STM:

$$I(z) \propto e^{-2\,z\,\sqrt{2m\Phi}/\hbar}\,. \tag{A.1}$$

The tunneling current I depends exponentially on the barrier width z. The work function of the sample is given by Φ. This exponential relation of the current on the distance allows the high spatial resolution achieved by STM.

A long time before the invention of STM, tunneling through planar junction was already used for transport measurements in experiments. Hence, theories describing the tunneling characteristics in such a junction were already elaborate [137]. However, the change of the junction geometry to the sharp apex of a metallic tip at one side, and the flat sample surface on the other side, required a new viewpoint.

A first theory was given by Tersoff and Hamann [138]. They started using the approach from Bardeen [137], who treated the tunneling process by first order perturbation theory. For an electron that scatters from an eigenstate of one electrode Ψ_t to an eigenstate of the second electrode Ψ_s, it reads according to Fermi's golden rule:

$$I = \frac{2\pi e}{\hbar} \sum_{t,s} f\left(E_t\right)\left[1 - f\left(E_s + eV\right)\right] \left|M_{ts}\right|^2 \delta\left(E_t - E_s\right) . \tag{A.2}$$

Here, $E_{t,s}$ are the energies of the two states, and V is the applied bias voltage between them. The Fermi-Dirac distribution $f(E)$ gives the occupation of each eigenstate. The transition matrix element which depends on the wave function overlap is given by M_{ts}. Note, that both eigenstates are non-orthogonal, and they belong to different Hamiltonians. Bardeen showed that M_{ts} can be obtained when integrating over an arbitrary surface $\mathbf{S}$ within the vacuum barrier:

$$M_{ts} = \frac{\hbar^2}{2m} \int d\mathbf{S} \cdot \left(\Psi_t^* \nabla \Psi_s - \Psi_s \nabla \Psi_t^*\right) . \tag{A.3}$$

Hence, the tunneling current depends essentially on the wave functions of both electrodes. Since the surface is a periodic system, Tersoff and Hamann assumed that Ψ_s is a Bloch wave decaying exponentially into the vacuum [eq. (A.4)]. The wave function of the tip, Ψ_t, has to describe the apex of a tip. Hence, they used a spherical potential well, with a local curvature R [eq. (A.5)].

$$\Psi_s \propto \sum_G e^{-\sqrt{k^2+\left|\mathbf{k}_G\right|^2}\, z}\, e^{i\mathbf{k}_G \mathbf{x}} , \tag{A.4}$$

$$\Psi_t \propto \frac{kR}{k\left|\mathbf{r} - \mathbf{r}_0\right|} e^{-k\left|\mathbf{r}-\mathbf{r}_0\right|} . \tag{A.5}$$

The reciprocal lattice vector of the surface is denoted by G. The surface Bloch wave vector is given by $\mathbf{k}_G$. Furthermore, z is the distance perpendicular to the surface, and $\mathbf{x}$ is the spatial vector parallel to the surface. The concept of these wave functions is sketched in fig. A.1. Although the assumptions for the tip geometry are quite simple, they turn out to deliver rather accurate results. Often, the tip apex is a single metal atom. There, the spatially largest orbital is s-like, and thus spherical, which matches well the model that was chosen.

A further extension of eq. (A.2) to eq. (A.5) finally leads to an expression for the tunnel matrix element which depends only on the DOS of both electrodes, $\rho_{\mathrm{t,s}}$, respectively. In

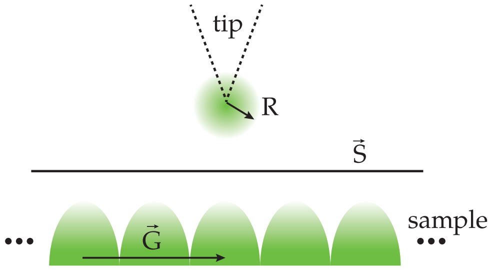

FIGURE A.1: Layout of the junction geometry assumed by Tersoff and Hamann [138]. The wave function of the tip is an exponentially decaying spherical potential well of radius R. The sample is modeled by a Bloch wave with reciprocal lattice vector **G**, which decays exponentially into the vacuum towards the tip. The integral of the tunnel matrix element in eq. (A.3) can be calculated along any surface **S** between tip and sample.

the Wentzel-Kramers-Brillouin (WKB) approximation it is given by [139]:

$$\begin{aligned} I(V,z) = \frac{4\pi e}{\hbar} \int_{-\infty}^{\infty} & \rho_{\mathrm{s}}\left(E_{\mathrm{F}} - V + \varepsilon\right) \rho_{\mathrm{t}}\left(E_{\mathrm{F}} + \varepsilon\right) \\ & \cdot \left[f\left(E_{\mathrm{F}} - V + \varepsilon\right) - f\left(E_{\mathrm{F}} + \varepsilon\right)\right] \left|M(\varepsilon, V, z)\right|^2 \mathrm{d}\varepsilon \,. \end{aligned} \tag{A.6}$$

The Fermi level E_{F} of both electrodes defines the occupation of the DOS by Fermi-Dirac statistics $f(E)$. The tunnel matrix element $M(\varepsilon, V, z)$ is given by:

$$|M(\varepsilon, V, z)|^2 = \exp\left(-\frac{2z\sqrt{2m}}{\hbar}\sqrt{\frac{\Phi_{\mathrm{s}} + \Phi_{\mathrm{t}}}{2} + \frac{eV}{2} - \varepsilon}\right). \tag{A.7}$$

It depends on the energy ε, on the sample bias V, on the tip-sample distance z, and on the work function of tip and sample $\Phi_{\mathrm{t,s}}$, respectively. Furthermore, eq. (A.6) considers both, tunneling from tip to sample, and vice versa. Hence, if the tip DOS is known, the sample DOS can be deduced from the measured tunneling current.

A common method to control the DOS of the tip is, e.g., to indent the tip into a clean part of the sample surface, which covers the tip with a known species of atoms. The ability to control the tip DOS has been further improved over the years. Today, sometimes adsorbates on the tip are intentionally used to functionalize it, and to emphasize certain physical quantities in the tunneling current by the modified tip wave function [140]. For example, one can display the gradient of the sample DOS by attaching a carbon monoxide molecule to the tip, which has a p-orbital shape [141].

A.1.2 Imaging with Scanning Tunneling Microscopy

The sensitivity of the tip-sample distance is used to image the surface topography by STM. The topography is defined by the iso-surface with a constant DOS. The tip is approached by a feedback loop to the sample until a tunneling current in the order of 0.01 nA to 10 nA is established. Commonly, images are recorded with a closed feedback loop, which keeps the current constant while scanning the sample surface. Measuring with an open feedback loop allows a faster scan speed, but increases the risk of a crash of the tip with the surface.

A.2 Scanning tunneling spectroscopy (STS)

The scanning tunneling microscope has a major advantage over other surface sensitive spectroscopic methods, namely the ability to address individual adsorbates, and probe their electronic structure. Several different methods have been established to measure this quantity. The most common one is the $I(V)$ spectroscopy. There, one measures the local conductance to deduce the local DOS.

A.2.1 $I(V)$ spectroscopy

The $I(V)$ spectroscopy is carried out by applying a small varying bias voltage V to the sample, and by recording in parallel the current across the junction, while the tip-sample distance is fixed. Differentiating the current [eq. (A.6)] with respect to the bias voltage gives the differential conductance $\mathrm{d}I/\mathrm{d}V(V)$. At zero temperature, we obtain:

$$\begin{aligned}\mathrm{d}I/\mathrm{d}V(V) = {} & \frac{4\pi e}{\hbar}\ \rho_\mathrm{s}(E_\mathrm{F}+V)\ \rho_\mathrm{t}(E_\mathrm{F})\ \ |M(V,V,z)|^2 \\ & + \frac{4\pi e}{\hbar}\int_0^V \rho_\mathrm{s}(E_\mathrm{F}+\varepsilon)\ \rho_\mathrm{t}(E_\mathrm{F}-V+\varepsilon)\frac{\mathrm{d}\,|M(\varepsilon,V,z)|^2}{\mathrm{d}V}\ \mathrm{d}\varepsilon \\ & + \frac{4\pi e}{\hbar}\int_0^V \rho_\mathrm{s}(E_\mathrm{F}+\varepsilon)\ \frac{\mathrm{d}\rho_\mathrm{t}(E_\mathrm{F}-V+\varepsilon)}{\mathrm{d}V}\ \mathrm{d}\varepsilon\,. \end{aligned} \tag{A.8}$$

The $\mathrm{d}I/\mathrm{d}V$ signal is the sum of three components. The first is a convolution of the tip and sample DOS. In this term, the fixed tip-sample distance during the experiment causes a constant tunnel matrix element M, as long as the bias voltage is low compared to the work functions ($V \ll \Phi_{\mathrm{s,t}}$). The second component becomes zero for the same reason. The third component becomes zero, if the sample DOS is only weakly voltage dependent. Hence, the $\mathrm{d}I/\mathrm{d}V(V)$ signal is — in first approximation — proportional to the DOS of tip (ρ_t) and sample (ρ_s):

$$\mathrm{d}I/\mathrm{d}V(V) \propto \rho_\mathrm{s}(E_\mathrm{F}+V)\ \ \rho_\mathrm{t}(E_\mathrm{F})\,. \tag{A.9}$$

$\mathrm{d}I/\mathrm{d}V(V)$ measurements with a lock-in amplifier

The technically easiest method to obtain the $\mathrm{d}I/\mathrm{d}V$ signal is, of course, to calculate the numerical derivative of the measured current across the junction. However, as every numeric method, it is extremely prone to noise. The sources of noise in our experiment are mechanical vibrations in the tunnel junction, external radio frequency radiation, and thermal noise within the amplifier electronics. Typically, the noise amounts to $1-2$ % of the wanted signal. Hence, one prefers to measure directly the $\mathrm{d}I/\mathrm{d}V(V)$ signal without further numerical operations. This is possible by using a *lock-in* amplifier, which is basically a frequency generator with a signal multiplier and an integration circuit.

The frequency generator adds a small oscillating modulation voltage $V_\mathrm{mod}\sin(\omega_\mathrm{ref}t)$ on top of the bias voltage V_b. Hence, the measured current oscillates at the same reference frequency (ω_ref). The period is chosen faster than the sensitivity of the microscope's feedback loop, so that the tip-sample distance is unaffected ($\omega_\mathrm{ref} \approx 900$ Hz). The measured junction current is then multiplied by the reference signal, and integrated over as many oscillation periods as possible. This filters all frequencies, except for the wanted signal oscillating with ω_{ref}.

$$I(V_{\mathrm{b}}) = \frac{1}{\pi} \int_{-\pi}^{+\pi} I\left[V_{\mathrm{b}} + V_{\mathrm{mod}} \sin\left(\omega_{\mathrm{ref}} t\right)\right] \cdot \sin\left(\omega_{\mathrm{ref}} t\right) \ \mathrm{d}(\omega_{\mathrm{ref}} t) \, . \tag{A.10}$$

Furthermore, the lock-in amplifier is able to directly output the differential conductance. Calculating the Taylor expansion of the static current at voltage V_{b}, while modulating it with a small amplitude V_{mod}, gives up to the third order in the sample bias V:

$$V_{\mathrm{bias}} \equiv V_{\mathrm{b}} + V_{\mathrm{mod}} \sin\left(\omega_{\mathrm{ref}} t\right) \tag{A.11}$$

$$\begin{aligned} I(V)|_{V_{\mathrm{bias}}} \approx\ & I(V_{\mathrm{bias}}) \\ & + \frac{\mathrm{d}I(V_{\mathrm{bias}})}{\mathrm{d}V} \left[V - V_{\mathrm{b}} - V_{\mathrm{mod}} \sin\left(\omega_{\mathrm{ref}} t\right)\right] \\ & + \frac{\mathrm{d}^2 I(V_{\mathrm{bias}})}{\mathrm{d}V^2} \frac{\left[V - V_{\mathrm{b}} - V_{\mathrm{mod}} \sin\left(\omega_{\mathrm{ref}} t\right)\right]^2}{2!} + \ldots \, . \end{aligned} \tag{A.12}$$

The first term is constant. It is averaged to zero when performing the integral in eq. (A.10). The second and third terms are directly proportional to the first and second derivative of the current. Hence, to directly obtain the $\mathrm{d}I/\mathrm{d}V$ signal, one simply sets the amplifier to the first harmonic of ω_{ref}. Moreover, the amplifier can also be set to higher harmonics, which gives higher derivatives of the current, but implies a proportionally reduced amplitude of the signal.

Limits of spectral resolution

In eq. (A.9) we pointed out that $\mathrm{d}I/\mathrm{d}V(V)$ spectra are commonly interpreted as DOS of the sample. However, the use of a lock-in amplifier has the flaw that its voltage modulation additionally broadens the data. The effective broadening can be calculated by an ansatz of Ref. [142]. It starts with eq. (A.10), where E is substituted by $V_{\mathrm{mod}} \sin\left(\omega_{\mathrm{ref}} t\right)$, and a partial integration is performed:

$$\begin{aligned} I(V_{\mathrm{b}}) &= \frac{1}{\pi} \int_{-V_{\mathrm{mod}}}^{+V_{\mathrm{mod}}} I\left(V_{\mathrm{b}} + E\right) \cdot \frac{E}{\sqrt{V_{\mathrm{mod}}^2 - E^2}} \frac{1}{V_{\mathrm{mod}}} \ \mathrm{d}E \\ I(V_{\mathrm{b}}) &= \frac{1}{\pi} \int_{-V_{\mathrm{mod}}}^{+V_{\mathrm{mod}}} \frac{\mathrm{d}I(V_{\mathrm{b}} + E)}{\mathrm{d}E} \cdot \frac{\sqrt{V_{\mathrm{mod}}^2 - E^2}}{V_{\mathrm{mod}}} \ \mathrm{d}E \, . \end{aligned} \tag{A.13}$$

Hence, the lock-in amplifier output is broadened by convolution with the function $\sqrt{V_{\mathrm{mod}}^2 - E^2}/V_{\mathrm{mod}}$. It is a semi sphere between $\pm V_{\mathrm{mod}}$ with a FWHM of $1.73\ V_{\mathrm{mod}}$. To observe narrow spectral features without broadening them artificially, the modulation amplitude has to be appropriately selected. It should be as large as possible, but stay well below other experimental broadening effects.

The largest experimental broadening, however, enters through thermal occupation of the electrodes DOS with Fermi-Dirac statistics. The derivative of the Fermi function is a Gaussian-like resonance, given by:

$$\frac{\mathrm{d}f(E)}{\mathrm{d}E} = \frac{1}{k_\mathrm{B}T} \frac{e^{-\frac{E}{k_\mathrm{B}T}}}{\left(1 + e^{-\frac{E}{k_\mathrm{B}T}}\right)^2} \,. \tag{A.14}$$

The width of this resonance is $\approx 3.5\,k_\mathrm{B}T$, which smears out all spectral features at non-zero temperature. However, we overcome the thermal resolution limit in our experiments, by using a superconducting tip. The tiny superconducting gap cuts of the tails of the Fermi-Dirac function, as long as the temperatures are well below the width of the superconducting gap. More details are discussed in section 2.3.1.

Spatial maps of the $\mathrm{d}I/\mathrm{d}V$ signal

The high lateral resolution of STM allows to map the differential conductance over larger areas. For time reasons, this is done mainly at discrete energies, which are selected prior to the measurement. Three common techniques have been established.

The first operates with a constant tunneling current. The feedback loop is closed. It gives a strong signal on topographically non-flat areas, since the current is always at the same level. However, it often gives rise to measurement artifacts. In addition to changes in the DOS of the sample, the tunnel matrix element changes by the variation of the tip-sample distance. Moreover, the exact influence of this change on the signal is often unknown.

The second mode operates at a constant tip-sample distance, which avoids the prior source of artifacts. However, this comes at the cost of a lower signal in regions of lower topographic height. This makes it difficult to map the influence of adsorbates on the surface DOS. At the adsorbate the signal is high, but it rapidly drops on the surface.

Both techniques are unsuited for our experiments. We are investigating the interaction of adsorbates with the superconducting substrate. This occurs mainly at energies below the superconducting gap. There, the surface without the substrate is not conducting at all. The solution is to use a hybrid of the two techniques mentioned above for our experiment. We perform a constant current map, which ensures a high signal on surface and adsorbate, but we control the feedback at a bias voltage with lies in a featureless region of both, tip, adsorbate and sample DOS. Hence, the actual signal of the adsorbate is not influenced by a change of the tunnel matrix element which also depends on the measured quantity.

A.3 Experimental setup: the Joule-Thomson Scanning Tunneling Microscope (JTSTM)

Our experimental setup is a commercially available Joule-Thomson Scanning Tunneling Microscope (JTSTM), manufactured by SPECS[1]. It operates at a base temperature of ≈ 1.1 K under ultra-high vacuum (UHV) conditions, and allows to apply a magnetic field up to $\pm$ 3 T perpendicular to the sample surface. Furthermore, it has elaborate radio-frequency filters for high energy resolutions in the order of 50 µeV when measuring with superconducting tips.

In our experiment we are interested in the intrinsic properties of the surface and its interaction with single well-defined adsorbates. Hence, to circumvent any contamination with other atoms and molecules, our setup operates at UHV conditions at pressures below 1×10^{-10} mbar. Thermal rearrangements of the adsorbates and thermally induced fluctuation of the tip-sample distance during the measurement are avoided by working at temperatures below ≈ 5 K. This is achieved by a liquid He cryostat, which cools the whole microscope to ≈ 4.5 K. Moreover, the temperature determines crucially the energy resolution of the setup. For our investigations in the µeV energy range we further cool the setup to its base temperature of ≈ 1.1 K by a Joule-Thomson unit.

A.3.1 Joule-Thomson Cooling

Joule-Thomson cooling is a common technique used in many applications, such as in refrigerators and in air-condition units. In our setup, the JTSTM, we use it to cool the sample below the temperature of liquid helium (≈ 4 K). It is based on the discovery by J.P. Joule and W. Thomson in 1852 that nearly all gases cool under adiabatic expansion. The process is parametrized by the thermodynamic derived Joule-Thomson coefficient which describes the rate of temperature change ∂T per pressure drop ∂P under the constant enthalpy H, so without heat exchange with the environment [143]:

$$\mu_{\mathrm{JT}} = \left(\frac{\partial T}{\partial p}\right)_H = \left[T\left(\frac{\partial V}{\partial T}\right)_P - V\right]\frac{1}{C_{\mathrm{P}}} = (\alpha T - 1)\frac{V}{C_{\mathrm{P}}}\,. \tag{A.15}$$

The volume of the system is given by V, the specific heat capacity of the gas by C_{P}, and the thermal expansion coefficient of the gas by α. A gas cools when the coefficient is positive, which means $\alpha > 1/T$. Interestingly, the ideal gas equation $PV = Nk_{\mathrm{B}}T$ yields $\alpha = 1/T$, which implies that cooling is only possible with gases that deviate from this model. It is a direct consequence of the interaction of the gas particles. In a non-ideal gas an expansion of the volume has two competing effects: On one hand, the attraction between the gas particles increases with the average distance between them. On the other hand, the larger joint volume of the particles decreases their collision probability and, thus, their potential energy. Depending on which of the processes dominates, the Joule-Thomson coefficient is positive or negative. A change in the potential energy has to be compensated by a change of the kinetic energy, as the energy in the system is conserved.

At room temperature almost all gases have the Joule-Thomson coefficient $\mu_{\mathrm{JT}} < 0$, which means they are cooled by expansion. In our setup, we use helium as cryogenic gas, and pre-cool it to ≈ 4 K, which is below its inversion temperature of about $32 - 50$ K at ambient pressure. The Joule-Thomson unit itself is thermally coupled to the microscope

---

[1] SPECS Surface Nano Analysis GmbH

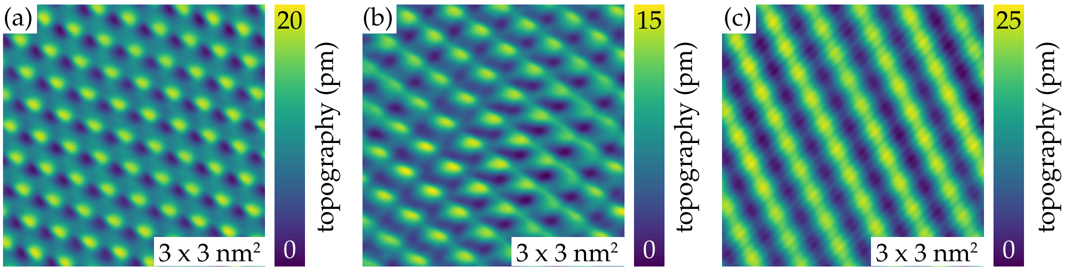

FIGURE A.2: High-resolution surface topographies of clean Pb(111), Pb(100), and Pb(110), respectively (from a–c). A 2D-reverse FFT filter was applied to each image, which highlights the crystalline periodicity. Setpoints: $50/-50/500$ mV, $50/50/70$ pA.

stage and consists of a thin gas capillary that tapers at the end. The gas is applied to the capillary at a pressure of about 2 bar and is expanded to a small reservoir which is pumped to a rough vacuum. This leads to a cooling power of the order of several milliwatt, and allows a continuous operation mode.

A.3.2 Magnetic field

The JTSTM has a pair of superconducting Helmholtz coils which encapsulate the whole microscope. They induce a homogeneous magnetic field at the center between the two coils, where sample and tip are positioned. The field strength follows the Biot-Savart law:

$$B_{\text{center}} = \left(\frac{4}{5}\right)^{3/2} \frac{\mu_0 n I}{R} \,. \tag{A.16}$$

Here, R is the radius of the coils, n is the number of windings, I is the current running through the coils, and μ_0 is the vacuum permeability. The maximally achieved magnetic fields in our setup are ± 3 T perpendicular to the sample surface, at a current of roughly 20 A through the coils. Hence, copper wires are no suitable coil material, as the induced ohmic heat would prevent measurements at ≈ 1.1 K. Therefore, they are made out of a superconductor cooled by the liquid helium cryostat.

A.4 Sample preparation

The superconducting substrates in our experiments are high purity single crystals of Pb. The bulk lattice of Pb is a face-centered cubic (fcc). For our experiments, the crystals were cut and polished[2] along the three main surface orientations [(100), (110), and (111)]. After transfer to UHV, they were cleaned by several cycles of neon ion sputtering at 900 eV at a pressure of 1.5×10^{-4} mbar (background pressure $< 1.5 \times 10^{-9}$ mbar). Heating to 430 K for 60 min anneals the damage that was introduced by the sputter cycles. This results in clean, flat, and superconducting terraces. Atomic resolution on each surface is shown in fig. A.2.

---

[2] Crystals are commercially available by MaTecK GmbH.

A.4.1 Evaporation of transition metal atoms

Transition metal atoms were evaporated by electron beam heating onto the sample at various temperatures. At high temperatures, thermal diffusion of the adsorbates is possible, at low temperatures the adsorbates stick to where they initially adsorb.

Single adatoms were obtained by evaporation at cold temperatures, with the sample installed in the microscope. Hence, the temperature stays below 15 K, and thermal diffusion is avoided. The surface gets covered randomly with adatoms in the order of $\simeq 100$ atoms per $100 \times 100\ \mathrm{nm}^2$, where single adatoms and dimers are found.

The growth of 1D atomic chains requires elevated temperatures and a larger coverage. Several regimes between 170 K and 390 K were tested in our experiments. We obtained an element specific optimal temperature for the formation of chains. Fe-chains self-assemble at room temperature, Co-chains at $\simeq 260$ K, and Mn-chains at 170 K. The appearance of Mn-chains differs significantly from the others. Details of their structure are still an open question.

List of Acronyms

1D	one-dimensional
2D	two-dimensional
3D	three-dimensional
Al	aluminum
ARPES	angle-resolved photo-emission spectroscopy
BCS	Bardeen-Cooper-Schrieffer
Co	cobalt
Cr	chrome
Cu	copper
DFT	density functional theory
DOS	density of states
fcc	face-centered cubic
Fe	iron
FFT	Fast-Fourier transformation
FWHM	full width at half maximum
Gd	gadolinium
He	helium
Hg	mercury
JTSTM	Joule-Thomson Scanning Tunneling Microscope
LT-STM	low-temperature scanning tunneling microscopy
Mn	manganese
MZM	Majorana zero mode
Nb	niobium
Ne	neon
Ni	nickel
NMR	nuclear magnetic resonance
Pb	lead
QPR	quasiparticle resonance
RKKY	Ruderman-Kittel-Kasuya-Yosida
Sc	scandium
SP	spin polarized
SPSTM	spin-polarized scanning tunneling microscopy
STM	scanning tunneling microscopy
STS	scanning tunneling spectroscopy
SQUID	superconducting quantum interference device
Ta	tantalum
Tc	technetium
TQC	topological quantum computation
UHV	ultra-high vacuum
V	vanadium
W	tungsten
WKB	Wentzel-Kramers-Brillouin
YSR	Yu-Shiba-Rusinov

Bibliography

[1] R. P. Feynman. “Simulating physics with computers”. In: *International Journal of Theoretical Physics* 21.6 (1982), pp. 467–488. ISSN: 1572-9575.

[2] P. Benioff. “Quantum mechanical hamiltonian models of turing machines”. In: *Journal of Statistical Physics* 29.3 (1982), pp. 515–546. ISSN: 1572-9613.

[3] P. W. Shor. “Algorithms for quantum computation: Discrete logarithms and factoring”. In: *Proc. 35^{nd} Annual Symposium on Foundations of Computer Science*. Ed. by Shafi Goldwasser. IEEE Computer Society Press, 1994.

[4] R. L. Rivest, A. Shamir, and L. Adleman. “A Method for Obtaining Digital Signatures and Public-key Cryptosystems”. In: *Commun. ACM* 21.2 (Feb. 1978), pp. 120–126. ISSN: 0001-0782.

[5] A.B. Finnila *et al.* “Quantum annealing: A new method for minimizing multidimensional functions”. In: *Chem. Phys. Lett.* 219.5 (1994), pp. 343–348. ISSN: 0009-2614.

[6] T. Kadowaki and H. Nishimori. “Quantum annealing in the transverse Ising model”. In: *Phys. Rev. E* 58 (5 Nov. 1998), pp. 5355–5363.

[7] E. S. Giuseppe and E. Tosatti. “Optimization using quantum mechanics: quantum annealing through adiabatic evolution”. In: *Journal of Physics A: Mathematical and General* 39.36 (2006), R393.

[8] A. Das and B. K. Chakrabarti. “*Colloquium* : Quantum annealing and analog quantum computation”. In: *Rev. Mod. Phys.* 80 (3 Sept. 2008), pp. 1061–1081.

[9] D. W. Marquardt. “An Algorithm for Least-Squares Estimation of Nonlinear Parameters”. In: *Journal of the Society for Industrial and Applied Mathematics* 11.2 (1963), pp. 431–441.

[10] J. A. Nelder and R. Mead. “A Simplex Method for Function Minimization”. In: *The Computer Journal* 7.4 (1965), pp. 308–313.

[11] C. Monroe *et al.* “Demonstration of a Fundamental Quantum Logic Gate”. In: *Phys. Rev. Lett.* 75 (25 Dec. 1995), pp. 4714–4717.

[12] J. I. Cirac and P. Zoller. “Quantum Computations with Cold Trapped Ions”. In: *Phys. Rev. Lett.* 74 (20 May 1995), pp. 4091–4094.

[13] D. G. Cory, A. F. Fahmy, and T. F. Havel. “Ensemble quantum computing by NMR spectroscopy”. In: *Proceedings of the National Academy of Sciences* 94.5 (1997), pp. 1634–1639.

[14] N. A. Gershenfeld and I. L. Chuang. “Bulk Spin-Resonance Quantum Computation”. In: *Science* 275.5298 (1997), pp. 350–356. ISSN: 0036-8075.

[15] S. Bandyopadhyay and Miller A. E. Das B. and. “Supercomputing with spin-polarized single electrons in a quantum coupled architecture”. In: *Nanotechnology* 5.2 (1994), p. 113.

[16] M. W. Johnson *et al.* “Quantum annealing with manufactured spins”. In: *Nature* 473.7346 (May 2011), pp. 194–198. ISSN: 0028-0836.

[17] V. L. Ginzburg and L. D. Landau. “On the theory of superconductivity”. In: *Zh. Eksp. Teor. Fiz.* 20 (1950), p. 1064.

[18] L. D. Landau. “On the theory of phase transitions”. In: *Zh. Eksp. Teor. Fiz.* 7 (1937), pp. 19–32.

[19] R. F. Gasparovic and W. L. McLean. “Superconducting Penetration Depth of Lead”. In: *Phys. Rev. B* 2 (7 Oct. 1970), pp. 2519–2526.

[20] K. Fossheim and A. Sudbo. *Superconductivity: physics and applications*. John Wiley and Sons Ltd., England, 2004. ISBN: 0-470-84452-3.

[21] A. A. Abrikosov. “The magnetic properties of superconducting alloys”. In: *J. Phys. Chem. Solids* 2.3 (1957), pp. 199–208. ISSN: 0022-3697.

[22] E. Maxwell. “Isotope Effect in the Superconductivity of Mercury”. In: *Phys. Rev.* 78 (4 May 1950), pp. 477–477.

[23] J. Bardeen, L. N. Cooper, and J. R. Schrieffer. “Microscopic Theory of Superconductivity”. In: *Phys. Rev.* 106 (1 Apr. 1957), pp. 162–164.

[24] J. Bardeen, L. N. Cooper, and J. R. Schrieffer. “Theory of Superconductivity”. In: *Phys. Rev.* 108 (5 Dec. 1957), pp. 1175–1204.

[25] N. N. Bogoljubov. “On a new method in the theory of superconductivity”. In: *Il Nuovo Cimento (1955-1965)* 7.6 (1958), pp. 794–805. ISSN: 1827-6121.

[26] L. N. Cooper. “Bound Electron Pairs in a Degenerate Fermi Gas”. In: *Phys. Rev.* 104 (4 Nov. 1956), pp. 1189–1190.

[27] M. Tinkham. *Introduction to Superconductivity: Second Edition*. Dover Publications, New York, 2004. ISBN: 978-0-486-43503-9.

[28] M. Ruby *et al.* “Experimental Demonstration of a Two-Band Superconducting State for Lead Using Scanning Tunneling Spectroscopy”. In: *Phys. Rev. Lett.* 114 (15 Apr. 2015), p. 157001.

[29] M. Ruby *et al.* “Tunneling Processes into Localized Subgap States in Superconductors”. In: *Phys. Rev. Lett.* 115 (8 July 2015), p. 087001.

[30] N. Hatter *et al.* “Magnetic anisotropy in Shiba bound states across a quantum phase transition”. In: *Nat. Comm.* 6 (2015), p. 8988.

[31] M. Ruby *et al.* “End States and Subgap Structure in Proximity-Coupled Chains of Magnetic Adatoms”. In: *Phys. Rev. Lett.* 115 (19 Nov. 2015), p. 197204.

[32] M. Ruby *et al.* “Orbital Picture of Yu-Shiba-Rusinov Multiplets”. In: *Phys. Rev. Lett.* 117 (18 Oct. 2016), p. 186801.

[33] M. Ruby *et al.* “Exploring a proximity-coupled Co chain on Pb(110) as a possible Majorana platform”. In: *in preparation* (2017).

[34] M. Ruby. “SpectraFox: A free open-source data management and analysis tool for scanning probe microscopy and spectroscopy”. In: *SoftwareX* 5 (2016), pp. 31–36. ISSN: 2352-7110.

[35] F. Schulz *et al.* “Epitaxial hexagonal boron nitride on Ir(111): A work function template”. In: *Phys. Rev. B* 89 (23 June 2014), p. 235429.

[36] R. C. Dynes, V. Narayanamurti, and J. P. Garno. “Direct Measurement of Quasiparticle-Lifetime Broadening in a Strong-Coupled Superconductor”. In: *Phys. Rev. Lett.* 41 (21 Nov. 1978), pp. 1509–1512.

[37] F. Marsiglio and J. P. Carbotte. “Electron-Phonon Superconductivity”. In: *Superconductivity: Conventional and Unconventional Superconductors*. Ed. by K. H. Bennemann and J. B. Ketterson. Berlin, Heidelberg: Springer Berlin Heidelberg, 2008, pp. 73–162. ISBN: 978-3-540-73253-2.

[38] M. Schackert *et al.* “Local Measurement of the Eliashberg Function of Pb Islands: Enhancement of Electron-Phonon Coupling by Quantum Well States”. In: *Phys. Rev. Lett.* 114 (4 Jan. 2015), p. 047002.

[39] P. Townsend and J. Sutton. “Investigation by Electron Tunneling of the Superconducting Energy Gaps in Nb, Ta, Sn, and Pb”. In: *Phys. Rev.* 128 (2 Oct. 1962), pp. 591–595.

[40] G. I. Rochlin. “Determination of the Anisotropy of the Energy Gap in Superconducting Pb by Superconductive Tunneling”. In: *Phys. Rev.* 153 (2 Jan. 1967), pp. 513–532.

[41] B. L. Blackford and R. H. March. “Tunneling Investigation of Energy-Gap Anisotropy in Superconducting Bulk Pb”. In: *Phys. Rev.* 186 (2 Oct. 1969), pp. 397–399.

[42] G. I. Lykken *et al.* “Measurement of the Superconducting Energy Gap and Fermi Velocity in Single-Crystal Lead Films by Electron Tunneling”. In: *Phys. Rev. B* 4 (5 Sept. 1971), pp. 1523–1530.

[43] T.-S. Choy *et al.* In: *Bull. Am. Phys. Soc.* 45 (2000), p. L36.

[44] J. R. Anderson and A. V. Gold. “Fermi Surface, Pseudopotential Coefficients, and Spin-Orbit Coupling in Lead”. In: *Phys. Rev.* 139 (5A Aug. 1965), A1459–A1481.

[45] B. N. Brockhouse *et al.* “Crystal Dynamics of Lead. I. Dispersion Curves at 100 K”. In: *Phys. Rev.* 128 (3 Nov. 1962), pp. 1099–1111.

[46] A. J. Bennett. “Theory of the Anisotropic Energy Gap in Superconducting Lead”. In: *Phys. Rev.* 140 (6A Dec. 1965), A1902–A1920.

[47] J. Nagamatsu *et al.* “Superconductivity at 39 K in magnesium diboride”. In: *Nature* 410.6824 (Mar. 2001), pp. 63–64. ISSN: 0028-0836.

[48] F. Giubileo *et al.* “Two-Gap State Density in MgB_2: A True Bulk Property Or A Proximity Effect?” In: *Phys. Rev. Lett.* 87 (17 Oct. 2001), p. 177008.

[49] F. Giubileo *et al.* “Strong coupling and double-gap density of states in superconducting MgB_2”. In: *Europhysics Letters* 58.5 (2002), p. 764.

[50] D. Roditchev *et al.* “Two-gap interplay in MgB_2: a tunneling spectroscopy study”. In: *Physica C: Superconductivity* 408–410 (2004). Proceedings of the International Conference on Materials and Mechanisms of Superconductivity. High Temperature Superconductors {VII} – {M2SRIO}, pp. 768–772. ISSN: 0921-4534.

[51] P. Martinez-Samper *et al.* “Scanning tunneling spectroscopy in MgB_2”. In: *Physica C: Superconductivity* 385.1–2 (2003), pp. 233–243. ISSN: 0921-4534.

[52] N. Emery *et al.* “Superconductivity of Bulk CaC_6”. In: *Phys. Rev. Lett.* 95 (8 Aug. 2005), p. 087003.

[53] T. E. Weller *et al.* “Superconductivity in the intercalated graphite compounds C6Yb and C6Ca”. In: *Nat. Phys.* 1.1 (Oct. 2005), pp. 39–41. ISSN: 1745-2473.

[54] M. Calandra and F. Mauri. “Theoretical Explanation of Superconductivity in C_6Ca”. In: *Phys. Rev. Lett.* 95 (23 Nov. 2005), p. 237002.

[55] N. Bergeal *et al.* “Scanning Tunneling Spectroscopy on the Novel Superconductor CaC_6”. In: *Phys. Rev. Lett.* 97 (7 Aug. 2006), p. 077003.

[56] H. Suhl, B. T. Matthias, and L. R. Walker. “Bardeen-Cooper-Schrieffer Theory of Superconductivity in the Case of Overlapping Bands”. In: *Phys. Rev. Lett.* 3 (12 Dec. 1959), pp. 552–554.

[57] H. J. Choi *et al.* “The origin of the anomalous superconducting properties of MgB_2”. In: *Nature* 418.6899 (Aug. 2002), pp. 758–760. ISSN: 0028-0836.

[58] A. Floris *et al.* “Two-band superconductivity in Pb from *ab initio* calculations”. In: *Phys. Rev. B* 75 (5 Feb. 2007), p. 054508.

[59] I. Y. Sklyadneva *et al.* “Electron-phonon interaction in bulk Pb: Beyond the Fermi surface”. In: *Phys. Rev. B* 85 (15 Apr. 2012), p. 155115.

[60] J. Heil *et al.* “Real Space Imaging of Ballistic Carrier Propagation in Bi Single Crystals”. In: *Phys. Rev. Lett.* 74 (1 Jan. 1995), pp. 146–149.

[61] O. Kurnosikov *et al.* “Long-Range Electron Interferences at a Metal Surface Induced by Buried Nanocavities”. In: *Phys. Rev. Lett.* 102 (6 Feb. 2009), p. 066101.

[62] A. Weismann *et al.* “Seeing the Fermi Surface in Real Space by Nanoscale Electron Focusing”. In: *Science* 323.5918 (2009), pp. 1190–1193. ISSN: 0036-8075.

[63] S. Lounis *et al.* “Theory of real space imaging of Fermi surface parts”. In: *Phys. Rev. B* 83 (3 Jan. 2011), p. 035427.

[64] P. W. Anderson. “Theory of dirty superconductors”. In: *J. Phys. Chem. Solids* 11.1–2 (1959), pp. 26–30. ISSN: 0022-3697.

[65] L. Yu. “Boung State in Superconductors with Paramagnetic Impurities”. In: *Acta Physica Sinica* 21.1, 75 (1965), p. 75.

[66] H. Shiba. “Classical Spins in Superconductors”. In: *Progress of Theoretical Physics* 40.3 (1968), pp. 435–451.

[67] A. I. Rusinov. “Superconductivity near a paramagnetic impurity”. In: *Zh. Eksp. Teor. Fiz. Red.* 9.2 (Jan. 1969), pp. 146–149.

[68] A. Yazdani *et al.* “Probing the Local Effects of Magnetic Impurities on Superconductivity”. In: *Science* 275.5307 (1997), pp. 1767–1770. ISSN: 0036-8075.

[69] M. I. Salkola, A. V. Balatsky, and J. R. Schrieffer. “Spectral properties of quasiparticle excitations induced by magnetic moments in superconductors”. In: *Phys. Rev. B* 55 (18 May 1997), pp. 12648–12661.

[70] R. Zitko, O. Bodensiek, and T. Pruschke. “Effects of magnetic anisotropy on the subgap excitations induced by quantum impurities in a superconducting host”. In: *Phys. Rev. B* 83 (5 Feb. 2011), p. 054512.

[71] A. V. Balatsky, I. Vekhter, and Jian-Xin Zhu. “Impurity-induced states in conventional and unconventional superconductors”. In: *Rev. Mod. Phys.* 78 (2 May 2006), pp. 373–433.

[72] S.-H. Ji *et al.* “High-Resolution Scanning Tunneling Spectroscopy of Magnetic Impurity Induced Bound States in the Superconducting Gap of Pb Thin Films”. In: *Phys. Rev. Lett.* 100 (22 June 2008), p. 226801.

[73] M. E. Flatté and J. M. Byers. “Local Electronic Structure of a Single Magnetic Impurity in a Superconductor”. In: *Phys. Rev. Lett.* 78 (19 May 1997), pp. 3761–3764.

[74] J. R. Schrieffer. “The Kondo Effect—The Link Between Magnetic and Nonmagnetic Impurities in Metals?” In: *J. Appl. Phys.* (1967), p. 1143.

[75] C. Moca *et al.* “Spin-resolved spectra of Shiba multiplets from Mn impurities in MgB_2”. In: *Phys. Rev. B* 77 (17 May 2008), p. 174516.

[76] D.-J. Choi *et al.* “Mapping the orbital structure of impurity bound states in a superconductor”. In: *ArXiv e-prints* (Aug. 2016).

[77] Y. Jean and C. Marsden. *Molecular orbitals of transition metal complexes*. Oxford University Press, 2005. ISBN: 9780198530930.

[78] G. C. Menard *et al.* “Coherent long-range magnetic bound states in a superconductor”. In: *Nat. Phys.* 11.12 (Dec. 2015), pp. 1013–1016. ISSN: 1745-2473.

[79] N. Y. Yao *et al.* “Enhanced Antiferromagnetic Exchange between Magnetic Impurities in a Superconducting Host”. In: *Phys. Rev. Lett.* 113 (8 Aug. 2014), p. 087202.

[80] S. Hoffman *et al.* “Impurity-induced quantum phase transitions and magnetic order in conventional superconductors: Competition between bound and quasiparticle states”. In: *Phys. Rev. B* 92 (12 Sept. 2015), p. 125422.

[81] M. A. Ruderman and C. Kittel. “Indirect Exchange Coupling of Nuclear Magnetic Moments by Conduction Electrons”. In: *Phys. Rev.* 96 (1 Oct. 1954), pp. 99–102.

[82] T. Kasuya. “A Theory of Metallic Ferro- and Antiferromagnetism on Zener’s Model”. In: *Progress of Theoretical Physics* 16.1 (1956), pp. 45–57.

[83] K. Yosida. “Magnetic Properties of Cu-Mn Alloys”. In: *Phys. Rev.* 106 (5 June 1957), pp. 893–898.

[84] T. Miyamachi *et al.* “Stabilizing the magnetic moment of single holmium atoms by symmetry”. In: *Nature* 503.7475 (Nov. 2013), pp. 242–246. ISSN: 0028-0836.

[85] C. Nayak *et al.* “Non-Abelian anyons and topological quantum computation”. In: *Rev. Mod. Phys.* 80 (3 Sept. 2008), pp. 1083–1159.

[86] A. Y. Kitaev. “Unpaired Majorana fermions in quantum wires”. In: *Phys.-Usp.* 44.10S (2001), p. 131.

[87] E. Majorana and L. Maiani. “A symmetric theory of electrons and positrons”. In: *Ettore Majorana Scientific Papers: On occasion of the centenary of his birth*. Ed. by Giuseppe Franco Bassani. Berlin, Heidelberg: Springer Berlin Heidelberg, 2006, pp. 201–233. ISBN: 978-3-540-48095-2.

[88] F. T. Avignone, S. R. Elliott, and J. Engel. “Double beta decay, Majorana neutrinos, and neutrino mass”. In: *Rev. Mod. Phys.* 80 (2 Apr. 2008), pp. 481–516.

[89] L. Fu and C. L. Kane. “Superconducting Proximity Effect and Majorana Fermions at the Surface of a Topological Insulator”. In: *Phys. Rev. Lett.* 100 (9 Mar. 2008), p. 096407.

[90] V. Mourik *et al.* “Signatures of Majorana Fermions in Hybrid Superconductor-Semiconductor Nanowire Devices”. In: *Science* 336.6084 (2012), pp. 1003–1007. ISSN: 0036-8075.

[91] R. M. Lutchyn, J. D. Sau, and S. Das Sarma. “Majorana Fermions and a Topological Phase Transition in Semiconductor-Superconductor Heterostructures”. In: *Phys. Rev. Lett.* 105 (7 Aug. 2010), p. 077001.

[92] Y. Oreg, G. Refael, and F. von Oppen. “Helical Liquids and Majorana Bound States in Quantum Wires”. In: *Phys. Rev. Lett.* 105 (17 Oct. 2010), p. 177002.

[93] J. D. Sau *et al.* “Non-Abelian quantum order in spin-orbit-coupled semiconductors: Search for topological Majorana particles in solid-state systems”. In: *Phys. Rev. B* 82 (21 Dec. 2010), p. 214509.

[94] L. P. Rokhinson, X. Liu, and J. K. Furdyna. “The fractional a.c. Josephson effect in a semiconductor-superconductor nanowire as a signature of Majorana particles”. In: *Nat. Phys.* 8.11 (Nov. 2012), pp. 795–799. ISSN: 1745-2473.

[95] A. Das *et al.* “Zero-bias peaks and splitting in an Al-InAs nanowire topological superconductor as a signature of Majorana fermions”. In: *Nat. Phys.* 8.12 (Dec. 2012), pp. 887–895. ISSN: 1745-2473.

[96] M. T. Deng *et al.* “Anomalous Zero-Bias Conductance Peak in a Nb–InSb Nanowire–Nb Hybrid Device”. In: *Nano Letters* 12.12 (2012), pp. 6414–6419.

[97] A. D. K. Finck *et al.* “Anomalous Modulation of a Zero-Bias Peak in a Hybrid Nanowire-Superconductor Device”. In: *Phys. Rev. Lett.* 110 (12 Mar. 2013), p. 126406.

[98] J. D. Sau *et al.* “Non-Abelian quantum order in spin-orbit-coupled semiconductors: Search for topological Majorana particles in solid-state systems”. In: *Phys. Rev. B* 82 (21 Dec. 2010), p. 214509.

[99] S. Das Sarma, M. Freedman, and C. Nayak. “Majorana zero modes and topological quantum computation”. In: *Npj Quantum Information* 1 (Oct. 2015), p. 15001.

[100] S. Nadj-Perge *et al.* “Proposal for realizing Majorana fermions in chains of magnetic atoms on a superconductor”. In: *Phys. Rev. B* 88 (2 July 2013), p. 020407.

[101] S. Nadj-Perge *et al.* “Observation of Majorana fermions in ferromagnetic atomic chains on a superconductor”. In: *Science* 346.6209 (2014), pp. 602–607. ISSN: 0036-8075.

[102] J. Li *et al.* “Topological superconductivity induced by ferromagnetic metal chains”. In: *Phys. Rev. B* 90 (23 Dec. 2014), p. 235433.

[103] Y. Peng *et al.* “Strong Localization of Majorana End States in Chains of Magnetic Adatoms”. In: *Phys. Rev. Lett.* 114 (10 Mar. 2015), p. 106801.

[104] H.-Y. Hui *et al.* “Majorana fermions in ferromagnetic chains on the surface of bulk spin-orbit coupled s-wave superconductors”. In: *Scientific Reports* 5 (Mar. 2015), p. 8880.

[105] J. D. Sau and P. M. R. Brydon. “Bound States of a Ferromagnetic Wire in a Superconductor”. In: *Phys. Rev. Lett.* 115 (12 Sept. 2015), p. 127003.

[106] Y. Peng *et al.* “Robust Majorana Conductance Peaks for a Superconducting Lead”. In: *Phys. Rev. Lett.* 115 (26 Dec. 2015), p. 266804.

[107] B. E. Feldman *et al.* “High-resolution studies of the Majorana atomic chain platform”. en. In: *Nat. Phys.* advance online publication (Nov. 2016). ISSN: 1745-2473.

[108] R. Wiesendanger. “Spin mapping at the nanoscale and atomic scale”. In: *Rev. Mod. Phys.* 81 (4 Nov. 2009), pp. 1495–1550.

[109] P. Gambardella *et al.* “Ferromagnetism in one-dimensional monatomic metal chains”. en. In: *Nature* 416.6878 (Mar. 2002), pp. 301–304. ISSN: 0028-0836.

[110] O. Pietzsch *et al.* “Spin-Polarized Scanning Tunneling Spectroscopy of Nanoscale Cobalt Islands on Cu(111)”. In: *Phys. Rev. Lett.* 92 (5 Feb. 2004), p. 057202.

[111] D. A. Papaconstantopoulos. *Handbook of the Band Structure of Elemental Solids*. Springer Science+Business Media New York. ISBN: 978-1-4419-8263-6.

[112] M. Weinert and A.J. Freeman. “Magnetism of linear chains”. In: *Journal of Magnetism and Magnetic Materials* 38.1 (1983), pp. 23–33. ISSN: 0304-8853.

[113] J. C. Slater. “Electronic Structure of Alloys”. In: *J. Appl. Phys.* 8 (1937), p. 385.

[114] S. M. Albrecht *et al.* “Exponential protection of zero modes in Majorana islands”. In: *Nature* 531.7593 (Mar. 2016), pp. 206–209. ISSN: 0028-0836.

[115] I. Dzyaloshinsky. “A thermodynamic theory of ‘weak’ ferromagnetism of antiferromagnetics”. In: *Journal of Physics and Chemistry of Solids* 4.4 (1958), pp. 241–255. ISSN: 0022-3697.

[116] T. Moriya. “Anisotropic Superexchange Interaction and Weak Ferromagnetism”. In: *Phys. Rev.* 120 (1 Oct. 1960), pp. 91–98.

[117] Y. Oreg, G. Refael, and F. von Oppen. “Helical Liquids and Majorana Bound States in Quantum Wires”. In: *Phys. Rev. Lett.* 105 (17 Oct. 2010), p. 177002.

[118] F. Pientka, L. I. Glazman, and F. von Oppen. “Topological superconducting phase in helical Shiba chains”. In: *Phys. Rev. B* 88 (15 Oct. 2013), p. 155420.

[119] F. Pientka, L. I. Glazman, and F. von Oppen. “Unconventional topological phase transitions in helical Shiba chains”. In: *Phys. Rev. B* 89 (18 May 2014), p. 180505.

[120] Y. Kim *et al.* “Helical order in one-dimensional magnetic atom chains and possible emergence of Majorana bound states”. In: *Phys. Rev. B* 90 (6 Aug. 2014), p. 060401.

[121] I. Martin and A. F. Morpurgo. “Majorana fermions in superconducting helical magnets”. In: *Phys. Rev. B* 85 (14 Apr. 2012), p. 144505.

[122] K. Pöyhönen *et al.* “Majorana states in helical Shiba chains and ladders”. In: *Phys. Rev. B* 89 (11 Mar. 2014), p. 115109.

[123] A. Westström, K. Pöyhönen, and T. Ojanen. “Topological properties of helical Shiba chains with general impurity strength and hybridization”. In: *Phys. Rev. B* 91 (6 Feb. 2015), p. 064502.

[124] M. Schecter *et al.* “Self-organized topological superconductivity in a Yu-Shiba-Rusinov chain”. In: *Phys. Rev. B* 93 (14 Apr. 2016), p. 140503.

[125] A. Heimes, P. Kotetes, and G. Schön. “Majorana fermions from Shiba states in an antiferromagnetic chain on top of a superconductor”. In: *Phys. Rev. B* 90 (6 Aug. 2014), p. 060507.

[126] J. Alicea *et al.* “Non-Abelian statistics and topological quantum information processing in 1D wire networks”. In: *Nat. Phys.* 7.5 (May 2011), pp. 412–417. ISSN: 1745-2473.

[127] R. Young, J. Ward, and F. Scire. "The Topografiner: An Instrument for Measuring Surface Microtopography". In: *Rev. Sci. Instrum.* 43.999 (1972).

[128] G. Binnig *et al.* "Surface Studies by Scanning Tunneling Microscopy". In: *Phys. Rev. Lett.* 49 (1 July 1982), pp. 57–61.

[129] G. Binnig *et al.* "Tunneling through a controllable vacuum gap". In: *Appl. Phys. Lett.* 40.2 (1982), pp. 178–180.

[130] T. Wolfram, ed. *Inelastic Electron Tunneling Spectroscopy*. Spinger-Verlag, Berlin, 1978. ISBN: 978-3-642-81230-9.

[131] B. C. Stipe, M. A. Rezaei, and W. Ho. "Single-Molecule Vibrational Spectroscopy and Microscopy". In: *Science* 280.5370 (1998), pp. 1732–1735. ISSN: 0036-8075.

[132] A. J. Heinrich *et al.* "Single-Atom Spin-Flip Spectroscopy". In: *Science* 306.5695 (2004), pp. 466–469. ISSN: 0036-8075.

[133] R. Berndt *et al.* "Photon Emission at Molecular Resolution Induced by a Scanning Tunneling Microscope". In: *Science* 262.5138 (1993), pp. 1425–1427. ISSN: 0036-8075.

[134] G. Hoffmann, L. Libioulle, and R. Berndt. "Tunneling-induced luminescence from adsorbed organic molecules with submolecular lateral resolution". In: *Phys. Rev. B* 65 (21 June 2002), p. 212107.

[135] X. H. Qiu, G. V. Nazin, and W. Ho. "Vibrationally Resolved Fluorescence Excited with Submolecular Precision". In: *Science* 299.5606 (2003), pp. 542–546. ISSN: 0036-8075.

[136] R. Wiesendanger *et al.* "Observation of vacuum tunneling of spin-polarized electrons with the scanning tunneling microscope". In: *Phys. Rev. Lett.* 65 (2 July 1990), pp. 247–250.

[137] J. Bardeen. "Tunnelling from a Many-Particle Point of View". In: *Phys. Rev. Lett.* 6 (2 Jan. 1961), pp. 57–59.

[138] J. Tersoff and D. R. Hamann. "Theory of the scanning tunneling microscope". In: *Phys. Rev. B* 31 (2 Jan. 1985), pp. 805–813.

[139] D. A. Bonnell, ed. *Scanning Probe Microscopy and Spectroscopy: Theory, Techniques, and Applications*. Wiley-VCH, Inc., New York, 2001.

[140] C. J. Chen. "Tunneling matrix elements in three-dimensional space: The derivative rule and the sum rule". In: *Phys. Rev. B* 42 (14 Nov. 1990), pp. 8841–8857.

[141] L. Gross *et al.* "High-Resolution Molecular Orbital Imaging Using a p-Wave STM Tip". In: *Phys. Rev. Lett.* 107 (8 Aug. 2011), p. 086101.

[142] J. Klein *et al.* "Inelastic-Electron-Tunneling Spectroscopy of Metal-Insulator-Metal Junctions". In: *Phys. Rev. B* 7 (6 Mar. 1973), pp. 2336–2348.

[143] D. W. Green and R. H. Perry. *Perry's Chemical Engineers' Handbook*. 8th ed. McGraw-Hill: New York, 2008. ISBN: 9780071422949.

Appendix B

Publications

The articles presented in the framework of this thesis are reprinted below in the order of their discussion in the main text. They were published by the author of this thesis, Michael KLEINERT, under his scientific pseudonym 'Michael RUBY'. The work was carried out in the research group of Prof. Dr. Katharina Franke under supervision of Dr. Benjamin Heinrich. The results were mostly achieved in close collaboration with theoretical physicists of the group of Prof. Dr. Felix von Oppen. Contributions of the authors to the publications are as follows:

- **SoftwareX 5, 31 (2016):** The software 'SpectraFox' was written over the period of five years by the author of this thesis. At the time of publication of the article, it was made available under an open source license, and comprised ≈ 43000 lines of code. The manuscript and software manual were written by the author of this thesis.
- **Physical Review Letters 114, 157001 (2015):** The author of this thesis performed the experimental measurements and the data analysis. All authors contributed to the interpretation of the data. The initial manuscript was written by the author of this thesis. All authors contributed to the writing of the final version.
- **Physical Review Letters 117, 186801 (2016):** The author of this thesis performed the experimental measurements and the data analysis. The theoretical model was developed by Y. Peng and F. von Oppen. All authors contributed to the interpretation of the data. The initial manuscript was written by the author of this thesis, the theoretical description in the supplement was written by Y. Peng. All authors contributed to the discussion and the writing of the final version of the manuscript.
- **Physical Review Letters 115, 087001 (2015):** The author of this thesis performed the experimental measurements and the data analysis. The theoretical analysis and interpretation was done by F. Pientka, Y. Peng, and F. von Oppen. The initial manuscript was written in close collaboration between the author of this thesis and F. Pientka. All authors contributed to the discussion and the writing of the final version of the manuscript.
- **Physical Review Letters 115, 197204 (2015):** The author of this thesis performed the experimental measurements and the data analysis. The theoretical analysis and simulations were done by F. Pientka, Y. Peng, and F. von Oppen. The initial manuscript was written by the author of this thesis, except for the theoretical part, which was written by F. Pientka. All authors contributed to the discussion and the writing of the final version of the manuscript.

B.1 SoftwareX 5, 31 (2016)

Michael Ruby

SpectraFox: A free open-source data management and analysis tool for scanning probe microscopy and spectroscopy

doi:10.1016/j.softx.2016.04.001

— For copyright reasons this publication is not included in the online version of this thesis. —

B.2 Physical Review Letters 114, 157001 (2015)

Michael Ruby, Benjamin W. Heinrich,
Jose I. Pascual, and Katharina J. Franke

Experimental Demonstration of a Two-Band Superconducting State for Lead Using Scanning Tunneling Spectroscopy

doi:10.1103/PhysRevLett.114.157001

PRL 114, 157001 (2015) PHYSICAL REVIEW LETTERS week ending 17 APRIL 2015

Experimental Demonstration of a Two-Band Superconducting State for Lead Using Scanning Tunneling Spectroscopy

Michael Ruby,[1] Benjamin W. Heinrich,[1] Jose I. Pascual,[1,2] and Katharina J. Franke[1]
[1] *Fachbereich Physik, Freie Universität Berlin, Arnimallee 14, 14195 Berlin, Germany*
[2] *CIC nanoGUNE and Ikerbasque, Basque Foundation for Science, Tolosa Hiribidea 78, Donostia-San Sebastian 20018, Spain*

(Received 16 September 2014; revised manuscript received 15 December 2014; published 14 April 2015)

The type I superconductor lead (Pb) has been theoretically predicted to be a two-band superconductor. We use scanning tunneling spectroscopy (STS) to resolve two superconducting gaps with an energy difference of 150 μeV. Tunneling into Pb(111), Pb(110), and Pb(100) crystals reveals a strong dependence of the two coherence peak intensities on the crystal orientation. We show that this is the result of a selective tunneling into the two bands at the energy of the two coherence peaks. This is further sustained by the observation of signatures of the Fermi sheets in differential conductance maps around subsurface defects. A modification of the density of states of the two bands by adatoms on the surface confirms the different orbital character of each of the two subbands.

DOI: 10.1103/PhysRevLett.114.157001 PACS numbers: 74.55.+v, 73.20.-r, 74.20.Fg, 74.25.Jb

The theory of Bardeen, Cooper, and Schrieffer (BCS) has been extremely successful in describing many aspects of superconductivity (SC). It predicts the formation of a condensate of quasiparticles, the so-called Cooper pairs, as a result of electron-phonon coupling. The corresponding quasiparticle excitation spectrum exhibits a characteristic gap of width 2Δ around the Fermi level, with Δ being the order parameter reflecting the bonding strength of the Cooper pairs. However, soon after the development of the BCS formalism, it was realized that the theory has to be extended for describing the properties of even the simplest elemental superconductors such as Pb, V, Ta, etc. In particular, two quasiparticle resonances have been observed in planar Pb tunneling junctions [1–4]. The initial interpretations of these experiments proposed an anisotropic electron-phonon coupling leading to a $\boldsymbol{k}$-dependent order parameter as the origin of this behavior [5].

With the discovery of superconductivity in highly anisotropic, composite materials, such as MgB_2, $NbSe_2$, CaC_6, etc., with two distinct energy gaps and unexpectedly high critical temperatures [6–14], the importance of the concept of multiband superconductivity, which had been proposed already in 1959 [15], was realized. This motivated a renewed theoretical treatment of conventional superconductors with state-of-the-art methods. These revealed that two disjoint Fermi sheets (FSs) with different electron-phonon coupling strengths lead to two distinct energy gaps and an increased critical temperature as compared to a single isotropic gap [16].

Floris *et al.* identified by density functional theory (SCDFT) that two-band superconductivity also plays a role in the elemental superconductor Pb [17]. They found that the Fermi surface of Pb is composed of a compact Fermi sheet with mostly s-p character and a tubular Fermi sheet of p-d character. The different orbital nature leads to different electron-phonon coupling strengths [18] and causes different pairing energies in the SC condensate.

Experimentally, it is difficult to distinguish between a two-band model and an anisotropic variation of the order parameter. Angle-resolved photoemission spectroscopy, a prime candidate for experimental band structure determination, lacks the required energy resolution. Planar tunneling junctions have revealed two peaks in the gap structure [1–4], but the tunneling current is the sum of all tunneling paths, including step edges, vacancies, impurities, etc. This prohibits an unambiguous interpretation of the tunneling spectra.

Here, we overcome this shortcoming using scanning tunneling microscopy (STM) and spectroscopy (STS) to probe atomically flat surfaces as well as well-defined defects and distinguish between the different contributions to tunneling. We present direct evidence for the two-band nature of superconductivity in Pb. Two BCS-like resonances with an energy separation of 150 μeV are observed. Depending on the surface orientation, the intensity of these peaks varies due to $\boldsymbol{k}$-selective tunneling into the two Fermi sheets. Scattering patterns around subsurface Ne impurities at the energies of the two coherence peaks reveal signatures of the shape of the respective Fermi sheets as a result of an anisotropic electron propagator in the crystal [19–22]. Furthermore, we show that the distinct orbital character of the Fermi sheets is reflected by the modification of density of states (DOS) at adatoms, which tends to increase the weight of tunneling into more localized d states over the delocalized s-p-derived states.

Our experiments were carried out in a SPECS JT-STM under ultrahigh vacuum conditions at a base temperature of 1.2 K. Pb is a type I superconductor with a critical temperature of $T_c = 7.2$ K and a coherence length of 83 nm. The single crystals were cleaned by cycles of

Ne^+ ion sputtering at 900 eV with a Ne pressure of 1.5×10^{-4} mbar (background pressure: $< 1.5 \times 10^{-9}$ mbar) and annealing to 430 K for 30 min until a clean, atomically flat, and superconducting surface was observed. To achieve high energy resolution, we cover etched W tips with Pb by deep indentations into the clean Pb surface until superconductor-superconductor tunneling spectra are measured [23] (see Supplemental Material for details [24]). The use of a superconducting tip together with an elaborated grounding and rf-filtering scheme yields an effective energy resolution of ≈ 45 μeV at 1.2 K (compared to ≈ 360 μeV with a normal metal tip, in which Fermi-Dirac broadening limits the energy resolution). Crystalline directions were determined by atomically resolved topographies of the clean Pb surface (see Fig. S1 [24]).

We record spectra of the differential conductance $dI/dV(V)$ on clean terraces of the three low-index surfaces (111), (100), and (110) of Pb single crystals to probe their superconducting energy gaps (Fig. 1). Around E_F, the superconducting gap (zero conductance) is framed by quasiparticle resonances (QPRs) at $\approx \pm 2.7$ meV [29]. In the spectra of all surface orientations, we observe two pairs of QPRs separated by ≈ 150 μeV [30]. Because of the superconducting state of the tip, the spectra are a convolution of two SC density of states. In particular the position of the QPRs is shifted by Δ_{tip}. To extract the exact energy positions and intensities of the two QPRs, we deconvolute the spectra as described in the Supplemental Material [24]. We can unambiguously link the appearance of the two peaks with ≈ 150 μeV separation to a property of all samples, independent of the tip's single gap. Similar splittings have been observed earlier in planar Pb tunnel junctions and attributed to the anisotropy of the FS and of the electron-phonon coupling of Pb [1,3–5]. More recently, however, Floris *et al.* predicted that Pb is a two-band superconductor with two well-separated FSs, with one of them being highly anisotropic and the other almost spherical (see the inset in Fig. 1) [17]. The inner FS (FS1) has an almost spherical shape. The outer FS (FS2) has a tubular shape [31]. FS1 is mostly of s-p character with a smaller pairing energy than FS2, which is of p-d-like character [17]. A manifestation of the different pairing energy associated to each FS is the different position of the corresponding quasiparticle resonances QPR1 and QPR2 in the $dI/dV(V)$ spectra. Hence, we identify the inner and outer peaks as tunneling into FS1 and FS2 of the sample, respectively. The existence of a single gap in the STM tip is in agreement with its expected microcrystalline character [32]. While the energy separation between QPR1 and QPR2 is constant for all surfaces, we observe distinct relative peak intensities for the different surface orientations (Fig. 1). The tunneling probability depends on transition matrix elements, which depend on the $k_\perp$ component of the wave vector $\boldsymbol{k}$. A strong tunneling contribution thus requires access to the FS with the wave vector $\boldsymbol{k}$ being mostly perpendicular to the surface. The insets in Fig. 1 show the top views of the two FSs for the given crystal orientations. FS1 is compact, which implies that tunneling with a strong $k_\perp$ contribution into the (111), (100), and (110) surface is possible. In contrast to this, FS2 exhibits open pores along the $\boldsymbol{k}_{\Gamma\to L}$ and $\boldsymbol{k}_{\Gamma\to X}$ directions. Hence, for these directions, tunneling into FS2 is only possible with wave vectors with a considerable $k_\parallel$ component, which is accompanied by a reduced tunneling probability. Therefore, the ratio of intensities of QPR1 and QPR2 is largest on the (111) surface, where FS2 exhibits the largest pore, followed by the (100) surface. On the (110) surface, QPR2 is even more intense than QPR1 (see the Supplemental Material for a quantitative analysis of the intensities [24]). Both FSs can be accessed by electrons with $\boldsymbol{k}$ vectors with a mostly $k_\perp$ contribution and can therefore participate almost equivalently in tunneling.

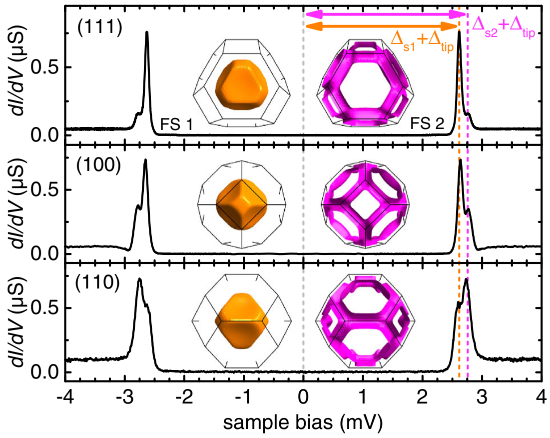

FIG. 1 (color online). $dI/dV(V)$ spectra on clean terraces of Pb(111), (100), and (110) single crystal surfaces. The superconducting gap around E_F is framed by QPRs at $\approx \pm 2.7$ mV, consisting of two peaks separated by ≈ 150 μeV. The energy of the peaks is given as the sum of the pairing energy of the tip (Δ_{tip}) and the sample (Δ_{s1} and Δ_{s2}, respectively). The insets show the corresponding top views on the two FSs of a Pb single crystal. 3D models from [28]. Lock-in modulation amplitude was 15 μV_{rms} at 912 Hz.

The observed energy splitting in STS together with the dependence of the QPR intensities on the surface orientation agrees well with the two-band superconductivity connected to the FSs of Pb, as predicted by Floris *et al.* [17]. The difference between the pairing energies of $\approx 10\%$ is, however, smaller than calculated ($\approx 30\%$ [17]). We link this to interband scattering, which diminishes the difference in the pairing energy of the two bands [33].

We now search for more direct evidence of the presence of the two FSs with different order parameters. One way to image the different symmetries of the two FSs is to inspect dI/dV maps around buried impurities which show characteristic modulation of the DOS around them (see Figs. 2 and S3 in the Supplemental Material [24]). On the Pb(100) surface we find typical patterns in STM topographies (see Fig. S2 [24]). These consist of a bright or dark center which is framed by patterns of fourfold symmetry.

The impurities are most likely Ne-filled subsurface nanocavities, which are residuals of the Ne^+ ion sputtering [20,34]. They act as scattering centers and give rise to quantum well states between the surface and the impurity [34]. The subsurface inclusion appears then as a protrusion or a depression, depending on whether or not the sample bias matches the quantization condition of the quantum well state. The quantum well state typically has a width of several hundreds of meV (e.g., Fig. S3h in the Supplemental Material [24]). Therefore, it is present in a wide energy range. Laterally away from the impurity center, the two constant-height dI/dV maps at the energy of the two QPRs show quite different patterns of charge density oscillations. The map at 2.64 meV, which results from tunneling into QPR1, exhibits a squarelike pattern with the edges along the $\langle 110\rangle$ directions around the bright center [highlighted by orange ellipses in Fig. 2(c)]. The map at the energy of QPR2 [2.76 meV, Fig. 2(d)] shows areas of high intensity along the $\langle 100\rangle$ (shaded purple ellipses) and $\langle 110\rangle$ (open purple ellipses) directions, respectively. Additionally, long-ranging oscillations appear in the dI/dV signal along the $\langle 110\rangle$ directions (indicated by purple stripes).

According to Weismann and his co-workers, the charge density oscillations result from a scattering and a focusing of bulk electrons (holes) at subsurface impurities with an anisotropic electron (hole) propagation [21]. Analogous to the Huygens principle, the group velocity of the electrons (holes) dE/dk is perpendicular to the FS and therefore nearly parallel for beams arising from areas of low FS curvature. This leads to a focusing of the electron propagator into the normal direction of these regions [19]. Hence, the real space distribution of the DOS on the surface above the impurity, which is resolved via dI/dV mapping, is directly related to the shape of the FS.

We can now assign the features of the dI/dV maps to low-curvature regions of FS1 and FS2, respectively. The curvature of the respective FSs is color coded onto the 3D models in Figs. 2(e) and 2(f). FS1 contains two groups of low-curvature regions [dark blue in Fig. 2(e)]: eight large regions with the group velocity (i.e., FS surface normal) pointing into the $\langle 111\rangle$ directions, i.e., along the Γ-L direction, and six smaller regions with the surface normal pointing towards $\langle 100\rangle$, i.e., along the Γ-X direction. Projected onto the (100) surface, we can assign the four squarelike stripes of high conductance [the orange ovals in Fig. 2(c)] to the focusing of electron propagation in the $\langle 111\rangle$ direction. Also, for the $\langle 100\rangle$ direction a higher intensity is expected. However, this direction is dominated by the quantum well state, as discussed above. Both signals are superimposed and are thus not distinguishable.

FS2 can be described as a complex structure with tubes connecting the U and W points, and connecting the K and W points, respectively. Despite having a large three-dimensional curvature [Fig. 2(h)], the tubes exhibit one-dimensional low-curvature regions (lines). Along the line the group velocity is therefore pointing in the same

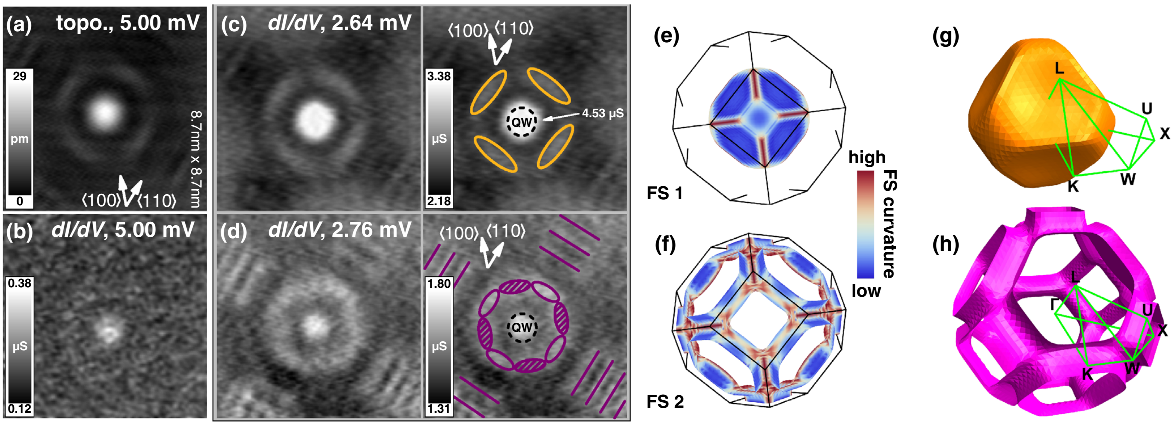

FIG. 2 (color online). (a)–(d) Subsurface Ne inclusion. High-resolution topography (a) on an atomically flat Pb(100) terrace (set point: 5 mV, 250 pA). Constant-height dI/dV maps at 5 mV (b), 2.64 mV (c), and 2.76 mV (d) (25 $\mu\mathrm{V}_{\mathrm{rms}}$, 912 Hz, set point: 5 mV, 500 pA). In the duplicated maps, prominent scattering signatures are highlighted as a guide for the eye. A quantum well state between the impurity and the surface leads to the higher conductance in the center of all maps. Note that the topography in (a) combines features visible in (c) and (d) because all states up to the applied bias—i.e., both Fermi sheets—contribute to the tunneling current. (e)–(h) 3D models of the two FSs of Pb from Ref. [28]. The curvature of the FS is color coded onto the 3D model in (e) and (f), which are oriented according to the crystalline directions in (a)–(d). Dark blue and dark red correspond to low and high curvature, respectively. Black lines in (e) and (f) mark the boundaries of the first Brillouin zone.

direction, giving rise to an enhanced scattering pattern, analogous to a decreased decay of Friedel oscillations in two dimensions [22]. The fourfold symmetry of the U-W and K-W tubes, respectively, then gives rise to the octagonal pattern [the purple ovals in Fig. 2(d)] projected on the surface, as seen in the dI/dV map. The oscillations at a larger distance can be linked to a long-range interference of electrons (holes) due to a scattering at side facets of the inclusion [20,35] or due to an interference of electrons (holes) with the same group velocity, but originating from different areas on the FS [22]. The distinct appearance of these patterns at QPR1 and QPR2 is thus further proof of the geometrically very different FSs with different pairing energies.

According to the SCDFT calculations in Ref. [17], each FS has a different orbital character. We expect that this character will be reflected in the interaction with local potentials. Adsorbates interact with the electronic bands of the surface and locally modify the corresponding density of states. To probe this interaction with both the s-p- and p-d-derived FSs, we deposited Pb adatoms from the lead-covered tip onto the surface by applying voltage pulses of 6 to 10 V at a tip-sample distance of approximately 1 nm. The inset of Fig. 3(b) shows a topography of an as-deposited adatom. The excitation spectrum above the center of the adatom [Fig. 3(a), bottom] shows that QPR2 is more intense than QPR1, in contrast to the spectrum on the clean surface [Fig. 3(a), top].

The spatial extension of this intensity variation is reflected in a series of spectra taken along a line over the adatom [see the inset of Fig. 3(b)]. The relative intensities $R = A_1/A_2$ of the QPRs—with A_1 and A_2 being the intensities of QPR1 and QPR2, respectively, after deconvolution—are shown in Fig. 3(b). The value decreases continuously from 2 over the clean surface to 0.65 on top of the adatom. Thus the adatoms increase the tunneling probability into FS2 compared to FS1. The variation of R is constricted to the adatom site [36]. In principle, a protruding feature such as an adatom geometrically favors tunneling with a large $k_\perp$ contribution and may thus enhance the tunneling probability into FS1, leading to a larger R. The opposite trend observed in the experiment suggests another scenario. The increased intensity of QPR2 indicates that tunneling into the band of FS2 is particularly enhanced at the localized potential of the Pb adatom. This is a consequence of a strong confinement of localized d-derived states around an impurity potential. Therefore the band that is associated with FS2 and is hybridized with d states is more affected than the extended s-p band that creates FS1 [18].

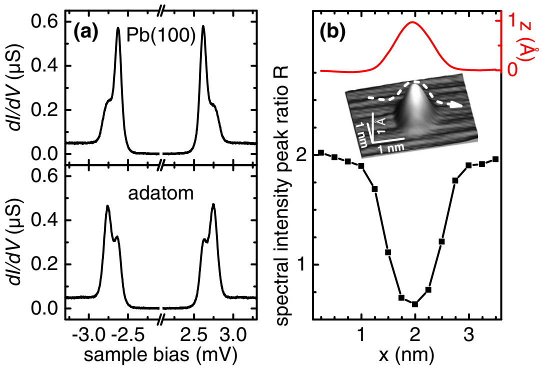

FIG. 3 (color online). Pb adatom on Pb(100). (a) $dI/dV(V)$ spectrum on clean Pb(100) (top) and on a Pb adatom (bottom). (b) Intensity ratio R of QPR1 vs QPR2 and apparent height across a Pb adatom, as sketched in the inset. R is determined by numerical deconvolution of the spectra, as discussed in the Supplemental Material [24].

Despite Pb being one of the best characterized type I superconductors, the theoretical prediction of Pb being a two-band superconductor has not been experimentally evidenced unambiguously to date. The early-on observed splitting of QPRs could either be described by an anisotropic electron-phonon coupling term or by two distinct electronic bands at the Fermi level. We have shown clear fingerprints of the two-band nature of superconductivity in Pb. STS resolved the differing pairing energy on the two bands as 150 μeV, which is smaller than was theoretically predicted. Calculations of interband scattering events may be able to explain this deviation. The energetically separated FSs allowed for a direct mapping of their symmetry in real space. This method is complementary to quasiparticle interference mapping by STM [38], which is frequently used to resolve characteristics of the FS of, e.g., high-T_c superconductors. Most importantly, the intensity of quasiparticle interference falls off too rapidly in three-dimensional electron systems (such as Pb) and, therefore, requires two-dimensional states. Furthermore, it does not involve reconstruction of the Fermi surface by Fourier transformation, but it directly reflects the symmetry of reciprocal space in real space.

The tuning of orbital contributions around atoms allows us, in a proof-of-principle experiment, to favor tunneling into one or the other FSs and might be used—together with the focusing properties of the curved FSs—for $\boldsymbol{k}$-selective filtering in future tunneling devices.

We gratefully acknowledge funding by the DFG through Sfb 658 and Grant No. FR-2726/4.

[1] P. Townsend and J. Sutton, Phys. Rev. **128**, 591 (1962).
[2] G. I. Rochlin, Phys. Rev. **153**, 513 (1967).
[3] B. L. Blackford and R. H. March, Phys. Rev. **186**, 397 (1969).
[4] G. I. Lykken, A. L. Geiger, K. S. Dy, and E. N. Mitchell, Phys. Rev. B **4**, 1523 (1971).
[5] A. J. Bennett, Phys. Rev. **140**, A1902 (1965).

[6] F. Giubileo, D. Roditchev, W. Sacks, R. Lamy, D. X. Thanh, J. Klein, S. Miraglia, D. Fruchart, J. Marcus, and P. Monod, Phys. Rev. Lett. **87**, 177008 (2001).

[7] F. Giubileo, D. Roditchev, W. Sacks, R. Lamy, and J. Klein, Europhys. Lett. **58**, 764 (2002).

[8] C. Buzea and T. Yamashita, Supercond. Sci. Technol. **14**, R115 (2001).

[9] T. E. Weller, M. Ellerby, S. S. Saxena, R. P. Smith, and N. T. Skipper, Nat. Phys. **1**, 39 (2005).

[10] N. Bergeal, V. Dubost, Y. Noat, W. Sacks, D. Roditchev, N. Emery, C. Hérold, J.-F. Marêché, P. Lagrange, and G. Loupias, Phys. Rev. Lett. **97**, 077003 (2006).

[11] M. Calandra and F. Mauri, Phys. Rev. Lett. **95**, 237002 (2005).

[12] D. Roditchev, F. Giubileo, F. Bobba, R. Lamy, E.-M. Choi, H.-J. Kim, W. N. Kang, S. Miraglia, J. Marcus, W. Sacks, J. Klein, A. M. Cucolo, S.-I. Lee, and D. Fruchart, Physica (Amsterdam) **408–410C**, 768 (2004).

[13] N. Emery, C. Hérold, M. d'Astuto, V. Garcia, C. Bellin, J. F. Marêché, P. Lagrange, and G. Loupias, Phys. Rev. Lett. **95**, 087003 (2005).

[14] P. Martinez-Samper, J. G. Rodrigo, G. Rubio-Bollinger, H. Suderow, S. Vieira, S. Lee, and S. Tajima, Physica (Amsterdam) **385C**, 233 (2003).

[15] H. Suhl, B. T. Matthias, and L. R. Walker, Phys. Rev. Lett. **3**, 552 (1959).

[16] H. J. Choi, D. Roundy, H. Sun, M. L. Cohen, and S. G. Louie, Nature (London) **418**, 758 (2002).

[17] A. Floris, A. Sanna, S. Massidda, and E. K. U. Gross, Phys. Rev. B **75**, 054508 (2007).

[18] I. Y. Sklyadneva, R. Heid, P. M. Echenique, K.-B. Bohnen, and E. V. Chulkov, Phys. Rev. B **85**, 155115 (2012).

[19] J. Heil, M. Primke, K. U. Würz, and P. Wyder, Phys. Rev. Lett. **74**, 146 (1995).

[20] O. Kurnosikov, J. H. Nietsch, M. Sicot, H. J. M. Swagten, and B. Koopmans, Phys. Rev. Lett. **102**, 066101 (2009).

[21] A. Weismann, M. Wenderoth, S. Lounis, P. Zahn, N. Quaas, R. G. Ulbrich, P. H. Dederichs, and S. Blügel, Science **323**, 1190 (2009).

[22] S. Lounis, P. Zahn, A. Weismann, M. Wenderoth, R. G. Ulbrich, I. Mertig, P. H. Dederichs, and S. Blügel, Phys. Rev. B **83**, 035427 (2011).

[23] K. J. Franke, G. Schulze, and J. I. Pascual, Science **332**, 940 (2011).

[24] See Supplemental Material at http://link.aps.org/supplemental/10.1103/PhysRevLett.114.157001, which includes Refs. [25–27], for the deconvolution method of the dI/dV spectra, experimental details, and additional data.

[25] J. Tersoff and D. R. Hamann, Phys. Rev. B **31**, 805 (1985).

[26] R. C. Dynes, V. Narayanamurti, and J. P. Garno, Phys. Rev. Lett. **41**, 1509 (1978).

[27] M. Ternes, W.-D. Schneider, J.-C. Cuevas, C. P. Lutz, C. F. Hirjibehedin, and A. J. Heinrich, Phys. Rev. B **74**, 132501 (2006).

[28] T.-S. Choy, J. Naset, S. Hershfield, C. Stanton, and J. Chen, Bull. Am. Phys. Soc. **45**, L36 (2000).

[29] Direct tunneling of Cooper pairs giving rise to a dc Josephson current is not observed due to the weak overlap of the condensate wave functions at the experimental tip-sample distance.

[30] In the $dI/dV(V)$ spectrum on Pb(100), a dip is observed at ±3 mV. Such dips are occasionally resolved on all three surfaces and depend on the tip employed. They are due to deviations from pure BCS-like DOS originating from interband scattering [33].

[31] J. R. Anderson and A. V. Gold, Phys. Rev. **139**, A1459 (1965).

[32] P. Anderson, J. Phys. Chem. Solids **11**, 26 (1959).

[33] Y. Noat, T. Cren, F. Debontridder, D. Roditchev, W. Sacks, P. Toulemonde, and A. San Miguel, Phys. Rev. B **82**, 014531 (2010).

[34] M. Schmid, W. Hebenstreit, P. Varga, and S. Crampin, Phys. Rev. Lett. **76**, 2298 (1996).

[35] O. Kurnosikov, O. A. O. Adam, H. J. M. Swagten, W. J. M. de Jonge, and B. Koopmans, Phys. Rev. B **77**, 125429 (2008).

[36] Atomic modulation of the gap structure of multiband superconductors was observed earlier [37]. Yet, the modulation strength of the effect observed here is unexpectedly high and hints towards a strong modification of the local density of states at the adatom site.

[37] I. Guillamon, H. Suderow, F. Guinea, and S. Vieira, Phys. Rev. B **77**, 134505 (2008).

[38] K. McElroy, R. W. Simmonds, J. E. Hoffman, D.-H. Lee, J. Orenstein, H. Eisaki, S. Uchida, and J. C. Davis, Nature (London) **422**, 592 (2003).

Supplemental Material

Experimental demonstration of a two-band superconducting state for lead using scanning tunneling spectroscopy

Michael Ruby[1], Benjamin W. Heinrich[1], Jose I. Pascual[1,2], Katharina J. Franke[1]
[1] *Fachbereich Physik, Freie Universität Berlin, Arnimallee 14, 14195 Berlin, Germany.*
[2] *CIC nanoGUNE and Ikerbasque, Basque Foundation for Science,*
Tolosa Hiribidea 78, Donostia-San Sebastian 20018, Spain
(Dated: March 23, 2015)

Numerical Deconvolution of dI/dV-spectra

A numerical deconvolution routine has been used to extract the spectral intensities of tip and sample from the dI/dV-data. The STM junction is modeled by a superconducting tip with a single-gap and a two-gap superconductor as the substrate. The current across the tunnel junction can be expressed as [1]:

$$I(V_{\text{bias}}) \approx \int_{-\infty}^{\infty} \mathrm{d}E\ \rho_{\text{tip}}(E,T,\varepsilon)\rho_{\text{sample}}(E+eV_{\text{bias}},T,\varepsilon)\left[f(E,T)-f(E+eV_{\text{bias}},T)\right]|M_{s,t}|^2\ . \tag{S1}$$

Here $\rho(E,T)$ represents the density of states of tip and sample, respectively, and $f(E,T)$ is the Fermi-Dirac distribution describing the occupation of the states. $M_{s,t}$ is the tunnel matrix element between initial and final state, which is assumed to be constant for the small bias voltages in our experiment.

The DoS of the tip is simulated by a conventional BCS DoS. The sample DoS is represented by a weighted sum of two BCS DoS. The weighting factors $A_{1,2}$ and their ratio $R = A_1/A_2$ reflect different tunneling contributions to the two Fermi sheets.

$$\begin{aligned}
\rho_{\text{tip}}(E,T,\varepsilon) &= \mathrm{Re}\left(\frac{E+i\varepsilon}{\sqrt{(E+i\varepsilon)^2-\Delta_{\text{t}}(T)^2}}\right)\ , \\
\rho_{\text{sample}}(E,T,\varepsilon) &= \frac{A_1\,\rho_{\text{s1}}(E)+A_2\,\rho_{\text{s2}}(E)}{A_2} \\
&= R\ \mathrm{Re}\left(\frac{E+i\varepsilon}{\sqrt{(E+i\varepsilon)^2-\Delta_{\text{s1}}(T)^2}}\right)+\mathrm{Re}\left(\frac{E+i\varepsilon}{\sqrt{(E+i\varepsilon)^2-\Delta_{\text{s2}}(T)^2}}\right)\ .
\end{aligned} \tag{S2}$$

The two gap parameters of the sample $\Delta_{\text{s1,2}}$ give the energy of the two sharp BCS resonances in the dI/dV-spectra. The imaginary energy $i\varepsilon$ is included to account for lifetime effects of the quasi-particles [2].

Instrumental broadening leads to a Gaussian-type broadening of the measured signal. Origins for this are the lock-in modulation voltage and radio frequencies in the set-up. To minimize the influence of the modulation voltage, we choose it such that no additional broadening of the measured signal could be detected. In our model, we account for all instrumental broadening by a convolution of the current (Eq. (S1)) with a Gaussian function of width ω. The numerical derivative dI/dV is then calculated and fitted to the experimental dI/dV-curves. The least χ^2-fit yields the set of parameters (T, Δ_{t}, Δ_{s2}, ε, ω, R). Note that $\Delta_{\text{t,s1,s2}}$ are not independent parameters in the fit as the energy position of the dI/dV resonance is the sum $\Delta_{\text{t}}+\Delta_{\text{s}}$. We therefore fix Δ_{s1} in all fits to 1.274 meV.

A set of experimental dI/dV curves on the different surface orientations together with their fits is shown in Fig. S1(a,d,g). The corresponding spectral intensity of the tip and sample contributions are shown in Fig. S1(b,e,h). We accompany these spectra with high-resolution topographies of the three surfaces (Fig. S1(c,f,i)). In (c) and (f) the atomic corrugation of the respective surface is resolved.

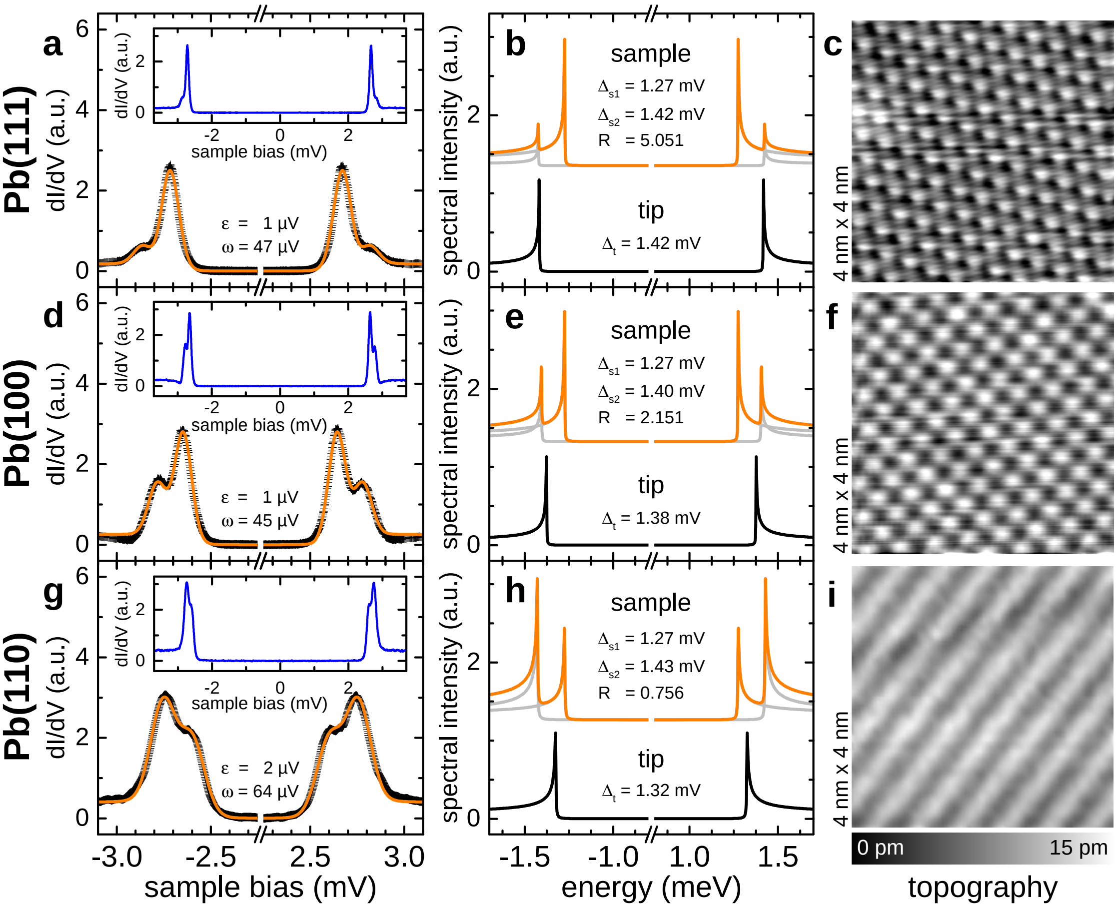

FIG. S1: (a,d,g) dI/dV spectra measured (black, setpoint: 5/4/5 mV, 500/400/400 pA) and simulated (*orange*) of Pb(111), Pb(100) and Pb(110). (b,e,h) The deconvoluted spectral intensities of the sample (*orange*) are a weighted linear-combination of two BCS DoS (*gray*). The tip spectral intensity is shown in black. The fit is referenced to the gap $\Delta_{s1} = 1.274$ meV. All fit parameters are given as inset in the corresponding figure. (c,f,i) High-resolution topographies of the corresponding clean surfaces (setpoint: 50/−50/5 mV, 50/50/400 pA).

Topography of Pb(100)

The Pb(100) single crystal surface was prepared by sputter/anneal cycles as described in the main manuscript. Typical surface topographies is shown in Figure S2. In (b) subsurface Ne inclusions are visible as square-like patterns as described in the main manuscript. The scattering patterns are of different size depending on the depth and size of the Ne inclusion. Most notably, the center of the pattern may appear bright or dark, depending on the quantum-well state, which is formed between the inclusion and the surface. If the energy of the tunneling electrons matches the quantization conditions, the center appears bright; if it is off-resonance, the center appears dark. This does not effect the symmetry of the scattering patterns at the energies of the quasi-particle resonances (compare Fig. S3 and Fig. 2 of the main text). Furthermore, we measured many samples with different impurity concentrations without any noticeable effect on the dI/dV spectra.

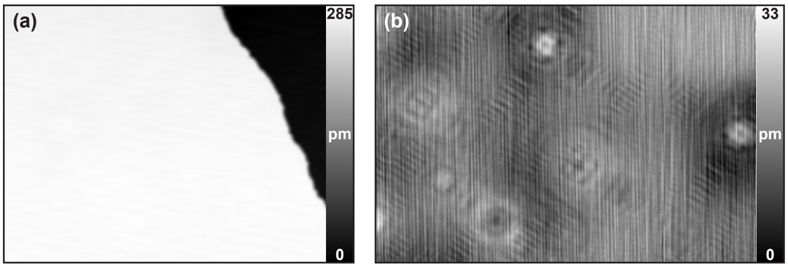

FIG. S2: Topographies of the Pb(100) surface: (a) $80 \times 100\,\mathrm{nm}^2$, feedback parameters: 50 pA; 40 mV; (b) $27 \times 40\,\mathrm{nm}^2$, feedback parameters: 50 pA; 50 mV. Subsurface Ne inclusions are visible in (b) as square-like scattering patterns.

Ne Inclusion

The topography and dI/dV maps in Fig. 2 of the main manuscript show the scattering pattern of a sub-surface Ne inclusion on the Pb(100) surface. In that case the Fermi energy matches the quantization conditions of the quantum-well established between the surface and the inclusion. This yields high intensity contrast in the center of the STM topography and dI/dV maps.

Here, we present data of a different sub-surface inclusion on the same surface (see Fig. S3). The dI/dV spectrum in Fig. S3(h) shows that the quantum-well state lies at $\approx -150\,\mathrm{mV}$, whereas the d$I$/d$V$ signal at E_F corresponds almost to the minimum between two quantum-well states. In the dI/dV maps in (d,e) the center of the scattering pattern is now no longer dominated by the increased intensity due to the quantum well state (as is the case in Fig. 2 of the main manuscript), but shows some signatures due to electron focusing effects from the Fermi sheets as described in the main manuscript. The dI/dV map at QPR1 shows a square-like pattern with the edges along the $\langle 110 \rangle$ directions highlighted by *orange ellipses* in Fig. S3(d). The dI/dV map at QPR2 exhibits areas of high intensity along the $\langle 100 \rangle$ (*shaded purple ellipses*) and $\langle 110 \rangle$ (*open purple ellipses*) directions, respectively (Fig. S3(e)). The intensity along the $\langle 100 \rangle$ directions is stronger than the intensity along the $\langle 110 \rangle$ directions, but with the latter being wider. Long-ranging oscillations as indicated by the *purple lines* are also present. Note that there are additionally long-range oscillations visible, which originate from nearby scatterers. Comparison to the scattering patterns presented in the main manuscript evidences the same characteristic features. Small deviations, as, *e.g.*, the different resolution, may be influenced by the size and depth of the Ne inclusion.

Tip Preparation and its Influence on dI/dV-Spectra

The main advantage of the use of a superconducting tip is the increased energy resolution beyond the temperature broadening of $\approx 360\,\mu\mathrm{eV}$ at 1.2 K of the Fermi-Dirac distribution [3]. To obtain a superconducting tip, we indent the tip into the Pb sample while applying a high voltage (100 V). At sufficiently thick coating the tip behaves as a "dirty" superconductor, in which the DoS can be described by a single gap due to the amorphous nature of the material [4]. The gap width strongly depends on the thickness of the coating. To assure bulk-like gap width, we first record

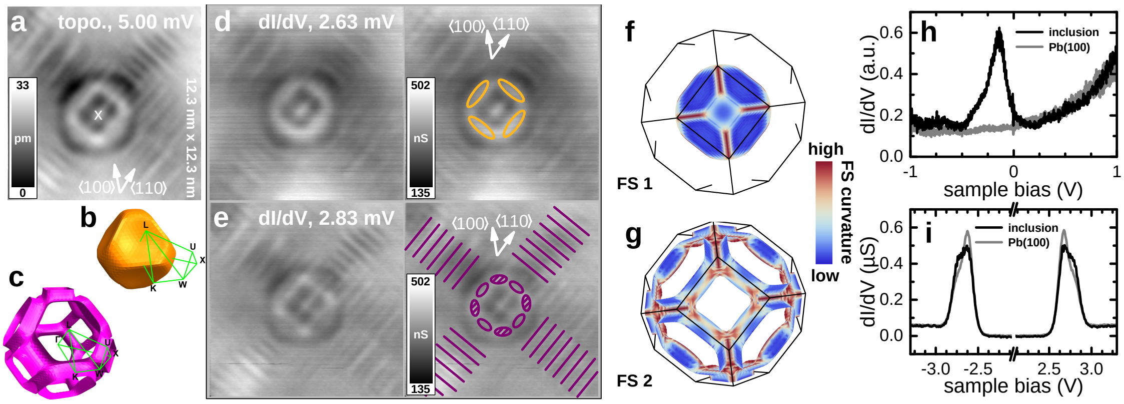

FIG. S3: (a–d) Subsurface Ne inclusion. High-resolution topography (a) on an atomically flat Pb(100) terrace (setpoint: 5 mV, 50 pA). The constant-height dI/dV spectrum (h) shows the maximum of a first quantum well state at ≈ −150 mV and the onset of the next quantum well state above 1 V (3 mV$_{\mathrm{rms}}$, 912 Hz, setpoint: 1 V, 1 nA). Constant-height dI/dV maps at 2.63 mV (d), and 2.83 mV (e), respectively (15 µV$_{\mathrm{rms}}$, 912 Hz, setpoint: 5 mV, 250 pA). In the duplicated maps, prominent scattering signatures are highlighted as guide for the eye. At E_{F} the quantization conditions are close to off–resonance (see dI/dV spectrum in (h)) and the center of the scattering pattern therefore appears as a depression in topography (a). (b,c,f,g) 3D-models of the two FSs of lead from Ref. 6. The curvature of the FS is color-coded onto the 3D model in (f) and (g), which are oriented according to the crystalline directions in (a,d,e). *Dark blue* and *dark red* correspond to low and high curvature, respectively. (i) constant-height dI/dV spectrum on the center of the scattering pattern (*black curve*, location marked by a cross in (a)) and on the clean surface away from the impurity (*grey*) (5 mV, 250 pA, 15 µV$_{\mathrm{rms}}$, 912 Hz).

dI/dV-spectra at 4.8 K. These exhibit additional resonances at $eV = \pm|\Delta_{\mathrm{s}} - \Delta_{\mathrm{t}}|$ due to the thermal occupation of the DoS. For a tip-coating with a gap parameter similar to the bulk superconductor, these *thermal* resonances appear at zero bias in dI/dV. This procedure is reliable if the junction resistance $R \gtrsim 20\,\mathrm{M\Omega}$, as Josephson tunneling and Andreev reflections are negligible in this regime [5].

Nevertheless small variations in the tip's gap parameter can not be resolved by this technique due to the limited energy resolution at 4.8 K. At 1.2 K, we then observe small variations of the gap parameter measured with different tips. Note that these variations only result in an overall shift of the resonances in the dI/dV, but do not affect their separation associated to the different gaps in the surface.

Magnetic field dependent dI/dV-spectra

A magnetic field is known to suppress superconductivity in type I superconductors above a critical field strength. Here, we present excitation spectra measured with a magnetic field of differing strength applied perpendicular to the surface (Fig. S4). The dI/dV spectra were acquired with a Pb-covered tip on a clean Pb(110) surface. At 0 T the dI/dV spectrum shows a gap with a width of ≈ 4Δ, which is due to the convolution of the superconducting DoS of tip and sample. The observed double resonance at the gap edge is linked to the two-band superconductivity in the sample as discussed in the main manuscript. The spectrum recorded at 100 mT exhibits a gap with a width of 2Δ and no signs of splitting of the BCS-like peaks. In this field, the superconducting state of the single crystal sample is quenched as expected for Pb (with its critical field strength of 80 mT). The shape of the tip favors an increased H_{c} compared to bulk Pb. Notably, the energy resolution is now limited to ≈360 µeV due to Fermi-Dirac broadening in the metallic sample DoS. At 200 mT additional broadening due to decoherence in the superconducting grain of the tip apex is observed. At a field of 500 mT, superconductivity in the tip is finally quenched. We note that the critical field of the tip varies significantly for different tips and depends on its microscopic structure.

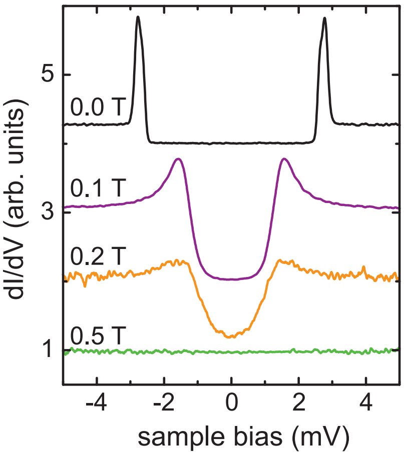

FIG. S4: Magnetic-field dependence of dI/dV spectra measured on Pb(110) with a Pb-cover tip at 1.2 K. Setpoint parameters: 550 pA, 10 mV; modulation amplitude: 20 µV$_{\mathrm{rms}}$ (0 T, 0.2 T and 0.5 T) or 50 µV$_{\mathrm{rms}}$ (0.1 T).

[1] J. Tersoff and D. R. Hamann, Phys. Rev. B **31**, 805 (1985).
[2] R. C. Dynes, V. Narayanamurti, and J. P. Garno, Phys. Rev. Lett. **41**, 1509 (1978).
[3] K. J. Franke, G. Schulze, and J. I. Pascual, Science **332**, 940 (2011).
[4] P. W. Anderson, Phys. Chem. Solids **11**, 26 (1959).
[5] M. Ternes, W.-D. Schneider, J.-C. Cuevas, C. P. Lutz, C. F. Hirjibehedin, and A. J. Heinrich, Phys. Rev. B **74**, 132501 (2006).
[6] T.-S. Choy, J. Naset, J. Chen, S. Hershfield, and C. Stanton, Bull. Am. Phys. Soc., 45(1):L36 42, (2000).

B.3 Physical Review Letters 115, 087001 (2015)

Michael Ruby, Falko Pientka, Yang Peng, Felix von Oppen,
Benjamin W. Heinrich, and Katharina J. Franke

Tunneling Processes into Localized Subgap States in Superconductors

doi:10.1103/PhysRevLett.115.087001

PRL **115,** 087001 (2015) PHYSICAL REVIEW LETTERS week ending 21 AUGUST 2015

Tunneling Processes into Localized Subgap States in Superconductors

Michael Ruby,[1] Falko Pientka,[2] Yang Peng,[2] Felix von Oppen,[2] Benjamin W. Heinrich,[1] and Katharina J. Franke[1]
[1]*Fachbereich Physik, Freie Universität Berlin, 14195 Berlin, Germany*
[2]*Dahlem Center for Complex Quantum Systems and Fachbereich Physik, Freie Universität Berlin, 14195 Berlin, Germany*

(Received 27 February 2015; published 20 August 2015)

We combine scanning-tunneling-spectroscopy experiments probing magnetic impurities on a superconducting surface with a theoretical analysis of the tunneling processes between (superconducting) tip and substrate. We show that the current through impurity-induced Shiba bound states is carried by single-electron tunneling at large tip-substrate distances and Andreev reflections at smaller distances. The single-electron current requires relaxation processes, allowing us to extract information on quasiparticle transitions and lifetimes.

DOI: 10.1103/PhysRevLett.115.087001 PACS numbers: 74.50.+r, 05.60.Gg, 74.25.F-, 74.55.+v

Introduction.—Impurity-induced subgap states provide a fruitful window into conventional and unconventional superconductors [1–3]. The Yu-Shiba-Rusinov states [4–6] bound by magnetic impurities in conventional s-wave superconductors are a simple model system for nonmagnetic impurity resonances in unconventional superconductors, probe the competition between superconducting and Kondo correlations [7–9], and might provide a platform for engineering topological superconducting phases with Majorana end states [10–13].

In scanning-tunneling spectroscopy, Shiba states induce resonances which occur symmetrically at positive- and negative-bias voltages [2,3,7,14]. Given their subgap nature, it is natural to describe the current into Shiba states as carried by Andreev processes. These processes transfer a Cooper pair into the condensate and are resonantly enhanced by the Shiba state [15–18]. Nevertheless, scanning-tunneling microscopy (STM) experiments on Shiba states are typically analyzed in terms of the tunneling density of states which is appropriate for single-electron tunneling [1,19,20]. This allows one to understand the observed asymmetry in height between the positive- and negative-bias peaks while Andreev processes would necessarily be symmetric in bias (for normal-state tips) [18].

Here, we combine scanning-tunneling microscopy and spectroscopy of Shiba states using superconducting tips with a comprehensive theoretical analysis to elucidate the nature of the tunneling processes. We show that both single-electron and Andreev tunneling contribute in experiments and explain the observed inversion of peak-height asymmetry as a function of tunneling rates. Our analysis shows that STM experiments on Shiba states provide access to quasiparticle relaxation rates in superconductors, complementing recent work on superconducting quantum dots [21–23] and Josephson junctions [24–27].

Experiments.—We have performed STM experiments probing Mn adatoms on a Pb(111) single crystal surface. The experiments were carried out with a SPECS JT-STM at the base temperature of 1.2 K as well as at 4.8 K. The Pb single crystal surface was cleaned by repeated sputter-anneal cycles until a clean, atomically flat, and superconducting surface was obtained (critical temperature $T_c = 7.2$ K and gap $\Delta = 1.35$ meV at 1.2 K). Mn adatoms were evaporated onto the clean sample at a temperature below 10 K, resulting in a density of 30 atoms per 100×100 nm^2 (see the Supplemental Material [28]). Our STM experiments were carried out with a Pb-covered, superconducting tip (see Ref. [7] for the preparation procedure) which improves resolution far beyond the Fermi-Dirac limit [30,31].

Figure 1 shows spectra of the differential conductance dI/dV as a function of sample bias V, acquired at various tip-sample distances and thus tunneling strengths with the tip placed above a Mn adatom. All spectra share the same characteristic peaks [32] but their intensities (normalized to the normal-state conductance) depend strongly on the tunneling strength and the sign of the bias voltage.

The peaks in the dI/dV spectra appear at thresholds for various fundamental tunneling processes between a superconducting tip and a superconducting substrate with a magnetic adatom. (i) Single electrons can tunnel when the negative-energy quasiparticle continuum of the tip overlaps with the positive-energy continuum of the substrate (or vice versa). This requires a threshold voltage $eV = \pm 2\Delta$. (ii) Thermally excited quasiparticles (holes) in the positive- (negative-) energy quasiparticle continuum induce a single-particle current even near zero bias. (iii) With a Shiba state of energy ϵ_0, a single-particle current flows when the negative-energy continuum of the tip overlaps with the Shiba state, or the positive-energy continuum with the symmetric energy $-\epsilon_0$. These processes have threshold biases $eV = \pm(\Delta + \epsilon_0)$. (iv) Because of thermal occupation, a single-electron current can also flow when the positive-energy continuum overlaps with the Shiba state (and symmetrically when the negative-energy continuum overlaps with $-\epsilon_0$). This requires a threshold bias

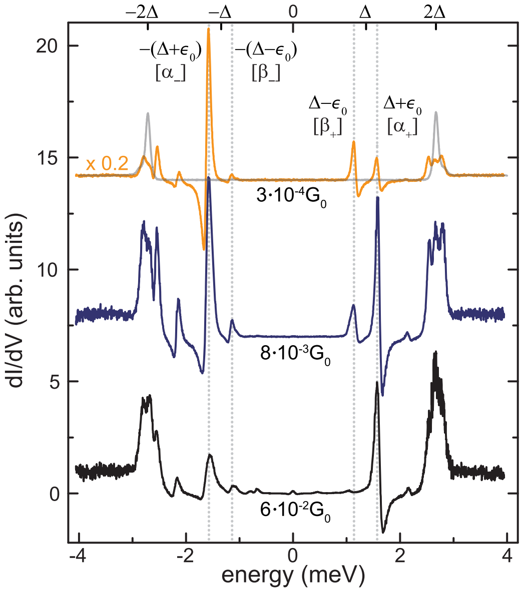

FIG. 1 (color online). dI/dV spectra measured on an isolated Mn adatom on Pb(111) for increasing tunneling strength from top to bottom (recorded with a lock-in modulation amplitude of 15 μV_{rms} at a frequency of 912 Hz). Spectra are normalized to the "normal-state" conductance measured at 4 meV (i.e., well outside the superconducting gap) in units of $G_0 = 2e^2/h$, offset for clarity and scaled when indicated for better visibility. The distance to the closest neighboring Mn atom was larger than 5 nm. A spectrum acquired above the clean Pb(111) surface overlays the smallest-conductance trace (top curve) for comparison. The four peaks originating from the deepest Shiba level are marked by dashed lines at $e|V| = \pm(\Delta \pm \epsilon_0)$.

$eV = \pm(\Delta - \epsilon_0)$. (v) At $e|V| < 2\Delta$, an electron from, say, the tip can be reflected as a hole, transferring a Cooper pair. As all tunneling electrons and holes gain an energy eV, (multiple) Andreev processes between the quasiparticle continua have thresholds $eV = \pm 2\Delta/n$, with $n = 2, 3, \ldots$. Andreev processes require two or more particles to cross the tunnel barrier and thus become relevant for strong tunnel coupling only [33]. (vi) Shiba states induce additional *resonant* Andreev processes which become relevant at much lower tunneling rates. An electron from the negative-energy continuum of the tip can virtually tunnel into the Shiba state, reflect as a hole, and resonantly transfer a Cooper pair into the condensate of the substrate. Together with a similar process at reverse bias, this leads to thresholds at $eV = \pm(\Delta + \epsilon_0)$ which *coincide* with those for the single-electron processes. The principal tunneling processes involving the Shiba states are sketched in Fig. 2.

There is an important difference between the single-electron and resonant Andreev processes [18]. Single-electron processes change the occupation of the Shiba state, while Andreev processes merely transfer Cooper

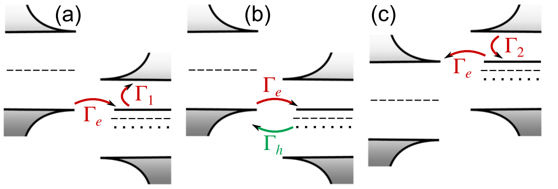

FIG. 2 (color online). Principal tunneling processes involving a Shiba state (solid line) within the superconducting gap (enclosed by BCS quasiparticle peaks). The chemical potential is represented by a dashed line. (a) Single-electron tunneling from tip to substrate [rate $\Gamma_e(\omega)$] with subsequent relaxation from the Shiba state to the quasiparticle continuum (rate Γ_1). (b) Andreev process transferring a Cooper pair to the substrate by electron and hole tunneling [with rates $\Gamma_e(\omega)$ and $\Gamma_h(\omega)$, respectively]. The processes in (a) and (b) both contribute near the threshold $eV = \Delta + \epsilon_0$. (c) Single-electron tunneling from substrate to tip [with rate $\Gamma_e(\omega)$] after occupation of the Shiba state by the relaxation of a thermal quasiparticle (with rate Γ_2), contributing to the thermal peak at $eV = -(\Delta - \epsilon_0)$. The current at the other two thresholds $eV = -(\Delta + \epsilon_0)$ and $eV = \Delta - \epsilon_0$ is carried by analogous hole processes (see the Supplemental Material [28]).

pairs into the condensate. Thus, a continuous current flow by single-electron processes requires relaxation processes which empty the Shiba state after it is occupied from the tip (or occupy the empty Shiba state); see Fig. 2. At finite temperature, a quasiparticle in the Shiba state can be excited to the continuum by absorption of a phonon or a photon (with rate Γ_1). Conversely, a thermally excited quasiparticle can relax into the Shiba state by emission (with rate Γ_2).

The observed peaks in the dI/dV spectra can now be correlated with Shiba states of energy $\simeq 0.22$, $\simeq 0.77$, and $\simeq 1.18$ meV, respectively. The multiple Shiba states may reflect different angular-momentum channels or spin states $S > 1/2$ [14,34,35]. To analyze the tunneling processes, we focus on the most intense Shiba state at $\epsilon_0 \simeq 0.22$ meV. This state not only leads to the two *main* peaks at $eV = \pm(\Delta + \epsilon_0)$ (with peak height $\alpha_\pm$), but also to two pronounced *thermal* peaks at $eV = \pm(\Delta - \epsilon_0)$ (with peak height $\beta_\pm$). As it is the deepest state, its theoretical interpretation turns out to be least affected by the presence of the other Shiba states.

The heights of the peaks associated with this Shiba state are plotted in Fig. 3(a) over several decades in normal-state tunneling conductance. We draw attention to two important features of these data. First, the peak heights vary linearly over a wide region before turning sublinear at larger tunneling rates. Second, the asymmetry in the peak heights $\alpha_\pm$ between positive and negative biases inverts as a function of tunneling strength: At small tunneling rates, $\alpha_+ < \alpha_-$, while at large tunneling rates, $\alpha_+ > \alpha_-$. It is also evident that the inversion of the peak heights occurs at the crossover between the linear and sublinear regimes.

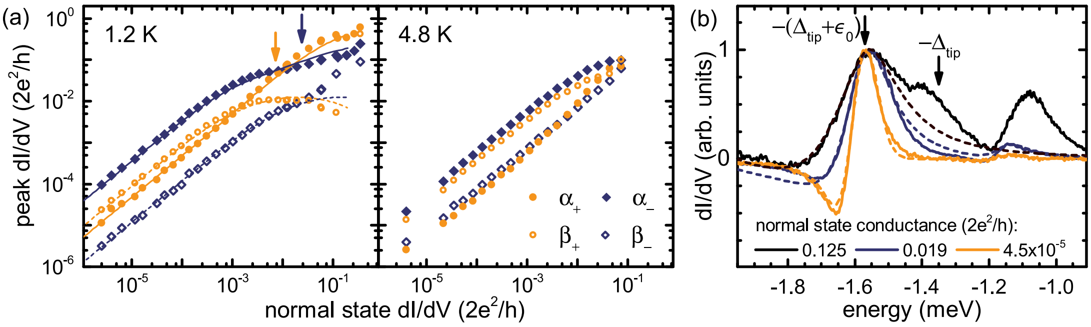

FIG. 3 (color online). (a) Peak heights $\alpha_\pm$ and $\beta_\pm$ of the four resonances associated with the deepest Shiba level (marked by dashed lines in Fig. 1) as a function of normal-state conductance at $T = 1.2$ K (left panel) and $T = 4.8$ K (right panel). The full (dashed) lines are fits to Eqs. (1) and (2) for the main (thermal) peaks. The crossover points between single-electron and Andreev contributions to $\alpha_\pm$ are indicated by arrows. (b) Experimental dI/dV traces of the Shiba peak near $eV = -(\Delta + \epsilon_0) \simeq -1.57$ meV at different junction conductances (solid lines). The spectra are normalized to the peak maximum. The dashed lines are theoretical fits of the Shiba peaks excluding multiple Andreev reflections.

Theoretical analysis.—It is often assumed [1] that the peak heights at positive and negative biases measure the electron and hole components u and v of the Shiba wave function. The observed inversion of peak heights implies that this cannot hold, in general. To gain further insight, we calculate the subgap current theoretically by a standard Keldysh calculation [36–38] (see the Supplemental Material for details [28]). Here, we focus on the physics underlying the results. Our calculation includes single-electron and Andreev processes involving the Shiba state as well as phenomenological rates Γ_1 and Γ_2 for relaxation processes between the Shiba state and the quasiparticle continuum. We neglect the nonresonant Andreev reflections at the superconducting tip (and thus multiple Andreev reflections [39]), which is justified except in the regime of very strong tunneling. With this approximation, the tunneling current becomes a sum of single-particle and Andreev currents, $I = I^s + I^a$, with

$$I^s = e\int \frac{d\omega}{2\pi\hbar}\left\{\frac{\Gamma_1[\Gamma_e n_F(\omega_-) - \Gamma_h n_F(\omega_+)]}{(\omega-\epsilon_0)^2 + (\Gamma/2)^2} - \frac{\Gamma_2\{\Gamma_e[1-n_F(\omega_-)] - \Gamma_h[1-n_F(\omega_+)]\}}{(\omega-\epsilon_0)^2+(\Gamma/2)^2}\right\}, \tag{1}$$

$$I^a = 2e\int \frac{d\omega}{2\pi\hbar}\frac{\Gamma_h\Gamma_e[n_F(\omega_-) - n_F(\omega_+)]}{(\omega-\epsilon_0)^2+(\Gamma/2)^2}. \tag{2}$$

Here, the Fermi functions n_F are evaluated at $\omega_\pm = \omega \pm eV$ and $\Gamma = \Gamma_e + \Gamma_h + \Gamma_1 + \Gamma_2$.

The expressions for I^s and I^a can be understood in terms of the basic processes discussed above. The Andreev current I^a involves tunneling of an electron, described by $\Gamma_e(\omega) = 2\pi u^2 \rho(\omega - eV)t^2$, and a hole, described by $\Gamma_h(\omega) = 2\pi v^2\rho(\omega + eV)t^2$. Here, t is the amplitude for tunneling between tip and substrate. The rates Γ_e and Γ_h are strongly ω dependent through the tip's BCS density of states $\rho(\omega)$. The denominator in Eq. (2) reflects the intermediate virtual occupation of the Shiba state. It includes the rates Γ_1 for depopulating the Shiba state by excitation to the continuum and Γ_2 for occupying the Shiba state by a thermally excited quasiparticle. The latter processes are assumed to be ω independent. The four contributions to the single-particle current I^s directly correspond to the peaks α_+ [term $\propto \Gamma_1\Gamma_e$; see Fig. 2(a)], α_- (term $\propto \Gamma_1\Gamma_h$), β_- [term $\propto \Gamma_2\Gamma_e$; see Fig. 2(c)], and β_+ (term $\propto \Gamma_2\Gamma_h$).

Equations (1) and (2) provide the following basic picture consistent with the data in Fig. 3(a): At weak tunneling, the relaxation rates Γ_1 and Γ_2 are faster than the tip-substrate tunneling. Once an electron tunnels into the Shiba state from the tip, it is rapidly excited to the quasiparticle continuum. In this regime, the tunnel current is dominated by the single-electron current I^s which is proportional to t^2, and thus to the normal-state conductance. The Andreev current I^a is a small correction scaling as t^4. This explains the wide linear regime in Fig. 3(a). At stronger tunneling, the tunneling rates become comparable to and eventually larger than the relaxation rates Γ_1 and Γ_2. Here, the t dependence of the broadening Γ leads to a sublinear or even a decreasing dependence of the peak heights on the normal-state conductance. As the relaxation processes are thermally activated, the crossover point between the linear and the sublinear regime is strongly temperature dependent, moving to lower normal-state conductances for lower temperatures. This is consistent with a comparison between the two panels of Fig. 3(a).

Linear regime.—This picture is substantiated by quantitatively analyzing the linear regime. At weak tunneling, the broadening is dominated by quasiparticle relaxation, $\Gamma \simeq \Gamma_1$ (for $\Gamma_1 \gg \Gamma_2$, i.e., $\epsilon_0 \gg T$). Then, Eq. (1) yields

$$\alpha_+ \sim \frac{2e^2}{h}\frac{\gamma_e\sqrt{\Delta}}{(\Gamma_1)^{3/2}}; \qquad \beta_- = \alpha_+\frac{\Gamma_2}{\Gamma_1} \tag{3}$$

for the peak heights [28]. Here, we introduced the normal-state electron (hole) tunneling rate $\gamma_e = 2\pi t^2\nu_0 u^2$ ($\gamma_h = 2\pi t^2\nu_0 v^2$), where ν_0 is the normal-state density of states of the tip. The expressions for α_- and β_+ simply differ by the substitution $u\leftrightarrow v$ (or $\gamma_e\leftrightarrow\gamma_h$). Thus, in this regime, the peak height is indeed a measure of the Shiba wave function at the tip position. From the data in Fig. 3(a), we extract $\alpha_+/\alpha_- = (u/v)^2 \approx 0.13$.

All four peaks are related by the relation $\alpha_+\beta_+ = \alpha_-\beta_-$. This is readily checked against the data in Fig. 3(a) and indeed, we find that this identity is well satisfied in the linear regime [28]. Moreover, the thermal and main peaks in Eq. (3) differ only by a ratio of relaxation rates, $\alpha_+/\beta_- = \Gamma_1/\Gamma_2 = \exp(\epsilon_0/T)$. Here, the last equality follows from detailed balance. This is in excellent agreement for the data at $T = 4.8$ K. At $T = 1.2$ K, we extract a slightly higher temperature of $T = 1.6$ K from the ratio of peak heights. Still, these considerations point to a relaxation process involving thermal activation rather than the quasiparticle bath suggested in Ref. [18].

Regime of strong tunneling.—At stronger tunneling, the broadening is dominated by tunneling, $\Gamma \simeq \Gamma_e + \Gamma_h$. Because of this broadening, the single-particle conductance reaches a maximum and eventually decreases with tunneling strength. As a result, the thermal peaks $\beta_\pm$ should exhibit a maximum vs normal-state conductance. The situation is different for the main peaks $\alpha_\pm$ with their additional Andreev contribution, which keeps increasing and eventually dominates the peak magnitude. Sufficiently far into this regime, Eqs. (1) and (2) yield

$$\alpha_+ \sim (2e^2/h)[\gamma_h\sqrt{\Delta/\epsilon_0}/(\gamma_e\sqrt{\Delta})^{2/3}], \tag{4}$$

$$\beta_- \sim (2e^2/h)[\Gamma_2/(\gamma_e\sqrt{\Delta})^{2/3}], \tag{5}$$

as well as α_- and β_+, which differ again by $u\leftrightarrow v$. The main peaks $\alpha_\pm$ keep increasing with tunneling $\gamma_{e,h}$, albeit with a sublinear dependence. The strong voltage dependence of the tunneling-induced broadening leads to a change in the line shape at strong tunneling. Indeed, we observe a vanishing of the negative differential conductance dip [see Fig. 3(b)] signaling the transition to the strong-tunneling regime [28].

Unlike for normal-metal tips [18,28], the Andreev contribution to the main peaks $\alpha_\pm$ is asymmetric for a superconducting tip, but with the asymmetry reversed relative to single-electron tunneling. While we have $\alpha_+/\alpha_- = (u/v)^2$ in the linear regime, Eq. (4) predicts $\alpha_+/\alpha_- = (v/u)^{10/3}$ in the Andreev-dominated regime. Indeed, an inversion of the peak heights $\alpha_\pm$ is seen in Fig. 3(a), as pointed out above.

Equation (5) predicts that the thermal peaks also invert, from $\beta_-/\beta_+ = (u/v)^2$ in the linear regime to $\beta_-/\beta_+ = (v/u)^{4/3}$ in the sublinear regime. This inversion is consistent with the data in Fig. 3(a). In addition, theory predicts that the thermal peaks will assume a maximum as a function of normal-state conductance. We observe such a maximum only for β_+. For β_-, the peak is expected to occur only at rather large normal-state conductance where our approximations of neglecting multiple Andreev reflections and a peak width smaller than ϵ_0 break down.

To further substantiate our analysis, we have used Eqs. (1) and (2) to fit all four peaks $\alpha_\pm$ and $\beta_\pm$ over the entire range of tunneling strengths; see Fig. 3(a) in the Supplemental Material [28]. There is excellent agreement between theory and experiment. We attribute the deviations for β_- at large normal-state conductance to additional contributions from multiple Andreev reflections. We can also extract the normal-state conductance at which the Andreev and single-particle contributions to the main peaks become comparable; see the arrows in Fig. 3(a). (Note that this is distinct from the crossover between linear and sublinear dependence.) For α_+, this happens when $2\Gamma_h(2\epsilon_0) \sim \Gamma_1$, and for α_-, when $2\Gamma_e(2\epsilon_0) \sim \Gamma_1$. As $v^2 > u^2$, the Andreev contribution sets in considerably earlier for α_+ than for α_-.

Relaxation rates.—At $T = 4.8$ K, the relaxation rate can be extracted directly from the peak width, yielding $\Gamma_1 \simeq 6$ ps. In contrast, the linewidth is resolution limited at $T = 1.2$ K, masking the broadening due to quasiparticle relaxation. We can still extract the relaxation rate by relying on the current. In the sublinear regime, the thermal peak β_+ contributes a current $I \sim e\Gamma_2/\hbar$ [28]. Moreover, Eq. (3) predicts $\Gamma_1 = (\alpha_+/\beta_-)\Gamma_2$ in the linear regime. Thus, we can extract both relaxation rates directly from the experimental data. This yields (to about a factor of 2) $\hbar/\Gamma_1 \simeq 0.2$ ns and $\hbar/\Gamma_2 \simeq 0.6$ ns.

For magnetic impurities binding a single Shiba state, relaxation relies on quasiparticle excitation to the continuum. This yields a ratio of relaxation rates at the two experimental temperatures of order $\sim 10^4$. We can account for the apparent discrepancy with our observations by including the second Shiba state at energy $\epsilon_1 \simeq 0.77$ meV. Then, relaxation can occur via the formation of Cooper pairs from quasiparticles in the first two Shiba states. This process is limited by the thermal occupation of the second Shiba state and thus involves a much smaller activation energy. Such processes are allowed even for Shiba states with equal spin due to the strong spin-orbit coupling of Pb. An analysis in terms of rate equations is quantitatively consistent with our observations [28].

Conclusions.—We show that STM experiments on subgap states in superconductors probe both single-electron and Andreev tunneling. We emphasize that such experiments are particularly fruitful when performed with superconducting tips. In this case, thermal smearing can be neglected and the temperature dependence of the current arises entirely from activated quasiparticle relaxation processes. Moreover, the additional thermal peaks facilitate the analysis and provide access to the relaxation rates. We find that at weak tip-substrate tunneling, the current is dominated by single-electron tunneling and is linear in the normal-state conductance. This regime can be used to map out the bound-state wave function. At stronger tip-substrate tunneling, the dependence on the normal-state conductance becomes sublinear. While the dependence on the Shiba wave function becomes more involved, this regime provides access to pertinent quasiparticle relaxation rates involving the subgap states. Specifically, we can extract the rates for quasiparticle relaxation into and out of the bound state. The present experiment was restricted to two different temperatures. To further probe the microscopic nature of the relaxation processes, it would be rewarding to perform more systematic experiments as a function of temperature.

We thank Piet Brouwer and Leonid Glazman for discussions, and we acknowledge financial support by the Deutsche Forschungsgemeinschaft through the collaborative research center SFB 658 and Grant No. FR2726/4 (K. F.) as well as research priority programmes SPP 1285 and SPP 1666 (F. v. O.), by a Consolidator Grant from the European Research Council “NanoSpin” (K. F.), and by the Helmholtz Virtual Institute “New States of Matter and Their Excitations” (F. v. O.).

[1] A. V. Balatsky, I. Vekhter, and J.-X. Zhu, Rev. Mod. Phys. **78**, 373 (2006).

[2] A. Yazdani, B. A. Jones, C. P. Lutz, M. F. Crommie, and D. M. Eigler, Science **275**, 1767 (1997).

[3] A. Yazdani, C. M. Howald, C. P. Lutz, A. Kapitulnik, and D. M. Eigler, Phys. Rev. Lett. **83**, 176 (1999).

[4] L. Yu, Acta Phys. Sin. **21**, 75 (1965).

[5] H. Shiba, Prog. Theor. Phys. **40**, 435 (1968).

[6] A. I. Rusinov, Pis’ma Zh. Eksp. Teor. Fiz. **9**, 146 (1968) [JETP Lett. **9**, 85 (1969)].

[7] K. J. Franke, G. Schulze, and J. I. Pascual, Science **332**, 940 (2011).

[8] J. Bauer, J. I. Pascual, and K. J. Franke, Phys. Rev. B **87**, 075125 (2013).

[9] N. Y. Yao, C. P. Moca, I. Weymann, J. D. Sau, M. D. Lukin, E. A. Demler, and G. Zarand., Phys. Rev. B **90**, 241108(R) (2014).

[10] S. Nadj-Perge, I. K. Drozdov, B. A. Bernevig, and A. Yazdani, Phys. Rev. B **88**, 020407(R) (2013).

[11] F. Pientka, L. I. Glazman, and F. von Oppen, Phys. Rev. B **88**, 155420 (2013).

[12] J. Klinovaja, P. Stano, A. Yazdani, and D. Loss, Phys. Rev. Lett. **111**, 186805 (2013).

[13] S. Nadj-Perge, I. K. Drozdov, J. Li, H. Chen, S. Jeon, J. Seo, A. H. MacDonald, B. A. Bernevig, and A. Yazdani, Science **346**, 602 (2014).

[14] S.-H. Ji, T. Zhang, Y.-S. Fu, X. Chen, X.-C. Ma, J. Li, W.-H. Duan, J.-F. Jia, and Q.-K. Xue, Phys. Rev. Lett. **100**, 226801 (2008).

[15] A. Levy Yeyati, J. C. Cuevas, A. López-Dávalos, and A. Martín-Rodero, Phys. Rev. B **55**, R6137(R) (1997).

[16] B. M. Andersen, K. Flensberg, V. Koerting, and J. Paaske, Phys. Rev. Lett. **107**, 256802 (2011).

[17] P. A. Ioselevich and M. V. Feigelman, New J. Phys. **15**, 055011 (2013).

[18] I. Martin and D. Mozyrsky, Phys. Rev. B **90**, 100508 (2014).

[19] M. E. Flatté and J. M. Byers, Phys. Rev. Lett. **78**, 3761 (1997).

[20] M. I. Salkola, A. V. Balatsky, and J. R. Schrieffer, Phys. Rev. B **55**, 12648 (1997).

[21] M. R. Buitelaar, T. Nussbaumer, and C. Schönenberger, Phys. Rev. Lett. **89**, 256801 (2002).

[22] S. De Franceschi, L. Kouwenhoven, C. Schönenberger, and W. Wernsdorfer, Nat. Nanotechnol. **5**, 703 (2010).

[23] A. P. Higginbotham, S. M. Albrecht, G. Kirsanskas, W. Chang, F. Kuemmeth, P. Krogstrup, T. S. Jespersen, J. Nygard, K. Flensberg, and C. M. Marcus, arXiv:1501.05155.

[24] L. Bretheau, C. Ö. Girit, H. Pothier, D. Esteve, and C. Urbina, Nature (London) **499**, 312 (2013).

[25] F. Kos, S. E. Nigg, and L. I. Glazman, Phys. Rev. B **87**, 174521 (2013).

[26] D. G. Olivares, A. Levy Yeyati, L. Bretheau, C. Ö. Girit, H. Pothier, and C. Urbina, Phys. Rev. B **89**, 104504 (2014).

[27] A. G. Kozorezov, A. A. Golubov, J. K. Wigmore, D. Martin, P. Verhoeve, R. A. Hijmering, and I. Jerjen, Phys. Rev. B **78**, 174501 (2008).

[28] See Supplemental Material at http://link.aps.org/supplemental/10.1103/PhysRevLett.115.087001, which includes Ref. [29], for more experimental data, a self-contained description of the theoretical analysis, and details of the theoretical interpretation of the experimental data.

[29] D. A. Ivanov and M. V. Feigel’man, JETP Lett. **68**, 890 (1998).

[30] B. W. Heinrich, L. Braun, J. I. Pascual, and K. J. Franke, Nat. Phys. **9**, 765 (2013).

[31] M. Ruby, B. W. Heinrich, J. I. Pascual, and K. J. Franke, Phys. Rev. Lett. **114**, 157001 (2015).

[32] At small tip-sample distances, weak additional resonances appear due to dc Josephson currents and multiple Andreev reflections.

[33] M. Ternes, W.-D. Schneider, J. C. Cuevas, C. P. Lutz, C. F. Hirjibehedin, and A. J. Heinrich, Phys. Rev. B **74**, 132501 (2006).

[34] C. P. Moca, E. Demler, B. Jankó, and G. Zaránd, Phys. Rev. B **77**, 174516 (2008).

[35] R. Zitko, O. Bodensiek, and T. Pruschke, Phys. Rev. B **83**, 054512 (2011).

[36] H. Haug and A.-P. Jauho, *Quantum Kinetics in Transport and Optics of Semiconductors* (Springer, New York, 2008).

[37] J. C. Cuevas, A. Martín-Rodero, and A. Levy Yeyati, Phys. Rev. B **54**, 7366 (1996).

[38] C. Berthod and T. Giamarchi, Phys. Rev. B **84**, 155414 (2011).

[39] D. Averin and A. Bardas, Phys. Rev. Lett. **75**, 1831 (1995).

Supplementary Material
Tunneling processes into localized subgap states in superconductors

Michael Ruby,[1] Falko Pientka,[2] Yang Peng,[2] Felix von Oppen,[2] Benjamin W. Heinrich,[1] and Katharina J. Franke[1]
[1]*Fachbereich Physik, Freie Universität Berlin, 14195 Berlin, Germany*
[2]*Dahlem Center for Complex Quantum Systems and Fachbereich Physik, Freie Universität Berlin, 14195 Berlin, Germany*

I. EXPERIMENTAL DETAILS

A. Topography of Mn adatoms on Pb(111)

The Pb(111) surface was cleaned by Ne^+ sputtering, followed by annealing to $T = 430\,\mathrm{K}$. This yields an atomically clean surface with terraces of several nm width, which are separated by mono-atomic steps [see Fig. S1(a)]. Residual Ne atoms from sputtering form nonmagnetic nano-cavities below the surface, which appear as hexagonal protrusions or depletions of different sizes in topography [1]. They do not show any signatures of subgap resonances.

Manganese atoms were deposited on the clean Pb(111) sample inside the STM at a temperature below 10 K. All Mn adatoms have the same apparent height after the evaporation. By contacting the adatom with the tip at a bias of 5 mV, we can induce a change in the adsorption configuration. The resulting species has a larger apparent height [Fig. S1(b) and (c)]. The manipulation is reversible: contact formation at a bias of $-180\,\mathrm{mV}$ results in the initial apparent height. After back-manipulation the adatom is shifted laterally with respect to the initial position [see line-profiles in Fig. S1(c)]. Thus, the manipulation controllably changes the adsorption site of the adatom. We took care that the absolute tip height did not change during the manipulation to rule out a change of the tip apex.

Both configurations show distinct $\mathrm{d}I/\mathrm{d}V$ spectra [Fig. S1(d)]. The initial adsorption site has been investigated by Ji *et al.* [2], showing multiple Shiba states. Our spectra on this configuration show the same characteristic features when considering an improved energy resolution [Fig. S1(d,i)]. In the main manuscript we focus on the manipulated species (ii), because it is stable upon tip approach at low bias. It thus allows the investigation of $\mathrm{d}I/\mathrm{d}V$ spectra over a large conductance range. We focus on adatoms with a next nearest neighbor distance larger than 5 nm, where we exclude coupling between Shiba states.

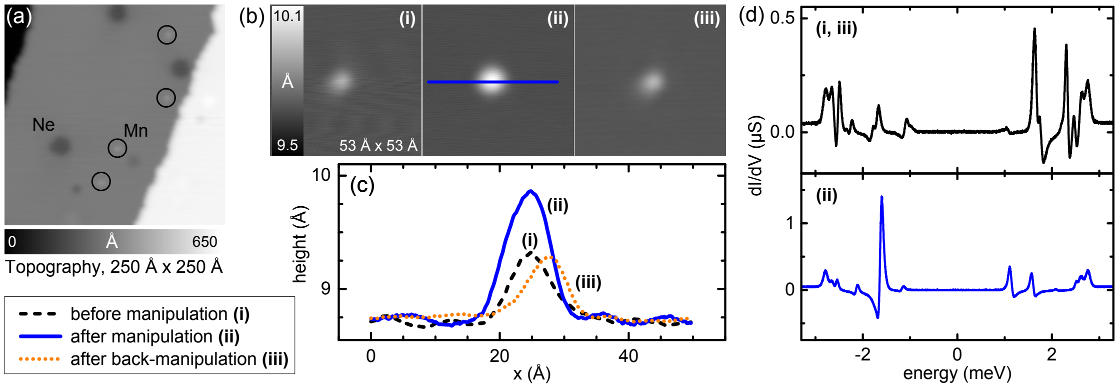

Figure S1: (a) Topography of three terraces of the Pb(111) surface with an evaporated Mn density of ≈ 30 adatoms per $100 \times 100\,\mathrm{nm}^2$. Mn adatoms are marked by black circles. The dark depletions of different sizes are nonmagnetic sub-surface inclusions of Neon, that originate from the sample cleaning process. Setpoint: 50 mV, 200 pA. (b) Topography of a single Mn adatom in its two different adsorption states. (c) Line profiles across the atom for all adsorption states. The lateral shift of the adatom after the back-manipulation (orange, dotted) is due to jumping into a neighboring adsorption site equivalent to the initial one. (d) $\mathrm{d}I/\mathrm{d}V$ spectra show multiple Shiba states for both configurations. Setpoint: 5 mV, 200 pA. Lock-in modulation: $15\,\mu\mathrm{V}_{\mathrm{rms}}$ at 912 Hz.

B. dI/dV spectra on a Mn adatom at 4.8 K

In Fig. S2 we show three examples of dI/dV spectra at the higher temperature of 4.8 K at different tip–sample distances, *i.e.*, different tunneling strengths. At this temperature, only two Shiba states are well resolved due to the increased width of the resonances. An additional zero-energy resonance is observed due to tunneling of thermally excited quasiparticles in tip and sample [process (ii), as described in the main text]. The peak heights α_+, α_-, β_+, and β_- as shown in the right panel of Fig. 3(a) were extracted from these spectra. Notice that the relative intensities of $\alpha_\pm$ change with increasing tunneling strength. However, unlike at 1.2 K, we do not observe a full inversion of peak heights due to the larger relaxation rate.

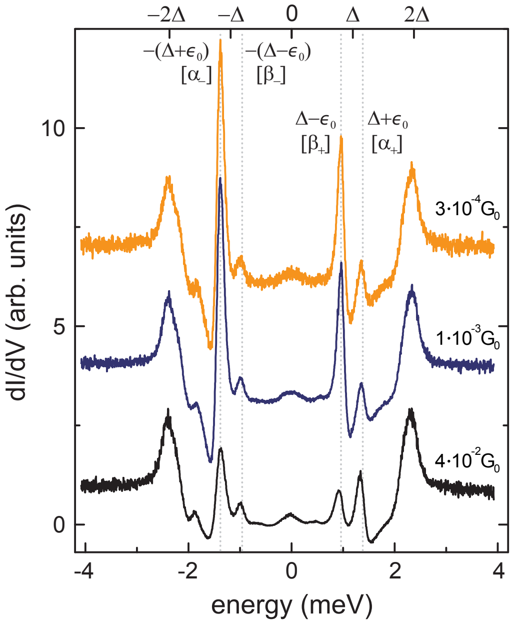

Figure S2: dI/dV spectra acquired on a Mn adatom at 4.8 K (912 Hz, 35 µV$_{\mathrm{rms}}$). Spectra are normalized to the normal-state conductance (indicated in the graph). The figure includes assignments of the peaks to the main peaks ($\alpha_\pm$) and the thermal peaks ($\beta_\pm$).

C. Experiments with a normal-metal tip at 1.2 K

In the main manuscript, we focus on experiments with a superconducting tip. For completeness, we include spectra and corresponding peak-height *vs.* conductance curves acquired with a normal-metal tip at 1.2 K (Fig. S3). Due to thermal broadening of the tip's Fermi edge (≈ 360 µV), the energy resolution is drastically decreased compared to measurements with superconducting tips and only one pair of Shiba resonances is resolved in Fig. S3(a). From a set of such spectra, we extract the peak heights $\alpha_\pm$ [Fig. S3(b)]. In agreement with Ref. [3], we observe an asymmetry in the weak coupling regime, which reduces when approaching the Andreev regime and reaches (almost) equal intensity for the strongest coupling accessible in the experiment.

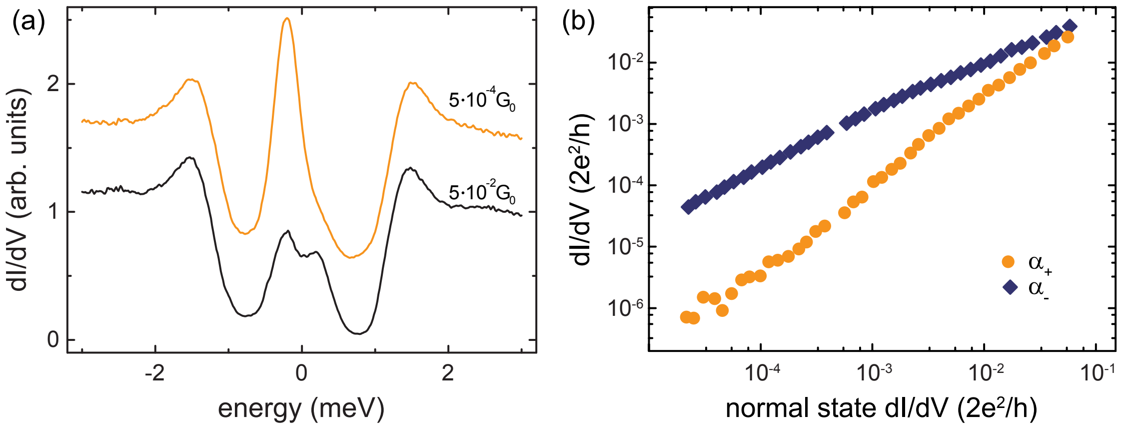

Figure S3: (a) Two dI/dV spectra acquired on a Mn adatom at 1.2 K with a normal-metal tip (912 Hz, 80 μV_{rms}). Spectra are normalized to the normal-state conductance, as indicated in the graph. (b) Peak heights α_+ and α_- of the Shiba level as a function of normal state conductance at $T = 1.2\,\text{K}$, measured with a normal-metal tip.

II. THEORETICAL DETAILS

Here, we derive the expressions for the tunneling current between a superconducting tip and a superconducting sample with magnetic impurity, as given in Eqs. (1) and (2) of the main text. We apply the nonequilibrium Green function method used in [4].

A. Green-function expression for the current

The system is described by the Hamiltonian $\hat{H} = \hat{H}_L + \hat{H}_R + \hat{H}_T$, where the three parts describe the tip, the substrate, and the tunnel coupling. The superconducting tip is described by the BCS Hamiltonian

$$\hat{H}_L = \int \frac{d\mathbf{k}}{(2\pi)^3}\left[\sum_\sigma \xi_k \hat{c}^\dagger_{L,\mathbf{k}\sigma}\hat{c}_{L,\mathbf{k}\sigma} + (\Delta\hat{c}^\dagger_{L,\mathbf{k}\uparrow}\hat{c}^\dagger_{L,-\mathbf{k}\downarrow} + \text{h.c.})\right], \tag{S1}$$

where $\xi_k = k^2/2m - \mu$, μ is the chemical potential, Δ is the superconducting gap, and $c_{L,\mathbf{k}\sigma}$ ($c^\dagger_{L,\mathbf{k}\sigma}$) annihilates (creates) an electron in the tip with momentum $\mathbf{k}$ and spin σ. The Hamiltonian of the substrate contains a magnetic impurity, located at the origin, with spin S pointing along the z direction. The impurity couples to the substrate via a potential $V\delta(\mathbf{r})$ and exchange coupling $JS\sigma_z\delta(\mathbf{r})$, where σ_z is a Pauli matrix in spin space. The Hamiltonian takes the form

$$\hat{H}_R = \int \frac{d\mathbf{k}}{(2\pi)^3}\left[\sum_\sigma \xi_k \hat{c}^\dagger_{R,\mathbf{k}\sigma}\hat{c}_{R,\mathbf{k}\sigma} + (\Delta\hat{c}^\dagger_{R,\mathbf{k}\uparrow}\hat{c}^\dagger_{R,-\mathbf{k}\downarrow} + \text{h.c.})\right] + \sum_\sigma (V - JS\sigma)\hat{c}^\dagger_{R,\sigma}\hat{c}_{R,\sigma}, \tag{S2}$$

where the operator $\hat{c}_{R,\sigma} = \int d\mathbf{k}\hat{c}_{R,\mathbf{k}\sigma}/(2\pi)^3$ annihilates an electron with spin σ at the origin. One can always choose a gauge such that the superconducting order parameters in tip and substrate are real. The superconducting phase difference $\phi(\tau)$ then enters the tunneling Hamiltonian

$$\hat{H}_T(\tau) = \sum_\sigma \left[te^{i\phi(\tau)/2}\hat{c}^\dagger_{L\sigma}(\tau)\hat{c}_{R\sigma}(\tau) + te^{-i\phi(\tau)/2}\hat{c}^\dagger_{R\sigma}(\tau)\hat{c}_{L\sigma}(\tau)\right], \tag{S3}$$

where τ is the time argument, t the hopping strength, and we have made the time dependence of $c_{L/R,\sigma}$ and $c^\dagger_{L/R,\sigma}$ explicit. In writing the tunneling Hamiltonian, we have assumed that the substrate is contacted at the impurity location. The time-dependent phase difference between the tip and the sample, $\phi(\tau) = \phi_0 + 2eV\tau$, depends on the voltage V applied to the junction.

The current operator can be obtained from the Heisenberg equation of motion $\hat{I} = -e\dot{\hat{N}}_L = ie[\hat{N}_L, \hat{H}_T]$, where $\hat{N}_L$ is the electron-number operator of the tip. We obtain

$$\hat{I}(\tau) = ie \sum_{\sigma} \left[te^{i\phi(\tau)/2} \hat{c}^{\dagger}_{L\sigma}(\tau)\hat{c}_{R\sigma}(\tau) - te^{-i\phi(\tau)/2} \hat{c}^{\dagger}_{R\sigma}(\tau)\hat{c}_{L\sigma}(\tau) \right]. \tag{S4}$$

Taking the expectation value yields

$$I(\tau) = e\,\mathrm{Tr}\left\{ \tau_z \left[\hat{t}(\tau) G^{<}_{RL}(\tau,\tau) - G^{<}_{LR}(\tau,\tau)\hat{t}^*(\tau) \right] \right\}, \tag{S5}$$

where τ_z is a Pauli matrix acting in Nambu space. In the last expression, we introduced the lesser Green function in Nambu space

$$G^{<}_{ij}(\tau_1,\tau_2) = i \begin{pmatrix} \langle c^{\dagger}_{j\uparrow}(\tau_2) c_{i\uparrow}(\tau_1) \rangle & \langle c_{j\downarrow}(\tau_2) c_{i\uparrow}(\tau_1) \rangle \\ \langle c^{\dagger}_{j\uparrow}(\tau_2) c^{\dagger}_{i\downarrow}(\tau_1) \rangle & \langle c_{j\downarrow}(\tau_2) c^{\dagger}_{i\downarrow}(\tau_1) \rangle \end{pmatrix}$$

with $i, j = L, R$ and the hopping matrix

$$\hat{t}(\tau) = \begin{pmatrix} te^{i\phi(\tau)/2} & 0 \\ 0 & -te^{-i\phi(\tau)/2} \end{pmatrix}. \tag{S6}$$

The time dependence only enters the phase difference and thus the current is a periodic function of time τ with period $2\pi/eV$. We can expand the current in a Fourier series in terms of the frequency $\omega_0 = eV$

$$I(\tau) = \sum_m I_m e^{im\omega_0\tau}. \tag{S7}$$

The nonequilibrium Green functions depend on two time arguments and have a generalized Fourier expansion

$$G(\tau_1,\tau_2) = \frac{1}{2\pi} \sum_m \int d\omega\, e^{-i\omega\tau_1} e^{i(\omega+m\omega_0)\tau_2} G(\omega, \omega + n\omega_0). \tag{S8}$$

We adopt the notation $G_{nm}(\omega) = G(\omega + n\omega_0, \omega + m\omega_0)$ for which the relation $G_{nm}(\omega) = G_{n-m,0}(\omega + m\omega_0)$ holds. The hopping matrix and its conjugate are given by

$$\hat{t}(\tau) = \hat{t}^{e}_{01} e^{i\omega_0\tau} + \hat{t}^{h}_{10} e^{-i\omega_0\tau} = \begin{pmatrix} t & 0 \\ 0 & 0 \end{pmatrix} e^{i\omega_0\tau} + \begin{pmatrix} 0 & 0 \\ 0 & -t \end{pmatrix} e^{-i\omega_0\tau}, \tag{S9}$$

$$\hat{t}^*(\tau) = \hat{t}^{h}_{01} e^{i\omega_0\tau} + \hat{t}^{e}_{10} e^{-i\omega_0\tau} = \begin{pmatrix} 0 & 0 \\ 0 & -t \end{pmatrix} e^{i\omega_0\tau} + \begin{pmatrix} t & 0 \\ 0 & 0 \end{pmatrix} e^{-i\omega_0\tau}, \tag{S10}$$

with $\hat{t}^{e/h}_{nm} = \hat{t}^{e/h}_{n-m,0}$. Here, we focus on the *dc* current which is given by the zeroth order in the Fourier expansion,

$$I_0 = \frac{e}{h} \int d\omega\ \mathrm{Tr}\left[\hat{\sigma}_z \left(\hat{t}^{e}_{01} G^{<}_{RL,10} + \hat{t}^{h}_{0,-1} G^{<}_{RL,-1,0} - G^{<}_{LR,01} \hat{t}^{e}_{10} - G_{LR,0,-1} \hat{t}^{h}_{-1,0} \right) \right] \tag{S11}$$

$$= \frac{e}{h} \int d\omega \left[tG^{<,ee}_{RL,10} + tG^{<,hh}_{RL,-1,0} - tG^{<,ee}_{LR,01} - tG^{<,hh}_{LR,0,-1} \right], \tag{S12}$$

where the superscripts *ee* and *hh* denote the two diagonal matrix elements in Nambu space. We do not include the nonresonant Andreev reflections at the superconducting tip and thus neglect multiple Andreev reflection processes, i.e., $g^{eh}_L = g^{he}_L = 0$, where g_L denotes the bare Green function of the tip in the absence of the tunnel coupling. Importantly, we retain Andreev reflections at the substrate as they may be resonantly enhanced due to the presence of Shiba bound states. We can now write the Green functions G_{LR} appearing in Eq. (S12) in terms of g_L and the sample Green functions G_R, which includes tunneling only through the self energy of the Shiba state. Using the Langreth rule [5]

$$G^{<}_{RL} = G^{r}_{R} \hat{t}^* g^{<}_{L} + G^{<}_{R} \hat{t}^* g^{a}_{L}, \tag{S13}$$

$$G^{<}_{LR} = g^{r}_{L} \hat{t} G^{<}_{R} + g^{<}_{L} \hat{t} G^{a}_{R}, \tag{S14}$$

we obtain

$$\begin{aligned} G^{<,ee}_{RL,10} &\simeq G^{r,ee}_{R,11}\hat{t}^{e}_{10}g^{<ee}_{L,00} + G^{<,ee}_{R,11}\hat{t}^{e}_{10}g^{a,ee}_{L,00}, &\text{(S15)}\\ G^{<,hh}_{RL,-1,0} &\simeq G^{r,hh}_{R,-1,-1}\hat{t}^{h}_{-1,0}g^{<,hh}_{L,00} + G^{<,hh}_{R,-1,-1}\hat{t}^{h}_{-1,0}g^{a,hh}_{L,00}, &\text{(S16)}\\ G^{<,ee}_{LR,01} &\simeq g^{r,ee}_{L,00}\hat{t}^{e}_{01}G^{<,ee}_{R,11} + \hat{g}^{<,ee}_{L,00}\hat{t}^{e}_{01}G^{a,ee}_{R,11}, &\text{(S17)}\\ G^{<,hh}_{LR,0,-1} &\simeq g^{r,hh}_{L,00}\hat{t}^{h}_{0,-1}G^{<,hh}_{R,-1,-1} + g^{<,hh}_{L,00}\hat{t}^{h}_{0,-1}G^{a,hh}_{R,-1,-1}. &\text{(S18)} \end{aligned}$$

Writing $G(\omega + neV) = G_{nn}(\omega)$, and $g_L = g_L^{ee} = g_L^{hh}$, we obtain for the current

$$\begin{aligned} I = \frac{e}{h}t^2 \int d\omega\, \Big\{ &\left[G_R^{r,ee}(\omega_+) - G_R^{a,ee}(\omega_+)\right] g_L^{<}(\omega) + G_R^{<,ee}(\omega_+)\left[g_L^{a}(\omega) - g_L^{r}(\omega)\right] \\ &- \left[G_R^{r,hh}(\omega_-) - G_R^{a,hh}(\omega_-)\right] g_L^{<}(\omega) - G_R^{<,hh}(\omega_-)\left[g_L^{a}(\omega) - g_L^{r}(\omega)\right] \Big\}, \end{aligned} \tag{S19}$$

where we used the short-hand notation $\omega_\pm = \omega \pm eV$. By using the relation $G^< - G^> = G^a - G^r$, we arrive at

$$\begin{aligned} I =& \frac{e}{h}t^2 \int d\omega \left\{ G_R^{>ee}(\omega) g_L^{<}(\omega_-) - G_R^{<ee}(\omega) g_L^{>}(\omega_-) \right\} \\ &- \frac{e}{h}t^2 \int d\omega \left\{ G_R^{>hh}(\omega) g_L^{<}(\omega_+) - G_R^{<hh}(\omega) g_L^{>}(\omega_+) \right\}. \end{aligned} \tag{S20}$$

B. Shiba-bound-state Green function

To determine the Green function G_R of the substrate, we first calculate the bare Green function g_R neglecting the tunnel coupling to the tip. Without the magnetic impurity, the Green function of a BCS superconductor in Nambu space evaluated at the origin is

$$g_{R0}(\omega) = -\frac{\pi\nu_0}{\sqrt{\Delta^2 - \omega^2}} \begin{pmatrix} \omega & \Delta \\ \Delta & \omega \end{pmatrix}. \tag{S21}$$

We can include the coupling to the impurity spin in Eq. (S2) by means of the Dyson equation $g_R^{-1} = g_{R0}^{-1} + JS - V\tau_z$, and obtain

$$\begin{aligned} g_R(\omega) &= \frac{\pi\nu_0\sqrt{\Delta^2 - \omega^2}}{(\omega + \alpha\sqrt{\Delta^2 - \omega^2})^2 - \Delta^2 - \beta^2(\Delta^2 - \omega^2)} \begin{pmatrix} \omega + (\alpha+\beta)\sqrt{\Delta^2 - \omega^2} & \Delta \\ \Delta & \omega + (\alpha-\beta)\sqrt{\Delta^2 - \omega^2} \end{pmatrix} \\ &= \frac{\pi\nu_0}{2\omega\alpha - (1 - \alpha^2 + \beta^2)\sqrt{\Delta^2 - \omega^2}} \begin{pmatrix} \omega + (\alpha+\beta)\sqrt{\Delta^2 - \omega^2} & \Delta \\ \Delta & \omega + (\alpha-\beta)\sqrt{\Delta^2 - \omega^2} \end{pmatrix}, \end{aligned} \tag{S22}$$

where we introduced the dimensionless parameters $\alpha = \pi\nu_0 JS > 0$ and $\beta = \pi\nu_0 V$. The subgap states with $|\omega| < \Delta$ correspond to the poles of the Green function. In particular, in our model the Shiba state energy is given by the pole of g_R,

$$\epsilon_0 = \Delta \frac{1 - \alpha^2 + \beta^2}{\sqrt{(1 - \alpha^2 + \beta^2)^2 + 4\alpha^2}}. \tag{S23}$$

To calculate the tunneling into the Shiba state, we only need $g_R(\omega)$ with ω close to ϵ_0. In this limit, we set $\omega = \epsilon_0 + \delta\omega$ and expand the denominator in Eq. (S22) to linear order in $\delta\omega$,

$$\begin{aligned} 2\omega\alpha - (1 - \alpha^2 + \beta^2)\sqrt{\Delta^2 - \omega^2} &\simeq 2(\epsilon_0 + \delta\omega)\alpha - (1 - \alpha^2 + \beta^2)\sqrt{\Delta^2 - \epsilon_0^2}\left(1 - \frac{2\epsilon_0\delta\omega}{\Delta^2 - \epsilon_0^2}\right)^{1/2} \\ &= \delta\omega\left(2\alpha + \frac{(1 - \alpha^2 + \beta^2)\epsilon_0}{\sqrt{\Delta^2 - \epsilon_0^2}}\right) \\ &= \delta\omega \frac{(1 - \alpha^2 + \beta^2)^2 + 4\alpha^2}{2\alpha}. \end{aligned} \tag{S24}$$

The numerator can be evaluated at $\omega = \epsilon_0$, which leads to

$$\omega + (\alpha \pm \beta)\sqrt{\Delta^2 - \omega^2} \simeq \Delta \frac{1 + (\alpha \pm \beta)^2}{\sqrt{(1 - \alpha^2 + \beta^2)^2 + 4\alpha^2}}. \tag{S25}$$

Thus the Green function has the approximate form

$$g_R(\omega) = \frac{1}{\omega - \epsilon_0} \begin{pmatrix} u^2 & uv \\ uv & v^2 \end{pmatrix} \tag{S26}$$

with

$$u^2, v^2 = \frac{2\alpha\pi\nu_0\Delta\left(1 + (\alpha \pm \beta)^2\right)}{\left((1 - \alpha^2 + \beta^2)^2 + 4\alpha^2\right)^{3/2}}. \tag{S27}$$

Here, u and v are the electron and hole components of the Shiba state (corresponding to the upper and lower sign, respectively). Note that in general $u \neq v$ when potential scattering by the impurity is included.

C. Self energy due to relaxation processes

Phonon or photon induced relaxation processes introduce a self energy $\Sigma_{\rm ph}$ into the substrate Green function

$$G = g + g\Sigma_{\rm ph}g + g\Sigma_{\rm ph}g\Sigma_{\rm ph}g + \dots \tag{S28}$$

Approximating the bare substrate Green function g by the contribution of the Shiba state,

$$g(\omega) = |\psi_S\rangle \frac{1}{\omega - \epsilon_0} \langle\psi_S| \tag{S29}$$

with

$$\langle \mathbf{r} | \psi_S \rangle = \begin{pmatrix} u(\mathbf{r}) \\ v(\mathbf{r}) \end{pmatrix}, \tag{S30}$$

we find

$$G(\omega) = |\psi_S\rangle \frac{1}{\omega - \epsilon_0 - \langle\psi_S|\Sigma_{\rm ph}(\omega)|\psi_S\rangle} \langle\psi_S|. \tag{S31}$$

We approximate the self energy by its value at $\omega = \epsilon_0$ and retain only the imaginary part,

$$\Gamma_{\rm ph} = 2{\rm Im}\langle\psi_S|\Sigma_{\rm ph}(\epsilon_0)|\psi_S\rangle. \tag{S32}$$

Thus, the retarded and advanced Green functions of the Shiba state read

$$g_R^{r,a}(\omega) = \frac{1}{\omega - \epsilon_0 \pm i\Gamma_{\rm ph}(\epsilon_0)/2} \begin{pmatrix} u^2 & uv \\ uv & v^2 \end{pmatrix}. \tag{S33}$$

Here we have again restricted attention to the Green function at the position of the impurity.

In quasi-equilibrium, the greater and lesser Green function can be expressed in terms of the retarded and advanced Green functions,

$$g_R^<(\omega) = f(\omega)(g_R^a(\omega) - g_R^r(\omega)) = \frac{\Sigma_{\rm ph}^<(\epsilon_0)}{(\omega - \epsilon_0)^2 + (\Gamma_{\rm ph}(\epsilon_0))/2)^2} \begin{pmatrix} u^2 & uv \\ uv & v^2 \end{pmatrix}, \tag{S34}$$

$$g_R^>(\omega) = -(1 - f(\omega))(g_R^a - g_R^r) = \frac{\Sigma_{\rm ph}^>(\epsilon_0)}{(\omega - \epsilon_0)^2 + (\Gamma_{\rm ph}(\epsilon_0)/2)^2} \begin{pmatrix} u^2 & uv \\ uv & v^2 \end{pmatrix}, \tag{S35}$$

where $f(\omega)$ is the quasi-equilibrium distribution function and we used the relations

$$-i\Sigma_{\rm ph}^< = \Gamma_{\rm ph} f\,, \qquad i\Sigma_{\rm ph}^> = \Gamma_{\rm ph}(1 - f)\,. \tag{S36}$$

We introduce $\Gamma_1 = i\Sigma_{ph}^>(\epsilon_0)$ and $\Gamma_2 = -i\Sigma_{ph}^<(\epsilon_0)$ which can be interpreted as the rates with which the Shiba level is emptied or occupied. Note that $\Gamma_{\rm ph} = \Gamma_1 + \Gamma_2$.

D. Self energy due to tip-substrate tunneling

We now include the tunnel coupling of the Shiba state to the tip. For simplicity, we assume that the tip position is identical with the impurity position. Then, the self energy due to the tunneling is local at the position of the impurity, and we can suppress spatial arguments in the following. The tunneling gives rise to the self energy

$$\Sigma_R^r = \hat{t}^h_{01} g^r_{L,11} \hat{t}^h_{10} + \hat{t}^e_{0-1} g^r_{L,-1,-1} \hat{t}^e_{-10} = t^2 \begin{pmatrix} g^r_L(\omega_-) & 0 \\ 0 & g^r_L(\omega_+) \end{pmatrix}, \tag{S37}$$

where we neglect Andreev reflections in the tip as discussed in the main text. Similar relations hold for the self energies $\Sigma_R^{a,<,>}$. The retarded and advanced Green functions of the Shiba level coupled to the tip can be obtained from the Dyson equation

$$G_R^{r,a} = \frac{1}{1 - g_R^{r,a}\Sigma_R^{r,a}} g_R^{r,a} = \frac{1}{\omega - \epsilon_0 \pm i\Gamma/2} \begin{pmatrix} u^2 & uv \\ uv & v^2 \end{pmatrix}, \tag{S38}$$

where the imaginary part of the self energy leads to a broadening $\Gamma = \Gamma_e(\omega) + \Gamma_h(\omega) + \Gamma_1 + \Gamma_2$ with

$$\Gamma_e(\omega) = 2\pi t^2 u^2 \rho(\omega_-), \tag{S39}$$

$$\Gamma_h(\omega) = 2\pi t^2 v^2 \rho(\omega_+) \tag{S40}$$

in terms of the BCS density of states

$$\rho(\omega) = \nu_0 \frac{|\omega|\, \theta(|\omega| - \Delta)}{\sqrt{\omega^2 - \Delta^2}} \tag{S41}$$

with ν_0 the normal density of states at the Fermi energy. In Eq. (S38) we have neglected the real part of the self energy which would lead to a shift of the resonance energy $\propto t^2$. The lesser Green function of the Shiba state is given by [5]

$$G_R^< = g_R^< + g_R^r \Sigma_R^r G_R^< + g_R^r \Sigma_R^< G_R^a + g_R^< \Sigma_R^a G_R^a \tag{S42}$$

$$= \frac{1}{1 - g_R^r \Sigma_R^r} [g_R^< (1 + \Sigma_R^a G_R^a) + g_R^r \Sigma_R^< G_R^a] \,. \tag{S43}$$

A straightforward calculation using the relations $g_L^<(\omega) = 2\pi i \rho(\omega) n_F(\omega)$ and $g_L^>(\omega) = -2\pi i \rho(\omega)(1 - n_F(\omega))$ reveals

$$G_R^< = i \frac{\Gamma_2 + \Gamma_e(\omega) n_F(\omega_-) + \Gamma_h(\omega) n_F(\omega_+)}{(\omega - \epsilon_0)^2 + (\Gamma_1 + \Gamma_2 + \Gamma_e(\omega) + \Gamma_h(\omega))^2/4} \begin{pmatrix} u^2 & uv \\ uv & v^2 \end{pmatrix}. \tag{S44}$$

Along the same lines we find

$$G_R^> = -i \frac{\Gamma_1 + \Gamma_e(\omega)(1 - n_F(\omega_-)) + \Gamma_h(\omega)(1 - n_F(\omega_+))}{(\omega - \epsilon_0)^2 + (\Gamma_1 + \Gamma_2 + \Gamma_e(\omega) + \Gamma_h(\omega))^2/4} \begin{pmatrix} u^2 & uv \\ uv & v^2 \end{pmatrix}. \tag{S45}$$

E. Expressions for the tunneling current

We can now evaluate the current in Eq. (S20) which yields $I = I^s + I^a$, where

$$I^s(V) = \frac{e}{h} \int d\omega \frac{\Gamma_1[\Gamma_e(\omega) n_F(\omega_-) - \Gamma_h(\omega) n_F(\omega_+)] - \Gamma_2[\Gamma_e(\omega)(1 - n_F(\omega_-)) - \Gamma_h(\omega)(1 - n_F(\omega_+))]}{(\omega - \epsilon_0)^2 + (\Gamma(\omega)/2)^2}, \tag{S46}$$

$$I^a(V) = \frac{2e}{h} \int d\omega \frac{\Gamma_e(\omega)\Gamma_h(\omega)}{(\omega - \epsilon_0)^2 + (\Gamma(\omega)/2)^2} [n_F(\omega_-) - n_F(\omega_+)] \,. \tag{S47}$$

The current I^a originates from resonant Andreev reflection, whereas I^s describes single-particle tunneling and subsequent relaxation of quasiparticles in the Shiba state. These two equations are given in the main text as Eqs. (1) and (2).

F. Relaxation processes

The intrinsic linewidth of the Shiba level is determined by the rates Γ_1 for emptying and Γ_2 for filling a Shiba state. These enter as phenomenological parameters in our theory, which may originate from various microscopic mechanisms. In Ref. [3] the authors considered elastic processes due to a coupling to a fermionic bath as a source of quasiparticle relaxation. Another possible relaxation mechanism involves transitions between the Shiba state and the quasiparticle continuum assisted by phonons or photons. This results in a thermal distribution of the Shiba state $f = n_F(\epsilon_0)$ in the absence of a tunnel coupling, where $f = \Gamma_2/(\Gamma_1 + \Gamma_2)$ [see Eq. (S36)]. Thus for purely thermal relaxation we generally find

$$\frac{\Gamma_1}{\Gamma_2} = e^{\epsilon_0/T}. \tag{S48}$$

The most basic relaxation process involves direct transitions between the Shiba state and the quasiparticle continuum. Such processes were studied in Ref. [6] where it was shown that the relaxation rates are given by

$$\Gamma_1 \sim \sqrt{\frac{T}{\Delta}} e^{-(\Delta-\epsilon_0)/T} \left[(\Delta - \epsilon_0) + (\Delta + \epsilon_0) e^{-\epsilon_0/T}\right], \tag{S49}$$

$$\Gamma_2 \sim \sqrt{\frac{T}{\Delta}} e^{-\Delta/T} \left[(\Delta - \epsilon_0) + (\Delta + \epsilon_0) e^{-\epsilon_0/T}\right]. \tag{S50}$$

The relaxation rate Γ_1 for leaving the Shiba state has a thermal factor $\exp[-(\Delta - \epsilon_0)/T]$ involving the required phonon energy of the transition to the continuum $\Delta - \epsilon_0$, whereas Γ_2 is limited by the thermal occupation $\exp(-\Delta/T)$ of the excited quasiparticles in the continuum. The ratio of the two rates indeed yields Eq. (S48). In the presence of multiple subgap states, more intricate relaxation dynamics are possible, e.g., pairs of quasiparticles from subgap states may inelastically relax to form a Cooper pair.

In Sec. III we present theoretical results for the conductance based on Eqs. (S46) and (S47) with phenomenological relaxation rates $\Gamma_{1/2}$. We then turn to a more detailed analysis of the relevant relaxation processes in the experiment in Sec. IV B.

III. CALCULATION OF CURRENT AND DIFFERENTIAL CONDUCTANCE AT THE THRESHOLDS

In this section, we provide details of the calculations underlying Eqs. (3–5) for the peak conductances in the main text. We also calculate the currents at these bias voltages which were used in the main text to extract relaxation rates. At the end of this section we illustrate these results by numerically calculating the current and the differential conductance as a function of tunneling strength. We organize the calculation by threshold voltages.

A. $eV = \Delta + \epsilon_0$

At this threshold, there are two contributing processes to the current, namely single-electron tunneling into the Shiba state as well as resonant Andreev processes: $I_{\Delta+\epsilon_0} = I^s_{\Delta+\epsilon_0} + I^a_{\Delta+\epsilon_0}$. We find

$$I_{\Delta+\epsilon_0} = \begin{cases} \frac{2e}{\hbar}(2\Gamma_h + \Gamma_1)\frac{\omega_e^{3/2}}{\Gamma_1^{3/2}} & \omega_e \ll \Gamma_1 \\ \frac{e}{3\hbar}(2\Gamma_h + \Gamma_1) & \omega_e \gg \Gamma_1 \end{cases} \tag{S51}$$

for the peak current and

$$\alpha_+ = \begin{cases} \frac{4\pi e^2}{h}\frac{2\Gamma_h+\Gamma_1}{\Gamma_1}\frac{\omega_e^{3/2}}{\Gamma_1^{3/2}} & \omega_e \ll \Gamma_1 \\ \frac{4\pi e^2}{9h}\frac{2\Gamma_h+\Gamma_1}{\omega_e} & \omega_e \gg \Gamma_1 \end{cases} \tag{S52}$$

for the peak conductance. We will now derive these results, first treating the single-electron processes and subsequently analyzing the Andreev process. The quantities entering into these expressions will be defined as the calculation proceeds.

1. *Single-electron tunneling*

The relevant single-electron process is shown in Fig. 2(a) in the main text. Analytically, this process contributes the term

$$I^s_{\Delta+\epsilon_0}(V) = e\int \frac{d\omega}{2\pi\hbar}\frac{\Gamma_1\Gamma_e(\omega)n_F(\omega-eV)}{(\omega-\epsilon_0)^2+(\Gamma/2)^2} \tag{S53}$$

to the current. Here, the subscript denotes the threshold and the superscript the single-particle (as opposed to Andreev) nature of the contributions. The integration variable ω denotes the energy of the tunneling electron as measured from the Fermi energy of the substrate superconductor. In Eq. (S53) and throughout this section we focus on contributions to the current which originate from the vicinity of the BCS singularity. Unlike the differential conductance, the full current at the main thresholds $e|V| = \Delta+\epsilon_0$ also includes the contributions from terms $\propto \Gamma_2$ in Eq. (S46), which are responsible for the thermal peaks. The quantitative comparison with experiment in Sec. IV A includes all contributions to the current.

At the threshold $eV = \Delta+\epsilon_0$, the coupling $\Gamma_e(\omega)$ becomes singular exactly at the Shiba energy $\omega = \epsilon_0$ because of the diverging BCS density of states $\rho(\omega - eV)$ [cf. Fig. 2(a)]. The dominant contribution to the current comes from the vicinity of the singularity at $\omega = eV-\Delta \sim \epsilon_0$ and we can approximate

$$\Gamma_e(\omega) = 2\pi u^2 t^2 \rho(\omega-eV) \simeq \gamma_e\sqrt{\frac{\Delta}{2}}\frac{\theta(eV-\Delta-\omega)}{\sqrt{eV-\Delta-\omega}} \tag{S54}$$

in terms of the normal-state tunneling rate $\gamma_e = 2\pi u^2\nu_0 t^2$. In the region of interest the thermal occupation of the tip is $n_F(\omega-eV)\simeq 1$. Note that this insensitivity to thermal smearing is a consequence of the superconducting tip. (Of course, the current is still sensitive to temperature which enters into the relaxation rates Γ_1 and Γ_2.) This also implies that the bias voltage enters into the current only via the BCS density of states which is quite distinct from the case of a normal-state tip.

With these ingredients, we can now compute the current in the vicinity of the threshold,

$$I^s_{\Delta+\epsilon_0}(V) \simeq e\gamma_e\Gamma_1\sqrt{\frac{\Delta}{2}}\int\frac{d\omega}{2\pi\hbar}\frac{1}{(\omega-\epsilon_0)^2+\left(\frac{\Gamma_1}{2}+\frac{\gamma_e\sqrt{\Delta/2}}{2\sqrt{eV-\Delta-\omega}}\right)^2}\frac{\theta(eV-\Delta-\omega)}{\sqrt{eV-\Delta-\omega}}. \tag{S55}$$

Here, we used that $\Gamma_1 \gg \Gamma_2$ for $\epsilon_0 \gg T$ and $\Gamma_h \ll \Gamma_e$. The latter will be justified below. Note that it is however important to keep both Γ_1 and Γ_e.

We simplify notation by measuring voltages from the threshold,

$$eV' = eV - (\Delta+\epsilon_0), \tag{S56}$$

and introducing the characteristic energy

$$\omega_e = \left(\frac{1}{2}\gamma_e\sqrt{\frac{\Delta}{2}}\right)^{2/3}. \tag{S57}$$

Then, we have

$$I^s_{\Delta+\epsilon_0}(V') \simeq 2e\omega_e^{3/2}\Gamma_1\int_0^\infty\frac{d\omega}{2\pi\hbar}\frac{1}{\sqrt{\omega}}\frac{1}{(\omega-eV')^2+\left(\frac{\Gamma_1}{2}+\frac{\omega_e^{3/2}}{\sqrt{\omega}}\right)^2} \tag{S58}$$

and

$$G^s_{\Delta+\epsilon_0}(V') \simeq 4e^2\omega_e^{3/2}\Gamma_1\int_0^\infty\frac{d\omega}{2\pi\hbar}\frac{1}{\sqrt{\omega}}\frac{\omega-eV'}{\left[(\omega-eV')^2+\left(\frac{\Gamma_1}{2}+\frac{\omega_e^{3/2}}{\sqrt{\omega}}\right)^2\right]^2} \tag{S59}$$

for the corresponding conductance $G = dI/dV$. The conductance involves an integral over the tip density of states $\sim 1/\sqrt{\omega}$ multiplied by the function $Z(\omega) = (\omega-eV')/[(\omega-eV')^2+(\Gamma_1/2+\omega_e^{3/2}/\sqrt{\omega})^2]^2$. We emphasize that $Z(\omega)$

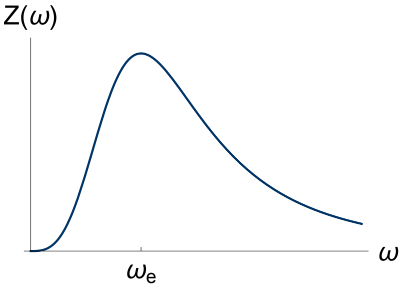

Figure S4: Characteristic function $Z(\omega)$ defined in the text at the threshold ($eV' = 0$) and for $\Gamma_1 = 0$. This function determines the conductance via Eq. (S59). It is zero at the Shiba state ($\omega = 0$) and peaks at ω_e.

is not the spectral function of the Shiba state as it would be for a normal metal tip. This special feature of the superconducting tip arises because the voltage dependence enters through the tip density of states rather than the occupation numbers. As shown in Fig. S4 $Z(\omega)$ vanishes at the Shiba state (now at $\omega = 0$) because of the divergent broadening induced by the superconducting tip and also vanishes far from the Shiba energy. In between, it peaks at a scale set by the maximum of the effective tunneling strength ω_e and the thermal relaxation rate Γ_1 (in Fig. S4 we have set $\Gamma_1 = 0$ in which case the peak is at ω_e).

We can now also discuss the hole tunneling rate $\Gamma_h(\omega)$ with an associated energy scale $\omega_h = (\gamma_h\sqrt{\Delta})^{2/3}/2$ in terms of the normal state hole tunneling rate $\gamma_h = 2\pi v^2 \nu_0 t^2$. In principle, hole tunneling introduces another term into the broadening of $Z(\omega)$. The broadening then becomes

$$\frac{\Gamma_1}{2} + \frac{\omega_e^{3/2}}{\sqrt{\omega}} + \frac{\omega_h^{3/2}}{\sqrt{\omega + 2\epsilon_0}}. \tag{S60}$$

We can neglect the last term (i.e., the hole contribution to the width of $Z(\omega)$) as long as $\max\{\Gamma_1, \omega_e\} \gg \sqrt{\omega_h^3/\epsilon_0}$. In principle, one may imagine situations in which $v \gg u$ so that $\Gamma_h(\omega)$ contributes significantly to the broadening in the strong tunneling regime. As this case is probably irrelevant for this experiment we exclude it from our analytical considerations. We discuss implications of a broadening due to $\Gamma_h(\omega)$ in the presentation of the numerical results at the end of this section.

We focus attention on the peak current and peak conductance. The peak occurs approximately at the threshold bias $eV = \Delta + \epsilon_0$ and we restrict our analytical considerations to the threshold, setting $eV' = 0$ in the following. While this makes our analysis more transparent it also introduces a small numerical error. We emphasize that our results exhibit the correct parametric dependence and the quantitative analysis in Sec. IV A is based on the numerically exact peak heights. The peak position and height relative to the threshold are discussed in detail in Sec. III F.

Evaluated at the threshold, the integral for $I^s_{\Delta+\epsilon_0}$ contains the two energy scales Γ_1 and ω_e. For weak tip-substrate tunneling, $\omega_e \ll \Gamma_1$, we can neglect the contribution of Γ_e to the broadening of $Z(\omega)$. In this limit, we find

$$\begin{aligned} I^s_{\Delta+\epsilon_0} &\simeq 2e\omega_e^{3/2}\Gamma_1 \int_0^\infty \frac{d\omega}{2\pi\hbar} \frac{1}{\sqrt{\omega}} \frac{1}{\omega^2 + \Gamma_1^2/4} \\ &= \frac{2\sqrt{2}e}{\pi\hbar} \frac{\omega_e^{3/2}}{(\Gamma_1)^{1/2}} \int_0^\infty \frac{dx}{\sqrt{x}} \frac{1}{x^2+1}. \end{aligned} \tag{S61}$$

The integral is elementary and we obtain the result

$$I^s_{\Delta+\epsilon_0} \simeq \frac{2e}{\hbar} \frac{\omega_e^{3/2}}{(\Gamma_1)^{1/2}}. \tag{S62}$$

The peak conductance in the regime $\omega_e \ll \Gamma_1$ can be calculated along the same lines,

$$\begin{aligned} G^s_{\Delta+\epsilon_0} &\simeq \frac{4e^2}{h}\omega_e^{3/2}\Gamma_1 \int_0^\infty d\omega \frac{\sqrt{\omega}}{\left[\omega^2+\Gamma_1^2/4\right]^2} \\ &= \frac{16\sqrt{2}e^2}{h}\frac{\omega_e^{3/2}}{(\Gamma_1)^{3/2}} \int_0^\infty dx \frac{\sqrt{x}}{[x^2+1]^2} \\ &= \frac{4\pi e^2}{h}\frac{\omega_e^{3/2}}{(\Gamma_1)^{3/2}}, \end{aligned} \tag{S63}$$

where the x-integration is again elementary.

In the opposite limit of strong tip-substrate tunneling, $\omega_e \gg \Gamma_1$, we can neglect the contribution of Γ_1 to the broadening of $Z(\omega)$. In this limit, we find

$$\begin{aligned} I^s_{\Delta+\epsilon_0} &\simeq 2e\omega_e^{3/2}\Gamma_1 \int_0^\infty \frac{d\omega}{2\pi\hbar}\frac{1}{\sqrt{\omega}}\frac{1}{\omega^2+\omega_e^3/\omega} \\ &= \frac{e}{\pi\hbar}\Gamma_1 \int_0^\infty \frac{dx}{\sqrt{x}}\frac{1}{x^2+1/x}. \end{aligned} \tag{S64}$$

Performing the integral yields

$$I^s_{\Delta+\epsilon_0} \simeq \frac{e\Gamma_1}{3\hbar}. \tag{S65}$$

The peak conductance in the regime $\omega_e \gg \Gamma_1$ can be calculated along the same lines,

$$\begin{aligned} G^s_{\Delta+\epsilon_0} &\simeq \frac{4e^2}{h}\omega_e^{3/2}\Gamma_1 \int_0^\infty d\omega \frac{\sqrt{\omega}}{\left[\omega^2+\omega_e^3/\omega\right]^2} \\ &= \frac{4e^2}{h}\frac{\Gamma_1}{\omega_e} \int_0^\infty dx \frac{\sqrt{x}}{[x^2+1/x]^2} \\ &= \frac{4\pi e^2}{9h}\frac{\Gamma_1}{\omega_e}. \end{aligned} \tag{S66}$$

2. *Andreev contribution*

The Andreev current is given by

$$I^a_{\Delta+\epsilon_0}(V) = 2e\int \frac{d\omega}{2\pi\hbar}\frac{\Gamma_e(\omega)\Gamma_h(\omega)[n_F(\omega-eV)-n_F(\omega+eV)]}{(\omega-\epsilon_0)^2+(\Gamma/2)^2}. \tag{S67}$$

The Fermi functions can be approximated by $n_F(\omega-eV)\simeq 1$ and $n_F(\omega+eV)\simeq 0$, since $\omega\sim\epsilon_0$ and $eV\sim\Delta+\epsilon$ and with $\omega_e \ll \epsilon_0$ we can approximate $\Gamma_h(\omega)$ by a constant. In the case $\epsilon_0 \ll \Delta$ it simply reads

$$\Gamma_h(\omega) \simeq \Gamma_h = \sqrt{\frac{2\omega_h^3}{\epsilon_0}}. \tag{S68}$$

With these approximations, the integrals become equal to those for the single-particle contribution, with the replacement $\Gamma_1 \to \Gamma_h$ in the numerator and an overall prefactor of two. Note that we can still ignore Γ_h in the broadening of $Z(\omega)$ under the assumptions spelled out above. This yields the result summarized in Eqs. (S51) and (S52) above.

B. $eV = -(\Delta+\epsilon_0)$

At threshold the current is again the sum of single-electron and Andreev processes. The relevant single-electron process is shown in Fig. S5. Analytically, this process contributes the term

$$I^s_{-\Delta-\epsilon_0}(V) = -e\int \frac{d\omega}{2\pi\hbar}\frac{\Gamma_1\Gamma_h(\omega)n_F(\omega+eV)}{(\omega-\epsilon_0)^2+(\Gamma/2)^2} \tag{S69}$$

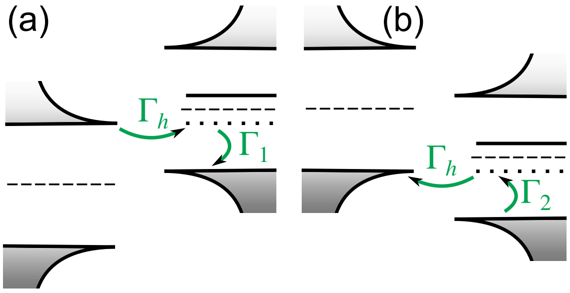

Figure S5: Single-particle tunneling processes at (a) $eV = -(\Delta+\epsilon_0)$ and (b) $eV = \Delta-\epsilon_0$. At the threshold in (a), an additional Andreev process contributes to the current (cf. Fig. 2(b) of the main text).

to the current. Up to overall signs, this differs from the corresponding process near $eV = \Delta + \epsilon_0$ discussed above by exchanging the roles of $\Gamma_e(\omega)$ and $\Gamma_h(\omega)$. The same exchange characterizes the Andreev contribution. Thus, in effect, we can obtain the results for this threshold by interchanging $u \leftrightarrow v$ in the expressions for $eV = \Delta + \epsilon_0$. This yields

$$I_{-\Delta-\epsilon_0} = \begin{cases} \frac{2e}{\hbar}(2\Gamma_h + \Gamma_1)\frac{\omega_h^{3/2}}{\Gamma_1^{3/2}} & \omega_h \ll \Gamma_1 \\ \frac{e}{3\hbar}(2\Gamma_h + \Gamma_1) & \omega_h \gg \Gamma_1 \end{cases} \tag{S70}$$

for the peak current and

$$\alpha_- = \begin{cases} \frac{4\pi e^2}{h}\frac{2\Gamma_h+\Gamma_1}{\Gamma_1}\frac{\omega_h^{3/2}}{\Gamma_1^{3/2}} & \omega_h \ll \Gamma_1 \\ \frac{4\pi e^2}{9h}\frac{2\Gamma_h+\Gamma_1}{\omega_h} & \omega_h \gg \Gamma_1 \end{cases} \tag{S71}$$

for the peak conductance.

C. $eV = -(\Delta - \epsilon_0)$

At this thermal threshold, only single-electron processes contribute which are shown in Fig. 2(c) in the main text. Analytically, this process is described by

$$I^s_{-\Delta+\epsilon_0}(V) = -e\int \frac{d\omega}{2\pi\hbar}\frac{\Gamma_2\Gamma_e(\omega)[1-n_F(\omega-eV)]}{(\omega-\epsilon_0)^2+(\Gamma/2)^2}\,. \tag{S72}$$

Noting that

$$1 - n_F(\omega - eV) \simeq 1 = 1 - n_F(e|V| + \omega) \simeq 1, \tag{S73}$$

we see that this differs from the expression for the single-electron current at the threshold $eV = \Delta + \epsilon_0$ merely by a factor Γ_2/Γ_1. Thus, we obtain

$$I_{-\Delta+\epsilon_0} = \begin{cases} \frac{2e}{\hbar}\Gamma_2\frac{\omega_e^{3/2}}{\Gamma_1^{3/2}} & \omega_e \ll \Gamma_1 \\ \frac{e}{3\hbar}\Gamma_2 & \omega_e \gg \Gamma_1 \end{cases} \tag{S74}$$

for the peak current and

$$\beta_- = \begin{cases} \frac{4\pi e^2}{h}\frac{\Gamma_2}{\Gamma_1}\frac{\omega_e^{3/2}}{\Gamma_1^{3/2}} & \omega_e \ll \Gamma_1 \\ \frac{4\pi e^2}{9h}\frac{\Gamma_2}{\omega_e} & \omega_e \gg \Gamma_1 \end{cases} \tag{S75}$$

for the peak conductance.

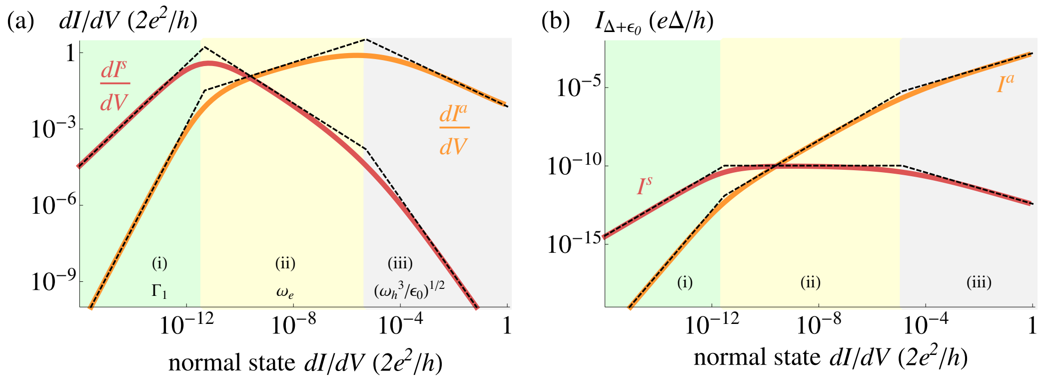

Figure S6: (a) Differential conductance and (b) current at the threshold $eV = \Delta + \epsilon$ *vs.* normal state conductance. The curves are obtained numerically from Eqs. (1) and (2) of the main text. The single-particle (red) and Andreev (orange) contributions have maxima at distinct values of normal state dI/dV which separate three regimes with dominating relaxation mechanisms Γ_1, ω_e, and $(\omega_h^3/\epsilon_0)^{1/2}$. While analytical expressions for the asymptotes (dashed lines) in the first two regimes are given by Eqs. (S51) and (S52), a similar analysis also yields expressions in regime (iii). The parameters are chosen such that all three regimes are visible. We have set $\Gamma_1 = 10^{-10}$, $\Gamma_2 = 0$, $u^2/\nu_0 = 0.001$, $v^2/\nu_0 = 1$, and $\epsilon_0 = 0.3$, where all energies are measured in units of Δ.

D. $eV = \Delta - \epsilon_0$

This thermal threshold is dominated by the contribution shown in Fig. S5 and given by

$$I^s_{\Delta-\epsilon_0}(V) = e \int \frac{d\omega}{2\pi\hbar} \frac{\Gamma_2 \Gamma_h(\omega)[1 - n_F(\omega + eV)]}{(\omega - \epsilon_0)^2 + (\Gamma/2)^2} \,. \tag{S76}$$

This differs from the thermal threshold at $eV = -\Delta + \epsilon_0$ by the replacement of $\Gamma_e(\omega)$ by $\Gamma_h(\omega)$. Thus, we obtain the current at this threshold by the replacement $u \leftrightarrow v$. This yields

$$I_{\Delta-\epsilon_0} = \begin{cases} \frac{2e}{\hbar}\Gamma_2 \frac{\omega_h^{3/2}}{\Gamma_1^{3/2}} & \omega_{\rm th} \ll \Gamma_1 \\ \frac{e}{3\hbar}\Gamma_2 & \omega_h \gg \Gamma_1 \end{cases} \tag{S77}$$

for the peak current and

$$\beta_+ = \begin{cases} \frac{4\pi e^2}{h}\frac{\Gamma_2}{\Gamma_1}\frac{\omega_h^{3/2}}{\Gamma_1^{3/2}} & \omega_h \ll \Gamma_1 \\ \frac{4\pi e^2}{9h}\frac{\Gamma_2}{\omega_h} & \omega_h \gg \Gamma_1 \end{cases} \tag{S78}$$

for the peak conductance.

E. Discussion and numerical results

In Fig. S6(a) we plot the differential conductance from the single-particle and Andreev currents at the threshold $eV = \Delta + \epsilon_0$ according to Eqs. (S46) and (S47) together with the analytical expression in Eq. (S52). We identify three regimes as a function of the normal state conductance $G_N \sim (2e^2/h)t^2\nu_0^2$ which exhibit characteristic power-laws as a function of tunneling strength. These regimes can be associated with different dominant broadening mechanisms (from weak to strong tunneling): (i) intrinsic relaxation Γ_1, (ii) electron tunneling ω_e, and (iii) hole tunneling $(\omega_h^3/\epsilon_0)^{1/2}$.

The crossover between regimes (i) and (ii) occurs at a normal state conductance G_N^1, which can be evaluated from the condition $\Gamma_1 \sim \omega_e$. Equivalently the second crossover point G_N^2 is obtained from $\omega_e \sim (\omega_h^3/\epsilon_0)^{1/2}$ and we find

$$G_N^1 \sim \frac{2e^2}{h}\frac{\nu_0\Delta}{u^2}\left(\frac{\Gamma_1}{\Delta}\right)^{3/2}, \tag{S79}$$

$$G_N^2 \sim \frac{2e^2}{h}\frac{u^4\nu_0\Delta}{v^6}\left(\frac{\epsilon_0}{\Delta}\right)^{3/2}. \tag{S80}$$

Figure S6(a) shows that the full differential conductance peak $\alpha_+ = dI^s/dV + dI^a/dV$ consists of the sum of two terms that peak at different tunneling strengths and thus typically exhibits two peaks as a function of normal state conductance. At the first crossover point the single-particle contribution dI^s/dV reaches a maximum of order $2e^2/h$. This is readily understood from the single-particle current in Eq. (S46), which can be viewed as a resonant tunneling process through the Shiba state with rates $\Gamma_e(\omega)$ and Γ_1 as depicted in Fig. 2(a) of the main text. When the effective electron tunneling rate ω_e is equal to Γ_1 the conductance reaches a universal value of the order of the conductance quantum. For stronger couplings the conductance decreases and the single-particle current shown in Fig. S6(b) saturates to a value determined by the relaxation rate. Indeed, Eq. (S51) yields a current $I^s = e\Gamma_1/3\hbar$ independent of tunneling strength in this regime. At even stronger coupling the Andreev current I^a exceeds the single-particle contribution and thus the total current, $I^s + I^a$, exhibits a shoulder as a function of tunnel coupling. We remind the reader that the current at the main thresholds would have additional contributions from the terms $\propto \Gamma_2\Gamma_{e/h}(\omega)$ in Eq. (S46), which we have excluded from our analytical considerations. We evaluate the full current for the quantitative comparison between theory of experiment in Sec. IV A.

We can estimate the normal state conductance G_N^* at which the Andreev current becomes the dominant contribution to the current at the threshold $eV = \Delta + \epsilon_0$ from $\Gamma_1 \sim \Gamma_h$. We obtain

$$G_N^* \sim \frac{2e^2}{h}\frac{\nu_0\Delta}{v^2}\sqrt{\frac{\epsilon_0\Gamma_1^2}{\Delta^3}}. \tag{S81}$$

In Fig. 3(a) of the main text we indicate G_N^* for the positive and negative main peaks by arrows using the parameters given in Sec. IV A.

At the crossover between regimes (ii) and (iii) the effective electron and hole tunneling rates are equal and the Andreev contribution to the conductance becomes resonant and reaches a maximum of order $2e^2/h$. In regime (iii) both contributions to the differential conductance decrease with tunneling strength. This peculiar feature arises because of the strong energy dependence of the density of states in the superconducting tip and this regime has a sizable extension only when u^2 and v^2 differ by several orders of magnitude. In the experiment this regime is presumably limited to very strong tunneling, $G_N > 0.1(2e^2/h)$, where our approach ceases to be valid as the peak width becomes of the order of ϵ_0. Furthermore the extension of this regime is too narrow to observe a decreasing peak height.

The thermal peak β_- originates entirely from single-particle tunneling and its peak height simply follows the single-particle contribution to α_+ up to a prefactor Γ_2/Γ_1 in regimes (i) and (ii). The remaining peaks α_- and β_+ have the same qualitative behavior as α_+ and β_- although with different regime boundaries, which are obtained from Eqs. (S79) and (S80) by interchanging $u \leftrightarrow v$. The peak heights of all four peaks are shown in Fig. S8(a) as a function of normal state conductance.

F. Lineshape of the Shiba resonance

In this section we analyze how the lineshape of the Shiba conductance peak is affected by the tunneling strength with important implications for fitting experimental dI/dV traces. In the linear regime the current is dominated by the single-particle contribution in Eq. (S53) and can be approximated near $eV = \Delta + \epsilon_0$ by a convolution of the BCS density of states and a Lorentzian of width Γ_1

$$I^s_{\mathrm{lin}}(V) = 2\pi e u^2 t^2 \int \frac{d\omega}{2\pi\hbar}\rho(\omega - eV)\frac{\Gamma_1}{(\omega-\epsilon_0)^2 + \Gamma_1^2/4}. \tag{S82}$$

This expression has been used previously [2, 7] to fit experimentally measured Shiba resonances. The intrinsic Lorentzian lineshape can be obtained by numerical deconvolution of the data with the BCS density of states of the tip.

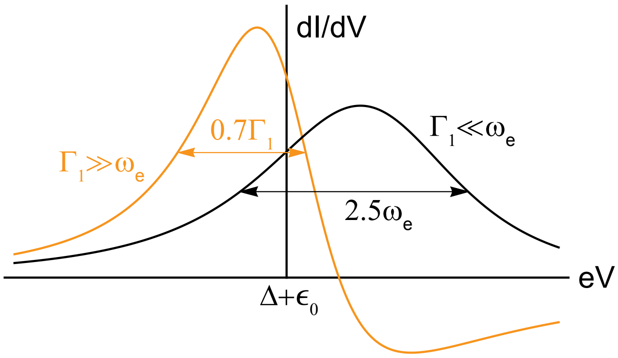

Figure S7: Lineshape of the differential conductance given by Eq. (S59) as a function of bias voltage near the main Shiba resonance at positive bias. The lineshapes differ qualitatively between the linear ($\Gamma_1 \gg \omega_e$, orange) and sublinear regimes ($\Gamma_1 \ll \omega_e$, black).

In the sublinear regime, where the broadening of the Shiba resonance is determined by the tunnel coupling Γ_e to the tip, the current reads

$$I_{\mathrm{sublin}}(V) = 2\pi e u^2 t^2 \int \frac{d\omega}{2\pi\hbar} \rho(\omega - eV) \frac{\Gamma_1 + 2\Gamma_h(\omega)}{(\omega - \epsilon_0)^2 + [\pi u^2 t^2 \rho(\omega - eV)]^2}. \tag{S83}$$

The tip density of states now also enters the width of the resonance, and this expression does not have the form of a convolution. Note that single-particle and Andreev currents give rise to almost identical lineshapes as $\Gamma_h(\omega)$ only weakly depends on energy. The lineshape of the Shiba resonance changes qualitatively from linear to sublinear regime as shown in Fig. S7, where we plot the voltage dependence of the differential conductance given by Eq. (S59). Strikingly, the maximum can occur above or below the threshold $eV = \Delta + \epsilon_0$ depending on the tunneling strength. This shift must be accounted for when determining the Shiba state energy by fitting experimental lineshapes. In addition, a characteristic negative differential conductance dip occurs for $\Gamma_1 \gg \omega_e$ but is absent in the opposite regime. The disappearance of this dip in the measured lineshape provides a further indication of the crossover between weak and strong tunneling regimes.

Our analytical results in the previous subsections refer to the differential conductance exactly at the threshold voltages $e|V| = \Delta \pm \epsilon_0$. The shift of the maximum away from the threshold yields a somewhat larger peak height. Given that the peak heights vary by orders of magnitude in the experiment this deviation of at most 35% only affects details but is inessential to our central results. Note that we calculate the actual peak height and not the threshold values in the quantitative comparison to the experimental data in Sec. IV A.

Figure 3(b) of the main text shows experimental lineshapes for different tunneling strengths. We indeed observe a vanishing of the negative differential conductance dip as the tunneling strength is increased from the linear to the sublinear regime. Along with the experimental data in Fig. 3(b) we also plot a theoretical fit based on Eqs. (S46) and (S47). To correctly fit the lineshape at the lowest normal-state conductance [$G_N = 4.5 \times 10^{-5}(2e^2/h)$, orange curve] we convoluted the theoretical $\mathrm{d}I/\mathrm{d}V$ trace with a Gaussian to model broadening introduced by the measurement setup (see also discussion in Sec. IV A). While there is overall good agreement between theory and experiment, the expected shift of the peak position is not observed. To fit the black curve [$G_N = 0.125(2e^2/h)$] we have added a voltage shift of $40\,\mu$eV. Such a shift may have various origins such as a decreasing tip gap or a smoothening of the tip's BCS singularity with increasing tunneling current. From the experiment, we cannot exclude a decrease of the tip gap by a few tens of μeV. Moreover, we consistently neglect Andreev reflections from the tip, which would introduce additional broadening terms that vary with bias voltage and shift the peak maximum. Finally, the black curve in Fig. 3(b) exhibits an additional Andreev peak with threshold $eV = -\Delta$ that overlaps with the bound state resonance at $eV = -(\Delta + \epsilon_0)$. This peak was excluded in the fit (a correct description is beyond the scope of our theory) and may shift the Shiba peak to smaller absolute voltages.

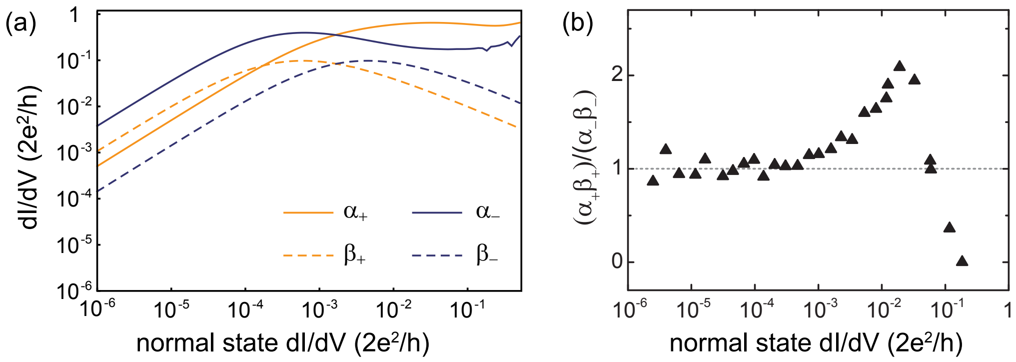

Figure S8: (a) Differential conductance peaks at the thresholds *vs.* normal state conductance according to Eqs. (S46) and (S47). We have used the parameters mentioned in Sec. IV A. (b) Plot of $(\alpha_+\beta_+)/(\alpha_-\beta_-)$ *vs.* conductance as extracted from Fig. 3(a) in the main manuscript. The ratio stays constant up to $10^{-3}\,\mathrm{G}_0$, where the sub-linear regime sets in.

IV. THEORETICAL ANALYSIS OF THE EXPERIMENTAL DATA

Our analysis implies that the subgap transport provides insight into the population dynamics of the Shiba state, as governed by the competition between tunneling and quasiparticle relaxation. We now fit the data against the results of our model and extract the quasiparticle lifetime in the Shiba state due to thermal relaxation processes. Besides demonstrating the validity of our description, this also yields valuable information about the dominant transport mechanisms in experiment as a function of the tunnel coupling between tip and sample.

A. System parameters and theory fit

Here we provide details of the theoretical fits to the conductance and current at the Shiba peaks as a function of normal state conductance, as shown in Fig. 3(a) of the main text and Fig. S9(a). Several physical parameters can be extracted directly from the measured data without fitting. The Shiba energy can be determined from the location of the Shiba peaks as a function of bias voltage. For instance, the separation between the two positive bias peaks α_+ and β_+ is $2\epsilon_0$. The same holds for α_- and β_-. From the data we estimate $\epsilon_0 \simeq 0.22\,\text{meV}$ for the lowest Shiba level. According to Eqs. (S52) and (S71) valid in the linear regime we furthermore obtain $(u/v)^2 = \alpha_+/\alpha_- \simeq 0.13$. Using Eq. (S78) in addition yields $\Gamma_1/\Gamma_2 = \alpha_+/\beta_- \simeq 4$. Finally, we can accurately determine $\Gamma_2 = 0.9(3)\,\mu\text{eV}$ from the saturation of single-particle processes as detailed in Sec. IV B. With this the dimensionless Nambu spinor component $u^2/\nu_0\Delta$ that describes the spectral weight of the Shiba state at the impurity site remains the only unknown parameter in our model. Our results also predict the relation $\alpha_+\beta_+/\alpha_-\beta_- = 1$ in the linear regime, which we can use as an additional check of the robustness of our theoretical description. According to the data shown in Fig. S8(b) this relation is satisfied remarkably well over more than two decades of normal state conductance, throughout the linear regime.

The theoretical conductance peak heights obtained numerically from Eqs. (S46) and (S47) are plotted in Fig. S8(a) as a function of the normal state conductance

$$G_N = \frac{4\pi^2\nu_0^2 t^2}{1+\pi^2\nu_0^2 t^2}. \tag{S84}$$

While several features of the theoretical curves qualitatively agree with the experimental data in Fig. 3(a) of the main text there are also notable deviations. Most prominently, theory predicts a peak in α_- at intermediate tunneling strength absent in the experiment. We attribute this deviation to broadening introduced by the measurement setup, *e.g.*, due to radio frequency noise. Indeed, in the low coupling limit we find a peak width $w \simeq 70\,\mu\text{eV}$ [see orange curve in Fig. 3(b) of the main text] exceeding Γ_1 by more than an order of magnitude. To account for the broadening we convolute the theoretical dI/dV curves with a Gaussian of width w and plot the resulting peak heights in Fig. 3(a)

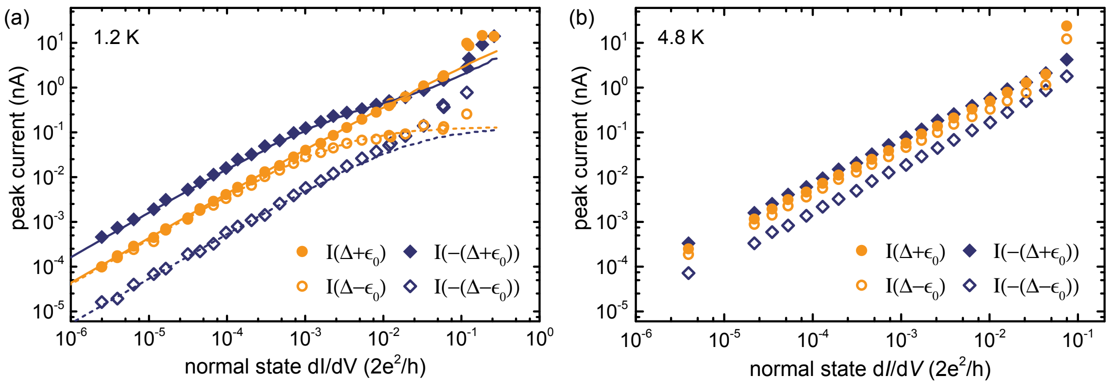

Figure S9: (a) Measured current at 1.2 K at the two main Shiba peaks ($eV = \pm(\Delta + \epsilon_0)$), and the corresponding two thermal peaks ($eV = \pm(\Delta - \epsilon_0)$). The lines show the theoretical curves using the parameters mentioned in the text. The parameters are the same as for the fit of the differential conductance in Fig. 3(a) of the main text. (b) Measured current at 4.8 K.

of the main text. We find remarkable agreement with the experimental data over the entire range of normal state conductance and determine $u^2/\nu_0\Delta \simeq 0.23$ from the fit. We associate deviations for β_- at large normal state conductances $G_N \gtrsim 0.02(2e^2/h)$ with a multiple Andreev reflection resonance involving the second Shiba state at $\epsilon_1 \simeq 0.77\,\text{meV}$. A resonance occurs at $eV = -(\Delta + \epsilon_1)/2 \simeq -1.06\,\text{meV}$ and therefore overlaps with the thermal Shiba peak at $eV = -(\Delta - \epsilon_0) \simeq -1.13\,\text{meV}$ [see black curve in Fig. 3(b) of the main text].

In Fig. S9(a), we plot the current measured at the position of the conductance peaks together with the theoretical curves. These fits use the *same* parameters as for the conductance fits, including the extrinsic broadening. We again find excellent agreement which corroborates that our model calculation correctly captures the essential tunneling processes.

B. Quasiparticle lifetime and relaxation mechanism

1. *Estimates of quasiparticle lifetimes in experiment*

The quasiparticle (quasihole) lifetimes of the Shiba state are related to the inverse relaxation rates $\tau_{1/2} = \hbar/\Gamma_{1/2}$. These rates could in principle be determined from the linewidth of the Shiba resonance at weak coupling (see Sec. III F). However, the measured linewidth is actually resolution-limited, i.e., increased by an additional broadening from the measurement setup ($\simeq 70\,\mu\text{eV}$). At $T = 1.2\,\text{K}$, the intrinsic linewidth is well below the resolution of the experiment (see Sec. IV A). A more robust way to determine the lifetime relies on the strong-tunneling regime where the data is unaffected by the energy resolution. As discussed in Sec. III E, the single-particle current saturates when $\Gamma_1 < \omega_e$ assuming a value of $I^s = e\Gamma_{1/2}/3\hbar$ at the main (thermal) thresholds. The current measured at the thermal threshold $eV = \Delta - \epsilon_0$ shown in Fig. S9(a) indeed exhibits a plateau at strong tunneling. At $eV = \Delta - \epsilon_0$, we extract a saturation current of 0.09 nA which yields relaxation rates $\Gamma_2 = 1.1\,\mu\text{eV}$ and $\Gamma_1 \simeq 4\Gamma_2 = 4\,\mu\text{eV}$. The corresponding lifetimes $\tau_1 \simeq 0.2\,\text{ns}$ and $\tau_2 \simeq 0.6\,\text{ns}$ are quoted in the main text. The current $I_{-(\Delta-\epsilon_0)}$ at the other thermal threshold does not saturate because of additional subgap features at strong tunneling discussed in Sec. IV A. The main source of uncertainty of our results is the unknown shift between the peak position, where we measure the current, and the threshold voltage, where the analytical relation between current and relaxation holds (see discussion in Sec. III F). We estimate that our results are accurate to within a factor of two.

Alternatively, we can determine Γ_1 from the current at the main threshold. Because of the additional Andreev contribution, the current $I_{-(\Delta+\epsilon_0)}$ exhibits a shoulder instead of a plateau when the single-particle current saturates [cf. Fig. S6(b)]. The current at the shoulder is 0.4 nA and thus $\Gamma_1 = 5\,\mu\text{eV}$, in agreement with the above value. While determining Γ_1 from the shoulder at the main thresholds typically has a larger uncertainty, it is furthermore subject to a systematic error due to extrinsic broadening introduced in the measurement as detailed in Sec. IV A. Note that the shoulder is absent in $I_{\Delta+\epsilon_0}$ because the Andreev current dominates already when the single-particle current saturates.

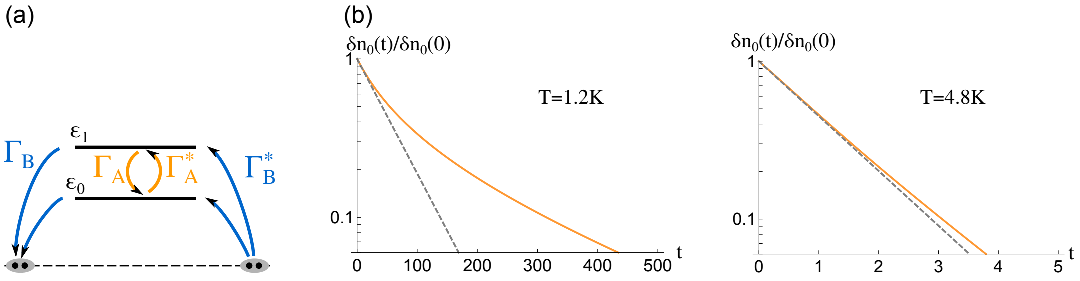

Figure S10: (a) Phonon-assisted transitions for a system of two Shiba states. Direct transitions between the bound states (with rates Γ_A and Γ_A^*) as well as exchanges of quasiparticle pairs with the condensate (Γ_B and Γ_B^*) are possible. We neglect transitions to the quasiparticle continuum. (b) Decay of a quasiparticle excitation in the first Shiba state according to Eqs. (S85) and (S86) with $n_0(0) = 1$, $n_1(0) = n_F(\epsilon_1)$, $\Gamma_A = \Gamma_B = 1$ at $T = 4.8\,\mathrm{K}$, and $\Gamma_A = 1.65$, $\Gamma_B = 1.4$ at $T = 1.2\,\mathrm{K}$. This choice accounts for a larger required phonon energy at the lower temperature. The Shiba energies $\epsilon_{0/1}$ are given in the text. The plot shows the nonequilibrium occupation number of the lower state $\delta n_0(t) = n_0(t) - n_F(\epsilon_0)$ normalized to its value at $t = 0$. The dashed lines mark the initial decay $\sim \exp(-\Gamma_{\mathrm{ph}} t)$ with $\Gamma_{\mathrm{ph}}(T = 1.2\,\mathrm{K}) = 0.016$ and $\Gamma_{\mathrm{ph}}(T = 4.8\,\mathrm{K}) = 0.8$.

This behavior is well captured by a quantitative comparison between theory and experiment in Fig. S9(a).

We finally turn to the physical mechanism underlying quasiparticle relaxation in the experiment (cf. Sec. II F). The experimental data shows no signatures of a quasiparticle bath at subgap energies as the Pb sample exhibits a hard gap away from the impurities. To assess the effect of inelastic transitions we also study transport at a higher temperature of $T = 4.8\,\mathrm{K}$. While the qualitative temperature dependence of the relaxation rates $\Gamma_{1/2}$ indicates thermal relaxation as discussed in the main text, a more quantitative analysis is required to assess the relevance of particular relaxation processes. At the higher temperature relaxation is strong enough that the single-particle current does not saturate in the tunneling regime $G_N \ll 2e^2/h$ as shown by the data in Fig. S9(b). To obtain an upper bound for the relaxation time, we estimate the saturation current to be $\gtrsim 2\,\mathrm{nA}$ which yields $\tau_2 \lesssim 30\,\mathrm{ps}$. From the conductance peaks shown in the right panel of Fig. 3(a) of the main text, we find $\alpha_-/\beta_+ = \Gamma_1/\Gamma_2 \simeq 1.6$ in the linear regime and thus $\tau_1 \lesssim 20\,\mathrm{ps}$.

We can more accurately determine $\Gamma_1 + \Gamma_2$ from the peak width in the weak-coupling regime which we find to be $\simeq 0.16\,\mathrm{meV}$ and thus larger than the broadening induced by the measurement setup. Assuming this broadening to be the same for both temperatures, we estimate $\Gamma_1 + \Gamma_2 \simeq 0.2\,\mathrm{meV}$ [note that the unbroadened peak width is $0.7(\Gamma_1 + \Gamma_2)$]. This yields $\Gamma_1 \simeq 120\,\mu\mathrm{eV}$ which corresponds to $\tau_1 \simeq 6\,\mathrm{ps}$ consistent with the upper bound estimated from the current. Hence we find the ratio of relaxation rates at the two temperatures $\Gamma_1(4.8\,\mathrm{K})/\Gamma_1(1.2\,\mathrm{K}) \simeq 35$.

2. *Relaxation dynamics for multiple Shiba states*

In Sec. II F, we have discussed relaxation based on quasiparticle transitions between Shiba state and quasiparticle continuum. This is the dominant relaxation mechanism for superconductors with only one subgap state. Based on the corresponding relaxation rate in Eq. (S49), however, we would expect a ratio $\Gamma_1(4.8\,\mathrm{K})/\Gamma_1(1.2\,\mathrm{K}) \simeq 10^4$ (using $\epsilon_0 = 0.20\,\mathrm{meV}$ and $\Delta = 1.21\,\mathrm{meV}$ at $4.8\,\mathrm{K}$). This reflects the exponential suppression of thermal relaxation at temperatures well below the activation energy $\Delta - \epsilon_0$. The large discrepancy to the experimental value suggests the presence of additional relaxation processes in this system.

Such additional relaxation processes are possible when taking the next Shiba state with energy $\epsilon_1 = 0.77\,\mathrm{meV}$ at $T = 1.2\,\mathrm{K}$ ($\epsilon_1 = 0.63\,\mathrm{meV}$ at $T = 4.8\,\mathrm{K}$) into account. Relaxation can then occur via inelastic transitions of pairs of quasiparticles from the two Shiba states to the condensate, see process Γ_B in Fig. S10(a). The strong spin-orbit coupling in Pb enables the creation of Cooper pairs even when the Shiba states have equal spin. This process dominates over transitions to the quasiparticle continuum at low temperatures as it only requires an activation energy $\epsilon_1 < \Delta - \epsilon_0$. A rough estimate for the relaxation rates based on the thermal occupation of the second Shiba state yields $\Gamma_1(4.8\,\mathrm{K})/\Gamma_1(1.2\,\mathrm{K}) \simeq 300$, which is already much closer to the experimentally observed value.

To obtain a more accurate description of the relaxation dynamics, we analyze a minimal rate-equation model of two Shiba states. Initially, we chose the lower state to be fully occupied (due to tunneling from the lead) and the higher state to be in thermal equilibrium, i.e., $n_0(0) = 1$ and $n_1(0) = n_F(\epsilon_1)$. Taking into account direct transitions between the two levels as well as transitions to the condensate with rates depicted in Fig. S10(a), we obtain the following nonlinear rate equations

$$\frac{dn_0}{dt} = -\Gamma_A^* n_0(1-n_1) + \Gamma_A(1-n_0)n_1 + \Gamma_B^*(1-n_0)(1-n_1) - \Gamma_B n_0 n_1, \tag{S85}$$

$$\frac{dn_1}{dt} = \Gamma_A^* n_0(1-n_1) - \Gamma_A(1-n_0)n_1 + \Gamma_B^*(1-n_0)(1-n_1) - \Gamma_B n_0 n_1. \tag{S86}$$

We assume the transition rates $\Gamma_{A/B}$ involving phonon emission to be quadratic in the required phonon energies $\epsilon_0 \pm \epsilon_1$ (which vary weakly with T) but otherwise temperature independent [8]. In contrast, the rates $\Gamma^*_{A/B}$ require absorption of a phonon and are suppressed by thermal factors $\Gamma_A^* = \Gamma_A \exp[-(\epsilon_1 - \epsilon_0)/T]$ and $\Gamma_B^* = \Gamma_B \exp[-(\epsilon_1 + \epsilon_0)/T]$. These relations ensure that the equilibrium occupation numbers of the two levels are given by the Fermi distribution $n_F(\epsilon)$.

Figure S10(b) shows the occupation number for the lower Shiba state relative to its equilibrium value as a function of time, as obtained from a numerical solution of the rate equations (S85) and (S86). At $T = 4.8\,\mathrm{K}$ the nonequilibrium occupation number can be well approximated by an exponential function $\sim \exp(-\Gamma_{\rm ph} t)$, from which we can estimate the relaxation rate $\Gamma_{\rm ph}$ defined in Sec. II C. In contrast, at $T = 1.2K$ the occupation number decays rapidly on short time scales before turning to a somewhat slower decay at longer times. This nonexponential decay follows from the nonlinearity of the coupled rate equations. The experimental estimate for the relaxation rate at $T = 1.2\,\mathrm{K}$ is based on the current relaxation in the strong tunneling regime, where the tunneling is faster than relaxation. In this limit, the dynamics between two tunneling events is fully determined by the short-time decay. By fitting the occupation number in Fig. S10(b) at short times with $\sim \exp(-\Gamma_{\rm ph} t)$, we obtain an approximate measure of the effective relaxation rate from which we determine $\Gamma_1 = \Gamma_{\rm ph}[1 - n_F(\epsilon_0)]$. The fit in Fig. S10(b) yields $\Gamma_1(4.8\,\mathrm{K})/\Gamma_1(1.2\,\mathrm{K}) \simeq 33$ in quantitative agreement with the experimentally observed ratio. We have checked that the same result is obtained when transitions to the condensate are suppressed by the need for spin-orbit interaction, $\Gamma_B < \Gamma_A$.

[1] M. Ruby, B.W. Heinrich, J. I. Pascual, and K. J. Franke, Phys. Rev. Lett. **114**, 157001 (2015).
[2] S.-H. Ji, T. Zhang, Y.-S. Fu, X. Chen, X.-C. Ma, J. Li, W.-H. Duan, J.-F. Jia, and Q.-K. Xue, Phys. Rev. Lett. **100**, 226801 (2008).
[3] I. Martin and D. Mozyrsky, Phys. Rev. B **90**, 100508 (2014).
[4] J. C. Cuevas, A. Martín Rodero, and A. Levy Yeyati, Phys. Rev. B, **54**, 7366 (1996)
[5] H. Haug and A.-P. Jauho, *Quantum Kinetics in Transport and Optics of Semiconductors*, (Springer, 2008).
[6] A.G. Kozorezov, A.A. Golubov, J.K. Wigmore, D. Martin, P. Verhoeve, R.A. Hijmering, and I. Jerjen, Phys. Rev. B **78**, 174501 (2008).
[7] K.J. Franke, G. Schulze, J.I. Pascual, Science **332**, 940 (2011).
[8] D.A. Ivanov and M.V. Feigel'man, JETP Lett. **68**, 890 (1998)

B.4 Physical Review Letters 117, 186801 (2016)

Michael Ruby, Yang Peng, Felix von Oppen,
Benjamin W. Heinrich, and Katharina J. Franke

Orbital Picture of Yu-Shiba-Rusinov Multiplets

doi:10.1103/PhysRevLett.117.186801

PRL **117,** 186801 (2016) PHYSICAL REVIEW LETTERS week ending 28 OCTOBER 2016

Orbital Picture of Yu-Shiba-Rusinov Multiplets

Michael Ruby,[1] Yang Peng,[2] Felix von Oppen,[2] Benjamin W. Heinrich,[1] and Katharina J. Franke[1]
[1]*Fachbereich Physik, Freie Universität Berlin, 14195 Berlin, Germany*
[2]*Dahlem Center for Complex Quantum Systems and Fachbereich Physik, Freie Universität Berlin, 14195 Berlin, Germany*

(Received 11 August 2016; published 24 October 2016)

We investigate the nature of Yu-Shiba-Rusinov (YSR) subgap states induced by single manganese (Mn) atoms adsorbed on different surface orientations of superconducting lead (Pb). Depending on the adsorption site, we detect a distinct number and characteristic patterns of YSR states around the Mn atoms. We suggest that the YSR states inherit their properties from the Mn d levels, which are split by the surrounding crystal field. The periodicity of the long-range YSR oscillations allows us to identify a dominant coupling of the d states to the outer Fermi sheet of the two-band superconductor Pb.

DOI: 10.1103/PhysRevLett.117.186801

Local magnetic moments in metals induce potential and exchange scattering of quasiparticles. When the metal enters the superconducting state, this leads to the formation of localized bound states within the superconducting gap, referred to as Yu-Shiba-Rusinov (YSR) states [1–3]. In the simplest picture, the magnetic moment is viewed as a classical impurity spin, which is exchange coupled to itinerant electrons with an isotropic Fermi surface. Treating the exchange coupling as local and isotropic, a single particle-hole symmetric pair of YSR states is predicted within the gap whose wave functions oscillate with a wavelength λ_F (λ_F being the Fermi wavelength) [3–6]. Anisotropy of the Fermi surface induces a scattering pattern reflecting the symmetry of the host lattice, as discussed theoretically and observed in recent experiments [7,8].

With sufficient resolution, experiments show not only one, but several pairs of YSR resonances [9–11]. The origin of multiple YSR resonances was assigned to scattering channels with different angular momenta ($l = 0, 1, 2, \ldots$) [9,12], or to the anisotropy splitting of the magnetic states of the adsorbate [11,13]. The arguments were based solely on the energetic alignment of the YSR states and not on the spatial extension and patterns of the states, which would allow one to establish a link with the orbital structure of the magnetic impurity.

Here, we address the origin of multiple YSR states by combining scanning tunneling microscopy and spectroscopy (STM and STS) experiments, which are powerful tools to map the energetic and spatial characteristics of energy levels, with a theoretical analysis.

Our study is based on Mn adatoms placed on a Pb substrate. The main advantage of this system is that the Mn adatoms are expected to be in the Mn^{++} configuration with five d electrons. According to Hund's rules, the Mn d shell is in a ${}^6S_{5/2}$ configuration and, hence, spherically symmetric. Thus, the ion cannot change the angular momentum of the conduction electrons in an isotropic environment and in the absence of spin-orbit coupling, which facilitates comparison between experiment and theory. The s-wave superconductor Pb is an experimentally well-studied substrate due to its high critical temperature ($T_c = 7.2$ K), which can be readily prepared by standard ultrahigh vacuum preparation techniques [9–11,14]. It also constitutes an appealing substrate for topologically nontrivial nanostructures [15–21]. Therefore, it would be rewarding to develop a more systematic understanding of magnetic adatom systems, reaching all the way from monomers and dimers to chains or even two-dimensional arrays. Because Pb possesses two disjunct Fermi surfaces, it is a two-band superconductor with two distinct gaps [22], which can be resolved in STM experiments [14]. Our study provides evidence that the YSR states in this system are predominantly associated with one of the two bands.

The experiments were carried out in a Specs JT-STM under ultrahigh vacuum conditions at a temperature of 1.2 K. The Pb single crystals were cleaned by Ne^+ ion sputtering (900 eV, 1.5×10^{-4} mbar, background pressure $<1.5 \times 10^{-9}$mbar). Annealing to 430 K for 30 min results in clean, flat, and superconducting terraces. Spectra of the differential conductance dI/dV as a function of sample bias V were acquired with a standard lock-in technique at a frequency of 912 Hz. To achieve high energy resolution, we cover etched W tips with Pb by deep indentations into the clean Pb surface until superconductor-superconductor tunneling spectra are measured. The use of a superconducting tip together with an elaborate grounding and rf-filtering setup yields effective energy resolutions of $\approx 60\ \mu$eV at 1.2 K. Using superconducting tips involves a convolution of the densities of states of tip and substrate, so that all subgap states ϵ appear shifted by the superconducting gap of the tip (Δ_{tip}) to an energy $\mathrm{eV} = \pm(\epsilon + \Delta_{\mathrm{tip}})$ [23]. Mn adatoms were evaporated onto the clean sample in the STM at a temperature below 15 K, resulting in a density of $\simeq 100$ atoms per $100 \times 100\ \mathrm{nm}^2$.

We first deposit Mn atoms on the Pb(001) surface. All Mn adatoms adsorb in equivalent sites, which we call $\mathrm{Mn}_{\mathrm{Pb}(001)}$.

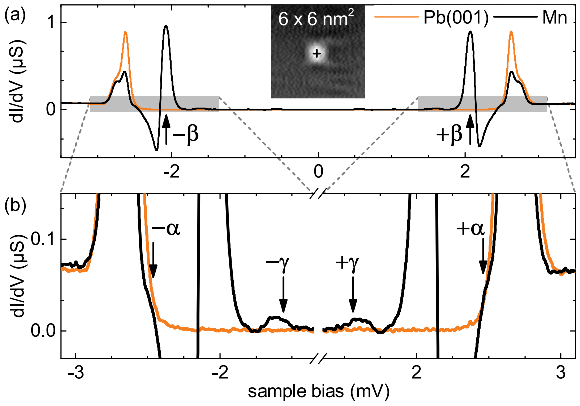

FIG. 1. (a),(b) dI/dV spectrum of a Mn adatom (black) and of clean Pb(001) (orange). The inset shows a topography of the adatom. Three subgap resonances $\pm\alpha$, $\pm\beta$, and $\pm\gamma$ are marked by arrows. Set point: 300 pA, 5 mV; modulation: 15 μV_{rms}.

The adsorption site is stable against manipulation with the tip. In topography, the adatoms display a fourfold shape and a height of 0.15 Å at 5 mV [Fig. 1(a), inset]. Spectra on top of the adatoms reveal three pairs of YSR resonances inside the superconducting gap. The one with the largest spectral intensity (labeled $\pm\beta$) is found at a bias voltage of $\simeq \pm 2.08$ mV [Fig. 1(a)], complemented by two faint resonances at $\simeq \pm 2.47$ and $\simeq \pm 1.61$ mV [Fig. 1(b)]. We label the latter resonances as $\pm\alpha$, and $\pm\gamma$, respectively.

The spatial patterns of all three YSR states show characteristic fourfold symmetries [Fig. 2(b)], with extensions up to ≈1.6 nm. This is an order of magnitude larger than the atomic radius. The resonances $\pm\beta$ show intensity mainly at the center of the impurity, with some weak intensity along the $\langle 110 \rangle$ directions. Because of their large intensity we observe a negative differential conductance (NDC) [see Figs. 1(a) and 1(b)]. The maps at $\pm\alpha$ are dominated at the center by this NDC because of the energetic overlap of $\pm\beta$ with $\pm\alpha$; hence, the maps show no spectral intensity here; they show no spectral intensity here. The intensity is largest at a distance of ≃0.9 nm away from the center. The map at $+\gamma$ resolves a clover leaf pattern along the $\langle 100 \rangle$ directions, whereas we hardly detect any signal for $-\gamma$.

The YSR patterns resemble the shape of d orbitals and thus suggest a correlation of the YSR resonances and the orbitals hosting an unpaired electron spin. This requires a splitting of the d states of Mn due to the crystal field imposed by the adsorption site. In a hollow site, the nearest neighbors form a square pyramidal coordination symmetry, which removes the degeneracy of the five d levels [Figs. 2(c) and 2(d)]. According to simple arguments of crystal field theory, the $d_{x^2-y^2}$-orbital lies highest, followed by the d_{z^2} orbital, the degenerate d_{xz} and d_{yz} orbitals, and the d_{xy} orbital at the lowest energy. The energy separation between $d_{xz/yz}$ and d_{xy} depends on the ratio of in-plane and out-of-plane bonding distances and the levels become degenerate for an adsorption configuration with all distances being equal. Indeed, we find hints that resonance $\pm\gamma$ is composed of almost degenerate states, as it splits up upon interaction with neighboring atoms (see Supplemental Material [24]).

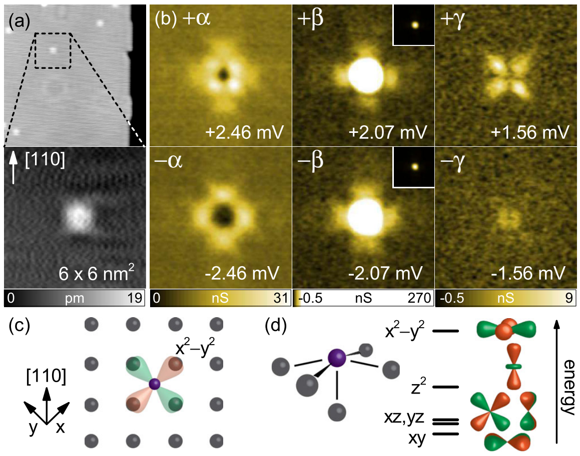

FIG. 2. (a) Topography of a Mn adatom on Pb(001). Set point: 50 mV (zoom: 5 mV), 150 pA. (b) dI/dV maps of the adatom depicted in (a) at the energy of the subgap resonances $\pm\alpha$, $\pm\beta$, and $\pm\gamma$ (feedback opened in each pixel at 5 mV and 150 pA; modulation: 25 μV_{rms}). The color scale of $\pm\beta$ is stretched to enhance low intensity features (inset shows $\pm\beta$ with linear scale). The center is ∼100 times more intense than the fourfold symmetric lobes. (c) Schematic top view of the adsorption of a Mn adatom in the (001) hollow site. (d) Corresponding crystal field splitting of the d levels.

Simple models of YSR states rely on scattering of $l = 0$ conduction electrons (for a notable exception, see Ref. [27]). However, as emphasized by Schrieffer [28], only $l = 2$ conduction electrons are (potential and exchange) scattered by Mn^{++} impurities in an isotropic metal, which is a consequence of their S-state nature. Starting with the isotropic case, we can then account for lattice and surface effects by the addition of anisotropic crystal fields which (partially) remove the degeneracy between the d levels and make the potential and exchange coupling with the impurity orbital dependent [27] (as follows from a standard Schrieffer-Wolff transformation [28,29]). This structure is then inherited by the YSR states (see Supplemental Material [24]). This picture suggests that Mn^{++} impurities actually induce five pairs of YSR states whose degeneracies and spatial patterns reflect the crystal-field-split d orbitals.

We now aim for an identification of the specific d orbitals that give rise to the YSR resonances $\pm\alpha$, $\pm\beta$, and $\pm\gamma$. The fact that β is the most intense resonance indicates that it has the largest wave function overlap with the tip

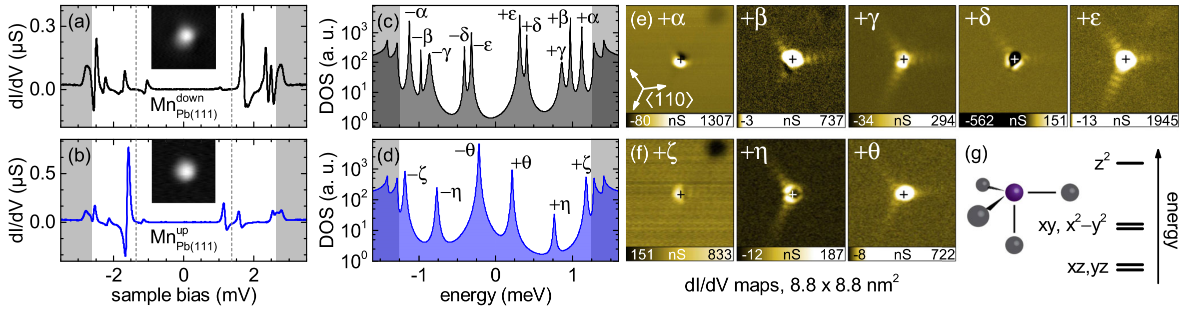

FIG. 3. (a),(b) dI/dV spectra of the same Mn adatom on Pb(111) in the two adsorption sites as indicated in the figure. The shaded areas mark the two BCS coherence peaks [14] and the normal state. The dashed lines indicate the tip gap (±1.38 mV). Set point: 100 pA, 5 mV; lock-in modulation: 15 μV_{rms}. The insets show topographies of the adatom in the respective adsorption site ($2.6 \times 2.6 \mathrm{nm}^2$). (c) Deconvolved sample density of states of $\mathrm{Mn}^{\mathrm{down}}_{\mathrm{Pb(111)}}$ exhibits five YSR resonances ($\pm\alpha, \ldots, \pm\epsilon$). (d) Deconvolved density of states of $\mathrm{Mn}^{\mathrm{up}}_{\mathrm{Pb(111)}}$ shows three YSR resonances ($\pm\zeta, \pm\eta, \pm\theta$). (e),(f) dI/dV maps of the YSR resonances in both adsorption sites (feedback opened in each pixel at 5 mV and 400 pA; modulation: 20 μV_{rms}). Crosses denote the same position in all maps. The dark spot in the top right corner is a subsurface neon inclusion. The color scale is stretched to give the best contrast to spatially extended features (for maps with linear color scale, see Supplemental Material [24]). (g) Crystal field splitting of the d levels for an adatom in a hollow site.

[note the color scale in Fig. 2(b)]. Moreover, the main intensity is spherically symmetric [inset of Fig. 2(b)]. Both arguments suggest that β originates from scattering at the d_{z^2} orbital, which is oriented along the surface normal. We note that both resonance α and γ exhibit the largest intensity along the $\langle 100 \rangle$ directions, i.e., towards the nearest neighbors. Hence, an assignment solely based on directions is not *a priori* possible. Instead, we rely on the above mentioned observation of the degeneracy of $\pm\gamma$. It includes the $d_{xz,yz}$ and d_{xy} orbitals as scattering centers, whereby the latter is oriented in plane and thus only contributes weakly to tunneling. Then, resonance α is induced by scattering from the $d_{x^2-y^2}$ orbital.

In addition to the influence of the orbital symmetry, the long-range scattering pattern obtains structure from the anisotropy of the Fermi surface [7]. In case of Pb(001), the projected Fermi surface obeys a C_4 symmetry. Electron (hole) propagation along the $\langle 110 \rangle$ directions appears enhanced due to focusing perpendicular to the low-curvature regions of the Fermi surface [14,30,31]. The anisotropy of the Fermi surface thus amplifies the C_{4v} angular dependence of the d orbitals. This imprints a faint fourfold shape on the YSR patterns. In the case of the d_{z^2} orbital ($\pm\beta$) it is ~100 times smaller than the spherically symmetric central part of the resonance [compare Fig. 2(b) with insets].

In order to test the validity of our model, we carried out similar experiments on Pb(111). This surface imposes a different crystal field on the adsorbate so that we expect different characteristic YSR energies and patterns. Deposition of Mn on Pb(111) leads to a unique adsorption site for all adatoms. In topography, they appear with a height of ≈0.5 Å at 50 mV and a slightly oval shape along one of the three $\langle 110 \rangle$ directions [see inset in Fig. 3(a)].

By approaching the STM tip on top of a Mn adatom at $V = +5$ mV until contact formation, the atom is transferred from the initial adsorption site to a site with a larger apparent height (≈1.1 Å at 50 mV) and a fully symmetric appearance in topography [10]. The initial adsorption configuration is recovered by contact formation at $V = -180$ mV, which yields the original height and shape, with the oval shape being oriented along one of the three $\langle 110 \rangle$ directions, though not necessarily the initial one. We refer to the two adsorption sites according to their apparent heights as $\mathrm{Mn}^{\mathrm{down}}_{\mathrm{Pb(111)}}$ and $\mathrm{Mn}^{\mathrm{up}}_{\mathrm{Pb(111)}}$, respectively.

Both adsorption sites show several YSR resonances inside the superconducting energy gap at $eV = \pm(\epsilon + \Delta_{\mathrm{tip}})$ [Figs. 3(a) and 3(b)]. [In addition, we also observe resonances at $eV = \pm(\Delta_{\mathrm{tip}} - \epsilon)$ which originate from thermally activated tunneling into or out of YSR states [10] and are restricted to small ϵ at 1.2 K.] The deconvolved density of states is plotted in Figs. 3(c) and 3(d) [32]. Interestingly, we observe different numbers of YSR resonances for the two adsoption sites, in addition to shifts in energy. For $\mathrm{Mn}^{\mathrm{down}}_{\mathrm{Pb(111)}}$ adatoms, we resolve five YSR resonances, independent of the direction of the oval appearance. In contrast, $\mathrm{Mn}^{\mathrm{up}}_{\mathrm{Pb(111)}}$ adatoms exhibit only three resonances.

The multiplicity of the YSR states is consistent with certain adsorption sites. The threefold multiplicity of the $\mathrm{Mn}^{\mathrm{up}}_{\mathrm{Pb(111)}}$ adsorption site agrees with a hollow site, which is subject to a trigonal pyramidal crystal field. This induces a d-level splitting with the d_{z^2} orbital lying highest in energy, followed by the degenerate d_{xy} and $d_{x^2-y^2}$ orbitals. Lowest in energy are the degenerate d_{xz} and d_{yz} orbitals [Fig. 3(g)]. The fivefold multiplicity of the YSR resonances of $\mathrm{Mn}^{\mathrm{down}}_{\mathrm{Pb(111)}}$ indicates the removal of all degeneracies of the d orbitals. This is the case when the atom is slightly displaced from a hollow site, which is consistent with its oval-shaped appearance.

Next, we investigate the spatial distribution of the YSR resonances by dI/dV maps at the respective energies. They are shown for positive bias voltages in Fig. 3(e) for $\mathrm{Mn}^{\mathrm{down}}_{\mathrm{Pb}(111)}$ and in Fig. 3(f) for the same atom after manipulation into the $\mathrm{Mn}^{\mathrm{up}}_{\mathrm{Pb}(111)}$ adsorption state. Maps at negative bias voltages reveal similar patterns (see Supplemental Material [24]). The maps do not reflect the typical fourfold shape of the Mn d orbitals. The $C_{3\mathrm{v}}$ symmetry of the ligand field polarizes the d orbitals due to hybridization with the p orbitals [33]. As a result, the characteristic d-orbital shapes are deformed, resulting in an overall twofold symmetry as reflected in the YSR maps. We may tentatively assign the YSR states by arguments of wave function overlap with the tip. Both $\pm\theta$ and $\pm\zeta$ show a large intensity signifying an out-of-plane extension of the wave function. The spherical symmetry of $\pm\theta$ at the impurity site suggests that it originates from scattering at the d_{z^2} orbital. Resonances $\pm\zeta$ would thus correspond to the degenerate d_{xz} and d_{yz} orbitals. The in-plane $d_{x^2-y^2}$ and d_{xy} orbitals possess the smallest wave function overlap and hence the lowest intensity at $\pm\eta$.

Another interesting feature is the large lateral extension of several of the YSR states. Three (β,γ, ε) of the five states of the $\mathrm{Mn}^{\mathrm{down}}_{\mathrm{Pb}(111)}$ adatoms and two (η, θ) of the three states of $\mathrm{Mn}^{\mathrm{up}}_{\mathrm{Pb}(111)}$ persist up to 4 nm away from the adsorbate [Figs. 3(e) and 3(f)]. The beamlike extension along the $\langle 110\rangle$ axes is due to the focusing of scattering electrons from the flat parts of the Fermi surface. We identify oscillating intensities within the beams. Indeed, an oscillation with $2k_F$ is expected for YSR states, because their wave functions obey [3]

$$\psi^{\pm}(r) \propto \frac{\sin(k_F r + \delta^{\pm})}{k_F r} \exp\left(-|\sin(\delta^{+} - \delta^{-})| \frac{r}{\xi}\right). \tag{1}$$

Here, k_F is the Fermi wave vector, ξ is the coherence length, and $\delta^{\pm}$ are the scattering phase shifts of the YSR states at positive and negative bias, respectively. The electron density $|\psi(r)|^2$ thus decays as $1/r^2$. We have removed this dependence by a fit to the decaying intensity of states $\pm\theta$ and $\pm\eta$ (for details see Supplemental Material [24]). The result is plotted in Fig. 4 and highlights the oscillations. We observe up to four periods with a periodicity of $\simeq$5.8 Å, which should be compared to the Fermi wavelength of the substrate. Pb possesses two disjunct Fermi sheets [22]. One sheet is s-p-like and originates from the second Brillouin zone, the other one is p-d-like and originates from the third Brillouin zone. The peculiar band structure gives rise to two superconducting energy gaps [14,22], which we also observe in the dI/dV spectra. The corresponding Fermi wavelengths along the $\langle 110\rangle$ direction are $\lambda_F = 7.8 \pm 0.8$ Å for the first, and $\lambda_F = 12.1 \pm 0.5$ Å for the second band [34]. The observed periodicity agrees with $\lambda_F/2$ of the second Fermi sheet. Hence, the YSR resonances arise due to magnetic scattering with electrons in the p-d-like band. This is a reasonable conjecture in view of the more localized character of this band compared to the more delocalized nature of the s-p-like band.

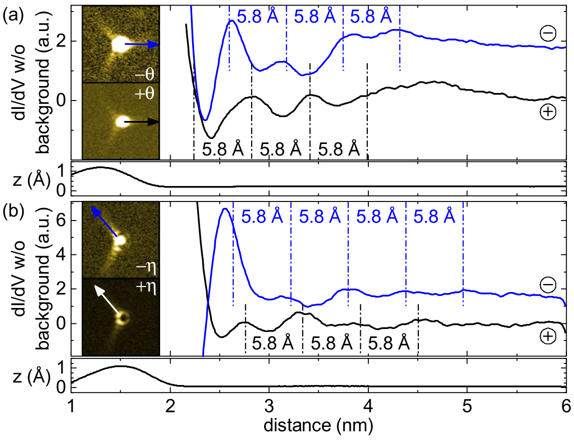

FIG. 4. Lateral evolution of the spectral intensity at positive (black) and negative bias (blue) of the two YSR resonances with lowest binding energy for $\mathrm{Mn}^{\mathrm{up}}_{\mathrm{Pb}(111)}$. Set point: 400 pA, 4 mV; modulation: 20 μV. The blue curve is offset by $+1.5$. The $1/r^2$ decay has been removed (for full data see Supplemental Material [24]). The insets show the dI/dV maps at the corresponding energies. The arrows mark the direction along which the intensity is plotted. The z profile gives the apparent height along the distance from the impurity center.

The oscillations of holelike and electronlike YSR resonances are phase shifted in Fig. 4 with a larger shift between resonances $\pm\theta$ compared to resonances $\pm\eta$. This agrees with the dependence of the binding energies of the YSR states on the phase shifts according to $\epsilon = \Delta\cos(\delta^{+} - \delta^{-})$. It implies that the closer states are to the gap edge the smaller is the phase shift between the positive and negative YSR component.

To summarize, we investigated YSR states of transition metal adatoms on high symmetry surfaces of the BCS superconductor Pb. The adsorption site imposes a distinct crystal field splitting on the d orbitals. We could show that the YSR states inherit the symmetry of the scattering potential from the individual d orbitals of the adatom. On the Pb(001) surface, spatially resolved conductance maps allow us to identify the corresponding d orbitals. The strong influence of the anisotropic Fermi surface overwhelms this assignment on the Pb(111) surface. The oscillatory patterns reveal the Fermi wavelength of the p-d-like Fermi sheet to be responsible for the scattering pattern. The long-range and directional nature of the states are promising for the design of coupled adatom structures.

We acknowledge funding by the Deutsche Forschungsgemeinschaft through Grant No. FR2726/4 and through collaborative research Grants No. Sfb 658, No. CRC 183, and No. SPP 1666, as well as by the European Research Council through Consolidator Grant NanoSpin.

Note added.—Recently, we became aware of related work on Cr atoms on Pb(111) [35].

[1] L. Yu, Acta Phys. Sin. **21**, 75 (1965).
[2] H. Shiba, Prog. Theor. Phys. **40**, 435 (1968).
[3] A. I. Rusinov, Zh. Eksp. Teor. Fiz. Pisma Red. **9**, 146 (1968) [JETP Lett. **9**, 85 (1969)].
[4] A. L. Fetter, Phys. Rev. **140**, A1921 (1965).
[5] A. Yazdani, B. A. Jones, C. P. Lutz, M. F. Crommie, and D. M. Eigler, Science **275**, 1767 (1997).
[6] A. V. Balatsky, I. Vekhter, and J.-X. Zhu, Rev. Mod. Phys. **78**, 373 (2006).
[7] M. I. Salkola, A. V. Balatsky, and J. R. Schrieffer, Phys. Rev. B **55**, 12648 (1997).
[8] G. C. Ménard, S. Guissart, C. Brun, S. Pons, V. S. Stolyarov, F. Debontridder, M. V. Leclerc, E. Janod, L. Cario, D. Roditchev, P. Simon, and T. Cren, Nat. Phys. **11**, 1013 (2015).
[9] S.-H. Ji, T. Zhang, Y.-S. Fu, X. Chen, X.-C. Ma, J. Li, W.-H. Duan, J.-F. Jia, and Q.-K. Xue, Phys. Rev. Lett. **100**, 226801 (2008).
[10] M. Ruby, F. Pientka, Y. Peng, F. von Oppen, B. W. Heinrich, and K. J. Franke, Phys. Rev. Lett. **115**, 087001 (2015).
[11] N. Hatter, B. W. Heinrich, M. Ruby, J. I. Pascual, and K. J. Franke, Nat. Commun. **6**, 8988 (2015).
[12] M. E. Flatté and J. M. Byers, Phys. Rev. B **56**, 11213 (1997).
[13] R. Zitko, O. Bodensiek, and T. Pruschke, Phys. Rev. B **83**, 054512 (2011).
[14] M. Ruby, B. W. Heinrich, J. I. Pascual, and K. J. Franke, Phys. Rev. Lett. **114**, 157001 (2015).
[15] S. Nadj-Perge, I. K. Drozdov, J. Li, H. Chen, S. Jeon, J. Seo, A. H. MacDonald, B. A. Bernevig, and A. Yazdani, Science **346**, 602 (2014).
[16] R. Pawlak, M. Kisiel, J. Klinovaja, T. Meier, S. Kawai, T. Glatzel, D. Loss, and E. Meyer, arXiv:1505.06078.
[17] M. Ruby, F. Pientka, Y. Peng, F. von Oppen, B. W. Heinrich, and K. J. Franke, Phys. Rev. Lett. **115**, 197204 (2015).
[18] J. Röntynen and T. Ojanen, Phys. Rev. Lett. **114**, 236803 (2015).
[19] Y. Kim, J. Zhang, E. Rossi, and R. M. Lutchyn, Phys. Rev. Lett. **114**, 236804 (2015).
[20] G. C. Ménard, S. Guissart, C. Brun, M. Trif, F. Debontridder, R. T. Leriche, D. Demaille, D. Roditchev, P. Simon, and T. Cren, arXiv:1607.06353v1.
[21] J. Li, T. Neupert, Z. Wang, A. H. MacDonald, A. Yazdani, and B. A. Bernevig, Nat. Commun. **7**, 12297 (2016).
[22] A. Floris, A. Sanna, S. Massidda, and E. K. U. Gross, Phys. Rev. B **75**, 054508 (2007).
[23] Note that the spectra reflect the density of states of the YSR states because they are recorded in the weak tunneling regime [10].
[24] See Supplemental Material http://link.aps.org/supplemental/10.1103/PhysRevLett.117.186801, which includes Refs. [25,26], for a description of the theoretical analysis of orbital-dependent Yu-Shiba-Rusinov states and of the crystal field splitting, as well as additional experimental data, i.e., dI/dV maps and raw data.
[25] A. M. Tsvelick and P. B. Wiegmann, Adv. Phys. **32**, 453 (1983).
[26] M. S. Dresselhaus, G. Dresselhaus, and A. Jorio, *Group Theory: Application to the Physics of Condensed Matter* (Springer, Berlin, 2007).
[27] C. P. Moca, E. Demler, B. Jankó, and G. Zaránd, Phys. Rev. B **77**, 174516 (2008).
[28] J. R. Schrieffer, J. Appl. Phys. **38**, 1143 (1967).
[29] A. C. Hewson, *The Kondo Problems to Heavy Fermions* (Cambridge University Press, Cambridge, England, 1993).
[30] O. Kurnosikov, J. H. Nietsch, M. Sicot, H. J. M. Swagten, and B. Koopmans, Phys. Rev. Lett. **102**, 066101 (2009).
[31] A. Weismann, M. Wenderoth, S. Lounis, P. Zahn, N. Quaas, R. G. Ulbrich, P. H. Dederichs, and S. Blügel, Science **323**, 1190 (2009).
[32] M. Ruby, SoftwareX, doi: 10.1016/j.softx.2016.04.001 (2016).
[33] Y. Jean, *Molecular Orbitals of Transition Metal Complexes* (Oxford University Press, New York, 2005).
[34] G. I. Lykken, A. L. Geiger, K. S. Dy, and E. N. Mitchell, Phys. Rev. B **4**, 1523 (1971).
[35] D.-J. Choi, C. Rubio-Verdú, J. de Bruijckere, M. M. Ugeda, N. Lorente, and J. I. Pascual, arXiv:1608.03752.

Supplementary Material
Orbital Picture of Yu-Shiba-Rusinov Multiplets

Michael Ruby,[1] Yang Peng,[2] Felix von Oppen,[2] Benjamin W. Heinrich,[1] and Katharina J. Franke[1]

[1] *Fachbereich Physik, Freie Universität Berlin, 14195 Berlin, Germany*

[2] *Dahlem Center for Complex Quantum Systems and Fachbereich Physik, Freie Universität Berlin, 14195 Berlin, Germany*

THEORETICAL BACKGROUND

The Manganese (Mn) adatoms are presumably in a $^6\mathrm{S}_{5/2}$ configuration. When placed in an isotropic environment, this implies that the exchange interaction is with the $l = 2$ conduction electrons and conserves angular momentum [1]. Lifting the degeneracy between the d-levels is the result of crystal-field splittings reflecting the anisotropy of the host, and the resulting multiplicities are largely determined by symmetry considerations. The splittings as well as the orbital dependence of the hybridization imply that the exchange and potential couplings between magnetic impurity and conduction electrons become orbital dependent.

When the magnetic impurity is placed in an isotropic superconductor, one thus expects five pairs of degenerate YSR states. Similar to the d-levels, the YSR states will split due to the symmetry reduction by crystal fields. One way of thinking about this splitting is as a result of the modification of the d-level energies and hybridizations mentioned above. Alternatively, we can first compute the Shiba states for a completely isotropic environment and then consider their splitting resulting from the symmetry reduction. As the results are controlled by group theory, both approaches give identical results as long as we do not attempt to compute specific values of energy levels. In the following, we briefly sketch the second approach.

Yu-Shiba-Rusinov states

Let us consider a homogeneous s-wave superconductor whose Hamiltonian in real space can be written as

$$H_s = \int dr \left\{ \sum_\sigma \psi^\dagger_\sigma(\mathbf{r}) \left[\frac{-\nabla^2}{2m} - \mu \right] \psi_\sigma(\mathbf{r}) + \Delta^* \psi_\uparrow(\mathbf{r}) \psi_\downarrow(\mathbf{r}) + \Delta \psi^\dagger_\downarrow(\mathbf{r}) \psi^\dagger_\uparrow(\mathbf{r}). \right\} \tag{S1}$$

Here $\psi_\sigma(\mathbf{r})$ annihilates an electron with spin σ at position $\mathbf{r}$, Δ is the superconducting order parameter and μ is the chemical potential. It is convenient to represent the electron field operators in the basis of spherical waves centered at the position of the impurity atom, namely

$$\psi_\sigma(\mathbf{r}) = \sum_{klm} c_{klm\sigma} \phi_{klm}(\mathbf{r}), \tag{S2}$$

where

$$\phi_{klm}(\mathbf{r}) = j_l(kr) Y_l^m(\hat{\mathbf{r}}), \quad m = -l, -l+1, \dots l \tag{S3}$$

with $l \in \mathbb{N}_0$, j_l the spherical Bessel function of order l, and Y_l^m the spherical harmonics of degree l and order m. Thus, we decompose the electrons in the superconductor into different angular-momentum channels,

$$H_s = \sum_{klm} c^\dagger_{klm\sigma} c_{klm\sigma} \xi_k + (-)^m \left[\Delta c_{klm\uparrow} c_{kl-m\downarrow} + \Delta c^\dagger_{kl-m\downarrow} c^\dagger_{klm\uparrow} \right] \tag{S4}$$

$$\xi_k = \frac{k^2}{2m} - \mu. \tag{S5}$$

In the situation we are considering here, the impurity atom is Mn^{++}, whose ground state is $^6S_{5/2}$ with a half-filled $3d$ shell. It was shown [1, 2] that, to lowest order, only the $l = 2$ channel electrons get scattered due to the impurity. Hence, in the following, we will only include the $l = 2$ conduction electrons in the Hamiltonian, and suppress this index. The full Hamiltonian including the impurity becomes

$$H = \sum_{m=-2}^{2} \left\{ \sum_{k\sigma} c^\dagger_{km\sigma} c_{km\sigma} \xi_k + (-)^m \sum_k \left(\Delta c_{km\uparrow} c_{k-m\downarrow} + \Delta c^\dagger_{k-m\downarrow} c^\dagger_{km\uparrow} \right) \right\} + \sum_{\sigma\sigma'} \sum_{kk'} \left(J \mathbf{S} \cdot \boldsymbol{\sigma}_{\sigma\sigma'} + V \delta_{\sigma\sigma'} \right) c^\dagger_{km\sigma} c_{km\sigma'}, \tag{S6}$$

where J and V are the strengths of the exchange the potential coupling between the impurity atom and the conduction electrons. If we assume the impurity spin $\mathbf{S}$ to be aligned along z direction, the last term in the Hamiltonian can be written as

$$JS(c^\dagger_{km\uparrow}c_{km\uparrow} - c^\dagger_{km\downarrow}c_{km\downarrow}).$$

Introducing Nambu spinor $C_{km} = (c_{km\uparrow}, c^\dagger_{k-m\downarrow})^T$, we have the Bogoliubov–de Gennes Hamiltonian

$$H = \sum_{m=-2}^{2}\left\{\sum_k C^\dagger_{km}\mathcal{H}_s C_{km} + \sum_{kk'}\left(JS + V\tau_z\right)C^\dagger_{km}C_{k'm}\right\} \tag{S7}$$

$$\mathcal{H}_s = \xi_k\tau_z + (-)^m\Delta\tau_x. \tag{S8}$$

Here, τ_α denotes Pauli matrices in particle-hole space.

The Green function corresponding to the above Hamiltonian fulfills the Dyson equation

$$G_{kk'm}(E) = g_{km}(E)\delta_{kk'} + g_{km}(E)\left(JS + V\tau_z\right)\sum_{k_1}G_{k_1k'm}(E), \tag{S9}$$

where g_{km} is the Green function of the homogeneous superconductor without the impurity,

$$g_{km}(E) = (E - \xi_k\tau_z - (-)^m\Delta\tau_x)^{-1} = \frac{E + \xi_k\tau_z + (-)^m\Delta\tau_x}{E^2 - \xi_k^2 - \Delta^2}. \tag{S10}$$

In particular, we have

$$\sum_k G_{kk'm}(E) = g_{k'm}(E) + \left[\sum_k g_{km}(E)\right]\left(JS + V\tau_z\right)\left[\sum_{k_1}G_{k_1k'm}(E)\right], \tag{S11}$$

which gives

$$G_{kk'm}(E) = g_{km}(E)\delta_{kk'} + (JS + V\tau_z)g_{km}(E)\left[1 - \sum_k g_{km}(E)(JS + V\tau_z)\right]^{-1} g_{k'm}(E). \tag{S12}$$

One can identify the T matrix as

$$T(E) = \left(JS + V\tau_z\right)\left[1 - \sum_k g_{km}(E)\left(JS + V\tau_z\right)\right]^{-1}. \tag{S13}$$

Since

$$\sum_k g_{km}(E) \simeq \int d\xi\,\nu_0\frac{E + (-)^m\Delta\tau_x}{E^2 - \xi^2 - \Delta^2} = \frac{-\pi\nu_0(E + (-)^m\Delta\tau_x)}{\sqrt{\Delta^2 - E^2}}, \tag{S14}$$

with ν_0 a one-channel density of states at the Fermi level ($\propto 1/(\pi v_F)$) for the conduction electrons, we find that

$$T(E) = \frac{1}{\pi\nu_0}\frac{(\alpha^2 - \beta^2)E + (\alpha + \beta\tau_z)\sqrt{\Delta^2 - E^2} + (-)^m(\alpha^2 - \beta^2)\Delta\tau_x}{(1 - \alpha^2 + \beta^2)\sqrt{\Delta^2 - E^2} + 2\alpha E}, \tag{S15}$$

whose poles give the Shiba state energies[1]

$$E_m = -\Delta\frac{1 - \alpha^2 + \beta^2}{\sqrt{(1 - \alpha^2 + \beta)^2 + 4\alpha^2}}, \tag{S16}$$

where $\alpha = JS\pi\nu_0 > 0$, $\beta = V\pi\nu_0$. This expression is the same as the one for the Shiba states induced by an exchange potential of the form of a δ-function. The difference is that the Shiba states obtained here are fivefold degenerate.

---

[1] J as defined here differs from the J in the real-space representation (for s-wave scatterers) $J\psi^\dagger(0)\boldsymbol{\sigma}\psi(0)\cdot\mathbf{S}$ by a normalization factor; however, the value of the dimensionless quantity α remains unaffected.

Table I. Character table for the irreducible representations for group C_{4v} and reducible representation D^+

	E	$2C_4$	C_2	$2\sigma_v$	$2\sigma_d$	linear, rotations	quadratic
A_1	1	1	1	1	1	z	x^2+y^2, z^2
A_2	1	1	1	-1	-1	R_z	
B_1	1	-1	1	1	-1		x^2-y^2
B_2	1	-1	1	-1	1		xy
E	2	0	-2	0	0	(x,y) (R_x,R_y)	(xz,yz)
D^+	5	-1	1	1	1		

Table II. Character table for the irreducible representations for group C_{3v} and reducible representation D^+

	E	$2C_3$	$3\sigma_v$	linear, rotations	quadratic
A_1	1	1	1	z	x^2+y^2, z^2
A_2	1	1	-1	R_z	
E	2	-1	0	(x,y) (R_x,R_y)	(x^2-y^2,xy) (xz,yz)
D^+	5	-1	1		

Crystal field splitting

Above, the Shiba states were obtained from scattering electrons of an isotropic superconductor off an impurity potential with a certain angular momentum component with $l=2$. Thus, the Shiba states are 5-fold degenerate, and their wave functions resemble the shape of d atomic orbitals. The degeneracy is (partially) removed by the crystal field describing the local environment of the magnetic impurity. The nature of the splitting is essentially determined by symmetry. We briefly summarize the standard results of group theory which govern these splittings for the surfaces of interest in the main text.

The point group symmetries for the Pb(001) and Pb(111) surfaces are C_{4v} and C_{3v} with the corresponding character tables in Tables I and II, respectively [3]. As long as the adsorption sites respect this symmetry, we can then read off the generic multiplicities of the Shiba states. In our experiments, we find this to be the case for the Pb(001) surface as well as the for $\mathrm{Mn}^{\mathrm{up}}_{\mathrm{Pb(111)}}$ site on the Pb(111) surface. If the adsorption site further reduces the symmetry, the Shiba states will split even further. In our experiments, we conclude that this is the case for the $\mathrm{Mn}^{\mathrm{down}}_{\mathrm{Pb(111)}}$ adsorption site. For the case that the absorption sites respect the symmetry of the surface, we thus find from the character tables:

- Pb(001):

  $$D^+ = A_1 \oplus B_1 \oplus B_2 \oplus E. \tag{S17}$$

  d_{xz} and d_{yz} orbitals are doubly degenerate, and d_{xy} , $d_{x^2-y^2}$ and d_{z^2} are nondegenerate.

- Pb(111):

  $$D^+ = A_1 \oplus 2E. \tag{S18}$$

  $d_{x^2-y^2}$ and d_{xy} are degenerate. d_{xz} and d_{yz} are degenerate. d_{z^2} is non degenerate.

EXPERIMENTAL DATA

dI/dV maps with full contrast and at negative bias voltages

In Fig. 3 of the main text we provided dI/dV maps at positive bias voltages for a Mn adatom in the $\mathrm{Mn}^{\mathrm{down}}_{\mathrm{Pb(111)}}$ and in the $\mathrm{Mn}^{\mathrm{up}}_{\mathrm{Pb(111)}}$ adsorption site. The contrast of some of the maps was stretched to emphasize the long-range patterns of the YSR states. For completeness, we provide the same maps with a linear color scale in Fig. S1 ($+\alpha$ to $+\epsilon$ and $+\zeta$ to $+\theta$). We provide also dI/dV maps of the YSR resonances at negative bias voltages, which show patterns similar to those at positive voltages.

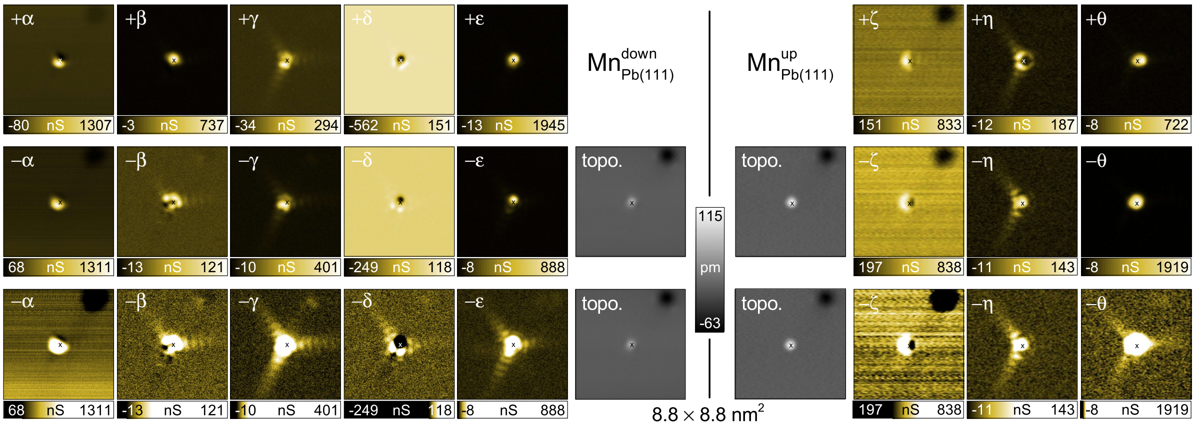

Figure S1. dI/dV maps of a Mn adatom on Pb(111) in the two adsorption sites denoted by $\mathrm{Mn}^{\mathrm{down}}_{\mathrm{Pb(111)}}$ ($\pm\alpha$, $\pm\beta$, $\pm\gamma$, $\pm\delta$, $\pm\epsilon$) and $\mathrm{Mn}^{\mathrm{up}}_{\mathrm{Pb(111)}}$ ($\pm\zeta$, $\pm\eta$ $\pm\theta$), respectively. The corresponding topographies are shown. × denotes the same position in all maps. The dI/dV maps are recorded with the tip-sample distance adjusted in each pixel to a setpoint of 400 pA at 5 mV. Lock-in modulation: 20 $\mu\mathrm{V}_{\mathrm{rms}}$. The maps of $+\alpha$ to $+\epsilon$ and $+\zeta$ to $+\theta$ reproduce the same data as in Fig. 3 (e,f) of the main text, but with a linear color scale. The maps of the negative energy resonances $-\alpha$ to $-\epsilon$ and $-\zeta$ to $-\theta$ are shown with a linear (top) and with a stretched (bottom) color scale, respectively. Note that the dark spot in the top right corner of the imaged area is a subsurface neon inclusion [4].

Further arguments for the orbital assignment

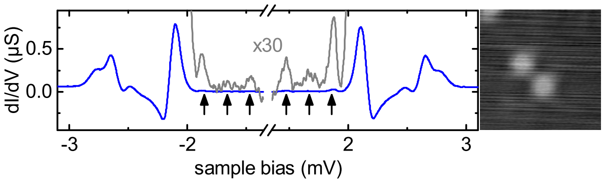

Figure S2. dI/dV spectrum recorded at a pair of adatoms, which lie at close distance. Splitting of the states reveals three resonances close to the original energy of $\pm\gamma$ (marked by arrows). Setpoint: 4 mV at 200 pA. Lock-in modulation: 15 $\mu\mathrm{V}_{\mathrm{rms}}$.

In the main text we deduced the symmetry of the scattering potential from the spatial pattern of the YSR-states observed in the dI/dV maps of a Mn adatom on Pb(001). We assigned the distinct states α, β and γ to originate from scattering of the Mn adatom's d-orbitals. The assignment of resonances $\pm\beta$ to d_{z^2} was unambiguous because the intensity is strongest at the center of the adatom and only weak into the $\langle 110\rangle$ directions. Resonances α and γ originate either from scattering at $d_{\mathrm{x}^2-\mathrm{y}^2}$ and/or from the orbitals $d_{\mathrm{xz,yz}}$ and d_{xy}. An assignment from the spatial shape of the YSR state alone is ambiguous. At higher coverage, we also observe pairs of adatoms at close distance. The interaction leads to a splitting of the resonances $\pm\gamma$ into three pairs of resonances [see Fig. S2]. This requires $\pm\gamma$ to actually consist of (at least) two resonances. Thus, we assigned $\pm\gamma$ resonances to scattering at the orbitals $d_{\mathrm{xz,yz}}$ and d_{xy}, which are degenerate in the single atom. Resonances $\pm\alpha$ then originate from scattering at $d_{\mathrm{x}^2-\mathrm{y}^2}$.

Lateral decay of dI/dV intensity

In the main text we showed the lateral decay of spectral intensity of YSR states along the $\langle 110\rangle$ high-symmetry directions in the vicinity of a $\mathrm{Mn}^{\mathrm{up}}_{\mathrm{Pb(111)}}$ adatom. The curves were extracted from high-resolution dI/dV maps at the energies of the YSR states. To emphasize the oscillatory intensity variations, we subtracted a background $b(r)$, which is derived from the $1/r$ dependence of the YSR wavefunction $\psi(r)$ at distances $r < \xi$ (ξ is the coherence length of the superconductor):

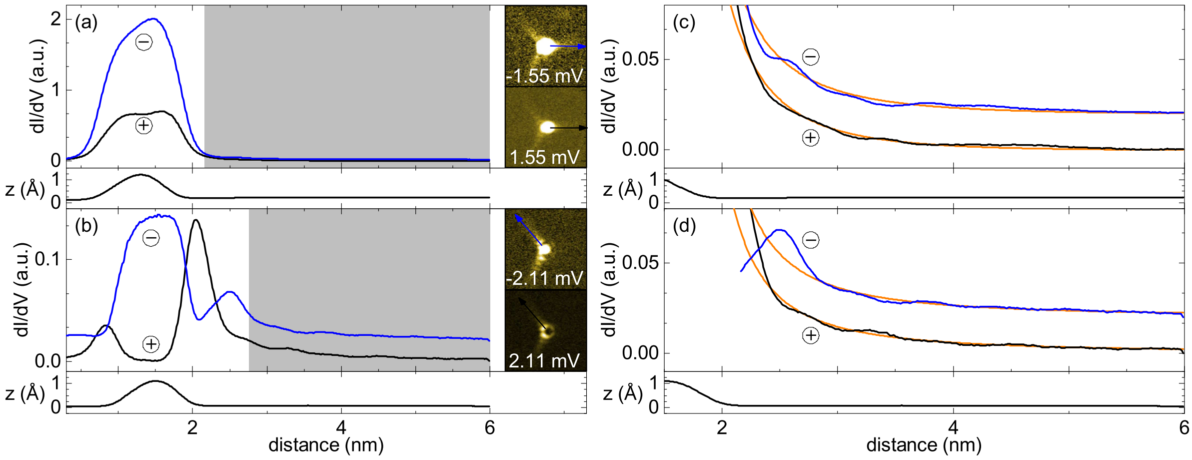

Figure S3. Lateral decay of the spectral intensity at positive (black) and negative bias (blue) of the two YSR resonances with lowest binding energy for an adatom on Pb(111) in the $\mathrm{Mn}^{\mathrm{up}}_{\mathrm{Pb(111)}}$ adsorption site. Setpoint: 400 pA, 4 mV. Lock-in modulation: 20 μV. The blue curves in (c,d) are offset for clarity by 0.02. (a,b) show the full profiles as extracted from high-resolution dI/dV maps along the $\langle 110 \rangle$ crystal directions. (c,d) show a zoom of the gray shaded areas in (a,b). Removal of the strongly decaying background, which is shown as orange line, leads to Fig. 3 of the main text. The z profiles show the apparent height as a function of distance from the impurity center.

$$b(r) = \left| y_0 + \frac{1}{k\,|r - r_0|} \right|^2 . \tag{S19}$$

Here, k and y_0 are independent fit parameters, and r_0 is set to the center of the adatom. Figure S3 shows the full datasets of the spectral intensity at positive and negative bias in (a,b). The region of interest is shaded with a gray background, and displayed in (c,d). Subtracting the decay function (orange) leads to Fig. 3 of the main text.

[1] J.R. Schrieffer, J. Appl. Phys. **38**, 1143 (1967).
[2] A.M. Tsvelick, P.B. Wiegmann, Adv. Phys. **32**, 453 (1983).
[3] M.S. Dresselhaus, G. Dresselhaus, A. Jorio, *Group Theory: Application to the Physics of Condensed Matter*, (Springer, 2007).
[4] M. Ruby, B.W. Heinrich, J.I. Pascual, and K.J. Franke, Phys. Rev. Lett. **114**, 157001 (2015).

B.5 Physical Review Letters 115, 197204 (2015)

Michael Ruby, Falko Pientka, Yang Peng, Felix von Oppen,
Benjamin W. Heinrich, and Katharina J. Franke

End states and subgap structure in proximity-coupled chains of magnetic adatoms

doi:10.1103/PhysRevLett.115.197204

PRL **115,** 197204 (2015) PHYSICAL REVIEW LETTERS week ending 6 NOVEMBER 2015

End States and Subgap Structure in Proximity-Coupled Chains of Magnetic Adatoms

Michael Ruby,[1] Falko Pientka,[2] Yang Peng,[2] Felix von Oppen,[2] Benjamin W. Heinrich,[1] and Katharina J. Franke[1]
[1]*Fachbereich Physik, Freie Universität Berlin, 14195 Berlin, Germany*
[2]*Dahlem Center for Complex Quantum Systems and Fachbereich Physik, Freie Universität Berlin, 14195 Berlin, Germany*

(Received 21 July 2015; published 4 November 2015)

A recent experiment [Nadj-Perge *et al.*, Science 346, 602 (2014)] provides evidence for Majorana zero modes in iron (Fe) chains on the superconducting Pb(110) surface. Here, we study this system by scanning tunneling microscopy using superconducting tips. This high-resolution technique resolves a rich subgap structure, including zero-energy excitations in some chains. We compare the symmetry properties of the data under voltage reversal against theoretical expectations and provide evidence that the putative Majorana signature overlaps with a previously unresolved low-energy resonance. Interpreting the data within a Majorana framework suggests that the topological gap is smaller than previously extracted from experiment. Aided by model calculations, we also analyze higher-energy features of the subgap spectrum and their relation to high-bias peaks which we associate with the Fe d bands.

DOI: 10.1103/PhysRevLett.115.197204 PACS numbers: 73.63.Nm, 74.20.-z, 75.70.Tj, 75.75.-c

Building on advances in nanofabrication [1], engineering topological phases by proximity in superconducting hybrid structures has come within reach of current experiments. A major motivation for realizing such phases is their non-Abelian Majorana quasiparticles [2–4], and their subsequent applications. The underlying topological superconducting phases can be realized in one-dimensional (1D) helical liquids contacted by conventional s-wave superconductors [5–9]. Among the most promising platforms studied in experiments are semiconductor nanowires [10–14], edges of two-dimensional topological insulators [15,16], and chains of magnetic adatoms [17,18]. While the proximity coupling to a superconductor is needed to induce a gap protecting the topological phase, it also has more subtle consequences. Magnetic interactions mediated by the superconductor can stabilize magnetic order in the 1D system [19–22]. Conversely, the spin structure may affect the superconductor. This is particularly apparent for adatom chains, where a band of subgap Shiba states [23–26] may strongly modify the low-energy properties of the system [8,27–31] and possibly induce trivial zero-energy features at the chain end [32]. At strong coupling, the 1D states bleed substantially into the superconductor, reducing the effective coherence length at low energies [33].

Nadj-Perge *et al.* [17] recently provided intriguing evidence for Majorana states in Fe chains on Pb(110). Here, we present data on the same system employing scanning tunneling microscopy (STM) and scanning tunneling spectroscopy (STS) with superconducting tips (see also Ref. [17]). We show that the use of superconducting tips not only provides enhanced resolution of the subgap structure but also allows for additional consistency checks on the interpretation of the data in terms of Majorana quasiparticles. Our observations indicate that the subgap spectrum comprises a flat Shiba band and strongly dispersing Fe states. An interpretation in terms of Majorana states suggests that the induced gap is smaller than the value previously extracted from experiment.

We carried out the experiments in a SPECS JT-STM at a temperature of 1.1 K. Cycles of sputtering and annealing of a Pb(110) single crystal ($T_c = 7.2$ K) resulted in an atomically flat and clean surface. We employed Pb-covered superconducting tips (see Ref. [34] for the preparation procedure), which provide a resolution beyond the Fermi-Dirac limit [35–37] (in our measurements: $\simeq 70$ μV). Fe chains were prepared by e-beam evaporation from an iron rod (99.99% purity) onto the clean surface at room temperature, similar to Ref. [17]. Without further annealing, we obtained chain lengths of up to $\simeq 10$ nm (measured between the chain end and the intervening Fe cluster). Single adatoms and dimers were prepared by e-beam evaporation onto the cold sample in the STM ($T < 10$ K) with a density of ≈ 350 adatoms per 100×100 nm^2. The differential conductance dI/dV as a function of sample bias was recorded using standard lock-in technique at 912 Hz (subgap spectra: bias modulation $V_{\text{mod}} = 15$ μV$_{\text{rms}}$, set point $V = 5$ mV, $I = 250$ pA; large-scale spectra: $V_{\text{mod}} = 2$ mV$_{\text{rms}}$, $V = 2$ V, $I = 850$ pA).

STS with a superconducting tip measures a convolution of the density of states of tip and sample as long as the tunneling rate is slower than the quasiparticle relaxation of the subgap states [38]. This is the case for all measurements presented in this Letter. As the tunneling electrons leave behind an unpaired electron in the tip, sample resonances are shifted by $\pm\Delta_{\text{tip}}$, the superconducting gap parameter of the tip. The coherence peaks of the superconductor appear at $eV = \pm(\Delta_{\text{tip}} + \Delta_{\text{sample}})$, while a subgap state of energy ε yields a resonance peak at $eV = \pm(\Delta_{\text{tip}} + \varepsilon)$. Accordingly, zero-energy Majorana states are signaled by resonances at $eV = \pm\Delta_{\text{tip}}$ [17]. At finite temperatures, quasiparticles can be thermally excited to the unoccupied subgap states. These excited quasiparticles contribute to tunneling and yield additional, "thermal" resonances that appear at $\pm(\Delta_{\mathrm{tip}} - \varepsilon)$ [34,38]. At our experimental temperature, this effect is limited to small energies ε.

Figure 1 shows subgap dI/dV spectra, recorded at the termination of six independent Fe chains. Figures 1(a)–(d) display chains terminated by a small cluster, visible as a protrusion in the STM images. The chains in Figs. 1(a) and 1(d) exhibit a clear zero-energy signature at a bias of $+\Delta_{\mathrm{tip}}$, which has been interpreted as a fingerprint of a Majorana bound state [17] (for the determination of the value of Δ_{tip}, see the Supplemental Material [39]). The zero-energy feature is accompanied by two resonances at higher energies. In contrast, the chains in Figs. 1(b) and 1(c) do not exhibit a clear peak at $+\Delta_{\mathrm{tip}}$, but they exhibit a low-energy resonance at a bias of around 1.47 and 1.52 mV, respectively. Figures 1(e) and 1(f) show data for chains without a protrusion at their ends. These appear rarely, and we can only provide data with reduced resolution ($\simeq 330$ μV) due to inferior tip preparation. These chains also lack an unambiguous signature of a zero-energy resonance, perhaps masked by the larger resonance, which contributes considerable spectral intensity at Δ_{tip}. However, the presence of a Majorana state only depends on the topological phase in the chain and should not be affected by structural details of the chain end, as long as the termination has a (trivial) energy gap.

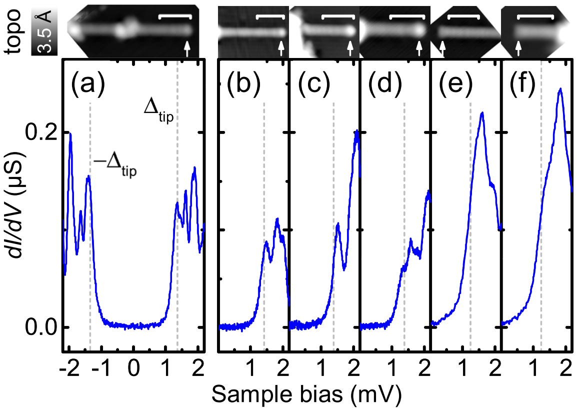

FIG. 1 (color online). dI/dV spectra recorded at the end of six different chains (small arrows mark the position on the chain). Chains in (a)–(d) are terminated by a small cluster; in (e),(f) they have a sharp cutoff. The energy resolution in (e),(f) is reduced (width of BCS resonance: $\simeq 330$ μV) due to nonbulklike superconductivity of the tip. Δ_{tip} in meV: (a) 1.36; (b) 1.42; (c),(d) 1.38; (e),(f) 1.24. Chain lengths measured between the chain end and the cluster onset in nm: (a) 13.9, (b) 9.5, (c) 6.2, (d) 6.0, (e) 7.7, (f) 4.0. Scale bars correspond to 4 nm. For the full spectra of (b)–(f), see the Supplemental Material [39].

Figure 1(a) shows that the peaks at opposite biases $\pm\Delta_{\mathrm{tip}}$ differ substantially in intensity. The same is observed in all other chains [39]. This is in contrast to expectations for Majorana peaks, which should be symmetric because a Majorana state has identical electron and hole wave functions [40]. This indicates that these peaks originate, at least partially, from trivial subgap states near zero energy. For a more detailed analysis, we focus on the chains shown in Figs. 1(a) and 1(b).

It is interesting to contrast the spectra of chains with those of individual Fe adatoms and dimers. Figure 2(a) shows the dI/dV signal of two species of single adatoms with different apparent heights. For both types, we observe a single, shallow Shiba state at $\varepsilon \simeq 1.1$ meV (type 1) and $\varepsilon \simeq 1.2$ meV (type 2), respectively. In contrast, the dimer shown in Fig. 2(b) exhibits a richer subgap structure with a series of resonances with energies as low as $\simeq 150$ μeV. We find that the subgap spectrum varies in detail between different dimers, depending on interatomic distance, angle, and adsorption site [39]. This demonstrates strong coupling

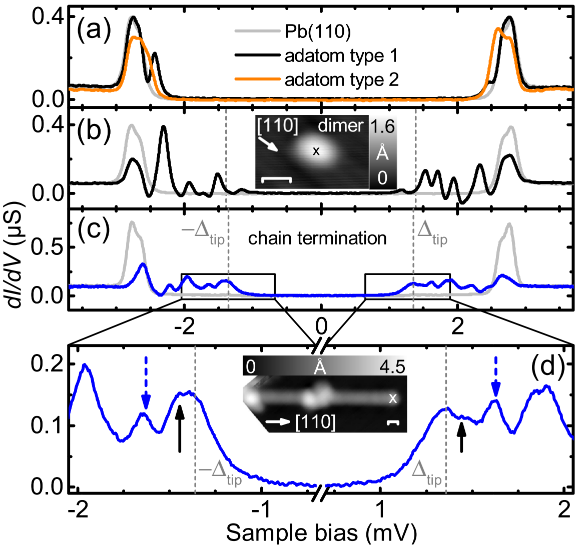

FIG. 2 (color online). dI/dV spectra of different Fe entities on Pb(110). (a) Two types of single adatoms: both spectra exhibit a single Shiba resonance close to the gap edge. The adatoms differ in apparent height by $\simeq 20$ pm at 50 mV, 50 pA. (b) Fe dimer: a variety of Shiba states with the lowest energy resonance at $\varepsilon \simeq 150$ μeV is observed. $\Delta_{\mathrm{tip}} = 1.39$ meV. (c) Chain end (the blue line) as in Fig. 1(a), and bare Pb(110) (the gray line) for comparison. (d) Zoom on (c): a manifold of Shiba resonances is resolved. A peak at $+\Delta_{\mathrm{tip}}$ may be the fingerprint of a Majorana bound state. Low-energy states lie at $\varepsilon \simeq 80$ μeV (the black solid arrow) and $\varepsilon \simeq 270$ μeV (the blue dashed arrow). At 1.1 K, low intensity thermal resonances are expected at $(\pm\Delta_{\mathrm{tip}} - \varepsilon)$ [38]. Albeit not resolvable, they contribute to the tail in intensity at biases between $\pm\Delta_{\mathrm{tip}}$. Scale bars in the topography insets correspond to 1 nm.

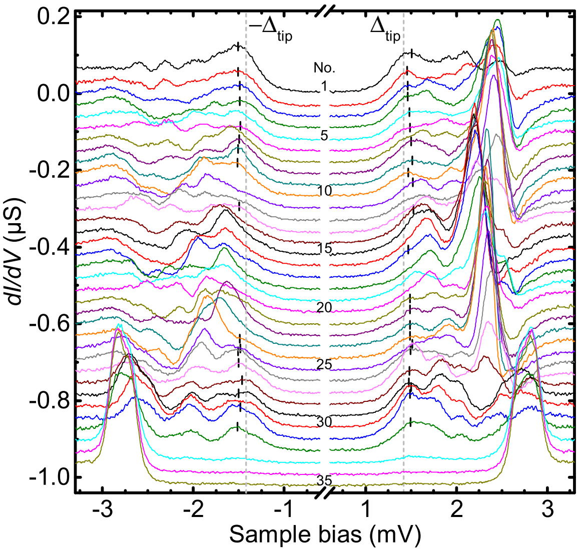

FIG. 3 (color online). Spatially resolved dI/dV spectra along the chain in Fig. 1(b), going from the onset of the Fe cluster (No. 1) to the bare surface (No. 35). At the chain end [No. 29, same as in Fig. 1(b) and Fig. S2(b)], a zero-energy resonance at $-\Delta_{\mathrm{tip}}$, and at the Fe cluster (No. 1), a resonance at $+\Delta_{\mathrm{tip}}$ are visible as local maxima. At the opposite bias, a shoulder is observed. The lowest nonzero energy resonance is found at $\varepsilon \simeq 80\ \mu$eV in No. 29 and is modulated along the chain. As a guide for the eye, local maxima or shoulders with energies $0 < \varepsilon < 100\ \mu$eV are marked by ticks. The high intensity peaks at positive bias shift along the chain with ε ranging from 700 to 1000 μeV. Offset for clarity: −30 nS/spectrum. Distance between spectra: 0.33 nm. $\Delta_{\mathrm{tip}} = 1.42$ meV.

of Shiba states which can ultimately lead to the formation of Shiba bands in adatom chains.

Figure 2(c) provides the data of Fig. 1(a) over a wider voltage range, with a zoom in on the voltage range near Δ_{tip} shown in Fig. 2(d). In addition to the peak at $+\Delta_{\mathrm{tip}}$ and a faint shoulder at $-\Delta_{\mathrm{tip}}$, there is a nearby subgap resonance at $\varepsilon \simeq 80\ \mu$eV (the black solid arrows). These combine into a plateaulike structure near and just above $\pm\Delta_{\mathrm{tip}}$. The data are also consistent with corresponding thermal resonances at $\pm(\Delta_{\mathrm{tip}} - 80\ \mu\mathrm{eV})$. The superposition with a low-energy subgap resonance may explain the asymmetric peaks in Fig. 1(a). While a Majorana peak must be symmetric, conventional subgap resonances can be asymmetric, reflecting the asymmetry between the electron and hole wave functions.

Further subgap peaks occur at higher energies, the next higher one at $\varepsilon \simeq 270\ \mu$eV [the blue dashed arrows in Fig. 2(d)]. Similar peaks were identified in Ref. [17] as the coherence peaks of the induced topological gap (estimated at 200–300 μeV). In view of the lower-energy peaks, this interpretation seems implausible for our chains. Instead, a Majorana-based interpretation would suggest that the lowest nonzero energy peak originates from the topological gap or is shifted above the topological gap by size quantization. This suggests that the topological gap is comparable to or smaller than $\simeq 80\ \mu$eV.

While the Majorana states should be localized at the chain end, the topological gap is a property of the bulk spectrum and should be observable throughout the entire chain. In Fig. 3, we present spatially resolved dI/dV spectra of the same chain as in Fig. 1(b) [and Fig. S2(b)]. Spectra at the end of the chain, e.g., Nos. 1 and 29, exhibit a peak or shoulder at $\pm\Delta_{\mathrm{tip}}$. The asymmetry may again be due to the overlap with nearby resonances with energies below 100 μeV. The latter resonances are observable throughout the chain, but they vary in intensity and/or energy (marked in Fig. 3). This is in contrast to the zero-energy resonances, which only exist at the ends of the chain.

The most likely scenario for topological superconductivity in adatom chains is that an odd number of spin-polarized d bands cross the Pb Fermi energy

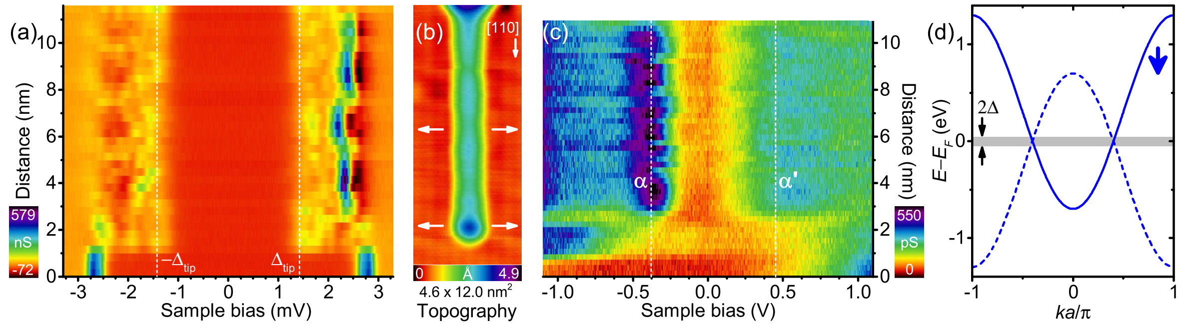

FIG. 4 (color online). False-color plot of the dI/dV spectra of (a) the subgap (the same spectra as in Fig. 3) and (c) the d-band structure, aligned with the topography in (b). The subgap structure (a) exhibits variations of the Shiba peak energies and intensities, as well as modulations of the low-energy resonance at $\varepsilon \simeq 80\ \mu$eV along the chain. A zero-energy resonance is found at both chain terminations. Resonances linked to the d-band structure (c) vary around −380 mV (α), and 450 mV (α') along the chain. (d) Sketch of a spin-polarized d band (the full line) and its hole complement (the dashed line) crossing the Fermi level of the superconductor.

[9,17,33], as illustrated in Fig. 4(d). Spin-orbit coupling in the substrate enables proximity-induced p-wave pairing even for ferromagnetic chains. The subgap bands combine the rapidly dispersing d bands, yielding gapped V-shaped structures and weakly dispersing Shiba-like states near $k = 0$ and $k = \pi/a$, where the d bands are far from the Fermi energy. The resulting subgap band is illustrated in Fig. 5(c) for a chain of spin-1/2 Anderson impurities on a BCS superconductor, assuming that the spin-up band is fully occupied and the spin-down band crosses the Pb Fermi energy. We now explore these relations between subgap excitations and high-energy band structure.

The weakly dispersing Shiba states contribute van Hove–like subgap resonances at nonzero energies. Indeed, in addition to the resonance at $\varepsilon \simeq 270$ μeV already mentioned above, many of the spectra exhibit a strong subgap resonance at a bias of $\simeq$2.3 mV. The false-color plot in Fig. 4(a) (the same dI/dV spectra as in Fig. 3) reveals that its intensity oscillates with a period of $\simeq$2 nm and shifts slightly to lower energy in the center of the chain. The lower-energy resonances near $\pm\Delta_{\text{tip}}$ do not show such a clear periodicity. Interestingly, the periodic variations appear correlated with the topography of the chain, as shown next to the false-color plot in Fig. 4(b). The apparent height and width of the chain show variations with a similar period of $\simeq$2 nm, in agreement with Ref. [17].

Moreover, the band edges of the Fe d bands contribute van Hove peaks in STS. In Fig. 4(c), we provide a false-color plot of dI/dV spectra along the chain in a larger bias range between $\pm$1.1 V. In the interior of the chain, we observe two prominent features: a narrow resonance α at around -380 mV and a broader resonance α' at around 450 mV. Similar resonances are present for all chains shown in Fig. 1, and they are in agreement with Ref. [17]. These resonances decrease in intensity and finally disappear at the end of the chain or close to the Fe cluster, respectively (see additional traces in Ref. [39]). We interpret these resonances as the van Hove singularities of the d bands. The simultaneous disappearance of α and α' suggests that these are the upper and lower edges of the same band crossing the Fermi level. Interestingly, resonance α shifts with the above observed periodicity of about 2 nm [39].

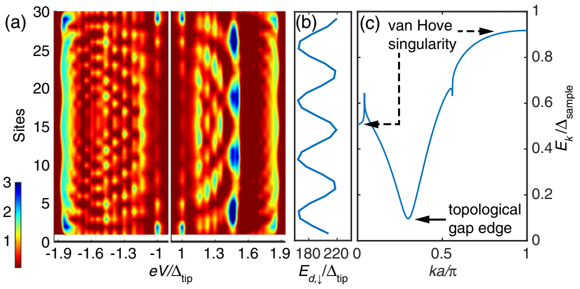

FIG. 5 (color online). Numerical results for a chain of 30 sites. (a) Color plot of the differential conductance along the chain at subgap energies for a superconducting tip. (b) Spatially varying on-site energies of impurity levels. (c) Bulk subgap band structure of an impurity chain on the surface of an s-wave superconductor. We used $\Delta_{\text{sample}}/\Delta_{\text{tip}} = 0.958$. See Ref. [39] for other parameters.

To understand how the spatial variations in the d bands affect the peaks in the subgap spectra, we have performed model calculations for a chain of Anderson impurities coupled to an s-wave superconductor with spin-orbit coupling (see Refs. [33] and [39]). We model the modulations by a potential which varies along the chain and reflects the local environment of the adatoms [see Fig. 5(b)]. We choose parameters such that one band crosses the Fermi level with band edges corresponding to α and α' and assume strong adatom-substrate coupling. Following Ref. [33], we calculate the subgap local density of states from a mean-field treatment of the impurity chain (see Ref. [39]) and the differential conductance. As temperature exceeds the typical energy separation between subgap levels, we assume efficient quasiparticle relaxation, which results in dominant single-particle tunneling. The experimental resolution is modeled by broadening of the tip density of states. Note that these conditions preclude the observation of a quantized Majorana peak height [40].

Figure 5(a) shows the subgap differential conductance of a finite chain, including the spatially varying potential. The numerical results are consistent with key features of the experimental data. (i) The Majorana bound state has a short decay length of a few lattice sites as a consequence of the strong chain-substrate coupling [33]. (ii) Prominent peaks at $eV = \pm 1.5\Delta_{\text{tip}}$ and $\pm 1.9\Delta_{\text{tip}}$ signal the van Hove singularities of the Shiba band. Their intensity modulations are correlated with the potential landscape of the impurity atoms. Here, the effect of the corrugation is most visible because the Shiba energy explicitly depends on the energy of the impurity level. (iii) The induced gap varies along the chain on atomic scales but is uncorrelated with the potential landscape. Indeed, at strong coupling the induced gap only depends on the substrate gap and the spin-orbit interaction and is insensitive to details of the impurities. The fluctuations reflect finite-size quantization which is most visible at low energies due to the low density of states in the V-shaped dip of the band structure [Fig. 5(c)].

Motivated by Ref. [17], we investigated the subgap spectra and the possible Majorana signatures of Fe chains on a superconducting Pb(110) substrate by scanning tunneling spectroscopy. Using superconducting tips, a Majorana state is expected to appear as a pair of resonances at $\pm\Delta_{\text{tip}}$ with symmetric intensities. We associate the absence of this symmetry in the data with a nearby low-energy subgap resonance at 80 μeV. Within a Majorana framework, it is natural to interpret this additional resonance as the coherence peak of the induced topological gap, which would then be smaller than previously measured. We show by model calculations that such an interpretation is, in principle, consistent with our observations. However, a conclusive confirmation of Majorana end states in adatom chains would be greatly facilitated by experiments at considerably lower temperatures. Using superconducting tips at temperatures well below the induced gap might even provide access to the elusive conductance quantization of Majorana states [40].

We acknowledge financial support by the Deutsche Forschungsgemeinschaft through the collaborative research center SFB 658 and Grant No. FR2726/4 (K. F.), as well as research priority programs SPP 1285 and SPP 1666 (F. v. O.), and also by a Consolidator Grant from the European Research Council “NanoSpin” (K. F.) and by the Helmholtz Virtual Institute “New States of Matter and Their Excitations” (F. v. O.).

[1] S. De Franceschi, L. Kouwenhoven, C. Schönenberger, and W. Wernsdorfer, Nat. Nanotechnol. **5**, 703 (2010).

[2] J. Alicea, Rep. Prog. Phys. **75**, 076501 (2012).

[3] C. W. J. Beenakker, Annu. Rev. Condens. Matter Phys. **4**, 113 (2013).

[4] S. R. Elliott and M. Franz, Rev. Mod. Phys. **87**, 137 (2015).

[5] L. Fu and C. L. Kane, Phys. Rev. B **79**, 161408(R) (2009).

[6] R. M. Lutchyn, J. D. Sau, and S. Das Sarma, Phys. Rev. Lett. **105**, 077001 (2010).

[7] Y. Oreg, G. Refael, and F. von Oppen, Phys. Rev. Lett. **105**, 177002 (2010).

[8] S. Nadj-Perge, I. K. Drozdov, B. A. Bernevig, and A. Yazdani, Phys. Rev. B **88**, 020407(R) (2013).

[9] J. Li, H. Chen, I. K. Drozdov, A. Yazdani, B. A. Bernevig, and A. H. MacDonald, Phys. Rev. B **90**, 235433 (2014).

[10] V. Mourik, K. Zuo, S. M. Frolov, S. R. Plissard, E. P. A. M. Bakkers, and L. P. Kouwenhoven, Science **336**, 1003 (2012).

[11] A. Das, Y. Ronen, Y. Most, Y. Oreg, M. Heiblum, and H. Shtrikman, Nat. Phys. **8**, 887 (2012).

[12] H. O. H. Churchill, V. Fatemi, K. Grove-Rasmussen, M. T. Deng, P. Caroff, H. Q. Xu, and C. M. Marcus, Phys. Rev. B **87**, 241401(R) (2013).

[13] M. T. Deng, C. L. Yu, G. Y. Huang, M. Larsson, P. Caroff, and H. Q. Xu, Nano Lett. **12**, 6414 (2012).

[14] A. D. K. Finck, D. J. Van Harlingen, P. K. Mohseni, K. Jung, and X. Li, Phys. Rev. Lett. **110**, 126406 (2013).

[15] S. Hart, H. Ren, T. Wagner, P. Leubner, M. Mühlbauer, C. Brüne, H. Buhmann, L. W. Molenkamp, and A. Yacoby, Nat. Phys. **10**, 638 (2014).

[16] V. S. Pribiag, A. J. A. Beukman, F. Qu, M. C. Cassidy, C. Charpentier, W. Wegscheider, and L. P. Kouwenhoven, Nat. Nanotechnol. **10**, 593 (2015).

[17] S. Nadj-Perge, I. K. Drozdov, J. Li, H. Chen, S. Jeon, J. Seo, A. H. MacDonald, B. A. Bernevig, and A. Yazdani, Science **346**, 602 (2014).

[18] R. Pawlak, M. Kisiel, J. Klinovaja, T. Meier, S. Kawai, T. Glatzel, D. Loss, and E. Meyer, arXiv:1505.06078.

[19] B. Braunecker and P. Simon, Phys. Rev. Lett. **111**, 147202 (2013).

[20] J. Klinovaja, P. Stano, A. Yazdani, and D. Loss, Phys. Rev. Lett. **111**, 186805 (2013).

[21] M. M. Vazifeh and M. Franz, Phys. Rev. Lett. **111**, 206802 (2013).

[22] Y. Kim, M. Cheng, B. Bauer, R. M. Lutchyn, and S. Das Sarma, Phys. Rev. B **90**, 060401(R) (2014).

[23] L. Yu, Acta Phys. Sin. **21**, 75 (1965).

[24] H. Shiba, Prog. Theor. Phys. **40**, 435 (1968).

[25] A. I. Rusinov, Zh. Eksp. Teor. Fiz., Pis’ma Red. **9**, 146 (1968) [JETP Lett. **9**, 85 (1969)].

[26] A. V. Balatsky, I. Vekhter, and J.-X. Zhu, Rev. Mod. Phys. **78**, 373 (2006).

[27] F. Pientka, L. I. Glazman, and F. von Oppen, Phys. Rev. B **88**, 155420 (2013).

[28] S. Nakosai, Y. Tanaka, and N. Nagaosa, Phys. Rev. B **88**, 180503(R) (2013).

[29] K. Pöyhönen, A. Westström, J. Röntynen, and T. Ojanen, Phys. Rev. B **89**, 115109 (2014).

[30] A. Heimes, P. Kotetes, and G. Schön, Phys. Rev. B **90**, 060507(R) (2014).

[31] P. M. R. Brydon, S. Das Sarma, H. Y. Hui, and J. D. Sau, Phys. Rev. B **91**, 064505 (2015).

[32] J. D. Sau and P. M. R. Brydon, Phys. Rev. Lett. **115**, 127003 (2015).

[33] Y. Peng, F. Pientka, L. I. Glazman, and F. von Oppen, Phys. Rev. Lett. **114**, 106801 (2015).

[34] K. J. Franke, G. Schulze, and J. I. Pascual, Science **332**, 940 (2011).

[35] S.-H. Ji, T. Zhang, Y.-S. Fu, X. Chen, X.-C. Ma, J. Li, W.-H. Duan, J.-F. Jia, and Q.-K. Xue, Phys. Rev. Lett. **100**, 226801 (2008).

[36] B. W. Heinrich, L. Braun, J. I. Pascual, and K. J. Franke, Nat. Phys. **9**, 765 (2013).

[37] M. Ruby, B. W. Heinrich, J. I. Pascual, and K. J. Franke, Phys. Rev. Lett. **114**, 157001 (2015).

[38] M. Ruby, F. Pientka, Y. Peng, F. von Oppen, B. W. Heinrich, and K. J. Franke, Phys. Rev. Lett. **115**, 087001 (2015).

[39] See Supplemental Material at http://link.aps.org/supplemental/10.1103/PhysRevLett.115.197204 for additional data on Fe dimers and Fe chains, the method to determine the tip gap, and the theoretical model.

[40] Y. Peng, F. Pientka, Y. Vinkler-Aviv, L. I. Glazman, and F. von Oppen, arXiv:1506.06763.

Supplementary Material
End states and subgap structure in proximity-coupled chains of magnetic adatoms

Michael Ruby,[1] Falko Pientka,[2] Yang Peng,[2] Felix von Oppen,[2] Benjamin W. Heinrich,[1] and Katharina J. Franke[1]
[1]*Fachbereich Physik, Freie Universität Berlin, 14195 Berlin, Germany*
[2]*Dahlem Center for Complex Quantum Systems and Fachbereich Physik, Freie Universität Berlin, 14195 Berlin, Germany*

I. Fe MONOMERS AND DIMERS

In the main text we show dI/dV-spectra of the two species of Fe adatoms, which are present on the (110) surface after the evaporation of Fe onto the cold sample ($T_{\text{sample}} < 10$ K). Both species are adsorbed in between the [110] corrugation lines of the surface, yet they have different apparent heights ($\Delta z \simeq 20$ pm at $V_{\text{bias}} = 50$ mV, $I = 50$ pA). In dI/dV spectroscopy between ±3.5 V, we did not detect any d-state resonances. We occasionally found – besides single adatoms – also larger protrusions of different size and shape. As diffusion is hindered at the temperature of deposition, it is reasonable to assume that the vast majority of these are Fe dimers. We show the dI/dV-spectra of three distinctly different dimers in Fig. S1. All of them show a rich subgap structure, indicating a strong interaction of the Shiba states. However, the subgap structure varies strongly, and depends on the inter-atomic distance, the angle, and the adsorption site of the Fe atoms.

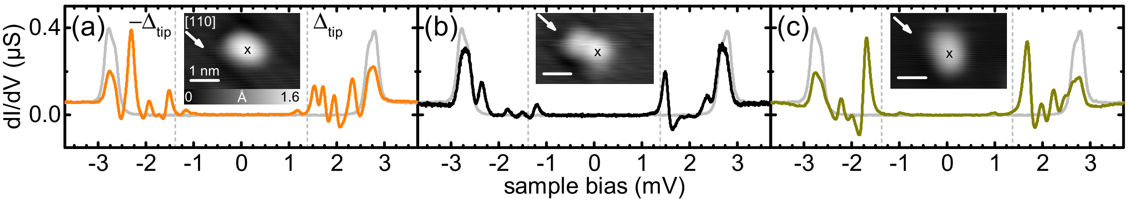

Figure S1: (a-c) dI/dV-spectra of various Fe dimers [reference spectrum on pristine Pb(110) in grey as guide to the eye]. The spectra show diverse subgap structures, probably due to different adsorption configurations. (a) is the dimer shown in Fig. 2(b) of the main text. Δ_{tip} in mV: (a) 1.39, (b) 1.38, (c) 1.37. Setpoint: 5 mV, 250 pA. Lock-in: 15 μV$_{\text{rms}}$, 912 Hz.

II. dI/dV-SPECTRA OF THE SUBGAP STRUCTURE OF SIX DIFFERENT CHAINS

In Fig. 1(a-f) of the main text we show dI/dV-spectra at positive bias voltage of the subgap structure at the end of six different chains. For the sake of completeness, we show here the same spectra, but both positive and negative bias side [Fig. S2(a-f)]. All spectra exhibit an asymmetric intensity of the spectral weight at $\pm\Delta_{\text{tip}}$, i.e., at zero-energy.

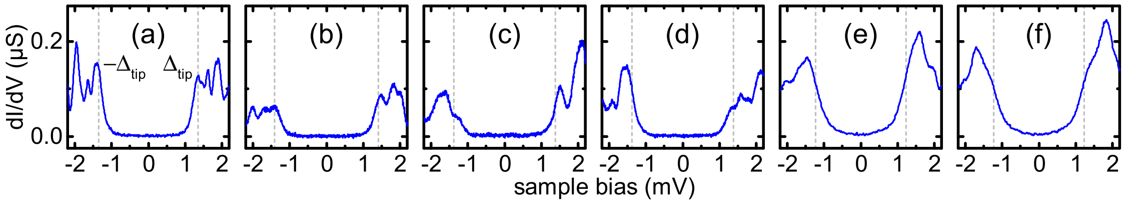

Figure S2: dI/dV-spectra recorded at the end of six different chains. Same spectra as in Fig. 1(a-f) of the main text, but here we present both positive and negative bias side. Chains in (a-d) are terminated by a small cluster, in (e,f) they have a sharp cut-off. The energy resolution in (e,f) is reduced (width of BCS resonance: $\simeq 330$ μV), due to non bulk-like superconductivity of the tip. Δ_{tip} in mV: (a) 1.36, (b) 1.42, (c,d) 1.38, (e,f) 1.24. Chain lengths measured between chain end and cluster onset in nm: (a) 13.9, (b) 9.5, (c) 6.2, (d) 6.0, (e) 7.7, (f) 4.0. Setpoint: 5 mV, 250 pA. Lock-in: 15 μV$_{\text{rms}}$, 912 Hz.

In the main text we plot in Fig. 3 the spatial dependence of the low-energy dI/dV-spectra along the chain shown in Fig. 1(b). To be able to compare the characteristic features of the spectra between the chains, we show in Fig. S3(a-f) a collection of the data recorded along the six chains.

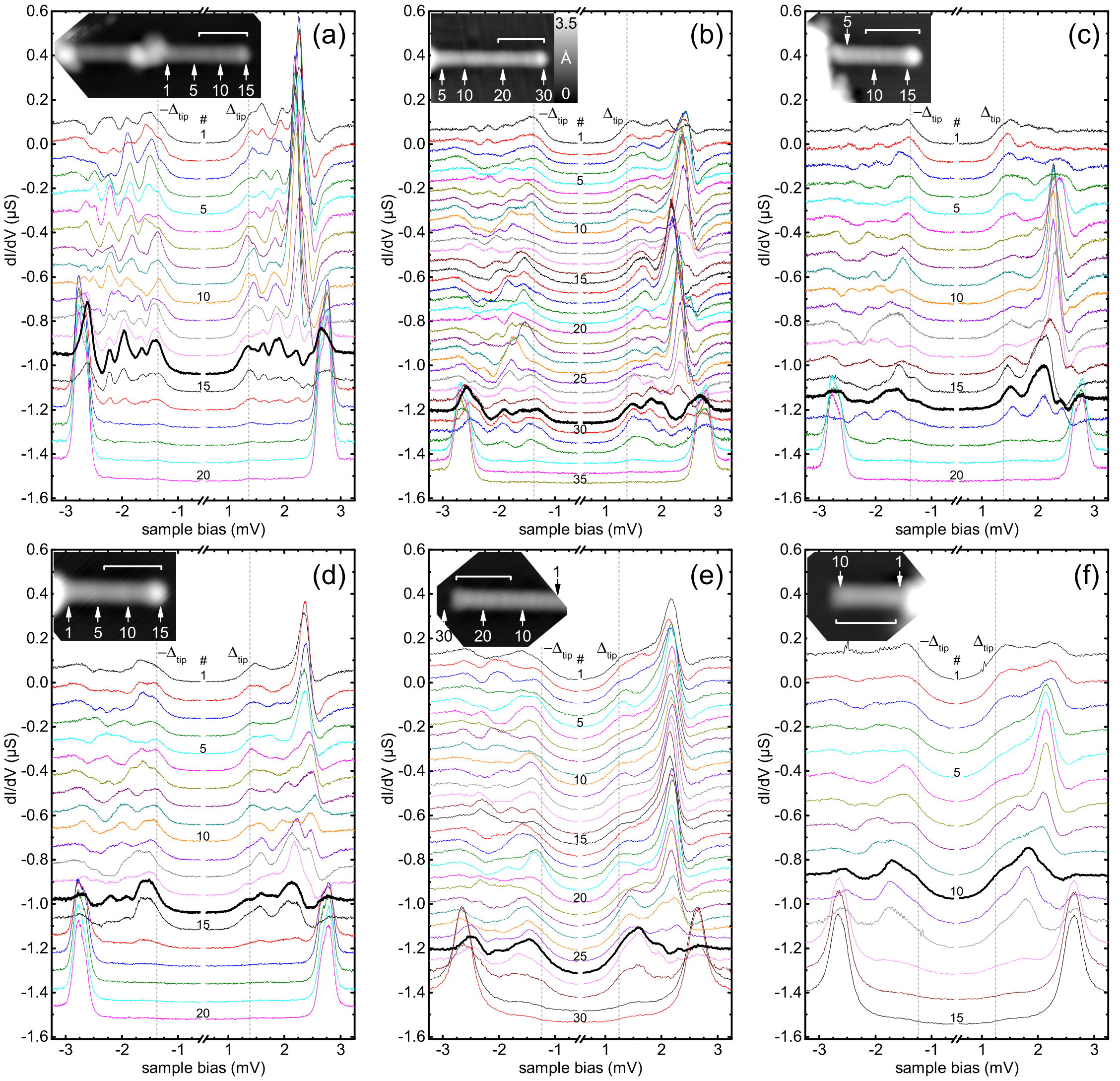

Figure S3: Spatial dependence of the dI/dV-spectra along the chains from Fig. 1(a-f) of the main text. Spectra at the chain ends [same as Fig. 1(a-f)] are printed bold. Fig. S3(b) is the same data as Fig. 3 of the main text. Chains in (a-d) are terminated by a small cluster, in (e,f) they have a sharp cut-off. The energy resolution in (e,f) is reduced (width of BCS resonance: $\simeq 330\ \mu$V), due to non bulk-like superconductivity of the tip. Δ_{tip} in mV: (a) 1.36, (b) 1.42, (c,d) 1.38, (e,f) 1.24. Chain lengths measured between chain end and cluster onset in nm: (a) 13.9, (b) 9.5, (c) 6.2, (d) 6.0, (e) 7.7, (f) 4.0. Scale bars correspond to 4 nm. Offset between spectra for clarity in nS: (a,c,d) -80, (b) -45, (e) -53, (f) -110. Spatial distance between the spectra along the chain in Å: (a,c,d,f) 0.4, (b,e) 0.3. Setpoint: 5 mV, 250 pA. Lock-in: 15 μV$_{\text{rms}}$, 912 Hz.

III. dI/dV-SPECTRA OF THE IRON CHAIN D-BANDS

Figure S4 shows dI/dV-spectra acquired on the chain presented in Fig. 4 of the main text. The spectra visualize the variations in intensity and energy of the resonances α and α' along the chain. At the protrusion at the chain end, these resonances have not yet developed. Instead, we observe a resonance around -930 mV (spectrum #40). It decays quickly along the chain. In spectrum (#38) it is hardly visibly anymore, while resonances α and α' start to gain intensity. Both increase in intensity when moving towards the center of the chain. In the center (∼#20), α' is resolved as double-peak structure. This correlates with the tight-binding calculations presented in Ref. [1], and may be a hint that the broad resonance α' actually consist out of two resonances. The simultaneous appearance of α and α' suggests that they originate from the same band. Different positions within the chain show a shift of the resonance α by up to 150 meV, which is plotted in the bottom right of Fig. S4. At the Fe cluster both resonances decrease in intensity again (#1).

A similar behavior of the state α is found in a chain, which is not terminated with an Fe cluster. As an example, we show a set of spectra in Fig. S5. The resonances α and α' again appear simultaneously close to the end of the chain. We do not observe a resonance at larger negative bias at the end of the chain, which resembles the one at -930 mV in Fig. S4. This supports the correlation of its appearance with the protrusion at the end of the chain. Though, approaching the large Fe cluster, α and α' vanish, and resonances at -800 mV and around 150 mV appear in the bottom of Fig. S5(e). Within the chain, resonance α exhibits a clear oscillation in its peak position with a periodicity $\simeq 2$ nm, similar to the previously described chain. Resonance α' also shows a variation in its peak position, but not with a clearly identifiable periodicity. We also present the corresponding subgap structure in Fig. S5(a). The most prominent Shiba state at 2.17 mV shows an intensity oscillation, in accordance with the variation of α. Due to the limited energy resolution in these spectra, we cannot unambiguously conclude on an energy variation.

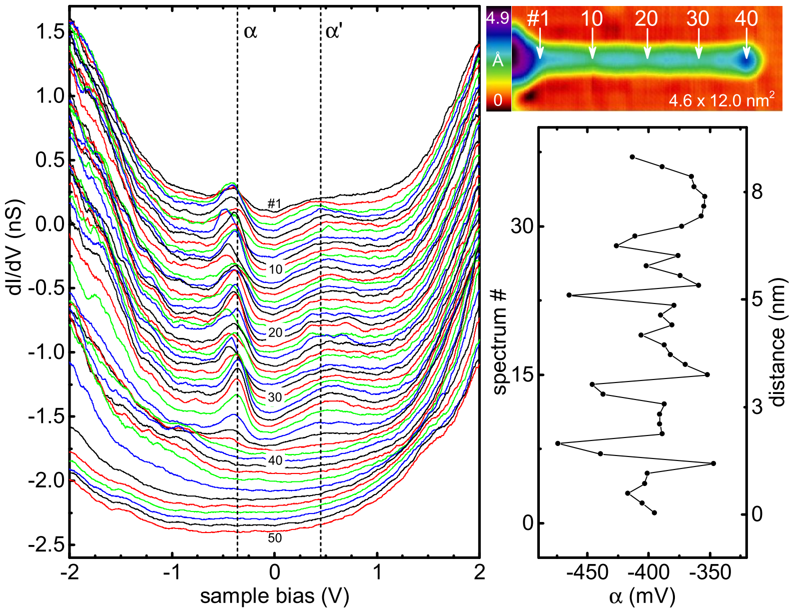

Figure S4: dI/dV-spectra (left) from top to bottom recorded along the chain (top right) starting from the iron cluster and going towards the chain end. The spectra are numbered from #1 to #50. The data is the same as plotted in Fig. 4(c) of the main text. Resonances α and α' are marked by dashed lines. The energetic position of α is plotted versus the spectrum number and the distance (bottom right). The values are determined from a fit with a Gaussian peak and a linear background. Spectra are smoothed to the adjacent average of 25 points. Point distance 230 pm. Offset for clarity: -0.05 nS/spectrum. Setpoint: 2 V, 850 pA. Lock-in: 2 mV$_{\mathrm{rms}}$, 912 Hz.

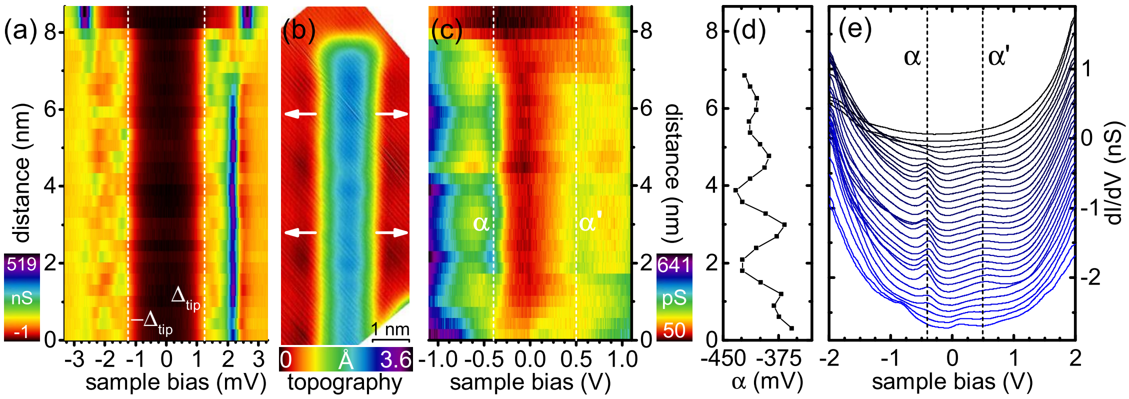

Figure S5: dI/dV-intensity of the subgap structure (a), and the large bias range (c) as color plot with respect to the location along the chain and the sample bias. The topography in (b) is aligned to the position of the spectra in the color plot. The chain is the same as shown in Fig. 1(e) of the main text. The tip has a reduced energy resolution of 330 μV. The position of α is plotted in (d). The values are determined from a fit with a Gaussian peak and a linear background. (e) shows the full dI/dV-spectra of the data shown in (c). Data is smoothed to the adjacent average of 15 points. Point distance 3 Å. Offset for clarity: -0.1 nS/spectrum. Setpoint: 2 V, 850 pA for (c) and (e), and 5 mV, 250 pA for (a). Lock-in: 2 mV$_{\mathrm{rms}}$, 912 Hz for (c) and (e), and 15 μV$_{\mathrm{rms}}$, 912 Hz for (a).

IV. DETERMINATION OF THE TIP GAP

We use superconducting tips in order to improve the energy resolution beyond the Fermi-Dirac limit at 1.1 K and to detect asymmetries in the electron and hole components of the subgap states. dI/dV-spectra show thus the measured spectral intensity of the sample convolved with the BCS-like density of states of the tip. A consequence of a superconducting tip with gap Δ_{tip} is the shift of a sample resonance with an energy $\pm\varepsilon$ to a bias value of $\pm\left(\Delta_{\mathrm{tip}} \pm \varepsilon\right)/e$. The exact determination of "real" energies of the sample resonances thus relies on the correct determination of the superconducting gap of the tip Δ_{tip}.

Pb is a two-band superconductor with two gap parameters ($\Delta_1 \simeq 1.42$ meV and $\Delta_2 \simeq 1.27$ meV). They originate from two separated Fermi surfaces, and give rise to the double-peak structure in the dI/dV-spectra [2]. The tip is prepared by controlled indentation into the clean Pb surface with a high voltage applied to the tip. This creates an amorphous superconducting Pb layer on the tip and yields a single gap parameter Δ_{tip}, which is averaged over all directions. Depending on the layer thickness and quality, Δ_{tip} can be similar or smaller than the bulk gap values.

We cannot determine the parameters Δ_1, Δ_2, and Δ_{tip} independently from the BCS resonances in the spectra of pristine Pb(110) alone. An independent determination of the full set of parameters (Δ_1, Δ_2, and Δ_{tip}) is only possible using spectra with a pronounced low-energy Shiba state, which gives rise to well-resolved thermal resonances. Fe dimers show such low-energy Shiba resonances (Fig. S1). The Shiba resonance and its thermal counterpart occur symmetric to Δ_{tip} at $\pm\left(\Delta_{\mathrm{tip}} + \varepsilon\right)$ and $\pm\left(\Delta_{\mathrm{tip}} - \varepsilon\right)$, respectively. This allows us to determine Δ_{tip} unambiguously. Spectra of the pristine surface acquired with the same tip show clear BCS resonances at $\Delta_{\mathrm{tip}} + \Delta_{1,2}$. Because Δ_1 and Δ_2 are bulk properties of the substrate, their energy can then serve to determine Δ_{tip} for every tip. This procedure enables a reliable determination of the energies of subgap resonances in each Fe chain.

V. THEORETICAL MODEL

We use the model introduced in Ref. [3], where the Fe adatoms are modeled as a chain of Anderson impurities, including both direct hopping between the adatom orbitals and hybridization with the substrate BCS superconductor. This describes the adatoms as spin-1/2 impurities, and their fully polarized spin-up and spin-down bands model the d-bands of the Fe chain. Consistent with the formation of a ferromagnetic state, we assume that the spin-up band is fully occupied, while the spin-down band crosses the Pb Fermi energy. Thus, there is only a single spin-polarized band at the Fermi energy and we expect the adatom chain to realize a topological superconducting phase by proximity coupling to the superconductor. Assuming the ferromagnetic ordering and treating the onsite Hubbard interactions

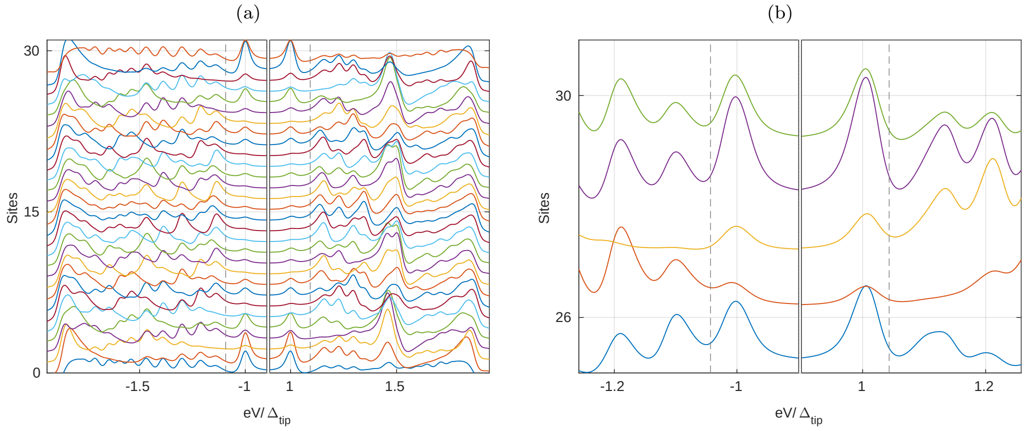

Figure S6: Numerical results for the differential conductance measured with a superconducting tip at subgap energies along a chain of 30 sites. (a) Sample with a larger p-wave induced gap with $k_{\mathrm{F}}a = 4.3\pi$, same as the color scale plot in Fig. 5(a) of the main text. (b) Sample with a smaller p-wave induced gap with $k_{\mathrm{F}}a = 8.3\pi$, only the last 5 traces around Δ_{tip} are shown. The dashed lines indicate $eV = \pm(\Delta_{\mathrm{tip}} + \Delta_p)$, with Δ_p the induced p-wave gap for an infinite chain. In (a) $\Delta_p = 0.096\Delta_{\mathrm{tip}}$ and in (b) $\Delta_p = 0.045\Delta_{\mathrm{tip}}$. The remaining model parameters and the process of evaluating the conductance are the same.

in mean-field theory, this model can essentially be solved analytically. This is described in detail in Ref. [3] and will not be reproduced here.

In addition to the Hamiltonian as discussed in Ref. [3], we include a spatially varying on-site energy of the Anderson levels to model the corrugation of the chain. As described in Ref. [3] we can evaluate the Green function within mean-field theory, from which we numerically obtain the local density of states (LDOS) at subgap energies. In our numerical calculations, the average on-site energy of the spin-down levels is $\overline{E}_{d,\downarrow} = 200\Delta_{\mathrm{sample}}$, with roughly 10% spatial modulation [see Fig. 5(b) of the main text]. The on-site energy of the spin-up states is $E_{d,\uparrow} = E_{d,\downarrow} - 40000\Delta_{\mathrm{sample}}$. We choose the bandwidth of the spin-down band as $1000\Delta_{\mathrm{sample}}$, the hybridization strength between the adatoms and the substrate superconductor $\Gamma = 256\Delta_{\mathrm{sample}}$, and the ratio $\Delta_{\mathrm{sample}}/\Delta_{\mathrm{tip}} = 0.958$. Finally, we set the Fermi wavevector $k_{\mathrm{F}}a = 4.3\pi$ and the Rashba spin-orbit wavevector $k_h a = 0.26\pi$ with a the lattice constant.

We start from the expression for the tunneling current (see supplement of Ref. [4]),

$$I = \frac{et^2}{2h}\int d\omega\ \mathrm{Tr}\left\{G_R^{>,ee}(\omega)g_L^{<}(\omega_-) - G_R^{<,ee}(\omega)g_L^{>}(\omega_-) + g_L^{>}(\omega_+)G_R^{<,hh}(\omega) - g_L^{<}(\omega_+)G_R^{>,hh}(\omega)\right\}, \tag{S1}$$

where R and L label the sample and the superconducting tip and all Green's functions are located at the tunneling position. The electron and hole blocks are denoted by ee and hh. In the experiment, the tunneling current is dominated by single-particle tunneling events (cf. Ref. [2]), and we can approximate

$$-iG_R^{<}(\omega) = A(\omega)f(\omega), \tag{S2}$$

$$iG_R^{>}(\omega) = A(\omega)(1 - f(\omega)), \tag{S3}$$

where $f(\omega)$ is the quasi-equilibrium distribution of the steady state and $A(\omega) = -2\mathrm{Im}G_R^r(\omega)$ the LDOS of the sample. The distribution $f(\omega)$ satisfies the condition $f(-\omega) = 1 - f(\omega)$, as in the case of the Fermi distribution function. For our numerical calculations, we assume that the system remains close to thermal equilibrium, $f(\omega) = n_F(\omega)$. Using the relations for the tip Green function $g_L^{<}(\omega) = 2\pi i\rho(\omega)n_F(\omega)$, $g_L^{>}(\omega) = -2\pi i\rho(\omega)n_F(\omega)$, we can write the current as

$$I = \frac{\pi et^2}{h}\int d\omega\, \rho(\omega_-)\,\mathrm{Tr}\,A_e(\omega)\,[n_F(\omega_-) - f(\omega)] - \rho(\omega_+)\,\mathrm{Tr}\,A_h(\omega)\,[n_F(\omega_+) - f(\omega)] \tag{S4}$$

$$= \frac{2\pi et^2}{h}\int d\omega\, \rho(\omega_-)\,\mathrm{Tr}\,A_e(\omega)\,[n_F(\omega_-) - f(\omega)]\,, \tag{S5}$$

where $A_{e,h}$ denotes the 2×2 electron (hole) block of A. In the last line, we have used $\mathrm{Tr}\,A_e(\omega) = \mathrm{Tr}\,A_h(-\omega)$ due to particle-hole symmetry, and the property $f(-\omega) = 1 - f(\omega)$. The conductance is then obtained by taking the

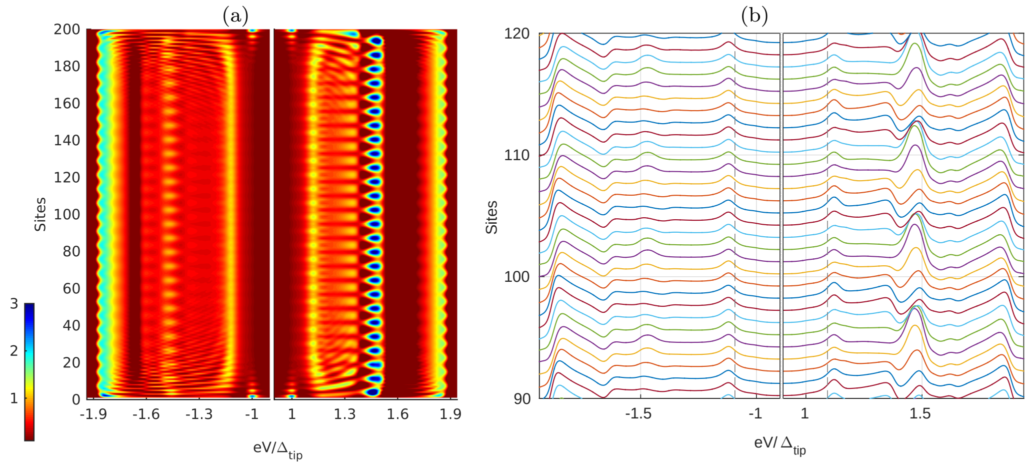

Figure S7: Numerical results for the differential conductance measured with a superconducting tip at subgap energies along a longer chain of 200 sites with the same parameters as in Fig. S6(a), in particular the same modulation in the on-site energy of impurities. (a) Color scale plot of the conductance. (b) Waterfall plot for 30 sites in the middle of the chain. The dashed lines indicate the bias $\pm(\Delta_{\text{tip}} + \Delta_p)$ corresponding to the p-wave gap of an infinite chain.

derivative with respect to the voltage,

$$G(eV) = -\frac{2\pi e^2 t^2}{h} \int d\omega \, \mathrm{Tr}\{A_e(\omega)\} \left\{\rho'(\omega_-) \left[n_F(\omega_-) - f(\omega)\right] + \rho(\omega_-) n'_F(\omega_-)\right\}, \tag{S6}$$

where $\rho'(\omega) = d\rho(\omega)/d\omega$, and $n'_F(\omega) = dn_F(\omega)/d\omega$. Inverting the sign of the bias voltage, we find

$$G(-eV) = -\frac{2\pi e^2 t^2}{h} \int d\omega \, \mathrm{Tr}\{A_e(-\omega)\} \left\{\rho'(\omega_-) \left[n_F(\omega_-) - f(\omega)\right] + \rho(\omega_-) n'_F(\omega_-)\right\}. \tag{S7}$$

Since in general $\mathrm{Tr}\, A_e(\omega) \neq \mathrm{Tr}\, A_e(-\omega) = \mathrm{Tr}\, A_h(\omega)$, the conductance is not necessarily symmetric under reversal of bias voltage. However, an isolated zero-energy resonance yields symmetric peaks at $eV = \pm\Delta_{\text{tip}}$ [4]. In Fig. S6(a) we show a waterfall plot of the differential conductance along the chain for the same parameters as the color plot in Fig. 5(a) of the main text. The dashed line indicates the p-wave gap for an infinite chain. The lowest-energy resonance in the finite chain is somewhat higher and varies along the chain due to finite size effects. In Fig. S6(b) we show that a smaller p-wave gap leads to an asymmetry at $eV = \pm\Delta_{\text{tip}}$. In Fig. S7 we show the conductance plot for a longer chain, where the lowest-energy resonance is now more homogenous along the chains and closer to the induced gap. The small offset from $eV = \pm(\Delta_{\text{tip}} + \Delta_p)$ originates from the energy-dependent density of states in the superconducting tip and is not due to finite-size effects.

[1] S. Nadj-Perge, I.K. Drozdov, J. Li, H. Chen, S. Jeon, J. Seo, A.H. MacDonald, B.A. Bernevig, A. Yazdani, Science **346**, 602 (2014).
[2] M. Ruby, B.W. Heinrich, J.I. Pascual, and K.J. Franke, Phys. Rev. Lett. **114**, 157001 (2015).
[3] Y. Peng, F. Pientka, L.I. Glazman, and F. von Oppen, Phys. Rev. Lett. **114**, 106801 (2015).
[4] Y. Peng, F. Pientka, Y. Vinkler-Aviv, L.I. Glazman, F. von Oppen, arXiv:1506.06763 (2015).

Acknowledgement

Many people deserve my gratitude, as they accompanied me during my PhD studies, and contributed in different ways to my work and my life.

First of all, I thank Prof. Dr. Katharina Franke (...ok ok ...simply Katharina ☺) for her support in every possible way. Almost eight years ago, she inspired me with her lectures on atomic and molecular physics, and conveyed to enter the field of scanning probe microscopy. Not only professionally wise she was a great supervisor, and her capacity to lead a large research group impressed me a lot. Thanks for the marvelous time.

Second, I want to thank Dr. Benjamin Heinrich, who taught me my experimental expertise. Whenever I came to him with some cool idea, he did not dare to ask nasty questions to destr... *eehmm*... make me rethink possible problems. He showed me that science is mainly about perfection.

Third, my admiration goes to my co-workers from the theory group, Prof. Dr. Felix von Oppen, Dr. Falko Pientka, and Yang Peng. They helped in so many different ways, especially by showing us new perspectives, and a totally different viewpoint from what we are used as experimental physicists. Working with them was fruitful and interesting.

Fourth, I want to mention my friend Dr. Nino Hatter, with whom I had funny, exciting, dangerous, unique, interesting, and hilarious moments. Not only during the hard work in the lab, but also on our various journeys to places around the world.

Fifth, I want to pay tribute to some of the members of our research group with which I spent a lot of time. There is Gelavizh Ahmadi, with whom I had many interesting discussions during our time in the office and the 'Kantine'. She is one of the people I admire for her experience in life. My gratitude then goes to Daniela Rolf. She is the rational calm anchor of the group, and open to talk about everything on one side, and pushes the group to social activities on the other side. I still think of the scratches I contracted during the boulder club, and the sunburn I got from the volleyball club. Furthermore, I also want to mention Laëtitia Farinacci, who is among the best experts on Kondo physics I got to know. She was an important member of our "Kindergarten Office", whose motto may be summarized with: 'Always have hoaxes and fun ...and don't forget the chewing gum ☺'. Finally, I want to thank and express my best wishes to Eva Liebhaber, my successor in the JT-lab and, during the Christmas parties, as Santa Claus. I am sure that she will do extraordinary science while always being in a good mood.

Finally, I should mention all other members and former members of Katharina's group, whom I thank for the great time and the many discussions, professionally wise and privately interesting. Especially, I enjoy thinking back of the time in the lab together with the bachelor and master students I had to advise, which were: Martin Trabant, Wibke Bronsch, Olof Peters, Daniela Zahn, Sergey Trishin, Marc Font Gual, and Lisa Rütten.

Last but not least, my gratitude goes to my parents Dr. Annemarie Kleinert and Dr. Hagen Kleinert. They covered my back and were always supporting in so many aspects. Without the wonderful atmosphere in our family I could not have led a life in harmony during 27 great years.

I furthermore acknowledge the designers of the LaTeX template that I modified to create this thesis. The original template is published on LaTeXTemplates.com under terms of the CC BY-NC-SA 3.0 license.

Curriculum Vitae

— Curriculum Vitae not included in the online version of this thesis —

Publications related to this thesis:

M. Ruby, B. W. Heinrich, J. I. Pascual, and K. J. Franke
Experimental Demonstration of a Two-Band Superconducting State for Lead Using Scanning Tunneling Spectroscopy
Physical Review Letters **114**, 157001 (2015), doi:10.1103/PhysRevLett.114.157001

M. Ruby, F. Pientka, Y. Peng, F. von Oppen, B. W. Heinrich, and K. J. Franke
Tunneling Processes into Localized Subgap States in Superconductors
Physical Review Letters **115**, 087001 (2015), doi:10.1103/PhysRevLett.115.087001

M. Ruby, F. Pientka, Y. Peng, F. von Oppen, B. W. Heinrich, and K. J. Franke
End states and subgap structure in proximity-coupled chains of magnetic adatoms
Physical Review Letters **115**, 197204 (2015), doi:10.1103/PhysRevLett.115.197204

N. Hatter, B. W. Heinrich, M. Ruby, J. I. Pascual, and K. J. Franke
Magnetic anisotropy in Shiba bound states across a quantum phase transition
Nature Communications **6**, 8988 (2015), doi:10.1038/ncomms99888

M. Ruby
SpectraFox: A free open-source data management and analysis tool for scanning probe microscopy and spectroscopy
SoftwareX **5**, 31 (2016), doi:10.1016/j.softx.2016.04.001

M. Ruby, Y. Peng, F. von Oppen, B. W. Heinrich, and K. J. Franke
Orbital Picture of Yu-Shiba-Rusinov Multiplets
Physical Review Letters **117**, 186801 (2016), doi:10.1103/PhysRevLett.117.186801

Publications in preparation related to this thesis:

M. Ruby, B. W. Heinrich, Y. Peng, F. von Oppen, and K. J. Franke
Exploring a proximity-coupled Co chain on Pb(110) as a possible Majorana platform
in preparation (2017)

M. Ruby, Y. Peng, F. von Oppen, B. W. Heinrich, and K. J. Franke
Formation of bonding and anti-bonding Yu-Shiba-Rusinov multiplets
in preparation (2017)

Publications not related to this thesis:

T. R. Umbach, I. Fernández-Torrente, M. Ruby, F. Schulz, C. Lotze, R. Rurali, M. Persson, J. I. Pascual, K. J. Franke
Atypical charge redistribution over a charge-transfer monolayer on a metal
New Journal of Physics **15**, 083048 (2013), doi:10.1088/1367-2630/15/8/083048

Contributions to conferences:

poster DPG-Frühjahrstagung der 'Sektion Kondensierte Materie' in Berlin 2012/02/27-03/02
Electron Localization in a Charge Transfer Salt on Au(111)

talk Workshop of the SFB 658-Integrated Research Training Group in Zeuthen 2013/05/16-05/17
Electron Momentum Anisotropy in Superconducting Tunneling Junctions

poster 543th WEH-Seminar in Bad Honnef 2013/10/28-10/31
Probing Two-Band Gap Anisotropy in Superconducting Tunnel Junction

talk DPG-Frühjahrstagung der 'Sektion Kondensierte Materie' in Dresden 2014/03/31-04/04
Probing Two-Band Superconductivity by Scanning Tunneling Spectroscopy

poster 563th WEH-Seminar in Bad Honnef 2014/05/19-05/21
Quantum interference in tunneling through a molecular Kondo system

talk Workshop of the SFB 658-Integrated Research Training Group in Lübben 2014/10/09-10/10
Probing the Fermi surfaces of the two-band superconductor Pb

poster 575th WEH-Seminar on in Bad Honnef 2014/11/17-11/19
Quantum interference in tunneling through a molecular Kondo system

talk DPG-Frühjahrstagung der 'Sektion Kondensierte Materie' in Berlin 2015/03/16-03/20
Probing the Fermi Surfaces of the two-band Superconductor Pb

poster DPG-Frühjahrstagung der 'Sektion Kondensierte Materie' in Berlin 2015/03/16-03/20
Tunneling processes into localized subgap states in superconductors

poster DPG-Frühjahrstagung der 'Sektion Kondensierte Materie' in Berlin 2015/03/16-03/20
Quantum interference in tunneling through a molecular Kondo system

talk European Conference on Surface Science (ECOSS) in Barcelona 2015/08/31-09/04
Tunneling processes into localized subgap states in superconductors

poster 598th WEH-Seminar on in Bad Honnef 2015/11/02-11/05
End states and subgap structure in proximity-coupled chains of magnetic adatoms

poster Majorana Workshop 2016 in Mainz 2016/02/22-02/25
End states and subgap structure in proximity-coupled chains of magnetic adatoms

talk DPG-Frühjahrstagung der 'Sektion Kondensierte Materie' in Berlin 2016/03/07-03/11
Tunneling processes into localized subgap states in superconductors

poster 628th WEH-Seminar in Bad Honnef 2016/11/14-11/18
Orbital Picture of Yu-Shiba-Rusinov Multiplets

Selbständigkeitserklärung

Hiermit versichere ich, Michael KLEINERT, dass diese Dissertation von mir selbständig verfasst wurde. Die in dieser Arbeit präsentierten Werke wurden unter meinem offiziellen Pseudonym Michael RUBY veröffentlicht. Sämtliche Stellen, an denen ich auf Hilfsmittel und Veröffentlichungen anderer zurückgegriffen habe, oder die Hilfe von anderen in Anspruch genommen habe, wurden entsprechend kenntlich gemacht. Diese Arbeit wurde zu keinem Zeitpunkt in einem früheren Promotionsverfahren eingereicht.